

**Institute of Bioorganic Chemistry  
Polish Academy of Sciences**

MSc Anna Wychowaniec

**Multi-analyte fluorescent small molecule probes  
for investigation of biologically relevant  
local microenvironment**

Doctoral dissertation

**Supervisor:** Dr hab. Jacek Ł. Kolanowski

**Assistant supervisor:** Dr Eng. Michał Jakubczyk

The work was prepared in the Department of Molecular Probes and Prodrugs

Poznań 2024



Experimental work described in this manuscript was carried out as a part of the project entitled “Low-molecular weight tools to investigate local microenvironment of proteins” funded by OPUS grant by National Science Center (grant no. 2018/29/B/ST4/01498). The infrastructure used for this work was also supported by the funding from the Ministry of Science and Higher Education in Poland within the project POL-OPENSREEN (decision no. DIR/WK/2018/06).



## ACKNOWLEDGEMENTS

First of all, I would like to thank all the members of the Department of Molecular Probes and Prodrugs as well as the Laboratory of Molecular Assays and Imaging. It has been and continues to be a very worthwhile journey, full of adventures, mutual support, lots of smiles, and a great sense of humor.

Above all, I would like to thank my supervisor and mentor, Dr hab. Jacek Ł. Kolanowski, for his inspiration, energy, motivation, time devoted to me, and almost the gentlest expression of criticism of anyone I know. Despite the distance that now separates us, the years devoted to my training have enabled me to now navigate the meanders of experiments almost on my own. The critical thinking I have trained under your guidance is in fact a lifelong learning experience. It is thanks to you that I have also dared to speak out more in public. Much of this is due to the cordial atmosphere at each of our lab group meetings. Thank you for giving me the opportunity to carry out this research and for the time you devoted to this work. At the same time I would like to thank Dr Dorota Kwiatek for her support in my time of need.

To Dr Michał Gładysz, for the endless moments together, every bit of patience, being always supportive, all the help and every smile. I am not sure if you are aware of how much of a positive impact you have on those around you with your personality.

To Dr Eng. Michał Jakubczyk for teaching me discipline in the lab, sharing knowledge, pro-tips and often sitting together in our room until the evening hours. It was not until I was under your wing, at the end of my lab struggles, that I felt what lab work was all about. Thank you for everything you brought to this work.

To all those who made it possible for me to complete the steps of my research. Dr. Agnieszka Fedoruk-Wyszomirska for showing me the world of confocal microscopy. Dr. Dorota Gurda-Woźna for sharing with me the nuances of cell culture. Dr. Łukasz Marczak for allowing me to perform the (how important!) analyses at his Laboratory. MSc Adrian Rūfli for our tests of my final probe.

My support group of PhD students, i.e. Francesca Canyelles I Font, Kinga Pokrywka and Lihn H. Tran. We were bound together by this shared adventure. We ended up here each from almost a different corner of the globe. There is something beautiful about being able to relive our beautiful moments together on the research path (and more often than not, however, complain together about the experiments). Thank you, Francesca, for those years together in the same room, watching over me and helping me with the experiments. I would also like to thank Kinga for her help in the recent battles with protein purification and beyond.

Finally, I would like to thank my Family. To my husband Kamil, for every moment spent together. My sister Asia for the love for life we share. My grandparents for everything.



# TABLE OF CONTENTS

ACKNOWLEDGEMENTS .....	5
ABSTRAKT .....	10
ABSTRACT .....	12
ABBREVIATIONS .....	14
1. Introduction.....	16
1.1. Intracellular microenvironment .....	16
1.1.1. Importance of the intracellular microenvironment .....	16
1.1.2. Importance of intracellular polarity .....	17
1.1.3. Importance of intracellular viscosity .....	19
1.1.4. Importance of intracellular pH .....	20
1.1.5. Importance of carbonic anhydrase .....	22
1.2. Fluorescence as imaging method .....	25
1.2.1. Physical basis of fluorescence .....	25
1.2.2. Tools for fluorescence imaging in biology .....	28
1.2.3. Scaffolds used for fluorescence imaging .....	31
1.3. Fluorescent responsive probes .....	34
1.3.1. Types of responses of fluorescent probes to the analytes .....	34
1.3.2. Probes responsive to polarity changes.....	37
1.3.3. Probes responsive to viscosity changes .....	40
1.3.4. Probes responsive to pH changes .....	43
1.3.5. Multi-analyte responsive probes to polarity/viscosity/pH changes .....	45
1.4. Strategies for intracellular fluorescent labeling .....	47
1.4.1. Classical tools for intracellular fluorescent labeling.....	47
1.4.2. Target labeling through genetic modification.....	49
1.4.3. Labeling of unmodified proteins .....	53
1.4.4. Ligand-directed affinity labeling LD.....	58
2. Aim of the thesis.....	60
3. Materials and methods .....	61
3.1. Materials and instruments .....	61
3.2. Synthesis details .....	63
3.2.1. General notes .....	63
3.2.2. Synthesis of intermediate compounds for the probe SOLpH1 .....	64
3.2.3. Synthesis of the final compound: probe SOLpH1.....	68
3.2.4. Synthesis of intermediate compounds for the probe SOLpH2 .....	69

3.2.5.	Synthesis of the final compound: probe SOLpH2.....	72
3.2.6.	Synthesis of the intermediate and control compound for the probe SOLpH1-Tos .....	73
3.2.7.	Synthesis of the final compound: probe SOLpH1-Tos.....	76
3.3.	Properties of fluorophores .....	77
3.3.1.	Optical properties.....	77
3.3.2.	pK <sub>a</sub> calculation .....	78
3.3.3.	Interference to pH detection.....	78
3.3.4.	Polarity changes sensing .....	79
3.3.5.	Viscosity changes sensing.....	79
3.4.	Cellular experiments .....	80
3.4.1.	Human cell culture and fluorescent live-cell imaging .....	80
3.4.2.	pH-dependent fluorescent live-cell imaging .....	80
3.5.	hCAII <i>in vitro</i> experiments .....	81
3.5.1.	Labeling experiments of the probe SOLpH1-Tos and SOLpH1-Bz for hCAII .....	81
3.5.2.	pH-dependent emission of the SOLpH1-Tos labeled to hCAII.....	81
3.5.3.	Evaluation of the enzymatic activity of hCAII labeled with SOLpH1-Tos .....	82
4.	Results and discussion.....	83
4.1.	Multianalyte polarity/viscosity/pH probe based on SBD (SOLpH1) .....	83
4.1.1.	Design of SOLpH1 .....	83
4.1.2.	Synthesis and characterization of SOLpH1.....	86
4.1.3.	Optical properties of SOLpH1.....	89
4.1.4.	Fluorescence response of SOLpH1 to pH .....	92
4.1.5.	Polarity-sensing properties of SOLpH1.....	96
4.1.6.	Viscosity-sensing properties of SOLpH1.....	102
4.1.7.	The effects of other biologically-relevant analytes .....	105
4.1.8.	Cellular localization of SOLpH1.....	109
4.1.9.	Intracellular pH-detection by SOLpH1.....	115
4.1.10.	Summary and discussion .....	118
4.2.	Multianalyte polarity/viscosity/pH probe based on naphthalimides (SOLpH2) .....	120
4.2.1.	Design of SOLpH2 .....	120
4.2.2.	Synthesis and characterization of SOLpH2.....	121
4.2.3.	Optical properties of SOLpH2.....	124
4.2.4.	Fluorescence response of SOLpH2 to pH .....	126
4.2.5.	Polarity-sensing properties of SOLpH2.....	129
4.2.6.	Viscosity-sensing properties of SOLpH2.....	133
4.2.7.	The effects of other biologically-relevant analytes .....	135



4.2.8.	Cellular localization of SOLpH2.....	139
4.2.9.	Intracellular pH-detection by SOLpH2.....	142
4.2.10.	Summary and discussion .....	144
4.3.	Ligand-directed affinity labeling probe (SOLpH1-Tos) .....	145
4.3.1.	Design of SOLpH1-Tos .....	145
4.3.2.	Synthesis and characterization of SOLpH1-Tos and SOLpH1-Bz .....	149
4.3.3.	Labeling experiments of human carbonic anhydrase II .....	152
4.3.4.	pH-dependent emission of SOLpH1 labeled to hCAII.....	157
4.3.5.	Evaluation of the enzymatic activity of hCAII labeled with SOLpH1-Tos .....	160
4.4.	Summary and discussion .....	164
5.	Conclusions and future impact.....	165
6.	Bibliography.....	168
7.	Supplementary data .....	194
7.1.	$^1\text{H}$ & $^{13}\text{C}$ NMR spectra .....	194
7.2.	HRMS-ESI spectra .....	213
7.3.	Spectroscopic studies .....	216

## ABSTRAKT

Komórki można porównać do nano-fabryk, w których kompartmentalizacja umożliwia zachodzenie przeciwstawnych procesów w tym samym czasie. Pomimo wieloletnich badań, szczegółowy wgląd w czasie rzeczywistym w te reakcje i poszczególne zmiany w nano-środowisku komórek pozostaje wyzwaniem. Obecnie dostępne metody koncentrują się głównie na określaniu zmian w całym regionie (np. organelle) lub nie są możliwe do wdrożenia *in cellulo*, bez zakłócania całego systemu i utraty wielu informacji (np. przy izolacji i testach *in vitro* makrocząsteczek). Uzyskanie bardziej szczegółowego obrazu na poziomie nanometrów zmieni sposób, w jaki patrzymy na procesy fizjologiczne i patologiczne, przybliżając nas do precyzyjnego zrozumienia i leczenia na poziomie molekularnym.

Środowisko wewnątrzkomórkowe podlega wielu zmianom jednocześnie. Obserwacja tych zmian jest w dużej mierze niemożliwa bez użycia specjalistycznych narzędzi, ponieważ większość elementów środowiska komórkowego nie generuje wykrywalnego sygnału. Jedną z takich metod zapewniających doskonałą rozdzielczość i powodujących minimalne zakłócenia homeostazy komórek jest obrazowanie fluorescencyjne. W szczególności, wrażliwe na środowisko narzędzia fluorogeniczne mają ogromny potencjał w monitorowaniu zmian, które w innym przypadku nie byłyby obserwowalne. Sondy fluorogeniczne stają się fluorescencyjne dopiero po interakcji z wybranym analitem, co pozwala na bardziej wiarygodne obrazowanie bez konieczności ich usuwania (tzw. „no-wash” znakowanie).

Aby uzyskać informacje na temat określonego celu (np. enzymu), sondy mogą być kowalencyjnie przyłączone do celu molekularnego. Jedną z najbardziej obiecujących metod znakowania opisanych w literaturze jest znakowanie oparte na powinowactwie. Sondy te składają się z trzech komponentów: odwracalnego liganda selektywnego względem białka (celu), grupy reaktywnej (podatnej na atak wybranego aminokwasu na białku) oraz części reporterowej (fluoroforu). Sondy te oferują selektywne znakowanie fluorescencyjne białek bez potrzeby modyfikacji genetycznej, umożliwiając potencjalną obserwację naturalnej aktywności celu. Teoretycznie sondy te mogą dostarczać informacji o analitach w mikrośrodowisku celu, umożliwiając obserwacje w czasie rzeczywistym, *in cellulo*, przy użyciu zaawansowanego obrazowania (np. mikroskopii superrozdzielczej). Jak dotąd nie osiągnięto jednak dodatkowego wykrywania analitów wokół określonych celów z użyciem tej technologii.

Głównym celem niniejszej pracy było zaprojektowanie, synteza i walidacja dwóch fluorogenicznych cząsteczek wrażliwych na środowisko i przekształcenie jednej z nich w opartą na powinowactwie sondę znakującą dla hCAII w celu wykrycia wybranego analitu (zmiany pH). Aby opracować takie sondy, przeprowadzono kompleksowy przegląd literatury w celu zidentyfikowania dwóch odpowiednich fluoroforów: 4-sulfonamidu benzo[c][1,2,5]oksadiazolu i 1,8-naftalimidu. Synteza docelowych sond opierała się na ustalonych metodach literaturowych, a wybrane fluorofory zostały zsyntetyzowane i wykorzystane do wytworzenia dwóch sond: **SOLpH1** i **SOLpH2** (potwierdzone metodami  $^1\text{H}$  NMR,  $^{13}\text{C}$  NMR i HRMS). Sondy te zostały tak zaprojektowane, aby były fluorogeniczne i wrażliwe na zmiany fizykochemiczne w ich najbliższym mikrośrodowisku (zmiany pH i/lub zmiany polarności). Ich fluorogeniczna natura była bezpośrednio związana z ich właściwościami wykrywania pH. Obie cząsteczki posiadają pierścień piperazynowy, z jedną wolną parą na atomie azotu niezaangażowaną w  $\pi$ -sprężone układy aromatyczne. Przy

wysokim pH sondy nie powinny emitować fluorescencji lub fluoryzować słabo z powodu wygaszania PeT. Gdy pH mikrośrodowiska spada, azot ulega protonowaniu i obserwuje się wzrost fluorescencji.

Zmierzono emisję sond oraz ich wrażliwość na polarność i lepkość w obecności zestawu biologicznie istotnych analitów. Podstawowe właściwości fotofizyczne (wydajność kwantowa fluorescencji, współczynnik ekstynkcji, jasność) zostały określone dla obu sond przy dwóch różnych wartościach pH (4,0 i 7,5) z wykorzystaniem wzorców o znanych właściwościach. Przeprowadzono eksperymenty kolokalizacji z trackerami mitochondriów i lizosomów w dwóch różnych liniach komórkowych (zdrowej HEK293T i nowotworowej A549). Ostatnim krokiem była wewnątrzkomórkowa detekcja pH w linii komórkowej HEK293T. **SOLpH1** został następnie wprowadzona do sondy znakowanej powinowactwem, **SOLpH1-Tos**. Sondę **SOLpH1-Tos** inkubowano z jej potencjalnym celem, hCAII (48 godzin), mieszaninę poddano trawieniu trypsyną, a uzyskane peptydy przeanalizowano w celu zidentyfikowania możliwych miejsc znakowania. Na koniec zbadano właściwości detekcji pH i aktywność enzymatyczną znakowanego białka **SOLpH1-hCAII**. Przeprowadzone eksperymenty potwierdziły oczekiwane właściwości nowych struktur fluoroforowych. Obie sondy wykazały właściwości pH-czułe ze wzrostem emisji pomiędzy pH=4.0 i pH=8.0 (14-krotny wzrost **SOLpH1** (exc/em 420/600 nm) i 13-krotny wzrost dla **SOLpH2** (exc/em 390/530 nm). Ich obliczone  $pK_a$  wynosiło odpowiednio 6.4 (**SOLpH1**) i 6.5 (**SOLpH2**), co czyni je odpowiednimi do zastosowań in cellulo. **SOLpH1** wykazał większe zmiany przesunięcia Stokesa między dwoma najbardziej polarnymi rozpuszczalnikami/roztworami i wykazał wyższą intensywność emisji wraz ze spadkiem polarności rozpuszczalnika. **SOLpH2**, z drugiej strony, zachował się w przeciwny sposób. Podczas gdy zarówno **SOLpH1**, jak i **SOLpH2** reagują na zmiany lepkości, w bardziej lepkich środowiskach **SOLpH1** wykazuje 12,5-krotny wzrost intensywności emisji, podczas gdy **SOLpH2** wykazuje fluktuacje intensywności emisji wraz ze zmianą lepkości. Eksperymenty kolokalizacyjne nie wykazały preferencji sond do lokalizacji w mitochondriach lub lizosomach. Co więcej, obie sondy były w stanie z powodzeniem monitorować wewnątrzkomórkowe zmiany pH.

Dokładne analizy uzyskanych danych doprowadziły do wyboru **SOLpH1** do dalszego rozwoju w kierunku sondy znakującej opartej na powinowactwie, **SOLpH1-Tos**. **SOLpH1-Tos** składa się z krótkiego łącznika z glikolu etylenowego, grupy reaktywnej tosylian/tosyl, łącznika kadawerynowego i odwracalnego inhibitora hCAII, benzenosulfonamidu. Eksperyment znakowania in vitro ludzkiej anhidrazy węglanowej II za pomocą sondy **SOLpH1-Tos** zakończył się sukcesem, a analiza uzyskanych danych potwierdziła reakcję zachodzącą między **SOLpH1-Tos** a aminokwasem znajdującym się w pobliżu miejsca aktywnego enzymu (histrydyna His64 przy wejściu do miejsca aktywnego białka, w przeciwieństwie do His67 w publikacji źródłowej). **SOLpH1-Tos** jest, zgodnie z posiadaną przez nas wiedzą, pierwszą sondą wrażliwą na pH do znakowania białek docelowych w oparciu o powinowactwo, bez konieczności stosowania genetycznie zakodowanego znacznika. Ta nowa sonda wykazuje użyteczność cząsteczki w eksperymentach opartych na pH, a po przyłączeniu do ludzkiej anhidrazy węglanowej II może zapewnić wgląd w niewielkie zmiany pH w bezpośredniej bliskości miejsca aktywnego enzymu. Takie lokalne zmiany pH mogą być istotne dla funkcji białka, potencjalnie kluczowe dla procesów fizjologicznych i patologicznych.

**Słowa kluczowe:** sondy wieloanalitowe, sondy responsywne, sondy fluorescencyjne, obrazowanie fluorescencyjne, sondy wrażliwe na środowisko, znakowanie oparte na powinowactwie

## ABSTRACT

Cells can be likened to nano-factories, where compartmentalization enables opposing processes to occur simultaneously. Despite years of research, obtaining a detailed real-time view of these reactions and the specific changes in the cellular nanoenvironment remains a challenge. Current methods focus on measuring changes within a whole region (e.g. organelle) or require disturbing the whole system, resulting in significant information loss (e.g. with isolation of chosen macromolecules and *in vitro* tests). Acquiring a more detailed picture at the nano scale will change the way we understand physiological and pathological processes, leading us closer to molecular-level understanding and precision treatments.

The intracellular environment undergoes multiple changes concurrently. Observation of these changes is largely impossible without use of specialized tools and techniques as most components of cellular environments do not intrinsically generate detectable signal. One such method providing excellent resolution and causing minimal disturbance to cell homeostasis is fluorescence imaging. In particular, environment-sensitive fluorogenic tools have great potential in monitoring otherwise non-observable changes. Fluorogenic probes become fluorescent only upon interaction with a chosen analyte, allowing for the possibility of more reliable imaging without the need for their removal (so called “no-wash” staining).

To gain information about a specific target (e.g. an enzyme), probes can be directed using a covalently attached sensing group. One of the most promising labelling methods described in the literature is known as affinity-driven (or affinity-based) labelling. These probes consist of three components: a reversible ligand selective to the target, a reactive group (prone to attack of a chosen amino acid on the target'), and a reporter part (fluorophore). These probes offer selective fluorescent labelling of target proteins without the need for genetic modification, allowing potential observation of natural target activity. In theory, these probes could provide information about analytes in the target's microenvironment, enabling real-time, *in cellulo* observations using advanced imaging (e.g. super-resolution microscopy). However, additional analyte detection around specific targets has not yet been achieved with affinity-driven probes.

The main objective of the current work was to design, synthesize and validate two fluorogenic environment-sensitive fluorophores and transform one of them into an affinity-based labelling probe for hCAII to possibly detect a chosen analyte (pH changes). To develop such probes, a comprehensive literature review was performed to identify two suitable fluorescent scaffolds: 4-sulfonamide benzo[c][1,2,5]oxadiazole and 1,8-naphthalimide. Synthesis of the final probes were based on established literature methods, and the selected scaffolds were synthesized and furnished to successfully produce two probes: **SOLpH1** and **SOLpH2** (confirmed by <sup>1</sup>H NMR, <sup>13</sup>C NMR and HRMS methods). These probes were designed with environment-sensitive properties, making them fluorogenic and sensitive to physicochemical changes in their closest microenvironment (pH changes and/or polarity changes). Their fluorogenic nature was directly related with their pH-sensing properties. Both molecules bear a piperazine ring, with one lone pair on the nitrogen atom not engaged in the  $\pi$ -conjugated aromatic systems. At high pH the probes should not emit fluorescence or fluoresce poorly due

to PeT quenching. Once the pH of microenvironment decreases, the nitrogen becomes protonated and an increase in fluorescence is observed.

The probes' emissions and sensitivity to polarity and viscosity was measured in presence of a set of biologically relevant analytes. Basic photophysical properties (fluorescence quantum yield, extinction coefficient, brightness) were determined for both probes at two different pH values (4.0 and 7.5) with use of standards with known properties. Colocalization experiments with mitochondria and lysosomes trackers in two different cell lines (healthy HEK293T and cancerous A549) were conducted. The last step was intracellular pH-detection in HEK293T cell line. The **SOLpH1** probe was then introduced into an affinity-labeling one, **SOLpH1-Tos**. The probe **SOLpH1-Tos** was incubated with its potential target, hCAII (48 hours), the mixture was digested with trypsin and the obtained peptides were analyzed to identify possible labeling locations. Last but not least, pH-sensing properties and enzymatic activity of **SOLpH1**-hCAII labeled protein were studied. The conducted experiments confirmed the expected properties of the novel fluorophore structures. Both probes showed pH-sensing properties with an increase of emission between pH=4.0 and pH=8.0 (14-fold increase **SOLpH1** (exc/em 420/600 nm) and 13-fold increase for **SOLpH2** (exc/em 390/530 nm). Their calculated  $pK_a$  were respectively 6.4 (**SOLpH1**) and 6.5 (**SOLpH2**), making them both suitable for *in cellulo* applications. **SOLpH1** exhibited larger Stokes shift changes between the two most polarity-extreme solvents/solutions, and showed higher emission intensity as polarity of the solvent decreased. **SOLpH2**, on the other hand, behaved in the opposite manner. While both **SOLpH1** and **SOLpH2** respond to viscosity changes, in more viscous environments, **SOLpH1** displays a 12.5-fold emission intensity increase, while **SOLpH2** presented fluctuating emission intensity with changing viscosity. Finally, colocalization experiments did not suggest any preference of the probes to localize in mitochondria or lysosomes. Furthermore, both probes were successfully able to monitor intracellular pH-changes.

Careful analyses of the obtained data resulted in the selection of **SOLpH1** for further development towards an affinity-based labeling probe, **SOLpH1-Tos**. **SOLpH1-Tos** consists of a short ethylene glycol linker, tosylate/tosyl reactive group, cadaverine linker and reversible inhibitor for hCAII, benzenesulfonamide. The *in vitro* labeling experiment of human carbonic anhydrase II with the probe **SOLpH1-Tos** was successful, and analysis of resulting data confirmed a reaction occurring between **SOLpH1-Tos** and an amino acid in close proximity to the active site of the enzyme (histidine His64 at the entrance of the protein's active site, as opposed to His67 in the source publication). **SOLpH1-Tos** is, to the best of our knowledge, the first pH-sensitive probe for affinity-driven labeling of a protein target without the need of genetically encoded tag use. This novel probe displays utility molecule in pH-based experiments, and once attached on human carbonic anhydrase II, could provide insight into minor pH changes in immediate proximity to the active site of the enzyme. Such local pH changes may be critical for protein function, potentially crucial to physiological and pathological processes.

**Keywords:** multi-analyte probes, responsive probes, fluorescent probes, fluorescent imaging, environment-sensitive probes, affinity labeling

## ABBREVIATIONS

**A549** – adenocarcinomic human alveolar basal epithelial cells isolated from lung tissue

**abs** – absorption

**ACN** – acetonitrile

**AIE** – aggregation-induced emission

**anh.** – anhydrous

**a.u.** – auxiliary units

**B-R buffer** – Britton-Robinson buffer

**C343** – coumarin 343

**CPB** – citrate phosphate buffer

**DCM** – dichloromethane

**DIPEA** - *N,N*-diisopropylethylamine

**DMAP** – 4-dimethylaminopyridine

**DMEM** – Dulbecco's Modified Eagle Medium

**DMF** – dimethylformamide

**DMSO** – dimethyl sulfoxide

**DTT** – dithiotreitol

**em** – emission

**ER** – endoplasmic reticulum

**EtOH** – ethanol

**ESIPT** – excited state intramolecular proton transfer

**exc** - excitation

**FBS** – fetal bovine serum

**FLUO** – fluorescein

**FRET** – Förster resonance energy transfer, fluorescence resonance energy transfer

**hCAII** – human carbonic anhydrase II

**HEK293T** – human embryonic kidney 293T cells

**HEPES** - 4-(2-hydroxyethyl)-1-piperazineethanesulfonic acid

**Hex** – hexane

**HOMO** – highest occupied molecular orbital

**IAA** – iodoacetamide  
**ICT** – intramolecular charge transfer  
**IR** – infrared  
**LTDR** – LysoTracker Deep Red  
**LUMO** – lowest unoccupied molecular orbital  
**MeOH** – methanol  
**MiliQ** – ultrapure water  
**MTDR** – MitoTracker Deep Red  
**NBD** – 4-nitrobenzo[*c*][1,2,5]oxadiazole  
**NMR** – nuclear magnetic resonance  
**PICT** – planar intramolecular charge transfer  
**PB** – phosphate buffer  
**PBS** – phosphate buffer saline  
**PEG** – polyethylene glycol  
**PeT** – photoinduced electron transfer  
**PROTAC** – proteolysis targeting chimera  
**pTLC** – preparative thin layer chromatography  
**RT** – room temperature  
**SBD** – 4-sulfonamide benzo[*c*][1,2,5]oxadiazole  
***t*BDMS** – *tert*-butyldimethylsilyl functional group  
**TES** – triethylsilane  
**TFA** – trifluoroacetic acid  
**THF** – tetrahydrofuran (oxolane)  
**TICT** – twisted intramolecular charge transfer  
**TMS** – tetramethylsilane  
**TLC** – thin layer chromatography  
**Tris** – tris(hydroxymethyl)aminomethane buffer  
**QS** – quinine sulphate  
**QY** – quantum yield  
**quant.** – quantitative / quantitatively

# 1. Introduction

## 1.1. Intracellular microenvironment

### 1.1.1. Importance of the intracellular microenvironment

The cellular microenvironment consists of physical and chemical signals that can influence cellular behavior in direct and indirect ways [1]. The intracellular environment is formed by a range of macromolecules (proteins, RNA/DNA, complex sugars) and small molecules (e.g. lipids, sugars, amino acids, reactive oxygen and nitrogen species, metal ions, etc.) [1, 2]. Moreover, physical parameters and mechanical forces due to movement of these components also impacts the microenvironment [3]. All cellular components may be additionally affected by changes in the extracellular matrix (ECM) [4].

The extraordinary construction of cell and its compartmentalization enable contradictory processes to occur at the same time within one cell but in different sublocations [5]. While small disturbances to subcellular reactions may be overcome by self-regulation mechanisms, there are limits to cells' ability to regenerate and non-desired processes may occur. Pathological changes may affect multiple components of a single cell, initiating a process potentially leading to disease [3, 6].

The cellular microenvironment plays a critical role in regulating cell behavior and functions, including differentiation, proliferation, and migration [3]. However, the biochemical and structural complexity of this environment limits our understanding of the key parameters that govern cell behavior [1]. Moreover, all the processes remain invisible both to the naked eye and even specialized equipment [7], because most of the elements involved do not produce quantifiable signal [8]. The ability to observe them with sufficient spatiotemporal resolution could improve our understanding of the changes in homeostasis of organisms on a microscopic level that directly translate to the effective phenotypes [9].

Interestingly, even once visualized, single cells within a chosen cell line may vary in some aspect and/or will undergo multiple changes on its own during its lifetime. It was suggested previously that cells within one single cell line may present some fluctuations, e.g. with intracellular viscosity level [10]. This emphasizes the biological complexity and heterogeneity of such systems, highlighting the importance of experimental reproducibility of *in cellulo* studies that are largely dependent on sufficient number of repetitions and the quality of the tools and methods used in minimizing the risk of false conclusions [11].



### 1.1.2. Importance of intracellular polarity

Polarity is a parameter defined by the overall solvation capability (or solvation power) of a solvent. It depends on the combined effects of all possible intermolecular interactions between solvent molecules and solutes, excluding interactions that result in chemical alterations of the solute (such as protonation, oxidation, chemical complex formation or reduction) [12, 13]. As solvent properties often influence reactions (their rate [14], mechanism and selectivity [15], equilibria [16], physical absorption [17] or emission of electromagnetic radiation [18]), one can foresee that intracellular processes (reactions) are affected by local polarity values/fluctuations as well [12, 18]. Increasing solvent polarity *in vitro* results in the formation of bipolar dipoles from solvent molecules, where dipoles may stabilize charge (charged molecules taking part in various reactions) [19, 20]. Moreover, polarity encompasses a range of non-covalent effects, including hydrogen bonding, dipolar interactions, polarizability, and hydration [21].

A similar theory may be applied to processes *in cellulo*, for example, in the case of dipoles localized at  $\alpha$ -helix termini in proteins [22, 23]. Such dipole-charge stabilization has been observed in specific types of proteins, ion channels (potassium, sodium, and chloride ones), where they contribute to the selectivity of ion channels [24, 25]. Moreover, ion-dipole interactions play an important role protein to in substrate/solute binding [26], catalytic intermediate stabilization [27], allosteric catalysis regulation [28], inter- and intraprotein interactions (structural stabilization) [29, 30]. As many cellular activities are regulated by the transient activation of various proteins in specific regions, polarity fluctuations are crucial to investigating protein activity in their native environment [31]. There is increasing evidence that polarity plays a crucial role in various physiological processes, including protein denaturation, conformational changes in enzymes, and peptide aggregation [32].

Most amino acids in enzyme active sites are hydrophobic and the enzyme-substrate complexes are often based on, among others, hydrophobic interactions (hydrophobic effect) [33]. In globular proteins, a hydrophobic core forms where hydrophobic side chains are shielded from water, stabilizing the folded state. Charged and polar side chains are located on the solvent-exposed surface, where they interact with surrounding water molecules. In other words, the primary driving force behind the protein folding process is the minimization of hydrophobic side chains exposed to water *in vitro* or cytosol *in cellulo* [34–36]. Interestingly, while some of enzymes' active site are positioned on the protein's surface, most of them are buried deeply in the structure [37]. Recent literature suggests presence of so-called "enzyme channels", "molecular channels", "enzyme tunnels" or "nanochannels" as transport routes for enzyme substrate within this non-polar core [37–40]. The presence of such transportation routes suggests fluctuations in polarity of this otherwise considered non-polar enzyme core, especially in case of more polar enzyme substrates.

Different organelles perform specialized functions within cells, creating diverse areas of local polarity [13]. This cellular environment is dominated by hydrophobic interactions [41–44], with membrane structure and function heavily influenced by lipid composition, especially cholesterol [31]. The cell membrane's phospholipid bilayer, featuring outward-facing hydrophilic heads and inward-facing hydrophobic tails, facilitates segregation of molecules

into functional clusters [45]. This architecture serves as a selective barrier between polar environments, with some organelles even providing a secondary bilayer for further compartmentalization. Overall, cell polarity serves as a key indicator of cellular status and regulatory mechanisms [46], underpinning crucial processes such as targeted membrane growth, directional cell migration, and precise molecular transport [47]. Importantly, fluctuations in intracellular polarity are closely linked to physiological and pathological states, providing valuable markers for conditions ranging from hepatic steatosis [48] and acute kidney injury to oxidative stress [49], protein aggregation [50], mitochondrial dysfunction [51], and viral infection [52].

Accurate monitoring of polarity changes *in cellulo* is therefore of great importance, but quantification of this parameter poses a significant challenge. Transient, subtle and dynamic changes combined with multiple factors affecting local polarity can interfere with monitoring, especially *in cellulo* [53]. Although several analytical methods, such as electrochemical analysis, spectral analysis, and chromatography, are advancing rapidly, ideal tools for detecting polarity remain scarce. Fortunately, fluorescence imaging technologies have made remarkable progress over the past decade [53]. *In cellulo* quantification of polarity is usually based on data obtained from *in vitro* experiments or connects data obtained from both *in vitro* and *in cellulo* ones. Quantitative estimation of polarity *in vitro* (various non-organic and organic solvents) may be based on the normalized polarity parameter  $E_T^N$  (where tetramethylsilane is given a value = 0 and water value = 1 as highly polar [54]), solvent acidity parameter (SA) and dipolarity scales (SDP) [55]. Further *in vitro* and *in cellulo* experiments using advanced imaging techniques can provide additional valuable information, such as fluorescence quantum yield or fluorescence lifetime values or absorption/emission changes, all of which are sensitive to polarity of the probe's environment [56]. A detailed description of methods used for *in cellulo* polarity quantification with use of fluorescence will be provided in subchapter **1.3.2**.

### 1.1.3. Importance of intracellular viscosity

Viscosity is understood as the resistance of a fluid to deformation caused by shear or tensile stress. The varying chemical and molecular compositions of biofluids influence their viscosity, which in turn can affect the movement of particles within the fluid [57]. Viscosity is a fundamental physical parameter among various cell properties, affecting diffusion and reaction kinetics in biological processes such as protein-protein interactions, signal transduction, and the transport of small solutes, macromolecules, and other cellular organelles in living cells [58]. At the sub-organelle level, microviscosity within e.g. mitochondria significantly affects respiratory states and the tricarboxylic acid cycle. This influence stems from the molecular effects of mechanical or osmotic stress on mitochondrial network organization, suggesting that variations in mitochondrial matrix viscosity can substantially impact mitochondrial metabolism [59]. The viscosity of the cell membrane significantly impacts various physiological processes (e.g. diffusion of small molecules within and across itself), as well as drug delivery and drug diffusion [60].

Viscosity changes were linked with multiple diseases and studied to better understand their importance inside cells. Those fluctuations were observed and analyzed in context of cell membranes construction [61], with a particular focus on, for example, oxidative stress and its relation to the study of neuroprotection [62] or the study of the relationship between the viscosity of mitochondria in brain tissues and the development of neurodegenerative diseases [63]. It is worth noting that the mitochondrial matrix is densely packed with enzymes and other proteins, and their diffusion is significantly restricted by the cristae, making mitochondria the most crowded compartments within cells [64]. Changes in this parameter have been linked to an overall increase in cellular stress, affecting i.a. lysosome function [65] and possibly leading to apoptosis [64].

Intracellular viscosity exhibits considerable heterogeneity, which may pose a challenge in obtaining a comprehensive cellular viscosity map with detailed information on organelles [66]. As mentioned, the viscosity parameter can change not only between different types of cell lines, but also within the same cell population [10]. It has been reported that the local microviscosity within cells ranges from 1 to 400 cP (centipoise; viscosity of water at 20°C is 1 cP) [67, 68]. Reports indicate that viscosity in normal cytoplasm is approximately 1–2 cP, whereas in pathological cells, it can increase significantly to 140 cP or even higher [59, 69]. The significance of membrane viscosity in cellular biology and physiology has driven the development of methods for quantitative measurements based on fluorescence [70]. Similarly to polarity quantification, viscosity measurements may be made based on direct comparison of known properties fluorescent molecules (probes) in set of solvents and *in cellulo* microenvironment [31]. Further information about application of fluorescence in viscosity-sensing is provided in subchapter **1.3.3**.

#### 1.1.4. Importance of intracellular pH

Intracellular pH plays critical roles in various cellular activities, including proliferation, apoptosis, multidrug resistance, ion transport, endocytosis, and muscle contraction [71–73]. Monitoring pH changes inside living cells is essential for studying cellular internalization pathways like phagocytosis and receptor ligand internalization [74]. Intracellular pH changes also affect the nervous system by influencing synaptic transmission, neuronal excitability, and signal cascades [75].

The typical pH values in different compartments are as follows: Golgi apparatus from 6.4 to 6.8, the cytoplasm is around 7.2, the nucleus ranges from 7.2 to 7.4, the endoplasmic reticulum (ER) from 7.0 to 7.4, and the mitochondria is approximately 8.0 [76] (**Figure 1**). Other specific organelles, like endosomes, have acidic pH values (4-6) necessary for protein denaturation or activation of certain enzymes, while lysosomes function optimally at pH 4.5-5.5 (or even 6.5) to degrade proteins [77]. The latter rely on pH to preserve their structure and function, with protonation-deprotonation events determining the charge of biological surfaces and playing a crucial role in many metabolic reactions [78, 79]. One of the most extreme examples are metabolic enzymes, such as the rate-limiting enzyme in glycolysis, phosphofructokinase [80], and the crucial ribosomal protein S6 [81]. Their transition from fully active to fully inactive happens with a pH shift of roughly 0.1 [82].

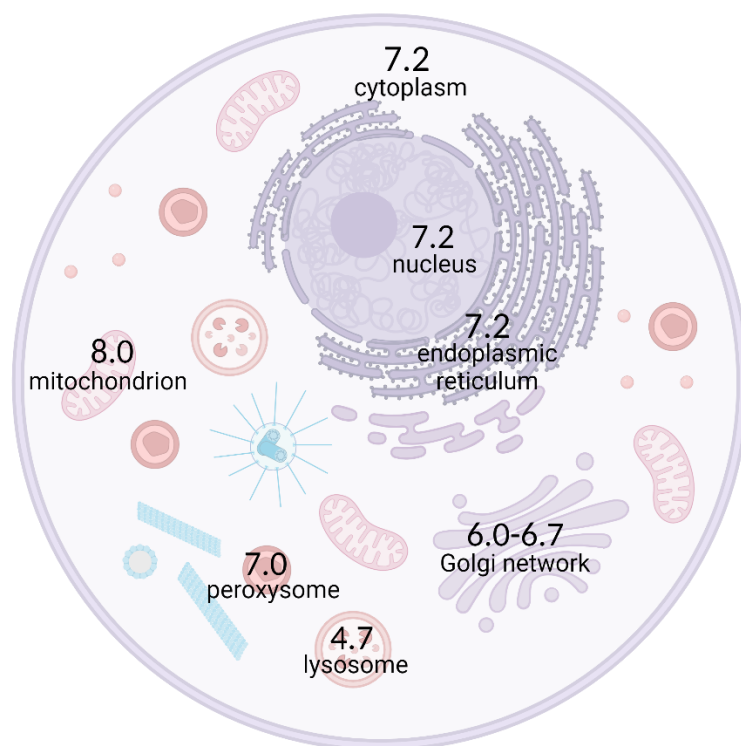


**Figure 1.** Schematic presentation of an animal cell together with average pH values in the different subcellular compartments. The mitochondrial pH refers to the pH of the matrix, the space enclosed by the inner mitochondrial membrane. The pH within the Golgi network may differ depending on the location in the network. Created with BioRender.com.

Protons ( $H^+$ ) play a key role in maintaining cellular pH and energy storage through electrochemical gradients across membranes [78]. Intracellular pH is strictly regulated through buffer systems and transporters, creating an equilibrium within cells [78, 83]. The  $pK_a$  values of intracellular molecules can vary significantly depending on their microenvironment, affecting their protonation and reactivity [78, 79, 84, 85]. Therefore, disruptions in pH equilibrium can lead to abnormal organelle pH levels, which is associated with dysfunction and disease [76, 86]. For instance, cancer cells typically exhibit an elevated intracellular pH ( $>7.4$ ) and reduced extracellular pH ( $<7.2$ ) [87], while Alzheimer's disease is characterized by an acidic intracellular environment [88]. These pH changes can significantly alter protein behavior and cellular processes, contributing to disease progression. Interestingly, the contrasting pH dynamics in cancer and Alzheimer's disease may explain their observed inverse relationship in patients [89]. Consequently, detecting abnormal subcellular pH levels could serve as a promising diagnostic technique for numerous diseases, including neurodegenerative, neuromuscular, infectious, and autoimmune disorders.

Qualitative measurements of intracellular pH can be obtained using fluorescent indicators (probes) that activate or deactivate at specific pH levels [90]. Predicted  $pK_a$  of a probe directed towards a specific organelle/region/compartiment or even tissue should ideally be around the pH of this chosen region (examples: [91, 92]) [93]. Given the significant variations in typical pH levels across cellular compartments and the limited dynamic range of optical pH sensors to 2-3 pH units, different probes must be utilized to achieve optimal resolution for specific applications [94]. Most of the probes described in the literature provide an average information about pH within cellular compartments, without resolution high enough to present slight local fluctuations. Recent reports suggest that visualization of minor changes 0.1-0.2 unit of pH value is possible though [95], especially with continuous development of super-resolution imaging techniques, exceeding the diffraction limit [96–98]. Application of fluorescence in pH-changes measurements is described in detail in subchapter **1.3.4**.

### 1.1.5. Importance of carbonic anhydrase

A significant group of macromolecules that strongly affect the intracellular environment are carbonic anhydrases. Carbonic anhydrases (CAs) are a group of  $Zn^{2+}$ -dependent metalloenzymes that catalyze the reversible conversion of carbon dioxide into bicarbonate [99, 100]. They are involved in various physiological processes in humans, such as respiration, bone metabolism, and the production of body fluids like urine, bile, pancreatic juice, gastric secretion, saliva, aqueous humor, cerebrospinal fluid, and sweat [101, 102]. Carbonic anhydrases provide as well carbon dioxide/bicarbonate for carboxylation reactions that incorporate carbon dioxide into substrates [103]. Additionally, CAs catalyze numerous other reactions, such as conversion of cyanate to carbamic acid, cyanamide to urea, sulfonyl chlorides to sulfonic acids, aldehydes to alcohols [104] (**Figure 2**). Although several isoforms of carbonic anhydrase have been identified in humans, their exact physiological roles and the implications of their dysfunction remain largely unknown, with some of them being considered even without catalytic function (CA VIII, X, and XI) [104, 105]. There are six types of carbonic anhydrases, named alpha, beta, gamma, delta, epsilon, and zeta; all human carbonic anhydrases (hCAs) are alpha-type ( $\alpha$ -type) [106].

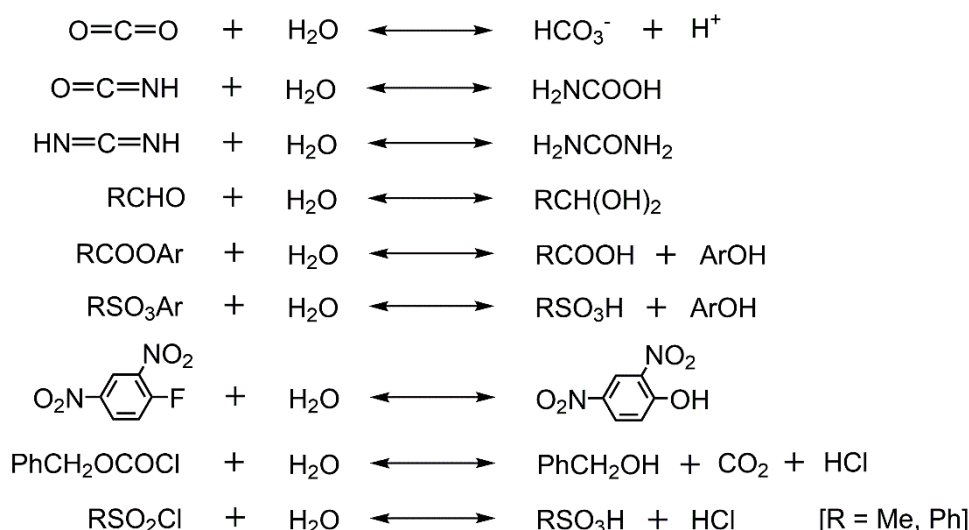


**Figure 2.** Reactions catalyzed by carbonic anhydrases (CAs) present in human organism ( $\alpha$ -CAs). Adapted from [104].

The active site of carbonic anhydrase is situated in a large cone-shaped cavity, with a  $Zn^{2+}$  ion positioned at the bottom [107, 108].  $Zn^{2+}$  is coordinated in a tetrahedral arrangement with three conserved His residues, and  $H_2O$  (or  $OH^-$ , an active form) acts as the fourth ligand. The catalytic mechanism includes two steps. The first step involves a nucleophilic attack by the  $Zn^{2+}$ -bound hydroxide ion on a  $CO_2$  molecule, resulting in the formation of the enzyme- $HCO_3^-$  adduct (B to C). This adduct is then displaced from the active site by a water molecule (C to D). The final step (D to A), which is the rate-limiting step, regenerates the catalytically active  $Zn^{2+}$ -bound hydroxide ion through a proton transfer from the  $Zn^{2+}$ -bound water molecule to an external proton acceptor or an active site [109]. The catalytic mechanism of CA is presented in the **Figure 3**.

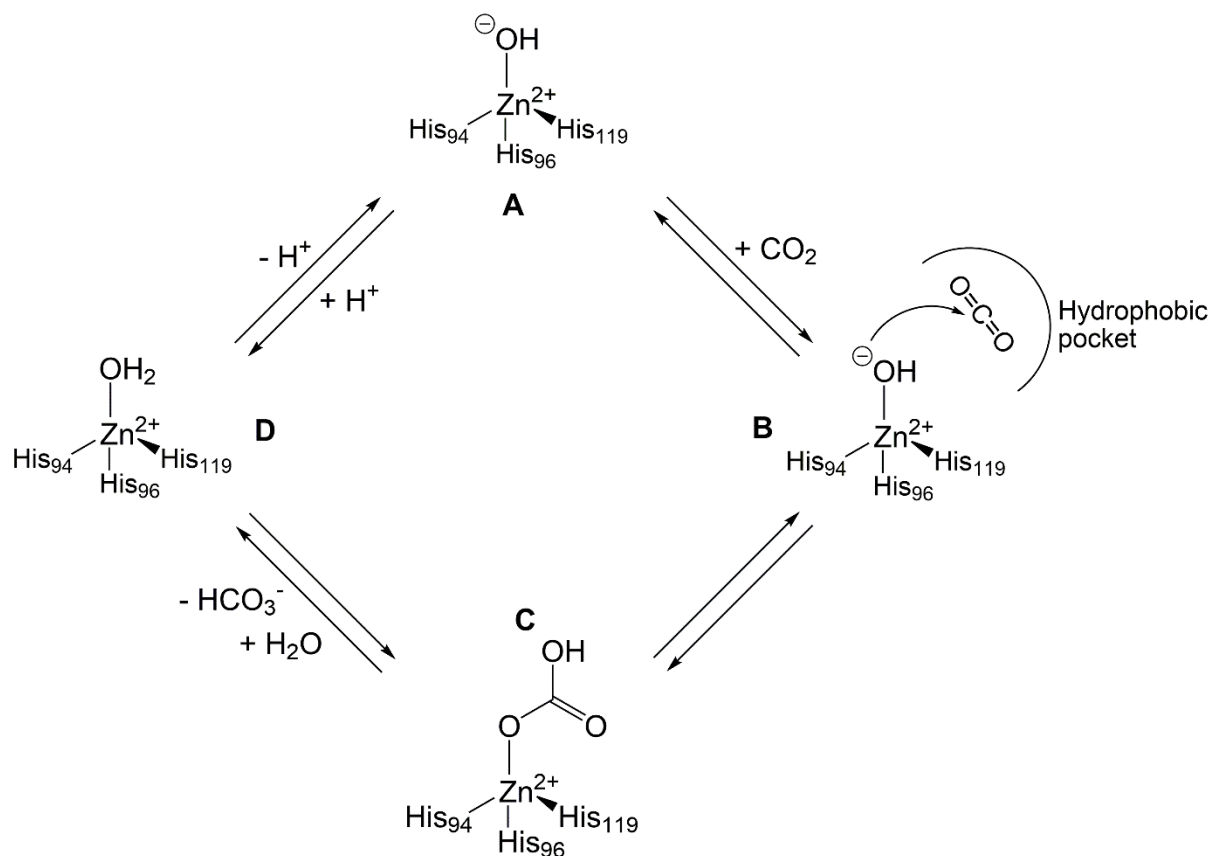


**Figure 3.** Catalytic mechanism of reversible hydration of CO<sub>2</sub> to HCO<sub>3</sub><sup>-</sup> and a proton (H<sup>+</sup>) in active site of carbonic anhydrase. The detailed description of a mechanism is presented in the text. Adapted from [107, 109].

Interestingly, carbonic anhydrase is one of the fastest enzymes known, hydrating 10<sup>4</sup> to 10<sup>6</sup> molecules of CO<sub>2</sub> per second [110]. The reaction rate of this enzyme is typically limited by the diffusion rate of its substrates. Carbonic anhydrase is often clustered along membranes or localized in extracellular spaces, which may enhance its ability to facilitate the intracellular diffusion of carbon dioxide and protons (H<sup>+</sup>). By increasing proton movement, carbonic anhydrase helps dissipate intracellular pH gradients, thereby maintaining a uniform cellular pH, critical especially for pH-sensitive processes [111]. Human carbonic anhydrase isoforms are known to differ by molecular features, cellular localization, distribution in organs and tissues, expression levels and response to different classes of inhibitors. hCA I–III, hCA VII, and hCA XIII are cytosolic isoforms, hCA IV, hCA IX, hCA XII, and hCA XIV are membrane-bound, and hCA VA and hCA VB are mitochondrial isoforms [104].

Carbonic anhydrase is a pharmacological target and biomarker for a variety of diseases [112]. Among all isoforms, human carbonic anhydrase II (hCAII) is noticeably expressed and widely distributed in human tissues [102]. Its inhibitors were used for treatment of numerous diseases including metabolic alkalosis [113], glaucoma [114], epilepsy [115], altitude sickness [116], obstructive sleep apnea [117], obesity [118] and cognition-related processes (neurodegenerative disorders as well as mental retardation) [119–121]. Furthermore, studies have demonstrated significant reductions in the levels of various cerebral isoforms of α-CA (primarily CA I and II) in patients with Alzheimer's disease [122]. This enzyme is suspected as well to play a role e.g. in the pathogenesis of vascular calcification [123]. Moreover, recent

studies suggest its non-catalytic proton shuttling function of hCAII, which supports lactate transport in cancer cells [124]. This activity results from residues on the enzyme's surface and is therefore independent of its enzymatic activity or inhibition. In other words, possible inhibition of hCAII activity through usual active site blocking would probably not result in inhibition of lactate transport in cancer cells [124].

Most pharmaceuticals or probes for carbonic anhydrase are based on reversible or irreversible inhibitors, providing specificity of action, particularly in the case of benzenesulfonamide derivatives. Those inhibitors usually bind to the protein as ligands to the zinc ion present in the protein active site [108]. Novel inhibitors were recently presented in the literature, with examples based on the “proteolysis targeting chimeras” (PROTAC) system or ubiquitination of carbonic anhydrase (so-called heterobifunctional degraders, [102]). The PROTAC system is a part of a few techniques collectively named “targeted protein degraders (TPDs)”. TPDs recruit endogenous cellular quality control mechanisms to transiently interact with a protein of interest (POI), selectively labeling it for degradation and thereby eliminating its function. In such molecules the degrader is bound to the ligand selective to the target with a linker, to provide selectivity of the interaction and higher control of the process. This approach presents a great potential for numerous targets and was FDA-approved in 2020 against two well-established cancer targets [125].

Carbonic anhydrase has been well-researched and was applied to protein function and protein-ligand binding studies as a model [108]. Since carbonic anhydrase significantly affects intracellular and extracellular pH, is present in numerous compartments in cells and its malfunction is suspected to play a role in multiple pathogenesises, further investigation of its function is conducted continuously. Even with 80 years of its studies [126], questions regarding its presence in chosen localizations within human organism still remain unanswered [104, 105].



## 1.2. Fluorescence as imaging method

### 1.2.1. Physical basis of fluorescence

#### *Jablonski diagram*

Phenomena related to the absorption and emission of visible and near-visible light by molecules result from the interaction of electrons with electromagnetic radiation at specific wavelengths, collectively known as photoluminescence. The primary explanatory tool for photoluminescence is the Jablonski diagram (**Figure 4**), named after the Polish physicist Aleksander Jablonski [127, 128]. This diagram illustrates the energy transfer between different energy levels. The vertical axis represents the energy amount (the higher the designated level – the higher its energy), while the horizontal axis displays the energetic levels with varying multiplicity. Consequently, the Jablonski diagram facilitates the understanding of diverse interactions between light and electrons, including fluorescence [127, 128].

Fluorescence is a phenomenon where an electron is excited by light and subsequently emits light from a state of the same spin multiplicity [128]. Specifically, the absorption of energy causes an electron to move from the ground state GS (usually the highest occupied molecular orbital – HOMO) to an excited state such as  $S_1$  or  $S_2$ . The electron can then transition from higher energy levels (e.g.,  $S_2$ ) to the lowest excited state energy level  $S_1$  (the lowest unoccupied molecular orbital – LUMO, relative to the initial GS) in process of internal conversion (IC). This process is also described by Kasha's rule that states that fluorescence always originates from the lowest excited singlet level ( $S_1$ ), while phosphorescence from the lowest excited triplet level ( $T_1$ ), regardless of the initial level to which the molecule is excited. The electron may lose energy through various pathways; if it returns to the GS radiatively, emitting the excess energy as a photon, the process is called fluorescence. Alternatively, if the electron undergoes non-radiative transfer to a triplet state T (involving a change in spin multiplicity) through intersystem crossing (ISC), followed by radiative return to the GS level, the result is phosphorescence. Compounds that emit light upon excitation are called luminophores, and if this emission occurs through fluorescence, they are referred to as fluorophores [128].

Moreover, for many small molecules capable of absorbing light in the UV-Vis region, the relaxation from an excited state to the ground state can be non-radiative (NR). This means the energy of an excited electron is released through other mechanisms, such as e.g. vibrations (vibrational relaxation, VR), molecular movement and/or collisions, chemical reactions, or energy transfer to other electrons. The processes mentioned and described in this section are presented schematically in the **Figure 4** [128].

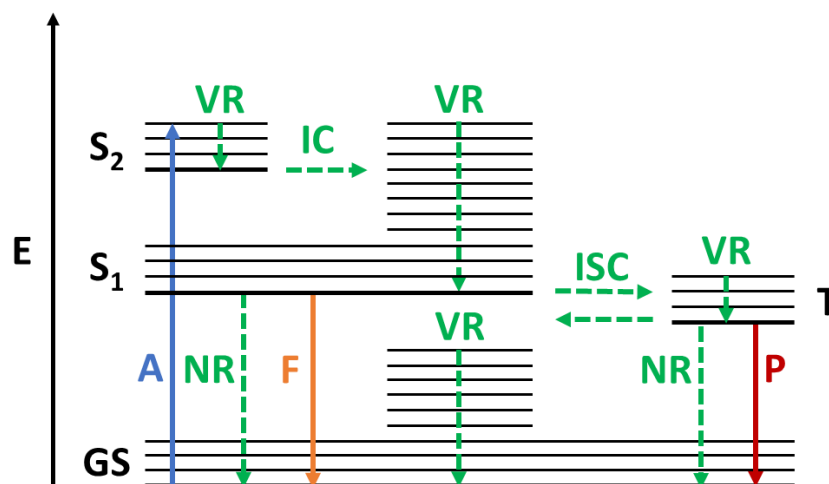


**Figure 4.** Jablonski diagram. E – energy; GS – ground state; S<sub>1</sub>, S<sub>2</sub> – singlet excited states; VR – vibrational relaxation; A – absorption; F – fluorescence; NR – non-radiative relaxation; IC – internal conversion; ISC – intersystem crossing; P – phosphorescence. The thick black horizontal lines represent energy levels, whereas thin black horizontal lines represent vibrational levels.

#### *Extinction coefficient, quantum yield & brightness*

A parameter useful for calculating the concentration of a fluorophore is the molar absorption coefficient,  $\epsilon$ . At a given wavelength, it indicates the relationship between the absorbed light and the fluorophore's concentration in solution. The quantum yield,  $\Phi_0$ , is another important parameter that describes the efficiency of quantum phenomena [128]. For instance, the fluorescence quantum yield is the ratio of photons emitted to photons initially absorbed by a fluorophore. According to Kasha's rule, the fluorescence quantum yield is independent of the wavelength of the exciting radiation because light emission occurs with significant quantum efficiency only from the lowest excited energy state [128, 129]. Fluorescence quantum yield is widely used in scientific literature to compare and select fluorophores for specific applications. Additionally, to describe the brightness of a fluorophore, a new parameter called brightness,  $B$ , has been proposed in modern literature [130, 131]. Brightness is the product of the fluorescence quantum yield,  $\Phi_0$ , multiplied by the molar absorption coefficient,  $\epsilon$  ( $B = \epsilon \times \Phi$ ).

#### *Stokes shift*

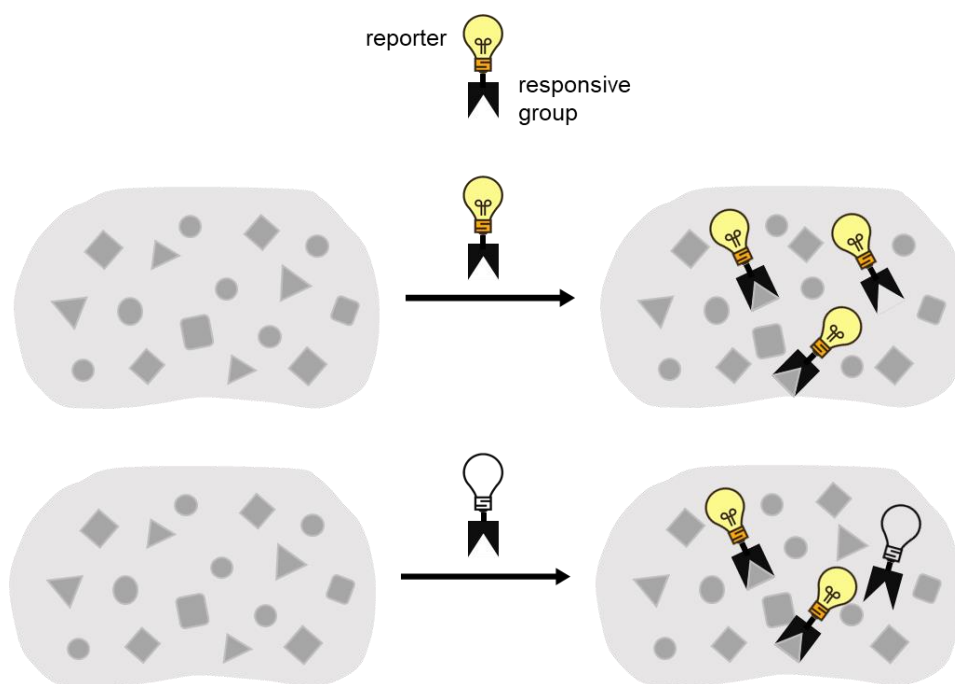
One key characteristic of fluorophores is the Stokes shift. This shift represents the difference between the peak positions of the absorption and emission spectra corresponding to the same electronic transition, typically expressed in  $\text{cm}^{-1}$ . The emission spectrum (a graphical representation of variations in light absorption or emission relative to its energy) of many compounds often mirrors the excitation spectrum [128]. This phenomenon is known as the Mirror Image Rule, and arises from Kasha's rule as well as the Franck-Condon principle. The latter dictates that electron transitions are vertical (they occur without change in nuclei position), and is applied equally to absorption and fluorescence [128, 132].

### *Fluorescence lifetime*

Fluorescence lifetime  $\tau$  is another parameter, which is increasingly used in the context of application of fluorophores in biology (e.g. in Förster Resonance Energy Transfer experiments [133] or Fluorescence Lifetime Imaging Microscopy [134, 135]). Fluorescence lifetime describes an expected average time when molecules stay in their excited state before emitting photons and returning to the ground state. In mathematical terms, it also refers to time when a population of fluorophores in excited state decay to  $1/e$  ( $\approx 0.368$ ) of the original number of molecules [128, 135].













### 1.2.2. Tools for fluorescence imaging in biology

One of the most widespread techniques for signal detection in the cell in basic and applied research is fluorescence microscopy. Its main advantages are the great variety and sophistication of instruments/microscopes or high temporal and spatial resolution (even down to the level of single molecules). In addition, this type of microscopy provides the possibility of observing multiple colors at the same time (multiplexing) and has a relatively non-invasive nature that allows *in cellulo* studies [136]. In this context, fluorescent probes play a key role as tools that produce a detectable signal that depends on the physicochemical environment, allowing visualization of otherwise "invisible" targets and parameters (as they do not produce a signal on their own). Fluorescent probes also make it possible to determine a target's intracellular localization and even to some extent quantify target concentrations. This information is crucial for determining the biological role and involvement of these endogenous elements in physiological and pathological processes and opens the door to understanding and manipulating them (e.g. to develop more effective bioactive molecules and therapies). Unlike tags, i.e. molecules that always invariably emit the same signal, fluorescent responsive probes usually allow for more reliable and easier-to-interpret detection. This is because the signal they emit changes as a result of interactions with the molecular target or as a consequence of changes in the physical properties of the environment (**Figure 5**) [137].



**Figure 5.** Schematic representation of the difference between “tag” (top) and “responsive probe” (bottom). The light gray element symbolizes the cell, while the dark gray elements (squares, circles, triangles) represent potential molecular targets inside the cell. The yellow bulb indicates active emission of the probe's luminescence, the transparent bulb indicates no emission. Adapted from [137].

Biological processes are complex to observe due to a high number of simultaneously interacting molecules, localized in the same microenvironment. Most commonly used fluorescence probes allow imaging of a single analyte and/or their use is limited to "in-buffer" (non-cellular) applications. Multi-analyte probes, on the other hand, allow for more reliable detection and monitoring of the relationships between multiple elements in a given biological system (i.e., chemical compounds, viscosity, polarity, etc.) than a multiple monoanalyte probes system (**Figure 6**) [138]. This is because, in contrast to the use of two independent probes targeting single analytes, a single probe for the detection of several analytes eliminates artifacts associated with, among other things, differences in localization and metabolism of different probes. This results in more straightforward interpretation of results and allowing more reliable correlation of the signal with the actual presence of the two analytes in proximity. Nevertheless, in addition to the typical criteria for responsive probes for reliable detection of analytes in biological models, such as selectivity, photostability, brightness and biocompatibility, the design and use of multi-analyte probes requires consideration of a number of additional aspects. First and foremost, in order to reliably detect multiple analytes simultaneously, a multi-analyte probe must generate a unique signal in the presence of both analytes (A and B), different from the signals generated for any other combination (e.g. A only, B only or neither – **Figure 6**) [139, 140]. A common analogy in the design of such tools is the structure of a logic gate, for which the presence of an analyte is the input signal and fluorescence is the output signal. Under this assumption, a circuit that meets the criterion of a unique signal in the presence of both analytes is an AND gate. Another system often considered is probes, which would generate a distinguishable signal for each possible combination (**Figure 6, (iii)**). Nonetheless, while this mode of response possibly allows for even more detailed investigation of the relationship of the analytes, it should be noted that such a probe is not a prerequisite for maintaining a reliable reading of the simultaneous presence of both analytes [137, 138].

	i	ii	iii
No analyte			
Analyte A			
Analyte B			
Analytes A + B			

**Figure 6.** Logic gate table describing the different types of responses possible from a selected multi-analyte probe; here using a two-analyte probe as an example. The bulb colors (yellow, pink, indigo) indicate examples (different from each other) of the probe's emission colors in response to analyte A, B or both analytes A+B. White bulb color indicates no emission. Inspired from [137, 138].

Despite the advantages of multi-analyte probes over mono-analyte probes in detecting the relationship between two analytes simultaneously, their design and validation in practice are quite challenging. Most mono-analyte probes are built based on a change in signal intensity (increase - so-called "on" probes - or decrease - so-called "off" probes) at one specific wavelength. This type of response entails several limitations arising from the inability to distinguish whether the increase/decrease in signal is due to a decrease/increase in probe concentration (without analyte involvement) or as a result of probe activation/deactivation with analyte. In the case of dual-analyte probes, for which both analyte A and B affect the intensity of the same signal, an additional parameter that makes interpretation of the reading even more difficult is the relative ratio of the two analytes to each other (i.e., several different combinations of analyte concentrations will give the same increase/decrease in intensity). Therefore, in practice, the only types of probes that allow reliable signal correlation with the co-presence of both analytes are those that emit a signal only when both analytes are present (**Figure 6, (i)** - specific probes) or a signal of a different color when both analytes are present, compared to single analytes or a lack thereof (**Figure 6, (ii)** and **(iii)** - selective probes). In order to reliably use dual-analyte probes in biological systems, it is crucial to thoroughly characterize their response to various combinations of the analytes being detected, as well as other individuals that may affect their performance [137, 138].

### 1.2.3. Scaffolds used for fluorescence imaging

The selection of fluorophores for small-molecule fluorescent probes typically revolves around several major classes and their derivatives [141], including cyanines [142], xanthenes (rhodamines, fluorescein) [143], oxazines [144], coumarins [145], BODIPY derivatives [146], and more. The design of these probes is guided by the desired properties of both the fluorophore and the final probe, such as absorption and emission spectra (with large Stokes shift = no self-quenching), compound brightness, stability (e.g. thermal- and photostability), and the presence of specific functional groups [141, 147]. Furthermore, the core structure should be readily modifiable to adjust the photophysical properties and incorporate biological targeting moieties [148].

Notably, despite the wide availability of UV-activated fluorophores, there is a preference for using fluorophores that can be excited with a light of a lower energy (visible and/or even infra-red – often described as “red-shifted”) [149]. UV light (100-400 nm, where 280-400 nm reaches the Earth’s surface directly [150]) is considered highly harmful to organisms [150, 151], especially on a cellular [151–154] and molecular level [154]. It causes damaging effects due to the increased production of reactive oxygen species in cells and direct DNA [152, 155] and/or protein aromatic scaffold damage [154]. This kind of radiation used for excitation of fluorophores widely available in literature may irreversibly affect the phenotype of the cells, result in misinterpretation of the observed data and should be omitted in *in cellulo* experiments.

Apart from potentially toxic and/or mutagenic influence of UV radiation on cells, UV-excited fluorophores usually emit in the range overlapped with emission of naturally occurring chromophores/fluorophores, primarily nicotinamide adenine dinucleotide phosphate (NADPH; absorption: 230-400 nm) and flavins (absorption: 380-490 nm, depending on the structure). Therefore, when selecting the spectroscopic properties of fluorophores for live-cell imaging, absorption and emission wavelengths in the far-red to near-infrared range (650–1350 nm) are beneficial [156]. Apart from reduction of background noises coming from autofluorescence, red emission can increase signal to noise ratio (SNR) [157]. Moreover, red emission, referred to as the optical window (near-infrared window, NIR window) in biological tissue [158, 159], can easily penetrate thick specimens because of its low Rayleigh scattering [160, 161]. It applies to 3D samples (e.g. spheroids or 3D cell colonies) as well as imaging tissues, organs or even whole organisms [158]. Since scattering weakly depends on wavelength, the NIR window is mainly restricted by light absorption from blood at shorter wavelengths and water at longer wavelengths (absorption for both: 300-1000 nm, with different intensity) [159].

Even though currently available techniques enable unmixing of channels (spectral unmixing; possibility of emission division between two or more emitting molecules in case of spectra overlapping) in case of overlapping, fluorophore emission in the visible spectrum is still preferred [149]. Data obtained from use of far-red fluorophores may be used directly without additional steps, saving time (choice of algorithm [162], its use and analysis of data), resources (chemicals, electricity) and space (possibly smaller equipment due to use of less detectors, photomultipliers etc.).

Molecules intended for application in live cells require a few more crucial properties beyond their spectral properties. Many fluorescent probes for labeling cellular structures suffer from unspecific interactions and low cell permeability [163–165]. One of the methods of increasing cell permeability and biocompatibility is adding poly(ethylene glycol) (PEG) chains to the fluorophore structures [166]. Depending on the surroundings of a molecule bearing such PEG chain, the chain may present its dual nature, analogous to micelles [167], facilitating a penetration of cell membrane. Furthermore, PEG chain addition may reduce non-specific interactions between fluorophore and proteins or even lipid membranes [168, 169]. Last but not least, a fluorophore should not present significant cytotoxicity and phototoxicity, especially in case of molecules used for time-dependent experiment purposes. It is worth to highlight that toxicity of a molecule may be increased in its excited state, as it becomes significantly more reactive than in its ground state. Moreover, the photo-excitation of fluorophores typically employed in biological imaging applications produces reactive oxygen species (ROS) [170]. Such general reactivity results in an irreversible loss of emission (fluorophore destruction), usually caused by a permanent change in the chemical structure (a photochemical reaction) [171]. Photoinduced fluorophore toxicity (phototoxicity) can cause unwanted disruptions to the biological system, potentially obscuring the signal of interest [170]. To potentially improve the fluorophore photostability and thus decrease its toxicity, blocking reactive sites and reducing molecule reactivity sterically with bulky groups are possible [172].

Once all described conditions are met, a fluorescent scaffold is equipped with a functional group or ligand to afford fluorogenic properties in the presence of target analytes. Fluorogenic molecules may be considered as “turn-on” ones, emitting fluorescence only upon interaction with a chosen analyte (ion, ROS, change in microenvironment like viscosity or polarity) [173]. This class of probes has garnered significant attention [174–177] and comprehensive reviews covering the subject are available in the literature [173, 178, 179]. Examples of such molecules are presented in **Figure 7**, together with names of tags, which were labeled and observable with use of these fluorophores [174]. The more detailed description of tag-labeling technology will be provided in subchapter **1.4.2**. One of the main advantages of fluorogenic probes is the possibility of no-wash imaging. Therefore, better background to signal ratio may be obtained as well as less disruption of cells themselves (possible in case of need of probe washing out) [176].



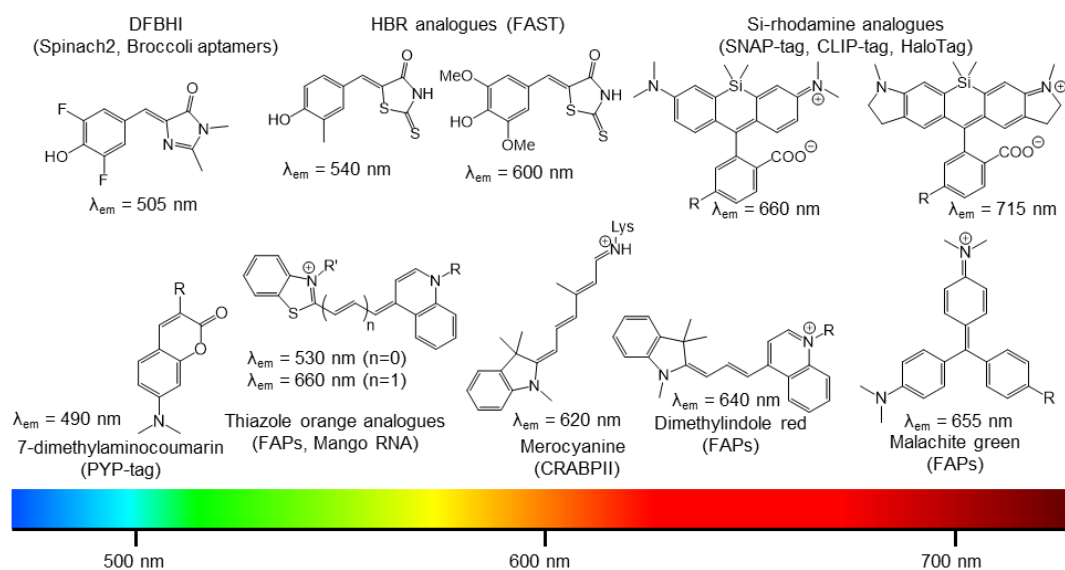


**Figure 7.** Examples of fluorophores that can be used and/or modified for fluorogenic labeling. The tags with which these fluorophores have been used are indicated in parentheses. DFBHI - 3,5-difluoro-4-hydroxy-benzylideneimidazolidinone; HBR - 4-hydroxybenzylideneorodanine. Adapted from [174].

From a whole array of available fluorogenic molecules, a few of the groups mentioned at the beginning of the subchapter are the center of attention recently. One of those are 1,8-naphthalimides [180–182] (**Figure 8**, right). Proper modification of the structure may provide fluorogenic properties [173, 183, 184]. Second group, significantly reduced in number in comparison to the first one, are derivatives of 4-sulfonamide benzo[*c*][1,2,5]oxadiazole (SBD) (**Figure 8**, left) and of 4-nitrobenzo[*c*][1,2,5]oxadiazole (NBD) (**Figure 8**, middle). Especially the first one (SBD) present fluorogenic properties without need of any modification [185, 186]. Both naphthalimide and SBD derivatives can be variably substituted at aromatic positions, enabling derivatization with substituents affecting spectroscopic or sensing properties [186–190], especially in case of 1,8-naphthalimides [180, 186, 190]. Majority of them present high fluorescent quantum yields, high photostabilities, significant Stokes shifts and excellent environment-sensitivity [173, 183–186]. In the upcoming subchapter **1.3**, introducing fluorescent responsive probes, vast majority of molecules will be based on those two fluorophore groups to highlight their excellent diversity and properties.

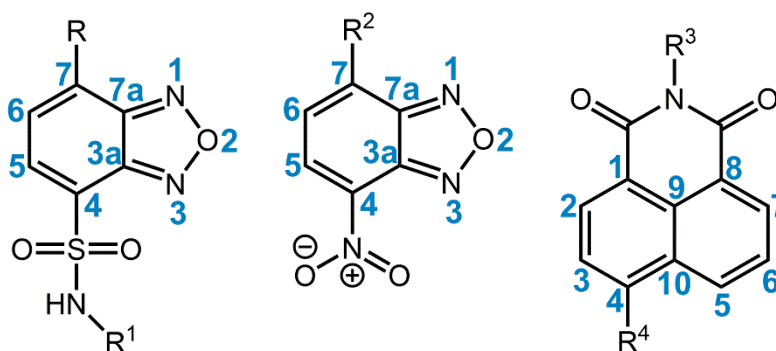


**Figure 8.** Structures of 4-sulfonamide 2,1,3-benzoxadiazole (SBD, left), 4-nitrobenzo[*c*][1,2,5]oxadiazole (NBD, middle) and 1,8-naphthalimide (NPH, right) with chosen numbered atoms in aromatic core of molecules. R, R<sup>1</sup>, R<sup>2</sup>, R<sup>3</sup>, R<sup>4</sup> – substituents.

### 1.3. Fluorescent responsive probes

#### 1.3.1. Types of responses of fluorescent probes to the analytes

Multi-analyte fluorescent probes consist of several key elements: one or more signal-emitting fragments (e.g., fluorophores) and at least two detection (target-interaction) motifs, each of which interacts specifically with one of the target analytes [191]. In the present work, we have chosen to classify published probes based on their mode of interaction with the analyte:

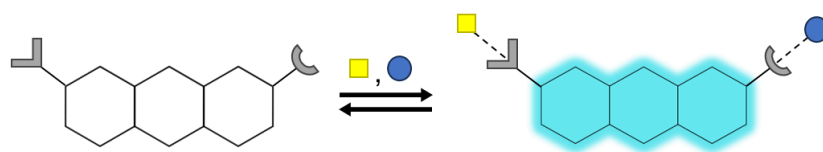
- Reversible non-covalent interaction (by forming a transient complex which existence depends on the concentration/microenvironment) [78, 192],
- Reversible covalent reaction (as in case of flavins, which undergo reversible oxidation/reduction processes [193, 194]) and
- Irreversible covalent reaction (by cleavage or virtually irreversible addition) [138, 192].

Reversible non-covalent interactions enable imaging of dynamic changes in cellular processes. Such probes may switch on and off in time and are not irreversibly consumed in the detection process. Reversible probes are mainly used to detect the presence of cations, anions or changes in pH (**Figure 9**, top) [31, 192]. A similar nature of the interaction occurs for probes that are sensitive to changes in environmental parameters, such as viscosity or polarity [46, 53, 195–197]. It is worth noting that even though such interactions are generally considered as reversible *in vitro* (test tube), their reversibility is dependent on the immediate environment. Lack of or low concentration of reagents in close proximity to the probe may result in irreversibility of analyte sensing, especially *in cellulo* [198].

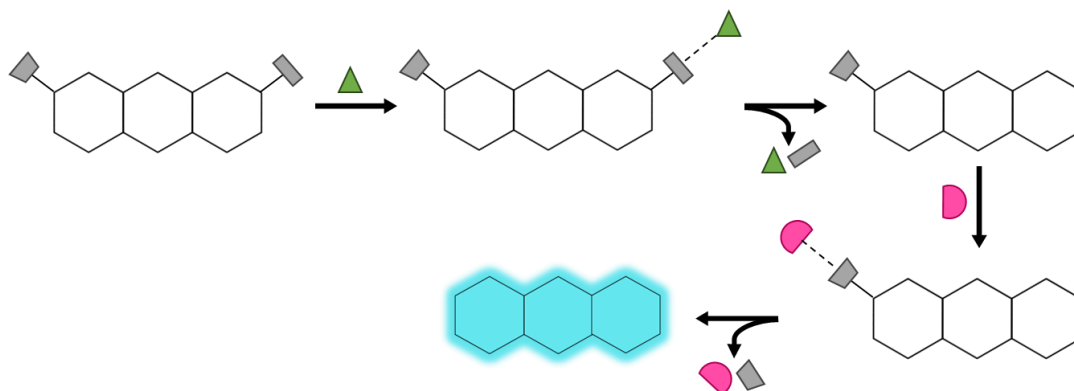
Irreversible covalent probes, on the other hand, are (semi)permanently altered after reacting with the analyte and therefore cannot detect it again; they usually have a specific reactive group that is sensitive only to the selected analyte of interest (e.g., selective against reactive oxygen species or the protein of interest) (**Figure 9**, middle) [192]. Such irreversible modification results in separation of two (or more) fragments in space, which cannot interact with each other anymore due to increasing distance (in time due to diffusion).

Reversible covalent reactions are primarily afforded by one group of responsive fluorescent probes: flavins [193, 194] (**Figure 9**, bottom). Derived from naturally occurring cellular redox cofactors, they were found to be excellent sensors of redox changes inside cells, especially isoalloxazine one (**Figure 10**, top). To provide redox sensitivity of the latter, hydrogen at position C-10 is substituted with different groups, to maintain reversibility of reduction [199]. Oxidation results in a significant increase in isoalloxazine fluorescent signal, while reduction leads to initial, non-fluorescent state [194]. The exemplary flavin probe transformation, based on the probe **NpFR1** [194], is presented in the **Figure 10**, bottom.

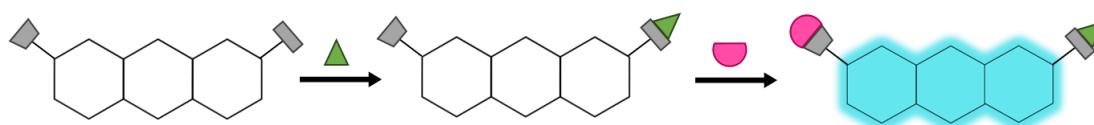
### REVERSIBLE NON-COVALENT INTERACTION



### IRREVERSIBLE PROBES (CLEAVAGE)



### IRREVERSIBLE PROBES (ADDITION)



### REVERSIBLE COVALENT INTERACTION



**Figure 9.** Diagram showing three different types of two-analyte probes: a) reversible non-covalent interaction probes; b) irreversible probes (respectively by cleavage and addition); c) reversible covalent probes. Three connected white cubes show the molecule in a form that does not emit fluorescence, whereas with a blue background showing emission (reporter part). The gray shapes attached on the sides are the response groups. The colored shapes symbolize molecular targets recognized by subsequent probes. Adapted from [137].

In addition to these three types of probe-analyte interactions, there exist mixed probes, which engage multiple interaction mechanisms. These can occur simultaneously; for example, where one part of the probe interacts with the analyte in a reversible manner, while the other reacts irreversibly and, for example, undergoes substitution, resulting in a change in the structure and thus in the properties of the probe. Another combination of responses is found in sequential probes. These probes detect two analytes, but the second target can only be detected if a different analyte first interacts with the probe. It is worth noting that within this dissertation, an analyte will refer to both individual entities (such as macromolecules, small molecules, ions, and reactive oxygen and nitrogen species) and changes in the biological environment within the cell (such as fluctuations in viscosity or polarity). For instance, a probe that is sensitive to both an enzyme's activity and changes in microenvironment polarity is considered a 'two-analyte' probe, being sensitive to two distinct parameters [137].

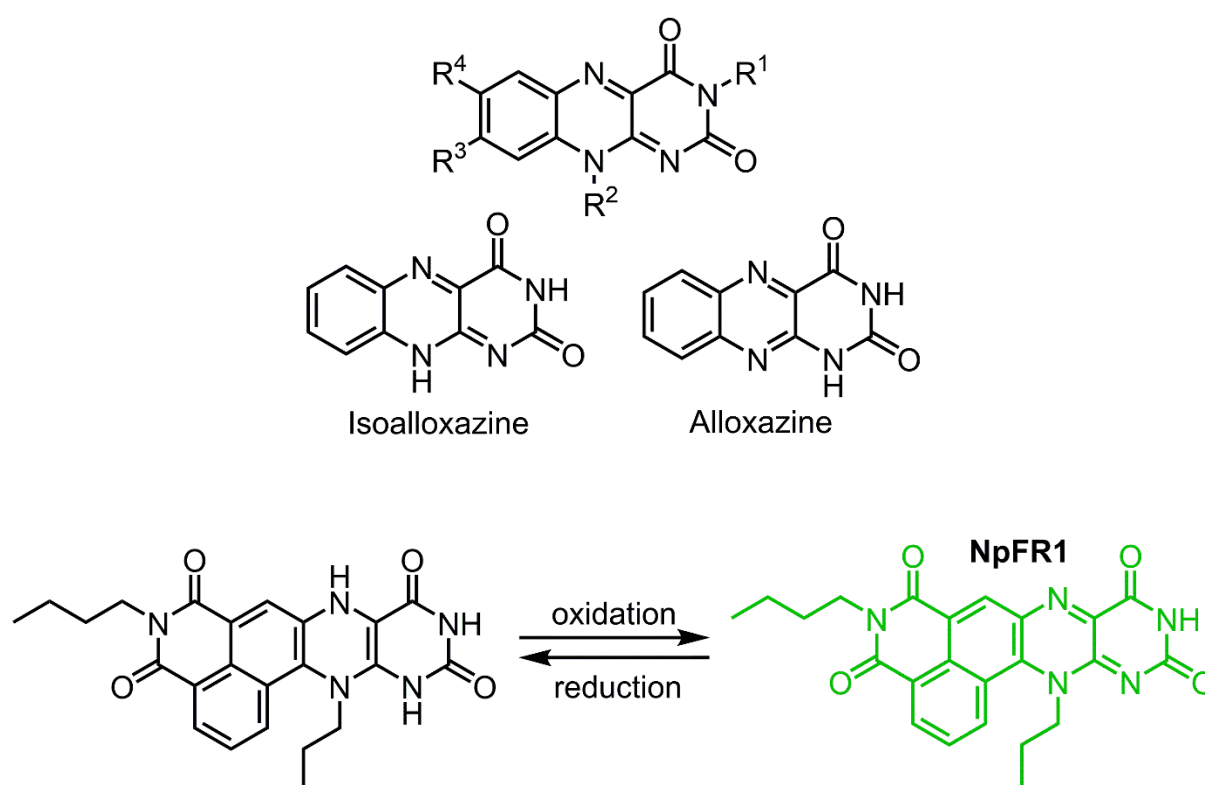


**Figure 10.** General structure of flavin (top) together with isoalloxazine and alloxazine structure (middle). Adapted from [200]. (bottom) Presentation of reversible covalent reaction, oxidation/reduction transformation, of flavin molecule on an example of the probe **NpFR1** [194]. R<sup>1</sup>, R<sup>2</sup>, R<sup>3</sup>, R<sup>4</sup> – substituents. The green color of the probe **NpFR1** symbolizes its “on” state (color of light/fluorescence emission), while the black form is in “off” one (lack of fluorescence).

### 1.3.2. Probes responsive to polarity changes

Polarity-sensitive probes are usually classified based on their target intracellular localization. Thus, we can divide probes into those that target mitochondria, lysosomes, endoplasmic reticulum, Golgi apparatus, lipid droplets etc. [53]. Polarity-sensitive fluorogenic dyes are of great interest in confocal and high-resolution microscopy because of the activation in their fluorescence after interaction with biological targets, enabling imaging with a better signal-to-background ratio [201]. A typical class of fluorogenic polarity-sensitive probes are silicon-rhodamines (or silica-rhodamines), undergoing ground-state isomerization [177]. Derived from a rhodamine structure, silica-rhodamine (or silicon-rhodamine) probes close (apolar environment, inactive fluorescence) and open their spiro-lactone rings (polar environment, fluorescence emission) depending on polarity of surroundings and have been successfully applied as intensity-based probes for imaging living cells [177, 202] (**Figure 11**).

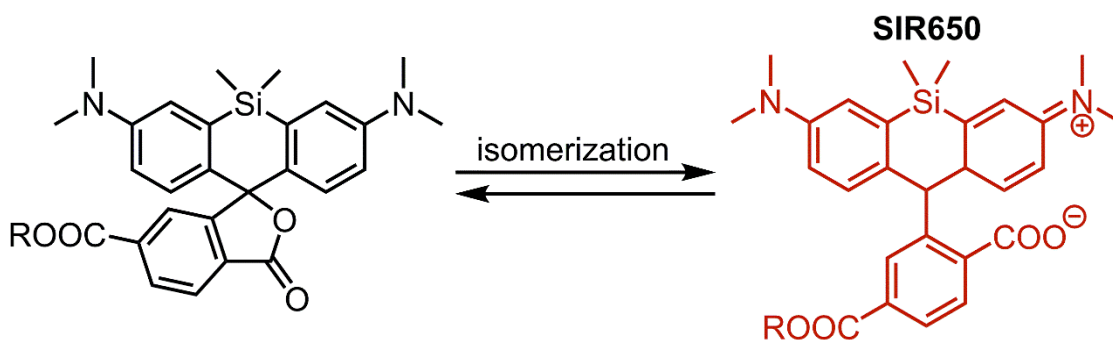


**Figure 11.** Presentation of polarity-sensitive probes based on silicon-rhodamine (silica-rhodamine) fluorophore, **SIR650**. Adapted from [177]. The dark red color of the probe **SIR650** symbolizes its “on” state (color of light/fluorescence emission), while the black form is in “off” one (lack of fluorescence).

Solvatochromic probes, on the other hand, undergo changes in color (i.e. energy) of absorption/emission and generate fluorescent signal via a push-pull mechanism. They contain electron-donating groups (donor groups, D) and electron-accepting groups (acceptor groups, A), and upon light absorption, the electron density shifts (in extreme situations, formal charge transfer) from the donor group to the acceptor group, resulting in a highly bipolar excited state (**Figure 12**, left). The molecule in the excited state then undergoes spatial rearrangement through stabilization by solvent molecules before light emission. The magnitude of this effect depends on the solvent polarity and its dielectric constant [203]. Polar solvents interact more strongly with the often more polar excited states of fluorophores, leading to greater stabilization of the latter and thus a shift in emission energy toward longer wavelengths (**Figure 12**, right). Typically, the response of solvatochromic probes is evident as a change in the maximum of the fluorescence emission spectrum (seen as change of fluorescence color) or both the absorption and emission spectra [204]. Apart from intensity or absorption/emission maxima change, polarity-sensitive probes may also present different values of fluorescence quantum yield or fluorescence lifetime in response to polarity fluctuations [46, 205].

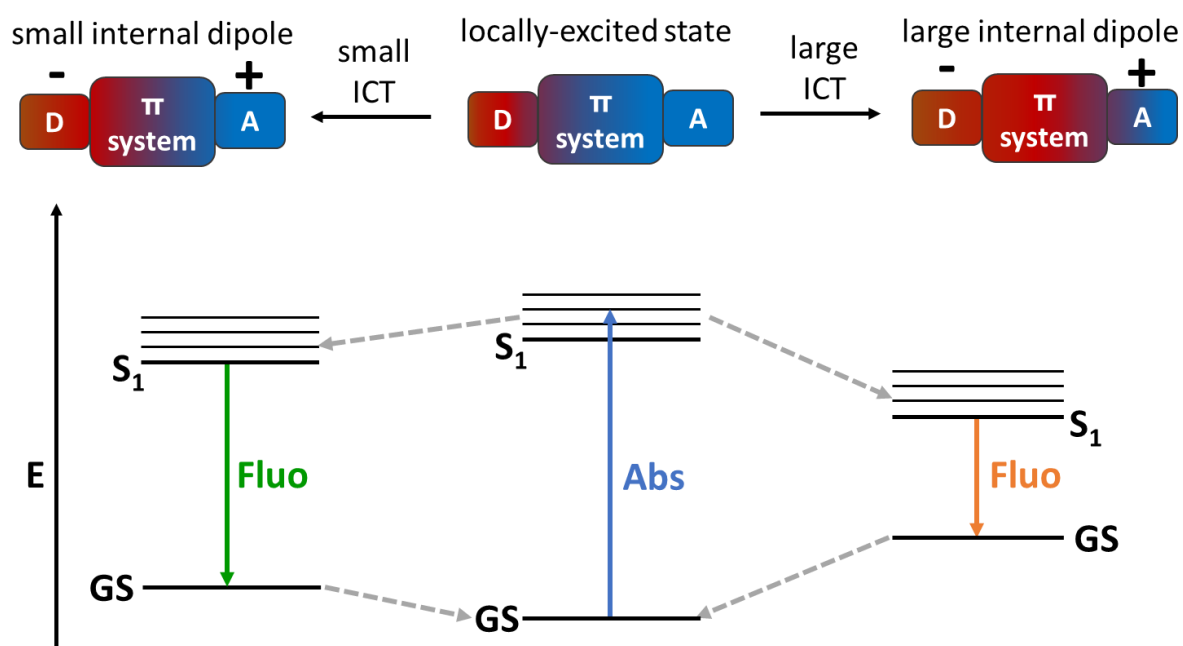


**Figure 12.** Schematic representation of the characteristics of polarity-sensitive probe. Proposed solvent effects on the fluorescence decay process. The more stabilizing effect of solvents, the more red-shifted emission. Adapted from [31].  $S_1$  – first excited singlet state; GS – ground state; D – donor group; A – acceptor group; ICT – intramolecular charge transfer; E – energy; Fluo – fluorescence (the color of arrow represents the color of fluorescence); Abs – absorption;  $\pi$  system –  $\pi$ -conjugated system of the polarity-sensitive fluorophore. The gradient shift in the D- $\pi$ -A system presents the intensity of charge separation in dipole – the more is covered by red color, the stronger charge separation.

By studying changes in intracellular polarity, it is possible to take leverage available data on well-characterized inorganic and organic solvents and compare the behavior of *in vitro* and *in cellulo* probes, correlating fluorescence color with specific polarity parameters of a given solvent and thus cell region. In this way, a specific quantification of the fluctuations in the polarity of the intracellular environment is possible [13, 206].

There is a wide array of probes described in the literature with focus on the influence of polarity fluctuations and other targets [31, 59, 207, 208]. For example, the **HX103** probe (**Figure 13**) was successfully used for a multicolor fluorescence-activated cell sorting, for preliminary test of the effects of various treatments of non-small cell lung cancer [209]. SBD fluorophore was there connected with pharmacofore (non-covalent inhibitor), Gefitinib, to create a probe **HX103**. Use of this improved probe for a known assay for discrimination of surgical specimens of non-small cell lung cancer increased the test's specificity and sensitivity. The interaction between the probe and the target, epidermal growth factor receptor (EGFR) creates a complex **HX103**-EGFR, and change of the probe microenvironment (polarity) results in significant increase of fluorescent signal. The publication is an interesting example of purely practical approach to use of the obtained probes, including a cost analysis of the method, proving its use as globally beneficial.

Another example is a polarity-sensitive probe, NATPA (**Figure 13**), used to investigate the relationship between intracellular changes in polarity and the presence of hydrogen peroxide ( $H_2O_2$ ) [210].  $H_2O_2$  is mainly formed in mitochondria and plays a key role as a signaling molecule in the cell cycle. The main purpose of using **NATPA** was to look at lipid droplets, where changes in polarity have a huge impact on lipid metabolism and protein-protein interactions. The probe was successfully applied for distinction between cancer cells and normal (healthy) cells.

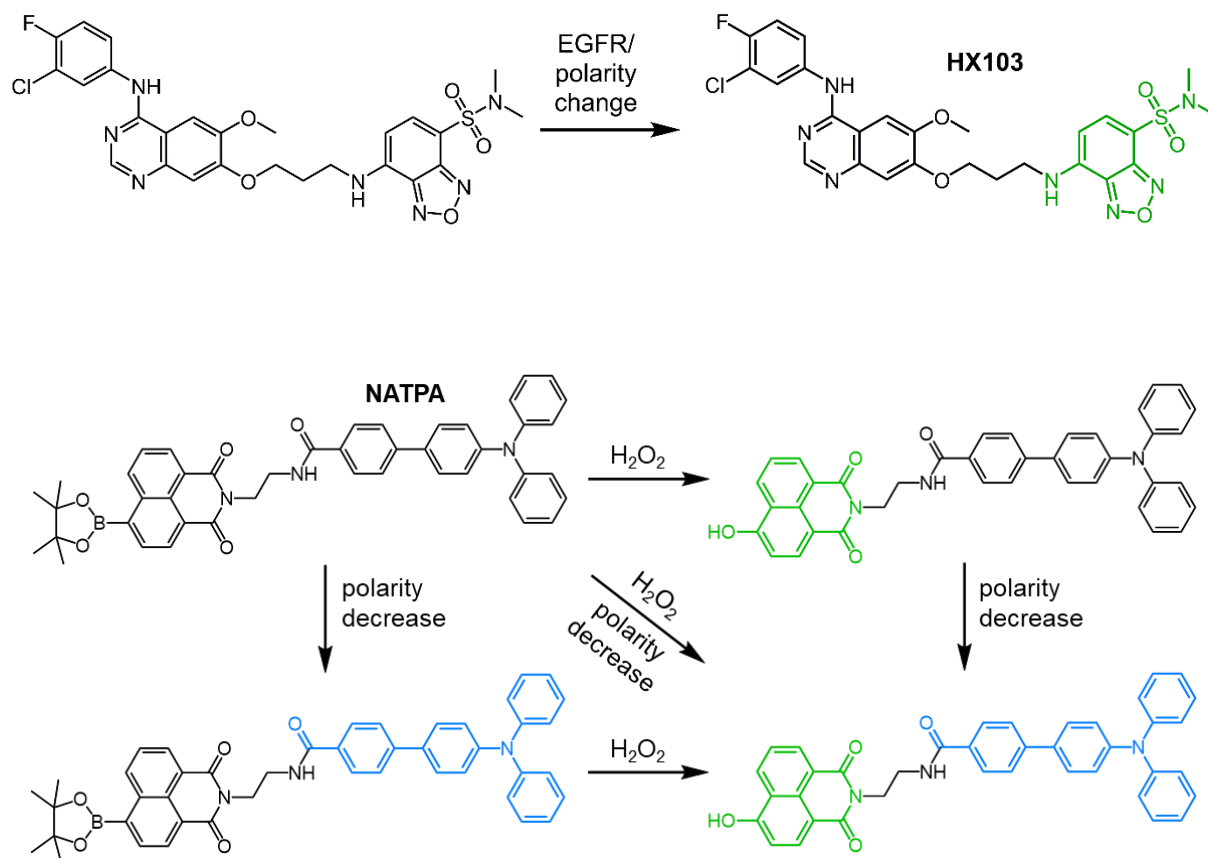


**Figure 13.** Examples of the probes sensitive to polarity changes and optionally one more chosen analyte. Adapted from [137, 209, 210]. EGFR – epidermal growth factor receptor. The colors of the probes symbolize “on” state (color of light/fluorescence emission), while the black form is in “off” one (lack of fluorescence).

### 1.3.3. Probes responsive to viscosity changes

Microviscosity-sensing fluorescent probes usually consist of a fluorophore linked to a rotational conjugated moiety capable of rotating independently. In low-viscosity environments, the rapid rotation dissipates the excitation energy, leading to substantial quenching of fluorescence or reduction in fluorescence lifetime. Conversely, in high-viscosity environments, the rotation is progressively restricted, which decreases the likelihood of non-radiative pathways and thus increases fluorescence intensity or extends the fluorescence lifetime [31].

The mechanism of the response to viscosity changes is usually based on one of the following:

- Charge transfer in the molecular rotor influenced by "twisting" and changing the position of the donor and acceptor groups relative to each other in space, known as TICT (twisted intramolecular charge transfer) [211],
- TICT-involved, non-radiative deactivation processes in molecular rotors (quenching by rotation) [196] and
- combination of TICT and e.g. PeT (photoinduced electron transfer) (example: [66]).

The term "molecular rotor" refers to a fluorescent molecule capable of intramolecular twisting in its excited state. A molecular rotor generally comprises three components: an electron donor unit, an electron acceptor unit, and an electron-rich spacer unit. The spacer unit features a network of alternating single and double bonds, which links the donor and acceptor units in conjugation [212]. This arrangement promotes electron transfer between the donor and acceptor while minimizing the overlap of their orbitals. Once excited, like conventional fluorophores, a molecular rotor goes through intramolecular charge transfer (ICT; increased dipole moment). While the three subunits generally adopt a planar or pseudo-planar configuration in the ground state, electrostatic forces cause these subunits to twist relative to one another within the molecule [213]. The molecule transitions into a nonplanar (twisted) state with reduced excited-state energy. Relaxation from this twisted state can result in either red-shifted fluorescence emission (**Figure 14**, left) or nonfluorescent relaxation (**Figure 14**, right), depending on the specific molecular structure [214, 215]. The first kind of rotors may present two different emission bands – from planar excited state or TICT state (more red-shifted), while the other only from the planar excited state.



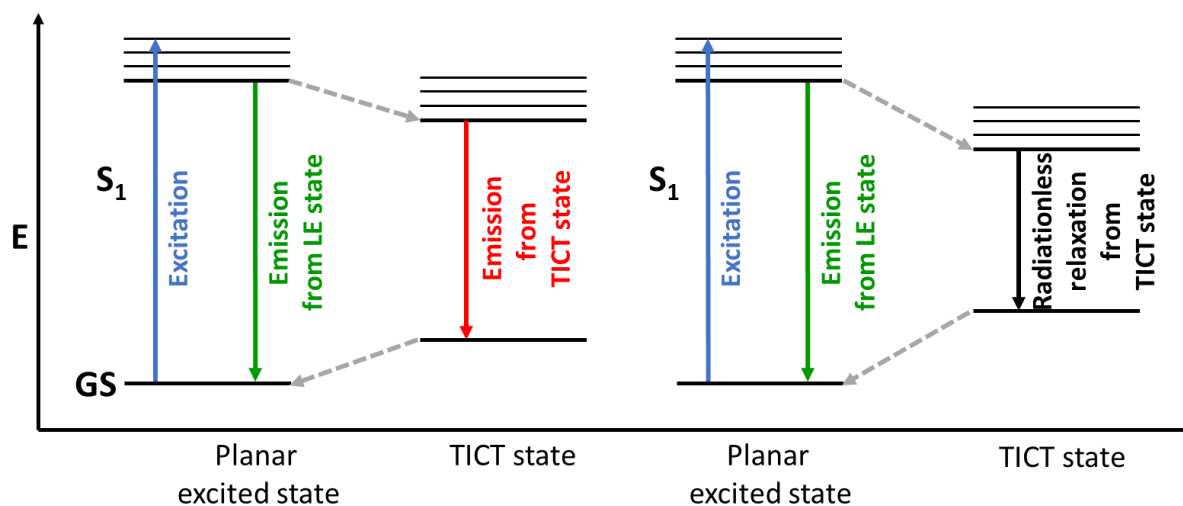


**Figure 14.** The extended Jablonski diagram depicts the fundamental operating principle of molecular rotors: after excitation to a locally excited state, the molecule can either undergo radiative decay (left) or engage in twisting (non-radiative decay; right). The competition between these two pathways is influenced by the viscosity of the rotor's surrounding environment. Adapted from [212].

The most significant characteristic of molecular rotors is the rate at which the twisted state forms, which depends on primarily the solvent's microviscosity. For molecular rotors that emit from the twisted state with a red-shifted emission, steric hindrance in high-viscosity solvents shifts the emission towards shorter wavelengths from the planar state [216]. Conversely, for molecular rotors that undergo nonradiative relaxation from the twisted state, the fluorescent emission (as well as quantum yield) increases in more viscous solvents [217].

Example of probes sensitive to the viscosity changes in their closest surroundings are presented in **Figure 15**. Both sensing mechanisms are based on TICT; with probe **1** also undergoing a PeT-based mechanism of quenching (photoinduced electron transfer; discussed in subchapter 4.1.4). Probe **1** was, according to the authors, the first probe to quantitatively map cellular viscosity with detailed organelle information based on the PeT mechanism [66]. Naphthalimide and anthracene are connected via a diamine linker, with an additional aniline group on the anthracene side, which behaves as a PeT donor. The covalently linked anthracene is able to rotate around a single bond linked to the aniline, creating a viscosity-sensing group. At the same time, anthracene behaves as a FRET (Förster resonance energy transfer) donor; naphthalimide behaves then as FRET acceptor. FRET energy transfer occurs when energy is transferred between two nearby molecular structures through space. This process involves exciting one fluorophore, which can then transfer energy to a second fluorophore if the emission spectrum of the first overlaps with the excitation spectrum of the second. There are 2 more requirements for FRET to occur: i) the acceptor and donor must be between 10–100 Å apart, and ii) the donor and acceptor transition dipole orientations must be approximately parallel. As the orientation of the naphthalimide and anthracene of probe **1** is dependent on local viscosity, it was utilized to create a detailed map of intracellular viscosity via measuring ratiometric emission changes and fluorescence lifetime. Moreover, measuring fluorescence lifetime enabled tracking of dynamic changes of intracellular viscosity over time (30 minutes).

A second example of viscosity-sensitive probe is based on the SBD scaffold, in which the  $\pi$ -conjugated system was elongated with use of a naphthalene ring [218]. From the three probes developed, **NY3** presented the highest signal-to-noise ratio for intracellular viscosity changes detection, in temperatures ranging from 37°C to 2-4°C. Intracellular viscosity fluctuations were further regulated with use of two agents: nystatin and carbonyl cyanide 3-chlorophenylhydrazone (CCCP). Both resulted in an increase of the signal coming from the probe **NY3**, as expected.

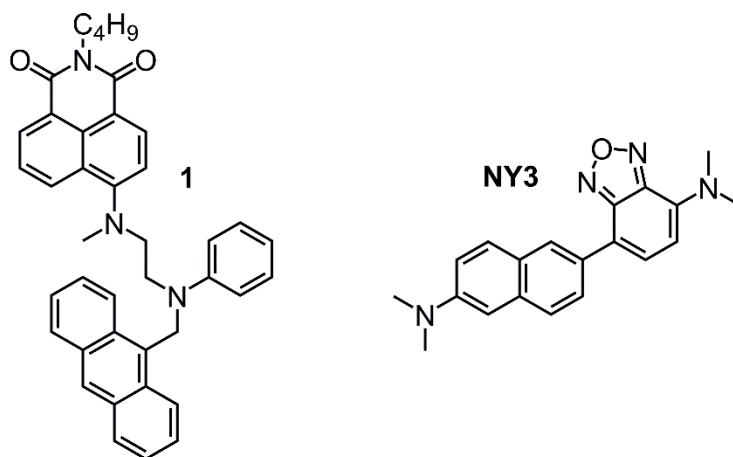


**Figure 15.** Examples of viscosity-sensitive probes, **1** and **NY3**. Adapted from [66, 218].

### 1.3.4. Probes responsive to pH changes

Many pH probes have been reported in literature, with some even being commercially available [219–222]. pH-sensing properties are usually based on the possibility of protonation or de-protonation of a functional group linked to a fluorophore scaffold. Interestingly, if a fluorescent probe becomes charged inside the cell, this usually leads to its intracellular capture and slower leakage, while the neutral fluorophores tend to diffuse away from cells [90].

Apart from *in vitro* probe validation in presence of possible cellular interferents (ions, ROS, RNS etc. at physiologically relevant concentrations), one direct method to evaluate probe behavior inside cells at different pH values is to change the intracellular pH using buffers. Incubation of a chosen cell line with a buffer should affect the intracellular pH, and, consequently, the probe's emission inside the cell [223–225]. The intracellular pH is expected to equilibrate with the extracellular buffer pH after sufficient incubation time.

Various buffers may be used for this purpose, such as Britton-Robinson buffer (pH range 2-12) [223, 226], high-potassium buffer [227] or Tris HCl buffer (working pH range 7-9) [228]. Britton-Robinson buffer bears a wide pH range: 2-12. [228]. High-potassium buffer often used in conjunction with nigericin, an ionophore which enables faster equilibration of intracellular and extracellular pH by transporting H<sup>+</sup> and K<sup>+</sup> ions across the cell membrane [222, 229]. It is worth noting that use of any ionophore can affect cellular homeostasis, including intracellular viscosity [226], which could complicate the analysis of experiment results especially in case of both polarity- and viscosity-sensitive probes.

A significant limitation of small molecule pH sensors is controlling their localization within the cell. These dyes are typically taken up into endosomal/lysosomal vesicles, but many are released from the endosomal compartment upon changing their protonation state [230]. As a result, it is difficult to ensure that the measured pH corresponds to a specific organelle [231]. To provide an additional information about the probe localization, one may introduce an organelle targeting group [232]. For example, in probes targeting lysosomes, the most used directing group is morpholine, which becomes protonated in the acidic pH within lysosomes, or other amine derivatives. Such pH-sensitive directing groups are included in numerous probes [233–235], and can also have a responsive function, expanding the number of analytes detected. The **Lyso-BFP** probe demonstrates this dual functionality, where the piperazine derivative provides both pH sensitivity and lysosome-targeting properties (**Figure 16**) [236].

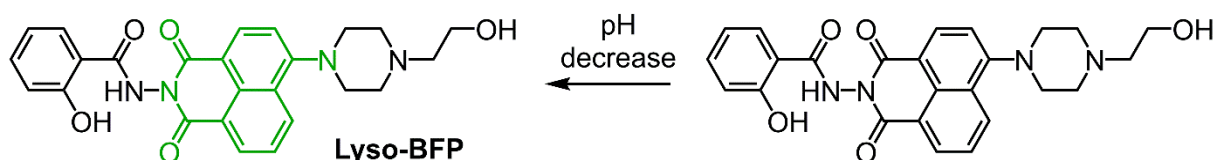


**Figure 16.** Example of a probe **Lyso-BFP**, bearing a piperazine derivative scaffold, which at the same time provides pH-sensitivity and lysosome-targeting properties. The PeT-based mechanism of fluorescence additionally provides fluorogenicity, thus no wash-labeling is possible. Green color of the molecule presents its emission color in “on” state, while the black one symbolizes non-fluorescent molecule. Adapted from [236].

Other pH-sensitive fluorescent probes, such as **NA1**, based on the naphthalimide scaffold, respond to pH changes via PeT inhibition at high pH (non-protonated) [237]. Upon protonation, PeT quenching is relieved and the fluorescence increases. Some probes can sense both pH changes and the presence of specific analytes simultaneously, for example in the case **DPFP** (**Figure 17**) [238]. **DPFP** exhibits dual color emission: blue for pH changes and green for the presence of formaldehyde. It was successfully introduced into live cells, demonstrating lysosomal localization and simultaneous intracellular imaging of formaldehyde. This is significant as formaldehyde, while considered a carcinogen [239] primarily generated from external sources [240], is also detected as a metabolic intermediate produced within the body by demethylase and oxidase enzymes [241]. Elevated levels of formaldehyde were found in damaged cells, tissues, which may lead pathological conditions including cancer, Alzheimer's disease, and chronic liver and heart disorders [242, 243]. Under certain physiological conditions, the levels of pH and formaldehyde are mutually dependent, making **DPFP** the first probe to image both analytes with different fluorescence responses *in cellulo* [238].

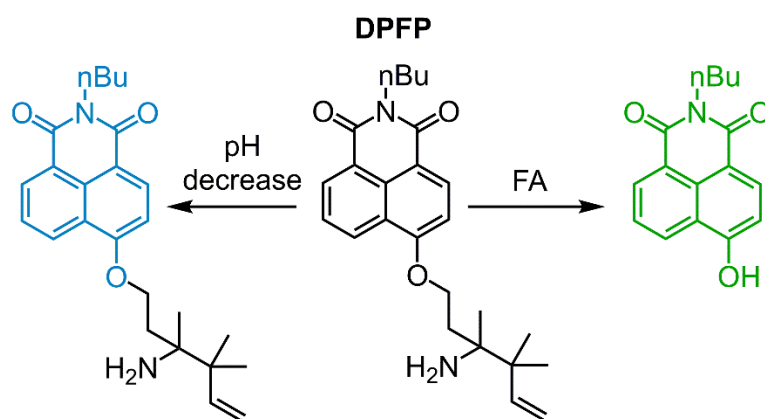


**Figure 17.** Naphthalimide-based probe **DPFP** sensitive to both pH and one more analyte (formaldehyde, FA). Blue/green color of the molecule presents its emission color in “on” state, while the black one symbolizes non-fluorescent molecule. Adapted from [238].

### 1.3.5. Multi-analyte responsive probes to polarity/viscosity/pH changes

There have also been probes developed that combine multiple detection strategies and allow users to visualize two physical parameter changes, and a selected few will be presented in this section.

The naphthalimide based **ND6** probe is sensitive to both pH and polarity changes [244]. Protonation of its amine substituent significantly increases emission by inhibiting photo-induced electron transfer (PeT) fluorescence quenching (**Figure 18**), similar to the activity observed in the **NA1** probe in the previous subchapter. **ND6** shows a clear change in fluorescence between pH 6 and 7, which correlates well with the typical intracellular pH fluctuations and makes **ND6** suitable for further application studies. The probe effectively labels the cell membrane with an excellent signal to noise ratio of 1300:1, and has been successfully used in tumor cells and tumor spheroids. These experiments revealed cholesterol's complex role in replenishing synaptic vesicle pools. Given that cell membrane dysfunction is associated with numerous diseases, including cancer and Alzheimer's disease [245]. **ND6** shows significant potential for studying membrane dynamics and synaptic functions in neurons and other secretory cells and tissues. Another example is probe **3** [246] (**Figure 18**), which responds to both viscosity and pH changes. Its structure, similar to other *N*-substituted 1,8-naphthalimides, suggests a mixed response mechanism involving both TICT and PeT mechanisms. It is worth mentioning that the presence of a methyl group on the piperazine ring enables pH-sensing properties, similar to probe **ND6**. Its viscosity-sensing properties, based on TICT and pH-response were confirmed in aqueous medium, but were not yet validated in cells. This demonstrates a common limitation of a wide range of dual-analyte fluorescent probes, highlighting also a practical challenge in developing tools that can retain their responsiveness in complex intracellular environments.

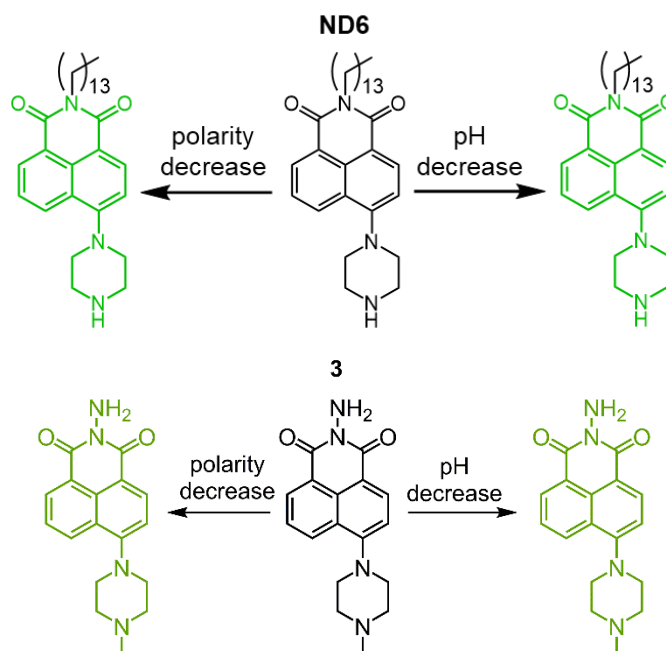


**Figure 18.** Examples of probes sensitive to viscosity and pH changes, **ND6** and **3**. Green color of the molecules presents its emission color in “on” state, while the black one symbolizes non-fluorescent molecule. Adapted from [137, 244, 246].

As probes become sensitive to more parameters, result interpretation becomes increasingly complex. There are examples of probes sensitive to both viscosity and polarity **PPBI** [247] or even additional analytes like H<sub>2</sub>S (**MQA-DNP** [248]) and nitroreductase (NTR) (**VPHP** [249]). All viscosity- and polarity-sensitive probes are presented in the **Figure 19**. However, changes in polarity sensed by these probes are often inversely related to changes in viscosity [247–249]. This makes it challenging to distinguish the relative contributions of each parameter to the fluorescent response. Additional experiments beyond fluorescence imaging may be necessary to fully characterize these multi-parameter probes.

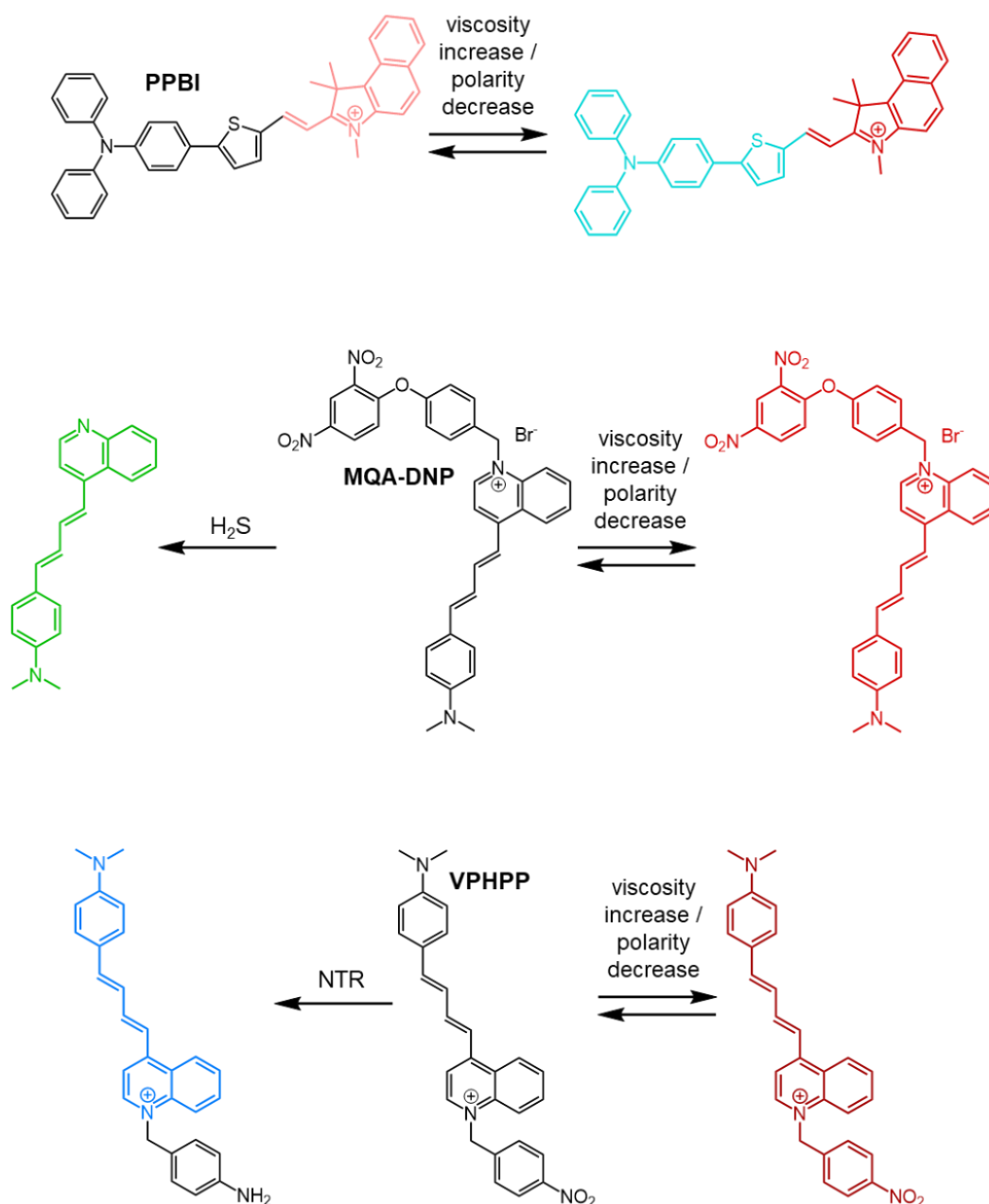


**Figure 19.** The probes sensitive to viscosity and polarity changes. Two of them present additional moieties sensitive to presence of one more analyte. Adapted from [137, 247–249].

## 1.4. Strategies for intracellular fluorescent labeling

### 1.4.1. Classical tools for intracellular fluorescent labeling

The low-molecular probes described in the previous subchapters have general applications and can provide base-level information about changes within a whole cell or a chosen compartment. To provide better selectivity and the possibility to observe a single target's local microenvironment, direct covalent labeling of analytes was introduced [250]. The covalent labeling of specific targets may provide information about transport, behavior or even interactions of the target with other species present inside cells [251]. It could also enable monitoring of the changes in its local microenvironment that might differ from the bulk. *In vitro* experiments showed that physicochemical parameters (polarity, proton concentration) may significantly vary with distance around spherical micelles in water, a simple membrane-based system [252, 253]. Since the intracellular environment is significantly more crowded and complex (**Figure 20**), such parameters within the nanoenvironment of different species may differ to even a greater extent and fluctuate very dynamically over time.

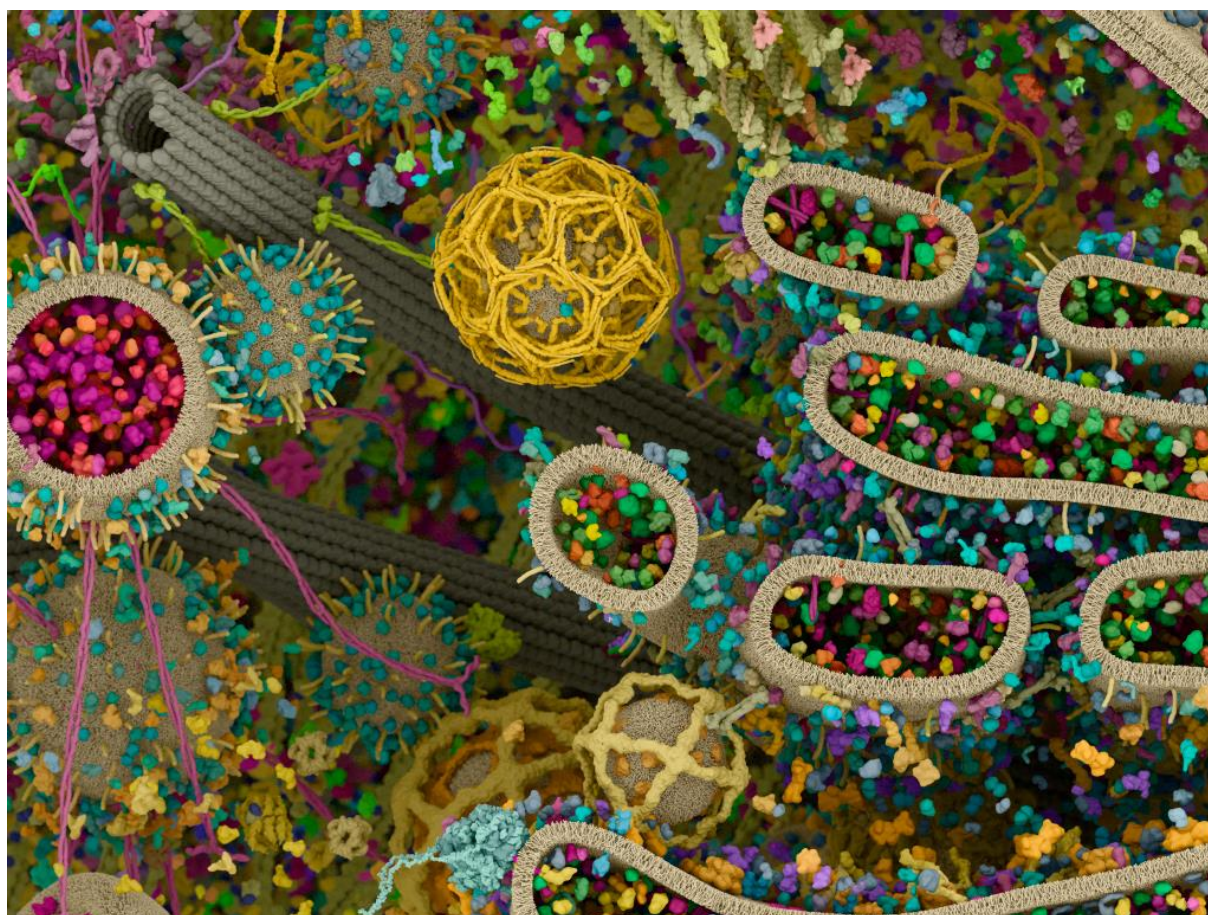


**Figure. 20.** 3D rendering of a eukaryotic cell – molecular landscape depicting key pathways and structures in vesicle trafficking, including post-translational modifications (right), Golgi and post-Golgi trafficking (center), cytoskeleton (top), and the endo-lysosomal compartment (left). Structural data derived from the PDB and/or EMDB (X-ray, NMR, cryo-electron microscopy) and modeled with Molecular Maya (mMaya). Credit: Evan Ingersoll, Scientific Animator, and Gaël McGill, Founder and CEO, Digizyme, Brookline, Massachusetts, USA, 2021.

Fluorescence-based labeling methods can be divided into two main categories: those that require genetic modification of the target and those that do not.

Genetically-based methods include enzyme-catalyzed labelling, fusion of biomolecules with a peptide tag containing a fluorescent probe, or incorporation of unnatural amino acids. Non-genetic methods, on the other hand, involve direct interaction between the target and chemical probe. The latter occurs when cells are incubated in a solution containing the probe, allowing accumulation of the probe inside the cell, where covalent labeling of the target takes place [251].

Proteins are particularly important targets to investigate using these methods, as they participate in or even govern multiple processes *in cellulo* [254]. To provide wider context to this discussion, different approaches to covalent protein labelling will be presented in the upcoming sections, including methods requiring genetic modification (subchapter **1.4.2.**) and direct labeling of endogenous proteins (subchapters **1.4.3.-1.4.4.**).



### 1.4.2. Target labeling through genetic modification

The complexity of intracellular environment poses challenges for the specific labeling of proteins. The most commonly used method to provide selectivity is to introduce a specific genetically encoded tag, which is co-expressed and co-translated with a target (protein of interest, POI) [255]. This tag is usually designed to provide bioorthogonality i.e. any chemical reaction that can take place *in vivo*, without interfering with native processes [256]. This type of chemistry has become a widely used approach for investigating biomolecular dynamics and functions within living systems. Due to its distinctive properties, bioorthogonal chemistry has been effectively utilized in a wide range of protein functional studies, including visualizing protein expression, tracking protein localization, measuring protein activity and identifying protein interaction partners in living systems [257]. In this subchapter, the most popular methods of protein target labeling through genetic modification will be discussed.

#### *His-tags and other short tags*

One of the first published techniques to covalently label targets of interest was based on genetic encoding of the polyhistidine motif (so called “His-tag”, e.g. hexa-tagged) to a target protein. The principal role of this tag is to facilitate the purification and isolation of the target with use of a Ni<sup>2+</sup>-nitrilotriacetate system of high His-tag affinity [258]. This tag was successfully repurposed to enable specific recruitment and subsequent intracellular labeling with a fluorescent probe bearing an optimized high His-tag affinity motif [259] to stabilize the probe-His-tag complex. The authors were able to use this approach to visualize DNA repair proteins in multiple cell lines. A similar approach was used to measure the distance between proteins, with use of the FRET mechanism [260].

Similarly, Strep-tag or FLAG-tag may be introduced into the genome to create fusion gene with protein of interest. Strep-tagged proteins may be isolated from cell lysates by biotin (known as vitamin H or B<sub>7</sub>), while FLAG-tag presents affinity towards high affinity monoclonal antibodies. There are now many published tags with multiple applications *in vitro* or *in cellulo*, such as the tetracysteine-tag, which is first expressed on a target and later labeled with a fluorogenic biarsenical dye *in cellulo* [261]. Even though such tags are relatively small in size (2-3 kDa), their low cell-permeability and low affinity results in relatively low complex stability. Therefore, alternative methods described in upcoming subchapters are often considered instead.

#### *Fluorescent proteins*

In recent years, genetically encoded fluorescent proteins like green fluorescent protein (GFP) and its color variants have been extensively used to visualize recombinant protein expression and localization in live cells [262, 263]. Despite their effectiveness, fluorescent protein tags are limited by their relatively large size (~27 kDa) and the potential to disrupt protein function. Moreover, in comparison to other fluorescence-emitting labeling methods, fluorescent proteins exhibit lower photostability than other fluorescence-based methods [264, 265]. Inspired by GFP multiple new classes of fluorescent proteins have emerged [266]. A relatively new class includes non-fluorescent proteins, which become fluorescent upon reaction with a chosen substrate, e.g. flavin mononucleotide or bilirubin. The development and use of fluorescent proteins have been characterized and reviewed comprehensively [267, 268].

### *Self-labeling enzymes*

Alternative to fluorescent proteins, genetically encoded tags like O<sup>6</sup>-alkylguanine-DNA-alkyltransferase (AGT, also known as SNAP-Tag in a modified form [269, 270]) have been developed [271, 272], known as self-labeling proteins (SLPs). SNAP-tag can be covalently labeled with O<sup>6</sup>-benzylguanine derivatives chemically coupled with various fluorogenic compounds, allowing the generation of highly fluorescent labels. Depending on the dyes used and their membrane permeability, this method can label both cell surface and intracellular proteins. In addition to SNAP-tag, other tags were further developed like HaloTag [272] and CLIP-tag [271]. These engineered protein tags are derived from mammalian (SNAP-tag, CLIP-tag) or bacterial enzymes (HaloTag), each designed to covalently bind specifically to synthetic ligands, enabling targeted labelling in cells.

A major advantage of these tags is the possibility of modification of their substrates to specific applications. Moreover, a few types of tags may be used in one experiment nearly simultaneously, since they are selective for specific substrates, which may be derivatized [271, 273–275]. Fluorophores linked to those substrates can have varying properties; they may activate on binding, emit light constantly, respond to environmental changes, or combine a few fluorophores in a single structure. Unfortunately, these tags still bear a high molecular mass (20-30 kDa) and therefore may affect the activity of the endogenous proteins, which could alter their native behavior [273]. In addition, similarly to fluorescent proteins, those tags need to adopt an appropriate 3D structure to enable their enzymatic substrate-specific reactivity. Therefore, since usually only a fraction of tags folds correctly in the cellular environment, labeling efficiency might be lowered [276].

Both SBD and 1,8-naphthalimide derivatives were successfully used to develop SLPs. SBD and its derivatives, where the oxygen atom is exchanged with sulfur, were successfully used as reporter covalently linked with substrates for both SNAP-tag and HaloTag [277–280]. The sensitivity of all SBD-based probes relies on changes of their emission due to fluctuations in their immediate microenvironment. It was observed that covalent linkage to SNAP-tag substrates quenches fluorescence of the fluorophore component. However, after reaction between the fluorophore-substrate and tag, the fluorescence typically increases upon covalent attachment of the fluorophore to the surface of the tag. This occurs because the polarity on the surface of the protein versus the bulk solution differs due to the presence of specific interacting amino acids. Interestingly, it was shown that modifying the length of HaloTag substrate may increase the fluorescence once the benzothiazole probe **P9** is linked to the HaloTag [277]. 1,8-naphthalimide derivatives are typically used as SNAP-tag probes [281–283]. All mentioned tag-targeted probes were successfully introduced into live cells expressing genetically modified tag-bearing protein targets. A selection of fluorophore-substrate molecules from this section are presented in the **Figure 21**.

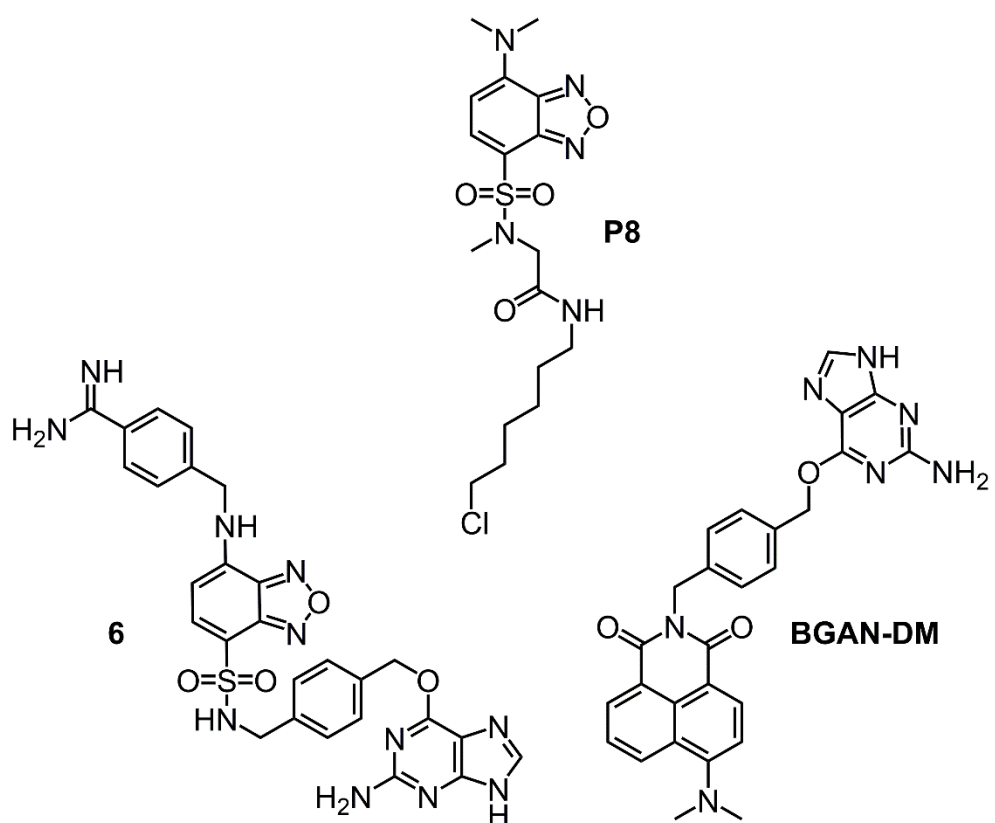


**Figure 21.** Examples of fluorogenic molecules structures used as substrates for chosen self-labeling proteins: **6** and **BGAN-DM** for SNAP-tag and **P8** for HaloTag. Adapted from [277–283].

### Use of non-canonical amino acids

The 2022 Nobel Prize in Chemistry, awarded to Carolyn R. Bertozzi, Morten P. Meldal and K. Barry Sharpless for “the development of click chemistry and bioorthogonal chemistry” affirmed the significant potential of click chemistry. This concept, first fully described in 2001 [284], has revolutionized many areas at the interface of chemistry and biology. Apart from its application in organic synthesis, the idea has been applied widely to develop the foundations of bioorthogonal reactions [285]. This has resulted in the successful labeling of targets in cell lysates and even live cells [286]. A recent innovation of note was the development of unnatural amino acids (also called non-proteinogenic or non-canonical amino acids) and their incorporation into protein structures, enabling labeling of targets with small molecule probes [287, 288]. Introducing unnatural amino acids into proteins, however, is complex and labor-intensive, requiring four components: unnatural amino acid (UAA), unused codon, tRNA that recognizes this codon and tRNA synthetase [288]. However, once every component is ready, the possibilities are extensive. The most popular pair of reagents currently used for such labeling are the tetrazine scaffold, which additionally quenches fluorescence of the reporter causing fluorogenic response of labeling, and a strained alkene or alkyne, which selectively reacts with the first heterocycle [289]. The UAA of choice may be directly connected to the fluorescent probe or be separately from fluorophore part introduced into cells. The examples of the first approach are 4-nitrobenzo[*c*][1,2,5]oxadiazole derivative [290] and the one based on 1,8-naphthalimide scaffold [291] (**Figure 22**). The second technology firstly introduce i) UAA of choice bearing strained click-group and afterward ii) fluorophore-tetrazine scaffold, compatible to i) [292] (**Figure 22**).

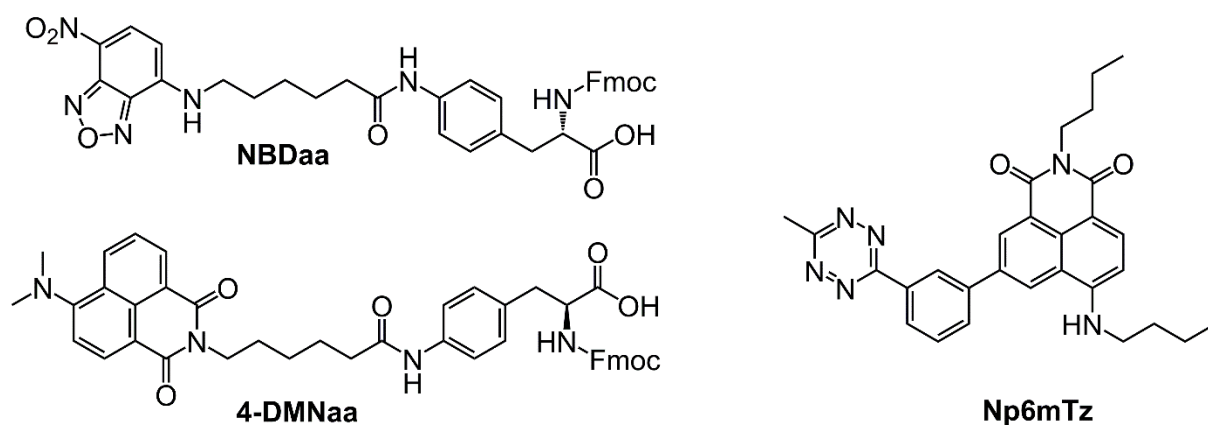


**Figure 22.** Examples of probes for unnatural amino acid use. The first two examples (**NBDaa**, **4-DMNaa**) present an approach, where one molecule is used as an unnatural amino acid and reporter (fluorophore) at the same time. The last one, **Np6mTz** is constructed from a tetrazine handle (to react with unnatural amino acid with strained reactive handle) and reporter (fluorophore). Adapted from [290–292].

### 1.4.3. Labeling of unmodified proteins

While the previously describe methods are indeed powerful, they are not applicable to natural (endogenous) proteins as they require the artificial expression of modified proteins or their fragments. Additionally, there are concerns that the resultant fusion protein may alter the original properties of the protein of interest (POI) such as structure, function, and localization, due to its size [273]. Therefore, labeling of non-modified (endogenous) proteins has become a focus for researchers in recent years [293] with a number of approaches developed. Labeling proteins may target multiple sites: surface amino acids, amino acids at the entrance of active site or even amino acids inside the active site.

#### *Labeling of surface amino acids*

One of the most straightforward techniques for labelling surface amino acids is to use chemoselective reactions [294, 295]. For example, thiol groups can react with maleimide esters in a Michael addition, or a terminal amine group of lysine may attack activated esters (**Figure 23**) [294]. Such reactive handles have been introduced into small-molecule probes, but often lack sufficient chemoselectivity, site-selectivity, suffer from long reaction time or low conversion [295].

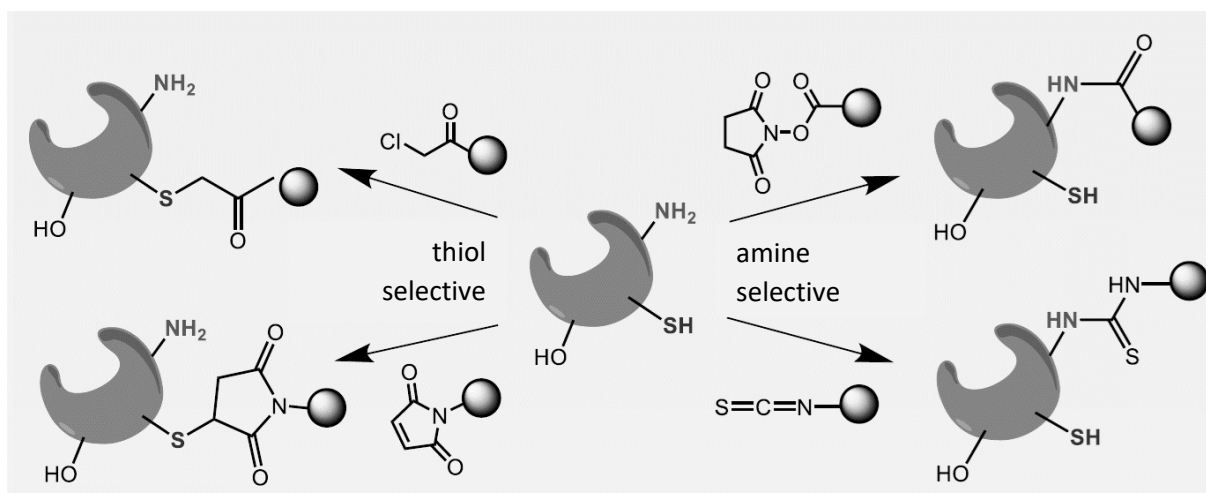


**Figure 23.** Examples of protein labeling approach with use of reactive handles in presence of amino acids with thiol or amine groups. Adapted from [294].

Nucleophilic or electrophilic properties of certain amino acid residues have also been investigated as a pathway to provide greater selectivity of interaction. One example of such probes is **MSBN (Figure 24)** [296], [296], based on the 1,8-naphthalimide scaffold, which has been used to selectively image thiols in live cells, providing a >100-fold turn-on signal upon labeling, enabling identification of various reversible protein thiol modification [296–298]. The authors were able to further modify the probe to clearly distinguish the reduced thioredoxin and the oxidized form. The latter could provide additional information about cellular redox regulation.

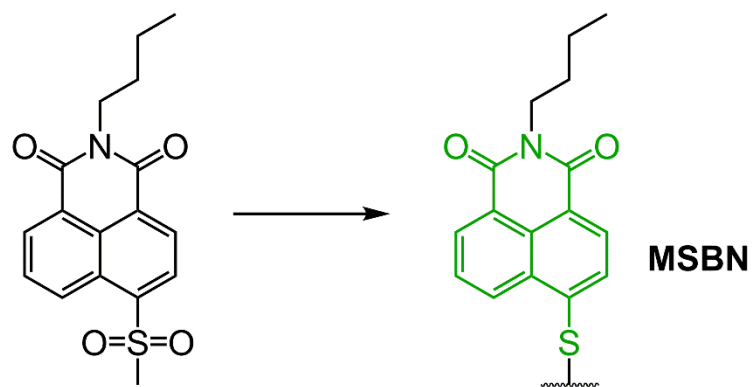


**Figure 24.** Example of a probe for labeling of surface amino acids. The probe presents a significant turn-on response to allosteric site's microenvironment. The green color-marked in a molecule in its turn-on, while the black-marked is not fluorescent. Adapted from [296].

### Labeling at active or allosteric site

Secondly, it is possible to directly label the active site of a POI, with multiple examples in literature. These probes do not fully block the active site and interact reversibly [299, 300]. To eliminate reversibility of interaction, the technique was modified to enable covalent labelling of amino acids at the active site of POIs. A drawback of this method is the inability to observe the natural activity of the targets. This inhibition can be beneficial in the development of therapeutic compounds [301, 302]. One approach used a library of 4-amino-1,8-naphthalimide-based probes (**Figure 25**) [303]. These probes exhibited unusual properties, including a hypsochromic shift in emission and higher brightness. The probes consisted of a fluorophore connected to a short peptide with a terminal reactive warhead, such as diphenyl phosphate for serine proteases. This design was used to successfully detect thrombin protease activity.

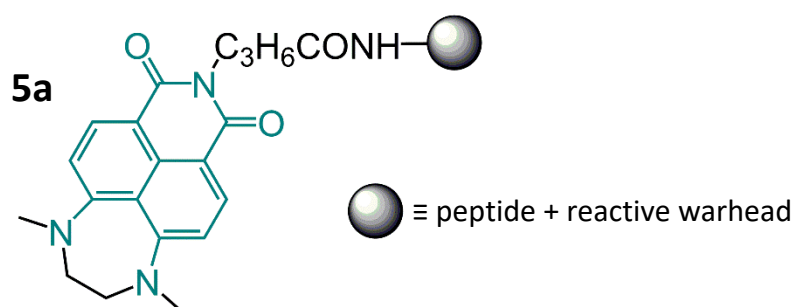


**Figure 25.** Example of a probe **5a** for labeling of active-site amino acids. The blue color represents color of emission of the probe in its “on” state. Adapted from [303].

An alternative approach to modulating protein activity is to label the allosteric site of POI. Allosteric sites can bind effectors (molecules or ions) that may result in, e.g. conformational changes affecting protein activity. The group of allosteric effectors consists of both activators and inhibitors. Such an example of allosteric labeling was presented with a biarsenical probe [301]. The probe targeted a cysteine residue in the allosteric site of the potentially oncogenic protein tyrosine phosphatase Shp2. The probe was successfully introduced *in cellulo* and present an interesting alternative to already-known inhibitors of active site of the POI. A similar study of a potential allosteric site for another protein from the same protein family was conducted with SBD as the fluorescent scaffold (**Figure 26**) [304].

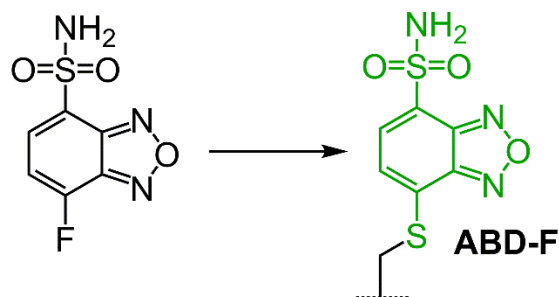


**Figure 26.** Example of a fluorogenic probe **ABD-F** for labeling of allosteric-site amino acid, cysteine. The probe presents a significant turn-on response to allosteric site’s microenvironment. The green color-marked in a molecule in its turn-on, while the black-marked is not fluorescent. Adapted from [304].

### Additional classes of labeling

While a few techniques have been mentioned in previous subchapters, there is a wide variety of methods available, with new examples emerging regularly. In theory, one could imagine combining nearly any techniques used for labeling of intracellular targets. However, designing and obtaining such probes may be time-consuming and many factors must be taken into account.

An example of an extended version of previously mentioned techniques is the use of a 1,8-naphthalimide-based probe for inhibitor screening via cross-linking and in-gel fluorescence [305, 306]. The authors synthesized a group of probes able to react with only selected proteins when the fluorophore-inhibitor molecule is irradiated (using an azido group; **Figure 27**). The relative efficiency of cross-linking with various probes can be considered indicative of their inhibition potencies. A significant advantage was the fact that the designed method can be used on impure protein mixtures, and the entire analysis is relatively short compared to the other methods. This method was applied to a few proteins, including human carbonic anhydrase II (hCAII).

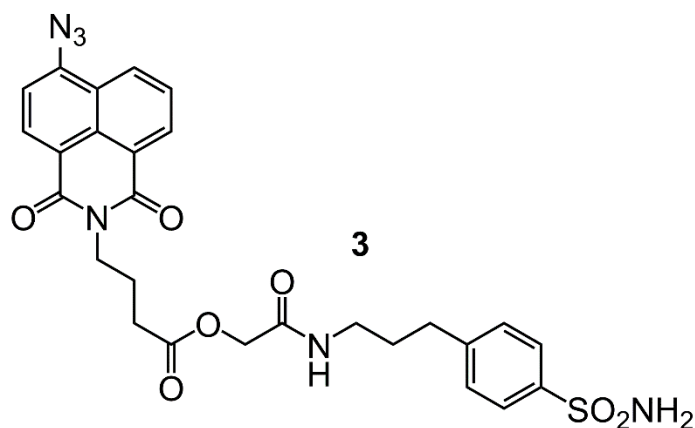


**Figure 27.** Example of a probe **3** for photo-crosslinking labeling of hCAII. Adapted from [305].

Another interesting example is a technique named covalent ligand directed release, abbreviated as CoLDR. [307]. Depending on the ligand used, it may or may not block the active site of the POI. Due to the presence of a ligand selective to the POI, the probe is transported towards the POI and then undergoes a *quasi*-intramolecular reaction. As a result, the ligand is covalently labeled to the POI in close proximity to its active site and fluorophore is released, inducing a turn-on response. This approach proved successful for labeling three different proteins and for use in high-throughput screening of inhibitors for a chosen POI. This technique serves as an excellent introduction to the next subchapter, which will delve into affinity-based, ligand-directed labelling technology for endogenous proteins. All methods described in subchapters **1.4.2.** and **1.4.3.** are schematically presented in the **Figure 28.**



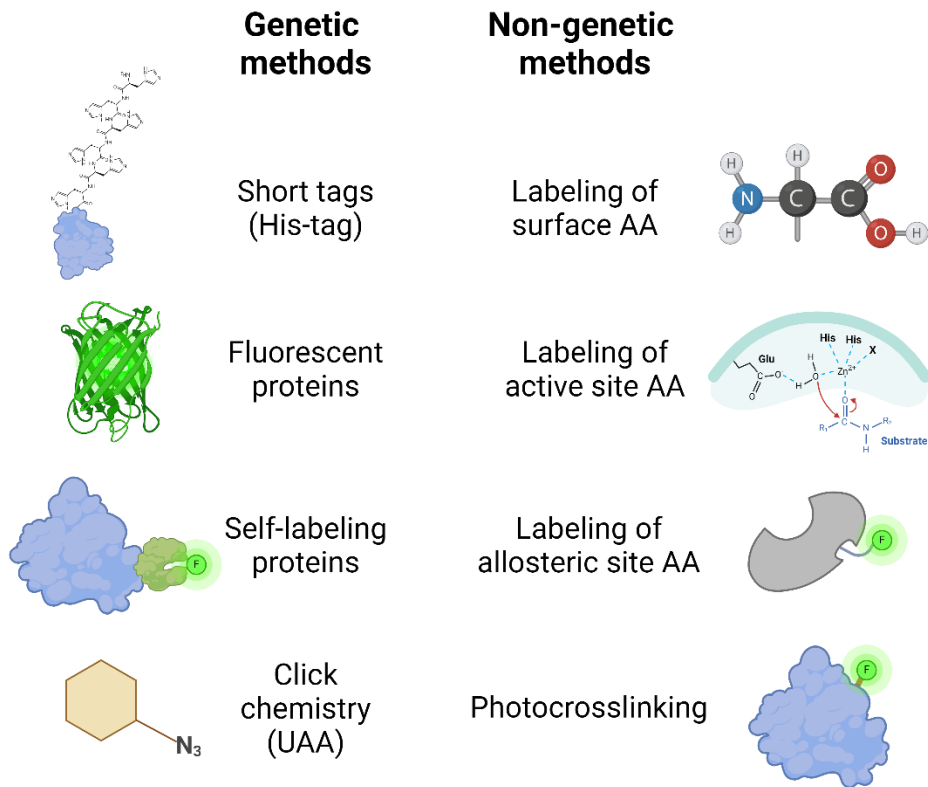


**Figure 28.** Schematic representation of methods of labeling with and without need of genetic modification. AA – amino acid. Created with BioRender.com.

#### 1.4.4. Ligand-directed affinity labeling LD

In 2009, the Hamachi group presented an interesting approach to protein labeling, without the need for genetic modification of the target, providing target-selectivity and site-specificity towards one or more amino acids in close proximity to active site. The technique was called *affinity-labeling* (or *ligand-directed labeling*) and was successfully introduced *in vitro*, *in cellulo* and *in vivo* [308]. The first reactive group published was a tosylate, originating from fundamental organic chemistry. The tosyl group is considered an excellent leaving group and has been introduced to multiple molecules, before conversion into desired products with use of nucleophilic reagents [309]). Depending on the choice of a reactive group, kinetics of the affinity-based labeling are comparable to different click-chemistry-based bioorthogonal techniques for protein labeling (**Figure 29**) [310].

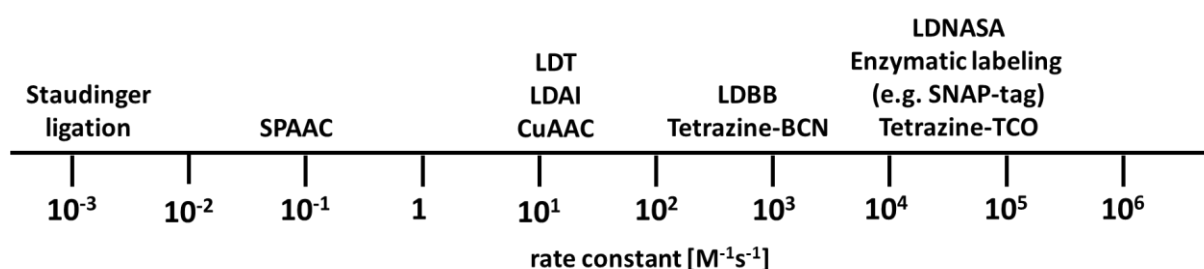


**Figure 29.** Comparison of rate constants between different kinds of covalent intracellular labeling methods of targets. Adapted from [310]. LDT – ligand-directed tosyl chemistry; LDAI – ligand-directed acyl imidazole chemistry; LDBB – ligand-directed dibromophenyl benzoate chemistry; LDNASA – ligand-directed *N*-acyl-*N*-alkyl sulfonamide; SPAAC – strain-promoted azide-alkyne click chemistry; CuAAC – copper-catalyzed azide-alkyne cycloaddition; BCN – bicyclo[6.1.0]non-4-yne; TCO – trans-cyclooctene.

The mechanism of action of such probes is based on the susceptibility to substitution of nucleophiles to different electrophilic moieties (S<sub>N</sub>2-type reaction) (**Figure 30**). Until now, most reactive groups presented in the literature include a carbonyl group carbon (e.g. dibromophenyl benzoate, LDBB [311]), methylene group carbon (e.g. tosyl, LDT [308]) or other electrophilic center such as a sulfur atom (e.g. *N*-sulfonyl pyridone, LDSP [312]). [312]). These carbon atoms are attacked in a *quasi*-intramolecular reaction by the nucleophilic amino acid near the active site of the target. It is worth to highlight that similar probes selective to acidic amino acids [313] have been published, however they will be not discussed as they are out of scope of this thesis.

Since 2009 [308], several new reactive groups for nucleophilic amino acids have been explored [314], [315], [316] (**Figure 31**, top) and [317–319] (**Figure 31**, bottom). The properties of those reactive groups are frequently validated in direct comparison to properties of the Hamachi group's reactive moieties (stability, kinetics, amino acid selectivity).

The *quasi*-intramolecular reaction between the probe and the target consists of a few steps, where they happen nearly or even at the same time (due to a proximity effect) [308]. The probe consists of a ligand, linker to a reactive group and a further linker to the reporter molecule (**Figure 30**, over the arrow). First, the ligand (built from a substrate or reversible inhibitor of the POI) recruits the probe to the target via ligand-active site reversible binding.

The active site is usually surrounded by different amino acids, creating the perfect conditions for attack by a nucleophilic amino acid (e.g. cysteine, lysine, histidine) on the electrophilic part of the probe [310]. This nucleophilic attack leads to formation of a covalent bond between the amino acid and reactive group, which is connected to a reporter moiety (fluorophore) [308]. The byproduct of this reaction diffuses away, leaving an unoccupied active site, preserving the intrinsic properties of the POI. A simple scheme of this labeling technique is presented in the **Figure 30**.

This ligand-directed approach may be combined with other techniques, including click-chemistry. This combination was reported by a pioneering group in 2021, who aimed to quantify neuronal glutamate receptor trafficking [320]. There are also analogous systems, with variations on the probe structure [321]. Additional use of a catalyst or ion-assisted labeling methods were also presented and described in the literature [293].

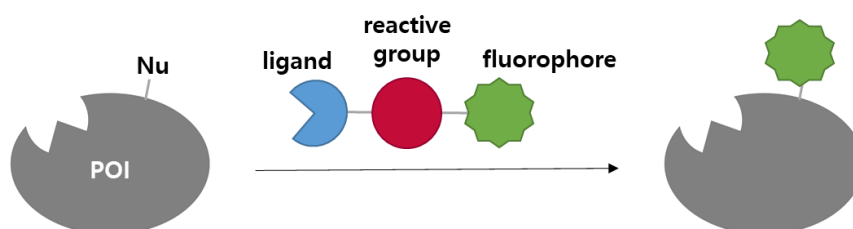


**Figure 30.** Schematic presentation of mechanism of labeling with use of an affinity-based labeling approach (ligand-directed labeling). Adapted from [322]. The probe consists of a few parts presented in the middle of the scheme (ligand, reactive group, fluorophore and two different or same linkers between them). POI – protein of interest; Nu – nucleophilic amino acid on protein surface, in close proximity to protein’s active site.

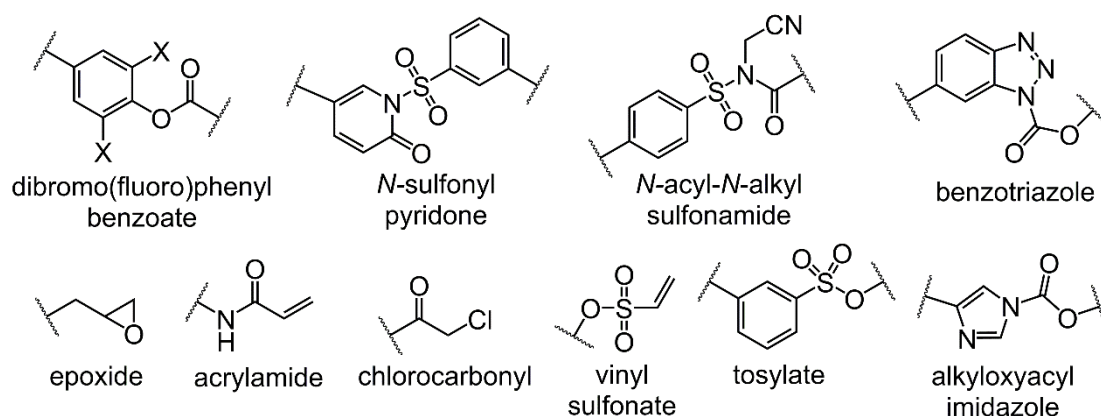


**Figure 31.** Examples of reactive groups presented in literature for covalent labeling of proteins. Adapted from [315]. X – Br or F.

## 2. Aim of the thesis

Parameters of the cellular microenvironment including viscosity, polarity and local pH are known to significantly affect intracellular homeostasis on multiple levels. Knowledge regarding the implications of these factors is constantly expanding, but there is insufficient evidence to explain their relative inter-dependencies to draw precise conclusions. Our understanding of both physiological and pathological processes could benefit greatly from investigating these relationships within the cellular microenvironment, opening previously unexplored areas of research and even treatment.

To contribute to this goal, the main aim of this thesis was to develop environment-sensitive and pH-responsive probes (dual- or multi-analyte ones) for intracellular applications and demonstrate the possibility of covalent introduction of such probe into the structure of the target protein without the need for genetic modification. This was to be achieved through the following objectives (**Figure 32**):

1. Synthesis and validation of an environment and pH sensitive probe based on SBD scaffold – **Chapter 4.1**
2. Synthesis and validation of an environment and pH sensitive probe based on naphthalimide scaffold – **Chapter 4.2**
3. Create a tool for covalent labelling of a protein of interest with an environment-sensitive and pH-responsive probe – **Chapter 4.3**

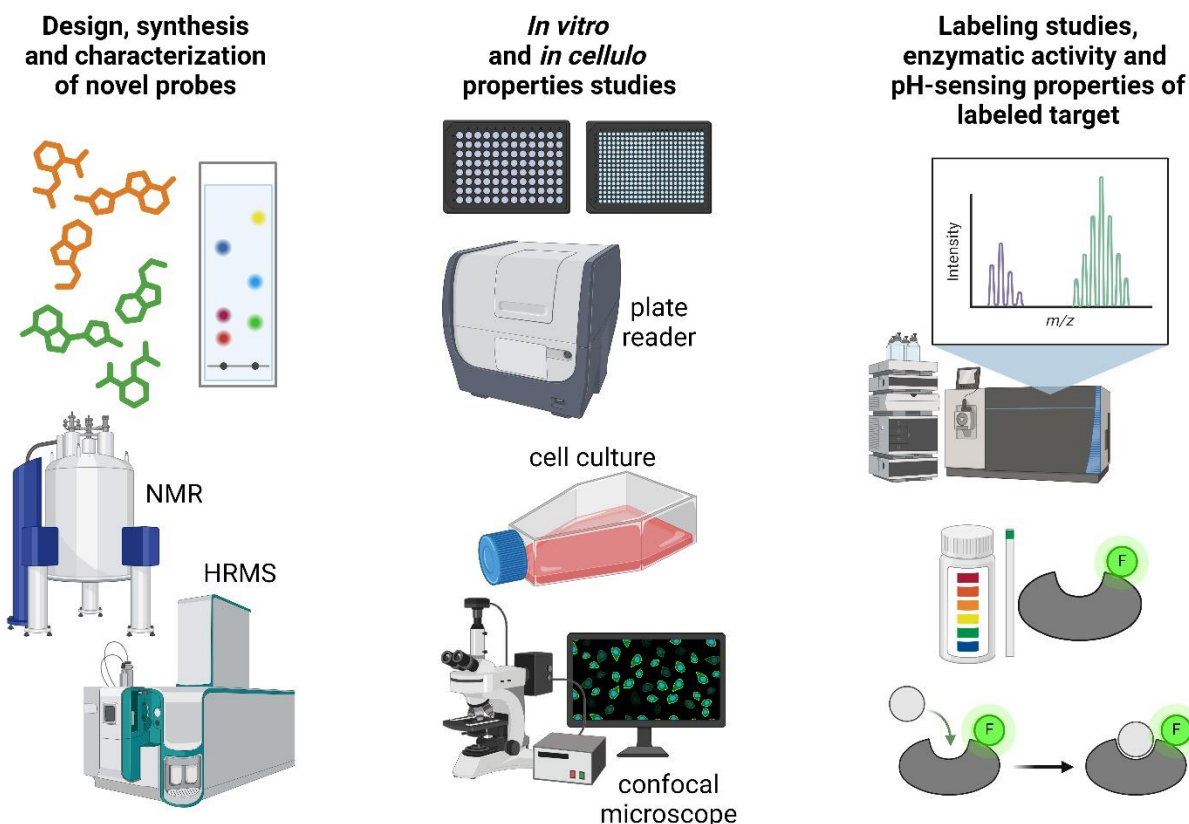


**Figure 32.** Schematic representation of project steps and main objectives. NMR – nuclear magnetic resonance; HRMS – high-resolution mass spectrometry; F – fluorophore. Created with BioRender.com.

### 3. Materials and methods

#### 3.1. Materials and instruments

**General materials for organic synthesis and analytical tests.** Unless otherwise specified, all chemicals were purchased from commercial suppliers and used without further purification. Piperazine, *tert*-butanol, di-*tert*-butyl dicarbonate (Boc<sub>2</sub>O), anhydrous ACN, benzyl bromide, trifluoroacetic acid (TFA), anhydrous DCM, 2-(2-aminoethoxy)ethanol, *tert*-butyldimethylsilyl chloride, 3M HCl in MeOH, diethylene glycol, silver(I) oxide, potassium iodide, Wang resin, *p*-nitrophenyl chloroformate, collidine, *N,N*-diisopropylethylamine (DIPEA), anhydrous DMF, potassium cyanide, 3-phenylpropan-1-ol, 4-dimethylaminopyridine (DMAP), triethylsilane (TES), fluorescein, quinine hemisulfate salt monohydrate, coumarin 343, *N,N,N',N'*-Tetramethyl-*O*-(*N*-succinimidyl)uronium tetrafluoroborate (TSTU), CDCl<sub>3</sub>, CD<sub>3</sub>OD, DMSO-*d*<sub>6</sub>, acetone-*d*<sub>6</sub>, iron(III) chloride hexahydrate, iron(II) sulfate heptahydrate, lead(II) nitrate, magnesium sulfate, potassium nitrate, silver nitrate, tetrakis(acetonitrile)copper(I) tetrafluoroborate, ammonium acetate, sodium phosphate dibasic, sodium phosphate monobasic, ammonium citrate and *N*-(2-Hydroxyethyl)piperazine-*N'*-(2-ethanesulfonic acid) (HEPES) were purchased from Merck. Ninhydrin, 4-bromo-1,8-naphthalic anhydride, 1,5-diaminopentane (cadaverine), sodium acetate, citric acid and zinc bromide were purchased from Fluorochem. Chlorosulfonic acid, ammonium iron(II) sulfate hexahydrate, cobalt(II) nitrate hexahydrate, lithium nitrate, potassium tetrachloroplatinate(II), zinc nitrate hexahydrate, aluminium nitrate nonahydrate, copper(II) nitrate trihydrate, nickel(II) nitrate hexahydrate and sodium nitrate were purchased from ThermoScientific. 4-Chloro-2,1,3-benzoxadiazole, *n*-butylamine were purchased from TCI. Solvents (DCM, EtOAc, MeOH, toluene, anhydrous EtOH, hexane), Et<sub>3</sub>N, sodium hydroxide, magnesium sulfate, sodium chloride, sodium bicarbonate, potassium carbonate, sodium sulfate, sodium citrate and sodium phosphate were purchased from POCH, Chempur or Warchem. Anhydrous DMSO (for biological purposes) was purchased from Acros. Imidazole was purchased from Fluka. Phenol was purchased from Roth. 3-(chlorosulfonyl)benzoyl chloride was purchased from Argenta. Cadmium nitrate tetrahydrate and gallium nitrate monohydrate were purchased from Alfa Aesar. Calcium nitrate tetrahydrate was purchased from Chmes. The water in all *in vitro* tests was high-purity MiliQ water.

**General materials for biochemical/biological experiments.** DMEM High Glucose was purchased from ThermoScientific or Capricorn Scientific. Fetal bovine serum was purchased from EURx. Penicillin-streptomycin 100X (100-time concentrated) was purchased from Capricorn Scientific. Trypsin-EDTA Solution 10X (10-time concentrated), Carbonic Anhydrase II human, 1,4-dithiothreitol and iodoacetamide were purchased from Merck. Fluorobrite DMEM and Slide-A-Lyzer MINI Dialysis Device (10000 MWCO) were purchased from ThermoScientific. PBS was purchased from Corning or EURx. MitoTracker Deep Red FM and LysoTracker Deep Red were purchased from Invitrogen. Carbonic Anhydrase (CA) Activity Assay Kit (Colorimetric) was purchased from Abcam. DMSO (for molecular biology, DNase, RNase and Protease free0) was purchased from Acros. The water in all *in cellulo* tests was high-purity MiliQ water.

**Instruments.**  $^1\text{H}$  NMR and  $^{13}\text{C}$  NMR spectra were recorded using the NMR 400 MHz (9.39 T) spectrometer AVANCE II Bruker. Chemical shifts were referenced to tetramethylsilane (TMS –  $^1\text{H}$ ) and solvent residual signals. Chemical shifts and coupling constants are specified in ppm and Hz, respectively. Reactions were controlled/monitored by TLC on normal-phase silica gel plates (Merck TLC Silica gel 60 F<sub>254</sub>) with visualization of components by UV light (254 and 365 nm), staining with ninhydrin solution (ingredients: ninhydrin, acetic acid, butanol) or with visual observation of the dye spots. Products were purified using flash column chromatography using Merck normal-phase silica gel 60 (0.063-0.200 mm) for column chromatography (70-230 mesh ASTM). Final purifications were performed using semiprepTLC on glass or aluminum plates. Mass spectra was measured by liquid chromatography high resolution mass spectrometry (Bruker micrOTOF-q) technique. Protein labeling analysis was conducted with the use of nanoLC-MS system Proxeon nanoLC & Bruker UltrafleXtreme, while the analysis of the obtained mass spectra was done with Mascot Search Engine. Absorption and fluorescence measurements were recorded using BioTek Cytation 5 Cell Imaging Multi-Mode Reader or Edinburgh Instruments Spectrofluorometer FS5, in 96-well or 384-well plates. Spectra were recorded with 5 nm steps unless mentioned otherwise. The pH measurement was performed using a pH meter (Mettler Toledo FiveEasy PLUS FP20 benchtop pH-meter). Cell imaging was performed using Leica TCS SP5 II confocal microscope with live-cell imaging chamber.

## 3.2. Synthesis details

### 3.2.1. General notes

Molecular sieves for additional drying of solvents (DCM, DMF) were activated with microwave irradiation (3 min heating). Solid support synthesis was conducted on Wang resin, which was rocked in a solvent of choice on a lab roller rotator. Kaiser test was done visually with control resin grains (negative control, no coloring of the grain after heating). Kaiser test for the synthesis on resin was conducted with a mix of three stock solutions prepared beforehand: i) reagent A ( $2 \cdot 10^{-4}$  M solution of KCN in water/pyridine mixture ratio 1:49), ii) reagent B (0.28 M solution of ninhydrin in n-butanol), iii) reagent C (21.25 M solution of phenol in n-butanol). The tested resin grains were put into the mixture of all three ingredients and heated at 110°C, until the color (dark blue/indigo/dark violet or no color in case of control sample) of the tested grains was observed. The ninhydrin stain for monitoring of reactions conducted in solution (round-bottom flask, stirring magnetic dipole) was prepared with the use of ninhydrin (1.5 g), which was dissolved in n-butanol (100 mL) and acetic acid (3 mL) mixture.

### 3.2.2. Synthesis of intermediate compounds for the probe SOLpH1

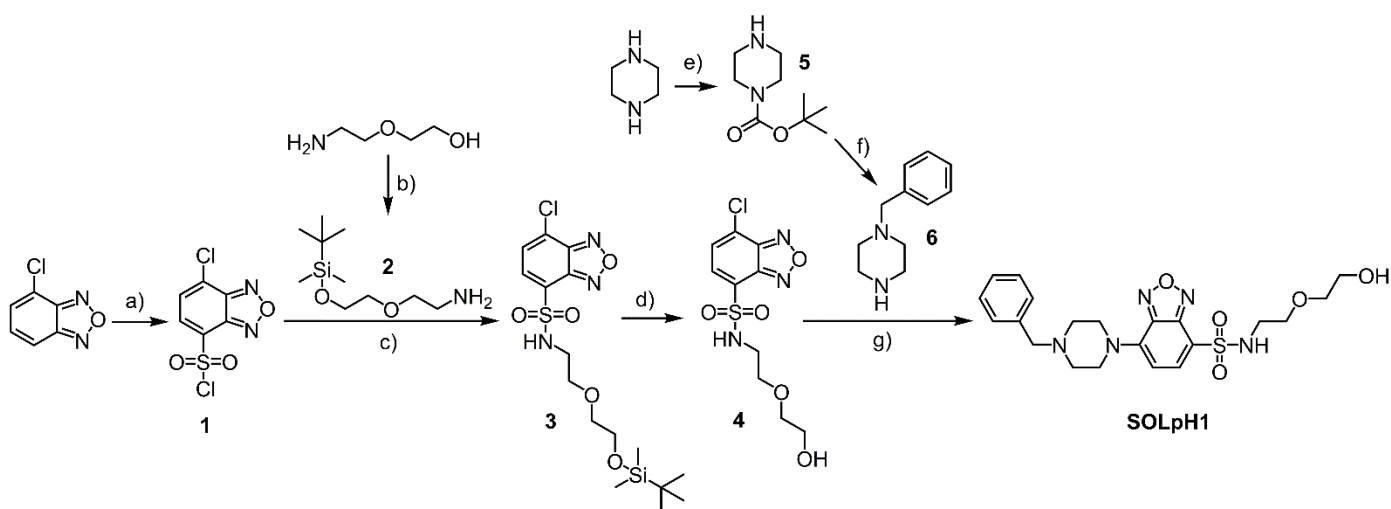


**Figure 33.** Synthetic pathway leading to the **SOLpH1** probe: a) chlorosulfonic acid, 3 h, 120°C, 81%; b) *tert*-butyldimethylsilyl chloride, imidazole, DCM, RT, 20 h, 57%; c) Et<sub>3</sub>N, DCM, 24 h, RT, 54%; d) 3M HCl in MeOH, 2 h, RT, quant.; e) di-*tert*-butyl dicarbonate, *tert*-butanol, NaOH 2M solution, 1 h, RT, 69%; f) benzyl bromide, Et<sub>3</sub>N, ACN, RT, 65%; g) TFA, DCM, RT, 1 h, quant.; h) Et<sub>3</sub>N, ACN, 80°C, 24 h, 59%. The first substrate, 4-chloro-2,1,3-benzoxadiazole, has its atoms partially numbered to track the substitutions described in the text.

#### 7-chlorobenzofurazan-4-sulfonyl chloride (**1**)

The synthesis was adapted from a known literature procedure [279]. Chlorosulfonic acid (15 mL) and 4-chloro-2,1,3-benzoxadiazole (1.52 g; 9.86 mmol) were added into a one-necked flask at 0°C. The mixture was stirred at 0°C for 15 min. Afterward, a condenser was installed and the temperature was increased to 120°C. After 5 h the reaction mixture was cooled down and gradually transferred with a Pasteur pipette onto water ice. After the ice melted completely, the aqueous phase was extracted with DCM (3 x 30 mL). Combined organic phases were dried over anhydrous MgSO<sub>4</sub> and evaporated under reduced pressure to give pure product (yellowish crystals, Y=87%). <sup>1</sup>H NMR (400 MHz, CDCl<sub>3</sub>) δ (ppm): 8.19- 8.17 (d, <sup>3</sup>J = 7.5 Hz, 1H, CH<sub>Ar</sub>), 7.67-7.65 (d, <sup>3</sup>J = 7.5 Hz, 1H, CH<sub>Ar</sub>). <sup>13</sup>C NMR (100 MHz, CDCl<sub>3</sub>) δ (ppm): 149.1, 143.8, 134.8, 132.0, 130.7, 128.6.



## 2-(2-((*tert*-butyldimethylsilyl)oxy)ethoxy)ethanamine (2)

The synthesis was adapted from a known literature procedure [323]. DCM was dried over 3Å molecular sieves one day before the use. Two flasks were dried with a heat gun while evacuating by an oil pump. Previously recrystallized from EtOAc imidazole (7.85 g; 115 mmol) was placed in the first flask and dissolved in dry DCM (20 mL). 2-(2-aminoethoxy)ethanol (3.85 mL; 38.5 mmol) was added and the obtained mixture was cooled down to 0°C. *Tert*-butyldimethylsilyl chloride (12.90 g; 85.7 mmol) was added into the second flask and dissolved in dry DCM (15 mL); after dissolving, it was added to the first solution dropwise at 0°C *via* syringe. The reaction mixture was stirred at room temperature (RT) for 24 hours. The reaction progress was controlled by TLC (DCM:MeOH, 8:2). Water (50 mL) and NaCl (5.0 g) were added to the reaction mixture and the aqueous phase was extracted with DCM (3 x 30 mL). The combined organic layers were dried over anhydrous MgSO<sub>4</sub> and evaporated under reduced pressure. The crude product was purified with flash column chromatography (DCM:MeOH, 99:1 → DCM:MeOH, 99:1). The product-containing fractions were evaporated under reduced pressure, the residuals were dissolved in DCM and washed with 0.5M NaHCO<sub>3</sub> (3 x 50 mL). The combined organic layers were evaporated under reduced pressure to give pure product (colorless oil, Y=57%). <sup>1</sup>H NMR (400 MHz, CDCl<sub>3</sub>) δ (ppm) 3.78-3.75 (t, <sup>3</sup>J = 5.3 Hz, 2H, CH<sub>2</sub>), 3.55- 3.51 (m, 4H, CH<sub>2</sub>), 2.89-2.86 (t, <sup>3</sup>J = 5.2 Hz, 2H, CH<sub>2</sub>), 2.06 (bs, 2H, NH<sub>2</sub>), 0.89 (s, 9H, CH<sub>3</sub>), 0.07 (s, 6H, CH<sub>3</sub>). <sup>13</sup>C NMR (100 MHz, CDCl<sub>3</sub>) δ (ppm) 77.2, 73.2, 72.6, 62.8, 41.9, 26.0, 18.5, -5.1.

## N-(2-(2-((*tert*-butyldimethylsilyl)oxy)ethoxy)ethyl)-7-chlorobenzo[*c*][1,2,5]oxadiazole-4-sulfonamide (3)

The synthesis was adapted from a known literature procedure [279]. DCM was dried over 3Å molecular sieves one day before the use. The reaction vessel was thoroughly dried using a heat gun and oven. Compound **2** (0.599 g; 2.73 mmol) was dissolved in dry DCM (10 mL). Compound **1** (0.691 g; 2.73 mmol) was added to the solution as well as Et<sub>3</sub>N (0.6 mL; 4.1 mmol). The mixture was stirred for 1 h at RT. The reaction was controlled by TLC (DCM:MeOH, 97:3). Since TLC control indicated the full consumption of the starting material, the solvent was evaporated under reduced pressure to obtain a yellow oil. The crude mixture was purified with flash column chromatography (DCM → DCM:MeOH, 98:2) to give a pure product (yellow oil; Y=54%). <sup>1</sup>H NMR (400 MHz, CDCl<sub>3</sub>) δ (ppm): 7.98-7.96 (d, <sup>3</sup>J = 6.8 Hz, 1H, CH<sub>Ar</sub>), 7.54-7.52 (d, <sup>3</sup>J = 7.1 Hz, 1H, CH<sub>Ar</sub>), 5.81 (bs, 1H, NH), 3.64- 3.62 (m, 2H, CH<sub>2</sub>), 3.53- 3.51 (m, 2H, CH<sub>2</sub>), 3.40-3.37 (m, 2H, CH<sub>2</sub>), 3.30-3.29 (m, 2H, CH<sub>2</sub>), 0.86 (s, 9H, CH<sub>3</sub>), 0.04 (s, 6H, CH<sub>3</sub>). <sup>13</sup>C NMR (100 MHz, CDCl<sub>3</sub>) δ (ppm): 145.2, 145.0, 133.3, 129.2, 128.5, 127.8, 72.7, 69.5, 62.7, 43.7, 26.1, 18.5, -5.2. HRMS-ESI (m/z) Calcd for (C<sub>16</sub>H<sub>25</sub>ClN<sub>3</sub>O<sub>5</sub>SSi) ([M-H]<sup>-</sup>): 434.0973, found: 434.0988

#### **7-chloro-*N*-(2-(2-hydroxyethoxy)ethyl)benzo[*c*][1,2,5]oxadiazole-4-sulfonamide (4)**

The synthesis was adapted from a known literature procedure [324]. Compound **3** (0.07 g; 0.161 mmol) was dissolved in MeOH (2 mL; dried over molecular sieves 24 h prior to use). The solution was cooled down to 0°C. 3M HCl in MeOH solution (1 mL) was added dropwise at 0°C. The mixture was stirred for 2.5 h at RT. TLC with eluent DCM:MeOH, 98:2 indicated the full consumption of the starting material. Therefore, the solution was neutralized (until pH=8-9, slightly basic) and the solvent was evaporated under reduced pressure to give the final product (colorless oil; quantitative yield). <sup>1</sup>H NMR (400 MHz, CDCl<sub>3</sub>) δ (ppm): 8.00-7.98 (d, <sup>3</sup>J = 7.3 Hz, 1H, CH<sub>Ar</sub>), 7.56-7.54 (d, <sup>3</sup>J = 7.3 Hz, 1H, CH<sub>Ar</sub>), 6.01 (bs, 1H, NH), 3.70- 3.68 (m, 2H, CH<sub>2</sub>), 3.57- 3.54 (m, 2H, CH<sub>2</sub>), 3.49- 3.47 (m, 2H, CH<sub>2</sub>), 3.32- 3.30 (m, 2H, CH<sub>2</sub>). <sup>13</sup>C NMR (100 MHz, CDCl<sub>3</sub>) δ (ppm): 149.0, 145.2, 133.6, 129.3, 128.3, 127.8, 77.2, 72.4, 69.5, 61.8, 43.5, 29.8. HRMS-ESI (m/z) Calcd for (C<sub>10</sub>H<sub>12</sub>ClN<sub>3</sub>O<sub>5</sub>S<sup>-</sup>) ([M-H]<sup>-</sup>): 320.0108, found: 320.0120

#### ***tert*-butyl piperazine-1-carboxylate (5)**

The synthesis was adapted from a known literature procedure [325]. Piperazine (0.987 g; 11.45 mmol) was suspended in *tert*-butanol (20 mL) and dissolved due to the addition of sodium hydroxide solution (2M, 2.3 mL). The mixture was stirred at RT for 15 min. Di-*tert*-butyl dicarbonate (1 g; 4.582 mmol) was also dissolved in *tert*-butanol (8 mL) in a separate flask and the obtained solution was added dropwise to the first solution. The reaction mixture was stirred for 1 h at RT. The reaction progress was controlled by TLC (CHCl<sub>3</sub>:MeOH, 10:1). The solvent was then evaporated under reduced pressure. Water (10 mL) was added to the crude mixture, what resulted in formation of a white precipitate; DCM (10 mL) was added and the phases were separated. The aqueous phase was extracted once more, organic phases were combined, dried over anhydrous MgSO<sub>4</sub> and evaporated under reduced pressure to give a pure product (colorless oil; Y=58%). <sup>1</sup>H NMR (400 MHz, CDCl<sub>3</sub>) δ (ppm): 3.41- 3.39 (m, 4H, CH<sub>2</sub>), 2.83- 2.81 (m, 4H, CH<sub>2</sub>), 1.46 (s, 9H, CH<sub>3</sub>). <sup>13</sup>C NMR (100 MHz, CDCl<sub>3</sub>) δ (ppm): 154.8, 79.4, 45.9, 45.0, 28.4.

### 1-benzylpiperazine (6)

The synthesis was adapted from a known literature procedure [326]. Compound **5** (0.4 g; 2.15 mmol) was dissolved in anhydrous ACN (10 mL); Et<sub>3</sub>N (1.5 mL; 10.7 mmol) was added. The mixture was stirred at 0°C for 10 minutes. Benzyl bromide (0.503 g; 2.94 mmol) was added dropwise to the solution. The mixture was stirred for 24 h at RT until TLC indicated full consumption of the starting material (CHCl<sub>3</sub>:MeOH, 10:1). The solvent was evaporated under reduced pressure. The crude mixture was diluted with water and extracted with DCM (3 x 30 mL). The organic phase was dried over anhydrous MgSO<sub>4</sub> and evaporated under reduced pressure to obtain solid, which was further purified with flash column chromatography (DCM, isocratic) to give pure product of the first step (yellowish solid; Y=65%; structure confirmed by <sup>1</sup>H NMR). Crude mixture (0.386 g; 1.4 mmol) was dissolved in anhydrous DCM (10 mL). Trifluoroacetic acid (2 mL; 26.1 mmol) was added dropwise to the prepared solution. The reaction mixture was stirred at RT for 1 h with constant Ar flow. Solvents were co-evaporated with set of solvents: DCM, MeOH and particularly toluene to give pure product (white solid; quantitative yield). <sup>1</sup>H NMR (400 MHz, DMSO-d<sub>6</sub>) δ (ppm): 7.43 (m, 5H, CH<sub>Ar</sub>), 4.04 (s, 2H, CH<sub>2</sub>), 3.26 (m, 4H, CH<sub>2</sub>), 3.02 (m, 4H, CH<sub>2</sub>); <sup>1</sup>H NMR (400 MHz, Acetone-d<sub>6</sub>) δ (ppm): 7.36-7.24 (m, 5H, CH<sub>Ar</sub>), 3.58 (s, 2H, CH<sub>2</sub>), 3.25-3.23 (m, 4H, CH<sub>2</sub>), 2.70-2.68 (m, 4H, CH<sub>2</sub>). <sup>13</sup>C NMR (100 MHz, Acetone-d<sub>6</sub>) δ (ppm) 138.7, 129.8, 129.1, 128.0, 63.0, 50.8, 44.4.

### 3.2.3. Synthesis of the final compound: probe SOLpH1

#### **SOLpH1: 7-(4-benzylpiperazin-1-yl)-N-(2-(2-hydroxyethoxy)ethyl)benzo[*c*][1,2,5]oxadiazole-4-sulfonamide**

The synthesis was adapted from a known literature procedure [279]. Compound **4** (0.474 g; 1.47 mmol) (0.085 g; 0.264 mmol) was dried in a flask on Schlenk line 3 x 45 min (vacuum/Ar cycles) and dissolved in anhydrous ACN (6 mL). Compound **6** (0.056 g; 0.317 mmol) and Et<sub>3</sub>N (0.073 mL; 0.528 mmol) were added to the solution. Afterward, a condenser was installed, the mixture was warmed up to 80°C and stirred at this temperature for 18 h under Ar until TLC monitoring indicated full consumption of the starting material (DCM:MeOH, 98:2). The solvent was evaporated under reduced pressure. The crude mixture was purified with flash column chromatography (DCM → DCM:MeOH, 99:1) to give a pure product (orange solid; Y=59%). <sup>1</sup>H NMR (400 MHz, CDCl<sub>3</sub>) δ (ppm): 7.89 (d, <sup>3</sup>J = 8.1 Hz, 1H, CH<sub>Ar</sub>), 7.39 – 7.27 (m, 5H, CH<sub>Ar</sub>), 6.26 (d, <sup>3</sup>J = 8.2 Hz, 1H, CH<sub>Ar</sub>), 5.60 (m, 1H, NH), 5.60 (t, <sup>3</sup>J = 5.8 Hz, 4H, CH<sub>2</sub>), 3.94 – 3.86 (m, 4H, CH<sub>2</sub>), 3.70 – 3.66 (m, 2H, CH<sub>2</sub>), 3.60 (s, 1H, CH<sub>2</sub>), 3.52 (t, <sup>3</sup>J = 5.1 Hz, 2H, CH<sub>2</sub>), 3.48 – 3.44 (m, 1H, CH<sub>2</sub>), 3.16 (q, <sup>3</sup>J = 5.3 Hz, 2H, CH<sub>2</sub>), 2.72 – 2.64 (m, 4H, CH<sub>2</sub>); <sup>1</sup>H NMR (400 MHz, CD<sub>3</sub>OD) δ (ppm): 7.90 (d, <sup>3</sup>J = 8.1 Hz, 1H, CH<sub>Ar</sub>), 7.39-7.26 (m, 5H, CH<sub>Ar</sub>), 6.52 (d, <sup>3</sup>J = 8.2 Hz, 1H, CH<sub>Ar</sub>), 3.95 – 3.88 (m, 4H, CH<sub>2</sub>), 3.62 (s, 2H, CH<sub>2</sub>), 3.53 (t, <sup>3</sup>J = 4.6 Hz, 2H, CH<sub>2</sub>), 3.44 (t, <sup>3</sup>J = 5.3 Hz, 2H, CH<sub>2</sub>), 3.37 (t, <sup>3</sup>J = 4.6 Hz, 2H, CH<sub>2</sub>), 3.15 (t, <sup>3</sup>J = 5.3 Hz, 2H, CH<sub>2</sub>), 2.72 – 2.67 (m, 4H, CH<sub>2</sub>); <sup>1</sup>H NMR (400 MHz, Acetone-d<sub>6</sub>) δ (ppm): 7.89 (d, <sup>3</sup>J = 8.1 Hz, 1H, CH<sub>Ar</sub>), 7.41-7.25 (m, 5H, CH<sub>Ar</sub>), 6.58 (d, <sup>3</sup>J = 8.2 Hz, 1H, CH<sub>Ar</sub>), 6.46 (m, 1H, NH), 3.95 – 3.91 (m, 4H, CH<sub>2</sub>), 3.61 (s, 1H, CH<sub>2</sub>), 3.50-3.46 (m, 4H, CH<sub>2</sub>), 3.38 – 3.34 (m, 2H, CH<sub>2</sub>), 3.15 (t, <sup>3</sup>J = 5.6 Hz, 2H, CH<sub>2</sub>), 3.05 (s, 1H, OH), 2.73 – 2.65 (m, 4H, CH<sub>2</sub>); <sup>13</sup>C NMR (100 MHz, CDCl<sub>3</sub>) δ (ppm): 146.3, 145.3, 143.3, 137.5, 129.3, 128.6, 127.6, 113.2, 104.0, 72.4, 69.4, 63.0, 61.8, 52.6, 49.0, 43.3; HRMS-ESI (m/z) Calcd for (C<sub>21</sub>H<sub>26</sub>N<sub>5</sub>O<sub>5</sub>S) ([M-H]<sup>-</sup>): 460.1655, found: 460.1658

### 3.2.4. Synthesis of intermediate compounds for the probe SOLpH2

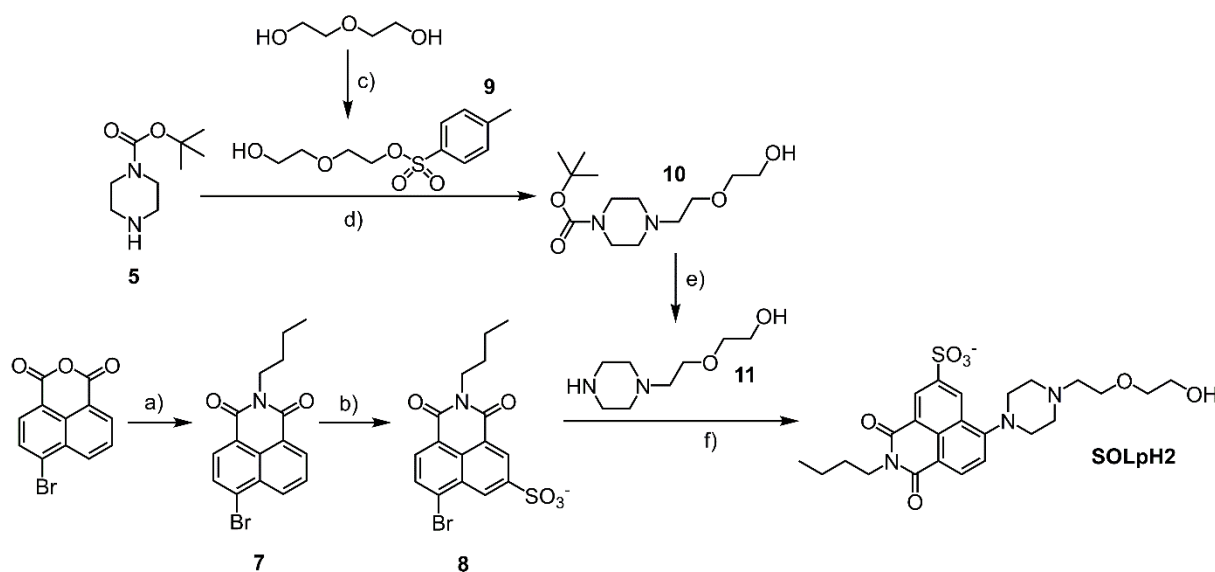


**Figure 34.** Synthetic pathway leading to the **SOLpH2** probe: a) n-butylamine, anh. EtOH, 78°C, Ar, 24 h, 23%; b) oleum, 90°C, 3 h, 65% (mixture of 2 regioisomers); c) tosyl chloride, Ag<sub>2</sub>O, KI, 3 h, 0°C, DCM, 65%; d) KI, K<sub>2</sub>CO<sub>3</sub>, ACN, 80°C, 22 h, 75%; e) TFA, DCM, RT, quant.; f) DMSO, 90°C, 24 h, 22%.

#### 6-bromo-2-butyl-1H-benzo[de]isoquinoline-1,3(2H)-dione (7)

The synthesis was adapted from a known literature procedure [186]. One-necked 100 mL flask was thoroughly dried with a heat gun and allowed to cool down under oil pump evacuation. 4-Bromo-1,8-naphthalic anhydride (1.1 g; 3.98 mmol) was transferred into the flask and suspended in anhydrous EtOH (25 mL). n-Butylamine (0.500 mL; 5 mmol) was added dropwise to the solution. The mixture was stirred at RT under constant Ar flow for 20 min. Afterward, a condenser was installed and the reaction mixture was stirred at 78°C under Ar for 22 h. TLC (neat DCM) confirmed the complete consumption of the starting material. The stirring was stopped, a flask cooled down and solvent evaporated under reduced pressure. The crude reaction mixture was submitted to flash column chromatography (Hexane:DCM → DCM → DCM:MeOH) to give a pure product (yellow powder; Y=23%). <sup>1</sup>H NMR (400 MHz, CDCl<sub>3</sub>) δ (ppm): 8.65 (d, <sup>3</sup>J = 7.3 Hz, 1H, CH<sub>Ar</sub>), 8.56 (d, <sup>3</sup>J = 8.5 Hz, 1H, CH<sub>Ar</sub>), 8.41 (d, <sup>3</sup>J = 7.9 Hz, 1H, CH<sub>Ar</sub>), 8.04 (d, <sup>3</sup>J = 7.9 Hz, 1H, CH<sub>Ar</sub>), 7.84 (t, <sup>3</sup>J = 7.9 Hz, 1H, CH<sub>Ar</sub>), 4.21 – 4.14 (m, 2H, CH<sub>2</sub>), 1.71 (dt, <sup>3</sup>J = 15.3, 7.6 Hz, 2H, CH<sub>2</sub>), 1.45 (sext, <sup>3</sup>J = 7.2 Hz, 2H, CH<sub>2</sub>), 0.98 (t, <sup>3</sup>J = 7.3 Hz, 3H, CH<sub>3</sub>); <sup>13</sup>C NMR (100 MHz, CDCl<sub>3</sub>) δ (ppm): 163.6, 133.1, 132.0, 131.2, 130.6, 130.2, 128.9, 128.1, 123.2, 122.3, 40.5, 30.3, 20.5, 13.9.

### **7-bromo-2-butyl-1,3-dioxo-2,3-dihydro-1*H*-benzo[*de*]isoquinoline-5-sulfonate (8)**

The synthesis was adapted from a known literature procedure [186]. Compound **7** (0.308 g; 0.927 mmol) was transferred into a one-necked 50 mL flask, dried on Schlenk line 3 x 45 min (vacuum/Ar cycles) and cooled down to 0°C. Oleum (4 mL) was carefully added dropwise into the flask at the same temperature. Afterward, a condenser was installed and the temperature of the mixture was increased to 90°C in a heating block and the mixture was stirred at this temperature for 3 h or until TLC monitoring (DCM:MeOH, 8:2) indicated that the majority of the starting material was consumed. The flask was allowed to cool down and the reaction mixture was gradually transferred onto ice water with a Pasteur pipette. A light brown precipitate formed during this process and was filtered off (the remaining substrate). The filtrate was carefully extracted with EtOAc (3 x 10 mL), the combined organic layers were dried with anhydrous MgSO<sub>4</sub> and evaporated under reduced pressure to obtain light brown solid mixture of regioisomers (total yield = 65%, confirmed by <sup>1</sup>H NMR), which was used without further purification. <sup>1</sup>H NMR (400 MHz, DMSO-*d*<sub>6</sub>) δ (ppm): 8.79 – 8.68 (m, 2H, CH<sub>Ar</sub>), 8.31 (d, <sup>3</sup>*J* = 7.9 Hz, 1H, CH<sub>Ar</sub>), 8.22 (d, <sup>3</sup>*J* = 7.9 Hz, 1H, CH<sub>Ar</sub>), 4.02 (t, <sup>3</sup>*J* = 7.4 Hz, 2H, CH<sub>2</sub>), 1.65 – 1.55 (m, 2H, CH<sub>2</sub>), 1.40 – 1.29 (m, 2H, CH<sub>2</sub>), 0.91 (t, <sup>3</sup>*J* = 7.3 Hz, 3H, CH<sub>3</sub>).

### **2-(2-hydroxyethoxy)ethyl 4-methylbenzenesulfonate (9)**

The synthesis was adapted from a known literature procedure [327]. DCM was dried over 3Å molecular sieves one day before the use. Diethylene glycol (2 g; 235.6 mmol) was dissolved in dry DCM (40 mL). Silver(I) oxide (6.58 g; 354.9 mmol), potassium iodide (0.8 g; 60.2 mmol) and 4-methylbenzenesulfonyl chloride (3.94 g; 258.4 mmol) were suspended in dry DCM (80 mL) and added gradually into the first solution. The mixture was stirred for 3 h at 0°C. After TLC monitoring (Hexane:EtOAc, 1:2) confirmed the complete consumption of the starting material, the silver(I) oxide was filtrated off with a syringe-silica plug. The residue gathered on silica gel was additionally washed with EtOAc (4 x 15 mL). The combined organic phases were evaporated under reduced pressure to obtain the crude mixture, which was further purified with flash column chromatography (Hex:EtOAc, 3:1 → EtOAc) to give a pure product (colorless oil; Y=57%). <sup>1</sup>H NMR (400 MHz, CDCl<sub>3</sub>) δ (ppm): 7.80 (d, <sup>3</sup>*J* = 8.3 Hz, 2H, CH<sub>Ar</sub>), 7.35 (d, <sup>3</sup>*J* = 8.0 Hz, 2H, CH<sub>Ar</sub>), 4.22-4.16 (m, 2H, CH<sub>2</sub>), 3.71-3.64 (m, 4H, CH<sub>2</sub>), 3.55-3.51 (m, 2H, CH<sub>2</sub>), 2.45 (s, 3H, CH<sub>3</sub>), 1.90 (br s, 1H, OH). <sup>13</sup>C NMR (100 MHz, CDCl<sub>3</sub>) δ (ppm): 145.0, 132.8, 129.7, 127.6, 69.9, 69.0, 62.1, 58.0.

### ***tert*-butyl 4-(2-(2-hydroxyethoxy)ethyl)piperazine-1-carboxylate (10)**

The synthesis was adapted from a known literature procedure [328]. One-necked 50 mL flask was thoroughly dried with a heat gun. The starting material **9** (0.327 g; 1.26 mmol) was added into the flask and dissolved in anhydrous ACN (14 mL). Dipotassium carbonate (0.347 g; 2.51 mmol) and potassium iodide (0.209 g; 1.26 mmol) were added to the solution. *Tert*-butyl piperazine-1-carboxylate was added to the reaction mixture. Afterward, a condenser was installed. The mixture was heated to 80°C, stirred for 28 h and controlled by TLC (CHCl<sub>3</sub>:MeOH, 10:1). After TLC indicated full consumption of the starting material, the reaction mixture was cooled down and the solvent evaporated under reduced pressure. The crude mixture was purified with flash column chromatography (DCM → DCM:MeOH, 95:5) to give a pure product (yellow oil; Y=51%). <sup>1</sup>H NMR (400 MHz, CDCl<sub>3</sub>) δ (ppm): 3.71-3.59 (m, 6H, CH<sub>2</sub>), 3.47-3.44 (m, 4H, CH<sub>2</sub>), 2.61-2.57 (m, 2H, CH<sub>2</sub>), 2.49-2.45 (m, 2H, CH<sub>2</sub>), 1.45 (s, 9H, CH<sub>3</sub>). <sup>13</sup>C NMR (100 MHz, CDCl<sub>3</sub>) δ (ppm): 154.9, 79.9, 77.2, 72.5, 67.8, 62.1, 58.1, 53.3, 28.6.

### **2-(2-(piperazin-1-yl)ethoxy)ethanol (11)**

The synthesis was adapted from a known literature procedure [326]. Compound **10** (0.32 g; 1.17 mmol) was dissolved in DCM (2 mL). The solution was cooled down to 0°C. Trifluoroacetic acid (2 mL; 22.41 mmol) was added dropwise. The mixture was stirred for 1 h at RT. The reaction was controlled by TLC (DCM:MeOH, 9:1) and ninhydrin staining. The solvent was co-evaporated with a set of solvents: DCM, MeOH and toluene to obtain the desired product (colorless oil; quantitative yield). The structure was confirmed by <sup>1</sup>H NMR and the crude mixture was used for the next step without further purification. <sup>1</sup>H NMR (400 MHz, CD<sub>3</sub>OD): δ (ppm) 3.84 – 3.81 (m, 2H, CH<sub>2</sub>), 3.73 – 3.69 (m, 2H, CH<sub>2</sub>), 3.63 – 3.59 (m, 2H, CH<sub>2</sub>), 3.53 (m, 8H, CH<sub>2</sub>), 3.37 (dd, <sup>3</sup>J = 9.3, 4.4 Hz, 2H, CH<sub>2</sub>).

### 3.2.5. Synthesis of the final compound: probe SOLpH2

#### **SOLpH2: 2-butyl-7-(4-(2-(2-hydroxyethoxy)ethyl)piperazin-1-yl)-1,3-dioxo-2,3-dihydro-1H-benzo[de]isoquinoline-5-sulfonate**

The synthesis was adapted from a known literature procedure [329]. Compound **8** (0.221 g; 0.537 mmol) was dried on Schlenk line 3 x 45 min (vacuum/Ar cycles) and dissolved in anhydrous DMSO (3.5 mL). Et<sub>3</sub>N (0.6 mL; 4.3 mmol) was added to the solution. 2-(2-(piperazin-1-yl)ethoxy)ethanol (0.472 g; 2.71 mmol) was dried (Schlenk line, 3 x 45 min vacuum/Ar cycles) in a separate flask and dissolved in anhydrous DMSO (4 mL). The solution from the second flask was added dropwise into the first one *via* syringe and the mixture was stirred for 1 h at RT under constant Ar flow. Afterward, a condenser was installed, the temperature was increased to 90°C and stirring was continued for 24 h. The reaction was controlled by TLC (DCM:MeOH, 8:2 or 7:3). The solvent was removed under vacuum and by lyophilization. The crude mixture was purified with flash column chromatography (DCM → DCM:MeOH, 8:2) and subsequently by preparative TLC (DCM:MeOH, 8:2) to give a pure product (yellowish solid; Y=22%). <sup>1</sup>H NMR (400 MHz, CD<sub>3</sub>OD) δ (ppm): 8.93 (dd, <sup>3</sup>J = 5.7, 1.6 Hz, 1H, CH<sub>Ar</sub>), 8.51 (d, <sup>3</sup>J = 8.1 Hz, 1H, CH<sub>Ar</sub>), 7.38 (d, <sup>3</sup>J = 8.2 Hz, 1H, CH<sub>Ar</sub>), 4.13 (t, <sup>3</sup>J = 7.5 Hz, 2H, CH<sub>2</sub>), 3.76 – 3.66 (m, 2H, CH<sub>2</sub>), 3.62 – 3.55 (m, 2H, CH<sub>2</sub>), 3.38 (m, 4H, CH<sub>2</sub>), 2.93 (m, 4H, CH<sub>2</sub>), 2.78 (t, <sup>3</sup>J = 5.4 Hz, 2H, CH<sub>2</sub>), 1.69 (dt, <sup>3</sup>J = 14.9, 7.5 Hz, 2H, CH<sub>2</sub>), 1.43 (sext, <sup>3</sup>J = 7.4 Hz, 2H, CH<sub>2</sub>), 0.99 (t, <sup>3</sup>J = 7.4 Hz, 1H, CH<sub>3</sub>).; <sup>13</sup>C NMR (100 MHz, CD<sub>3</sub>OD) δ (ppm): 173.0, 165.2, 158.2, 144.1, 134.7, 129.4, 128.8, 116.9, 73.5, 69.0, 62.3, 58.9, 54.6, 53.8, 41.0, 31.2, 30.8, 30.4, 30.3, 21.3, 14.2; <sup>13</sup>C NMR (100 MHz, DMSO) δ (ppm): 163.4, 163.0, 156.1, 145.7, 132.4, 128.9, 128.3, 126.3, 124.8, 122.6, 115.5, 72.3, 68.3, 60.3, 57.3, 53.1, 52.7, 29.7, 29.0, 28.7, 19.8, 13.8; HRMS-ESI (m/z) Calcd for (C<sub>24</sub>H<sub>30</sub>N<sub>3</sub>O<sub>7</sub>S<sup>-</sup>) ([M]<sup>-</sup>): 504.1810, found: 504.1807



### 3.2.6. Synthesis of the intermediate and control compound for the probe SOLpH1-Tos

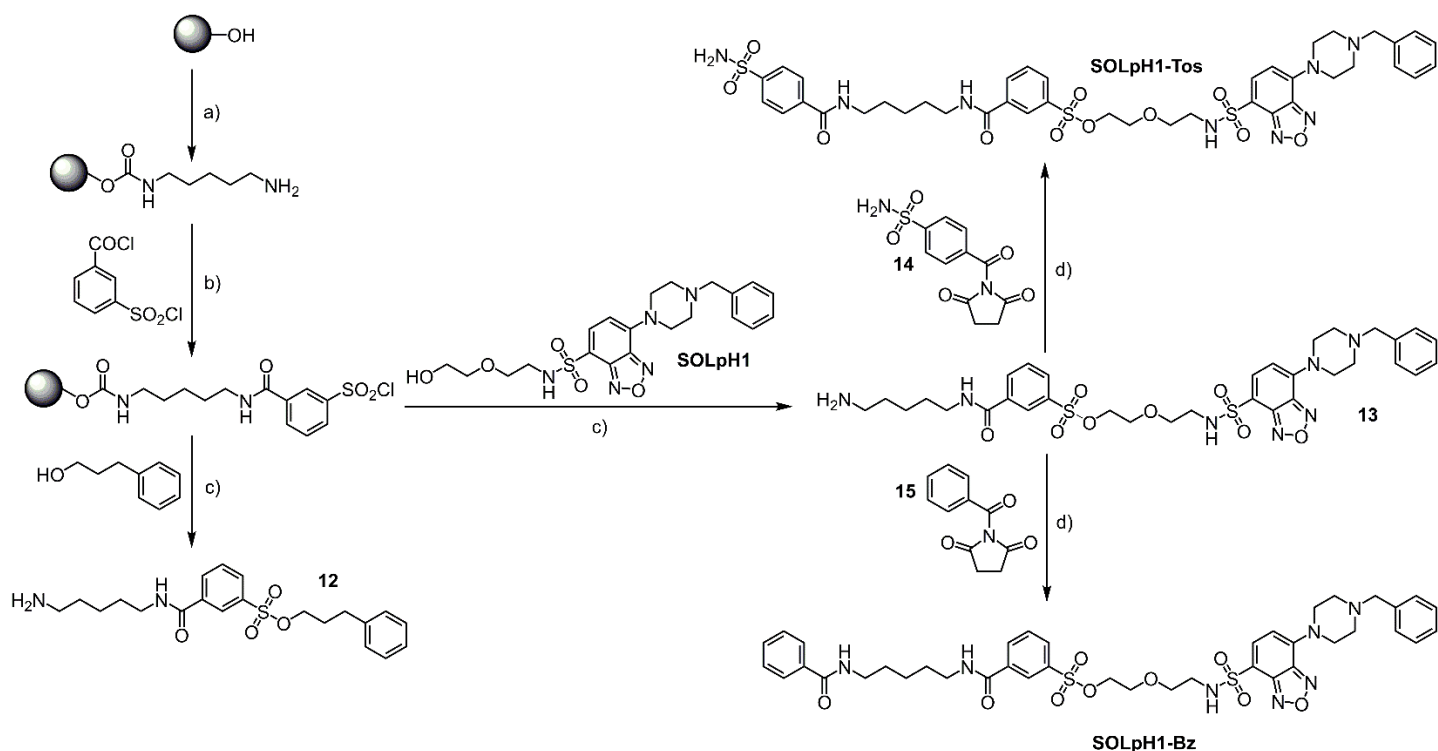


**Figure 35.** Synthetic pathway leading to the test compound **12**, **SOLpH1-Tos** probe and control compound **SOLpH1-Bz**: a) i) *p*-nitrophenyl chloroformate, collidine, DCM, RT, 9 h; ii) 1,5-diaminopentane, DIPEA, DMF, RT, 16 h; c) DIPEA, DCM, RT, 2h; d) i) 50% TFA/TES in DCM, RT, 2h (quant. For all 3 compounds); ii) DIPEA, DMF, 1h (8% both for **SOLpH1-Bz** and **SOLpH1-Tos**).

#### 3-phenylpropyl 3-((5-aminopentyl)carbamoyl)benzenesulfonate (**12**)

The synthesis was adapted from a known literature procedure [330]. DCM and DMF were dried over 3Å molecular sieves one day before the use. A solution of *p*-nitrophenyl chloroformate (0.154 g; 0.764 mmol; 3 equiv.) and collidine (0.227 g; 1.87 mmol; 7.6 equiv.) in anhydrous DCM (3 mL) was added to a Wang resin (previously swelled in DCM; 0.204 g; 0.255 mmol; 1 equiv.). The mixture was shaken for 9 h at RT. The solvent was removed and the resin was washed with DCM (2 x 4 mL), 10% DCM in DMF (2 x 4 mL), DMF (2 x 4 mL) and dried 10 min with Ar flow. Afterward, a solution of 1,5-diaminopentane (cadaverine; 0.2 g; 0.240 mmol; 3 equiv.) and DIPEA (0.251 mL; 0.186 g; 1.440 mmol; 6 equiv.) in anhydrous DMF (3 mL) was added to the resin and the mixture was shaken for 16 h. The resin was washed with 10% DMF in DCM (3 x 4 mL) and DCM (3 x 4 mL) and dried thoroughly on Schlenk line with Ar for 10 min. Kaiser test was performed, together with negative control; a positive result (indigo color) was observed for test reaction resin. 3-(Chlorosulfonyl)benzoyl chloride (0.186 mL; 0.287 g; 1.2 mmol; 5 equiv.) and DIPEA (0.251 mL; 0.186 g; 1.44 mmol; 6 equiv.) were dissolved in anhydrous DCM (2 mL). The solution was added to the resin. The mixture was shaken for 2 h and a Kaiser test was performed (negative result, no color). The resin was washed with DCM (6 x 4 mL) and dried for 10 min with Ar. A solution of 3-phenylpropan-1-ol (0.104 mL; 0.104 g; 0.764 mmol; 3 equiv.), DIPEA (0.251 mL; 0.186 g; 1.440 mmol; 6 equiv.) and 4-dimethylaminopyridine (DMAP; 0.003 g; 0.0246 mmol; 0.1 equiv.) in anhydrous DCM (2 mL)

was added to the resin and the mixture was shaken for 16 h. The resin was filtered off and washed with DCM (6 x 4 mL). A solution of trifluoroacetic acid/triethylsilane 98:2 was added to the resin. The mixture was shaken for 2 h. Afterward, filtration was performed, the filtrate was evaporated under reduced pressure and co-evaporated with toluene and DCM to give the final product as a colorless oil (Y=15%). TLC analysis was performed with a mixture of DCM/MeOH 3:1. <sup>1</sup>H NMR (400 MHz, CD<sub>3</sub>OD) δ (ppm): 8.35 (s, 1H, CH<sub>Ar</sub>), 8.18 (d, <sup>3</sup>J = 7.5 Hz, 1H, CH<sub>Ar</sub>), 8.06 (d, <sup>3</sup>J = 7.7 Hz, 1H, CH<sub>Ar</sub>), 7.74 (t, <sup>3</sup>J = 7.8 Hz, 1H, CH<sub>Ar</sub>), 7.21-7.04 (m, 5H, CH<sub>Ar</sub>), 4.08-4.05 (t, <sup>3</sup>J = 6.1 Hz, 2H, CH<sub>2</sub>), 3.45-3.42 (t, <sup>3</sup>J = 7.1 Hz, 2H, CH<sub>2</sub>), 2.99 – 2.90 (m, 2H, CH<sub>2</sub>), 2.64-2.61 (t, <sup>3</sup>J = 7.5 Hz, 2H, CH<sub>2</sub>), 1.98-1.93 (quint, <sup>3</sup>J = 13.6, 6.8 Hz, 2H, CH<sub>2</sub>), 1.75-1.66 (sext, <sup>3</sup>J = 15.0, 7.6 Hz, 4H, CH<sub>2</sub>), 1.55 – 1.42 (quint, 2H, CH<sub>2</sub>). <sup>13</sup>C NMR (100 MHz, CD<sub>3</sub>OD) δ (ppm): 167.8, 141.7, 138.1, 137.1, 133.5, 131.6, 131.0, 129.9, 129.4, 127.8, 127.1, 71.6, 40.7, 40.6, 32.3, 31.6, 29.8, 28.2, 24.8.

### **2-(2-((7-(4-benzylpiperazin-1-yl)benzo[c][1,2,5]oxadiazole)-4-sulfonamido)ethoxy)ethyl 3-((5-aminopentyl)carbamoyl)benzenesulfonate (13)**

The synthesis was adapted from a known literature procedure [330]. DCM and DMF were dried over 3Å molecular sieves one day before the use. A solution of *p*-nitrophenyl chloroformate (0.154 g; 0.764 mmol; 3 equiv.) and collidine (0.227 g; 1.87 mmol; 7.6 equiv.) in anhydrous DCM (3 mL) was added to a Wang resin (previously swelled in DCM; 0.200 g; 0.240 mmol; 1 equiv.). The mixture was shaken for 9 h at RT. The solvent was removed and the resin was washed with DCM (2 x 4 mL), 10% DCM in DMF (2 x 4 mL), DMF (2 x 4 mL) and dried with Ar for 10 min. Afterward, a solution of 1,5-diaminopentan (cadaverine; 0.085 mL; 0.074 g; 0.724 mmol; 3 equiv.) and DIPEA (0.251 mL; 0.186 g; 1.440 mmol; 6 equiv.) in anhydrous DMF (3 mL) was added to the resin and the mixture was shaken for 16 h. The resin was washed with 10% DMF in DCM (3 x 4 mL) and DCM (3 x 4 mL), and dried with Ar for 10 min. Kaiser test was performed, together with negative control; a positive result (indigo color) was observed for test reaction resin. A solution of 3-(chlorosulfonyl)benzoyl chloride (0.186 mL; 0.287 g; 1.2 mmol; 5 equiv.) and DIPEA (0.251 mL; 0.186 g; 1.44 mmol; 6 equiv.) in anhydrous DCM (2 mL) was added to the resin. The mixture was shaken for 2 h and Kaiser test was performed (negative result, no color). The resin was washed with DCM (6 x 4 mL) and dried with Ar for 10 min. A solution of **SOLpH1** (0.195 g; 0.423 mmol; 1.8 equiv.), DIPEA (0.251 mL; 0.186 g; 1.440 mmol; 6 equiv.) and 4-dimethylaminopyridine (DMAP; 0.003 g; 0.0246 mmol; 0.1 equiv.) in anhydrous DCM (2 mL) was added to the resin and the flask was shaken for 16 h. The resin was washed with DCM (6 x 4 mL). A solution of trifluoroacetic acid/triethylsilane 98:2 was added to the resin. The mixture was shaken for 2 h. Afterward, filtration was performed. The filtrate was evaporated under reduced pressure and co-evaporated with toluene and DCM to give the final product as a yellow oil (estimated yield of crude mixture 15%). The crude mixture was used in the next step without further purification, after preliminary confirmation of product formation by <sup>1</sup>H NMR (400 MHz, CD<sub>3</sub>OD).

### 2,5-dioxopyrrolidin-1-yl 4-sulfamoylbenzoate (14)

The synthesis was adapted from a known literature procedure [331]. DMF was dried over 3Å molecular sieves one day before the use. Anhydrous DMF (12 mL) was added into a one-necked 100 mL round-bottom flask. 4-Sulfamoylbenzoic acid (0.5 g; 2.49 mmol), *N,N,N',N'*-tetramethyl-*O*-(*N*-succinimidyl)uronium tetrafluoroborate (TSTU; 0.898 g; 2.98 mmol) and DIPEA (0.519 mL; 0.385 g; 2.98 mmol) were added to the reaction vessel and dissolved. The reaction mixture was stirred for 16 h at RT. The solvent was evaporated under reduced pressure. The residue was dissolved in DCM (30 mL) and extracted with 5% CH<sub>3</sub>COOH solution (3 x 20 mL). The aqueous phase was extracted with DCM (1 x 20 mL). The combined organic phases were dried over anhydrous MgSO<sub>4</sub> and evaporated under reduced pressure to give a yellowish powder (estimated purity ~70%). The reaction and work-up was controlled with TLC (CHCl<sub>3</sub>:MeOH, 10:1). The structure was confirmed by <sup>1</sup>H NMR and the crude mixture was used without further purification. <sup>1</sup>H NMR (400 MHz, DMSO-d<sub>6</sub>) δ (ppm): 8.29 (d, *J* = 8.3 Hz, 2H, CH<sub>Ar</sub>), 8.07 (d, *J* = 8.3 Hz, 2H, CH<sub>Ar</sub>), 7.69 (s, 1H, NH<sub>2</sub>).

### 2,5-dioxopyrrolidin-1-yl benzoate (15)

The synthesis was adapted from a known literature procedure [331]. DMF was dried over 3Å molecular sieves one day before the use. Anhydrous DMF (16 mL) was added into a one-necked 100 mL round-bottom flask. Benzoic acid (1.210 g; 8.900 mmol), *N,N,N',N'*-tetramethyl-*O*-(*N*-succinimidyl)uronium tetrafluoroborate (TSTU; 3.35 g; 11.1 mmol) and DIPEA (1.86 mL; 1.38 g; 10.7 mmol) were added to the reaction vessel and dissolved. The mixture was stirred for 16 h at RT. The solvent was evaporated under reduced pressure and the residue was re-dissolved in DCM (50 mL). The obtained organic phase was extracted with 5% CH<sub>3</sub>COOH solution (3 x 15 mL). The acid phase was extracted with DCM and all organic phases were combined, dried over anhydrous MgSO<sub>4</sub> and evaporated under reduced pressure to give a yellowish powder (estimated purity ~90%). The structure was confirmed by <sup>1</sup>H NMR and crude mixture was used without further purification. <sup>1</sup>H NMR (400 MHz, Acetone-d<sub>6</sub>) δ (ppm): 8.14 (d, <sup>3</sup>*J* = 8.0 Hz, 2H, CH<sub>Ar</sub>), 7.82 (t, <sup>3</sup>*J* = 7.5 Hz, 1H, CH<sub>Ar</sub>), 7.65 (t, <sup>3</sup>*J* = 7.8 Hz, 2H, CH<sub>Ar</sub>), 2.97 (s, 4H, CH<sub>2</sub>).

**SOLpH1-Bz: 2-(2-((7-(4-benzylpiperazin-1-yl)benzo[c][1,2,5]oxadiazole)-4-sulfonamido)ethoxy)ethyl 3-((5-benzamidopentyl)carbamoyl)benzenesulfonate**

DMF was dried over 3Å molecular sieves one day before the use. Compound **13** (0.175 g; 0.240 mmol) was dissolved in anhydrous DMF (5 mL). DIPEA (0.334 mL; 0.248 g; 1.920 mmol) and compound **15** (0.075 g; 0.344 mmol) were added and the mixture was stirred at RT for 1 h. The reaction was controlled by TLC until a full consumption of the starting material. The solvent was evaporated under reduced pressure. The compound was purified with preparative TLC (DCM:MeOH, 10:1) to give a pure compound (yellow oil, Y=8%). <sup>1</sup>H NMR (400 MHz, Acetone-d<sub>6</sub>) δ (ppm): 8.36-8.35 (m, 1H, CH<sub>Ar</sub>), 8.24 – 8.22 (m, 1H, CH<sub>Ar</sub>), 8.13-8.12 (m, 1H, NH), 8.04 – 8.01 (m, 1H, CH<sub>Ar</sub>), 7.88 – 7.85 (m, 4H, CH<sub>Ar</sub>), 7.76-7.72 (m, 3H, CH<sub>Ar</sub>, NH), 7.50-7.25 (m, 10H, CH<sub>Ar</sub>), 6.57-6.55 (d, <sup>3</sup>J = 8.2 Hz, 1H), 6.48-6.45 (t, <sup>3</sup>J = 5.9 Hz, 1H, NH), 4.13-4.11 (m, 2H, CH<sub>2</sub>), 3.93 – 3.90 (m, 4H, CH<sub>2</sub>), 3.60 (s, 1H, CH<sub>2</sub>), 3.52 – 3.50 (m, 2H, CH<sub>2</sub>), 3.46 – 3.38 (m, 6H, CH<sub>2</sub>), 3.12-3.07 (q, <sup>3</sup>J = 5.8 Hz, 2H, CH<sub>2</sub>), 2.68 – 2.65 (m, 4H, CH<sub>2</sub>), 1.71-1.62 (sext, <sup>3</sup>J = 14.7, 7.5 Hz, 4H, CH<sub>2</sub>), 1.50 – 1.43 (m, 2H, CH<sub>2</sub>). <sup>13</sup>C NMR (100 MHz, Acetone-d<sub>6</sub>) δ (ppm): 167.4, 165.6, 147.3, 146.3, 143.7, 139.1, 138.0, 137.6, 137.3, 136.2, 133.3, 131.8, 130.8, 130.6, 129.9, 129.1, 128.0, 127.3, 115.3, 105.7, 71.0, 70.4, 69.0, 63.2, 53.3, 49.8, 43.6, 40.6, 40.2, 25.0. HRMS-ESI (m/z) Calcd for (C<sub>40</sub>H<sub>48</sub>N<sub>7</sub>O<sub>9</sub>S<sub>2</sub><sup>+</sup>) ([M+H]<sup>+</sup>): 834.2955, found: 834.2874

**3.2.7. Synthesis of the final compound: probe SOLpH1-Tos**

**SOLpH1-Tos: 2-(2-((7-(4-benzylpiperazin-1-yl)benzo[c][1,2,5]oxadiazole)-4-sulfonamido)ethoxy)ethyl 3-((5-(4-sulfamoylbenzamido)pentyl)carbamoyl)benzenesulfonate**

DMF was dried over 3Å molecular sieves one day before the use. Compound **13** (0.040 g; 0.0548 mmol) was dissolved in anhydrous DMF (5 mL). DIPEA (0.06 mL; 0.0445 g; 0.344 mmol) and compound **14** (0.039 g; 0.131 mmol) were added and the mixture was stirred at RT for 1 h. The reaction was controlled by TLC (DCM/MeOH 9:1). After reaction was done, the solvent was evaporated under reduced pressure. The compound was purified by preparative TLC (DCM:MeOH, 10:1) to give a pure compound (yellow oil, Y=8%). <sup>1</sup>H NMR (400 MHz, CD<sub>3</sub>OD) δ (ppm): 8.31 (m, 1H, CH<sub>Ar</sub>), 8.12-8.10 (m, 1H, CH<sub>Ar</sub>), 8.05-7.85 (m, 6H, CH<sub>Ar</sub>), 7.72-7.68 (t, <sup>3</sup>J = 7.9 Hz, 1H, CH<sub>Ar</sub>), 7.39-7.26 (m, 5H, CH<sub>Ar</sub>), 6.49-6.47 (d, <sup>3</sup>J = 8.2 Hz, 1H, CH<sub>Ar</sub>), 4.08-4.06 (m, 2H, CH<sub>2</sub>), 3.91 – 3.88 (m, 4H, CH<sub>2</sub>), 3.60 (s, 2H, CH<sub>2</sub>), 3.45-3.39 – 3.35 (m, 6H, CH<sub>2</sub>), 3.06-3.03 (t, <sup>3</sup>J = 5.5 Hz, 2H, CH<sub>2</sub>), 2.69 – 2.66 (m, 4H, CH<sub>2</sub>), 1.70-1.64 (m, 4H, CH<sub>2</sub>), 1.56 – 1.43 (m, 2H, CH<sub>2</sub>); <sup>1</sup>H NMR (400 MHz, Acetone-d<sub>6</sub>) δ (ppm): 8.36 (s, 1H, CH<sub>Ar</sub>), 8.24-8.22 (d, <sup>3</sup>J = 7.9 Hz, 1H, CH<sub>Ar</sub>), 8.17 (br s, 1H, NH), 8.05 – 7.92 (m, 5H, CH<sub>Ar</sub>), 7.89-7.87 (d, <sup>3</sup>J = 8.1 Hz, 1H, CH<sub>Ar</sub>), 7.76-7.72 (t, <sup>3</sup>J = 7.8 Hz, 1H, CH<sub>Ar</sub>), 7.66-7.61 (m, 2H, CH<sub>Ar</sub>), 7.43-7.17 (m, 7H, CH<sub>Ar</sub>), 6.70 (br s, 2H, NH<sub>2</sub>), 6.57-6.55 (d, <sup>3</sup>J = 8.2 Hz, 1H, CH<sub>Ar</sub>), 6.49 (m, 1H, NH), 4.14 – 4.12 (m, 2H, CH<sub>2</sub>), 3.93 – 3.90 (m, 4H, CH<sub>2</sub>), 3.60 (s, 2H, CH<sub>2</sub>), 3.53 – 3.50 (m, 2H, CH<sub>2</sub>), 3.46 – 3.40 (m, 6H, CH<sub>2</sub>), 3.12-3.08 (dd, <sup>3</sup>J = 11.2, 5.6 Hz, 2H), 2.68-2.66 (m, 4H, CH<sub>2</sub>), 1.71 – 1.63 (m, 4H, CH<sub>2</sub>), 1.51-1.43 (m, 2H, CH<sub>2</sub>). HRMS-ESI (m/z) Calcd for (C<sub>40</sub>H<sub>49</sub>N<sub>8</sub>O<sub>11</sub>S<sub>3</sub><sup>+</sup>) ([M+H]<sup>+</sup>): 913.2682, found: 913.2604

### 3.3. Properties of fluorophores

#### 3.3.1. Optical properties

The synthesized probe **SOLpH1** or **SOLpH2** was dissolved in DMSO to prepare 10 mM stock solution and consequently diluted to desired concentration. Calculated volume of chosen buffer (citrate phosphate buffer CPB or phosphate buffer PB) and volume of fluorophore stock solution were added into a clean black 96-well plate with transparent (polystyrene plate) or black bottom (polystyrene or polypropylene plate). The final concentration in a well was 20  $\mu\text{M}$  for **SOLpH1** and 15  $\mu\text{M}$  for **SOLpH2**. Concentration range for fluorescence measurements of samples was chosen so that absorbance would not exceed 0.1 (to minimize re-absorption effects aka. inner filter effects). The absorption, emission and excitation spectra of compounds were measured at changing pH 4-8, where CPB was used for pH 4.0, 5.0, 6.0 and PB for 6.0, 7.0, 7.5, 8.0. The excitation wavelength was 435 nm for **SOLpH1** and 390 nm for **SOLpH2**. The emission gathered for **SOLpH1**: 475-700 nm, **SOLpH2**: 430-700 nm. The experiment was repeated in triplicates.

#### *Determination of fluorescence quantum yields*

Molar extinction coefficients  $\epsilon$ , fluorescence quantum yields  $\Phi_F$  and brightness  $B$  for compounds: **SOLpH1** were calculated with use of comparative method of Williams et al. [332] It involves use of samples with known  $\Phi_F$ . Data were collected on multi-well plate reader on 96-well plates with transparent bottom to enable a simultaneous measurement of absorbance and fluorescence for each sample. A typical procedure would involve a collection of absorption spectra for 5 different concentrations (for absorbances below 0.1 to avoid inner filter effects) at excitation wavelength followed by a fluorescence spectra collection for excitation wavelength being the same as absorbance (405, 430 and 475 nm for **SOLpH1**). The experiment was repeated in triplicates. Subsequently, molar extinction coefficients were calculated through a linear fitting of an absorbance data at 7 different concentrations for each compound, followed by the calculation of molar extinction coefficient from a coefficient  $a$  in the linear regression formula:  $\epsilon = a / l$  (where  $l$  is a light path and it is 0.28 cm for 100  $\mu\text{L}$  in a standard 96-well plate). An obtained coefficient  $a$  was then multiplied 1 million times (since concentrations in  $\mu\text{M}$  were used) to calculate molar extinction coefficient for each compound. In order to calculate a fluorescence quantum yield, a graph of integrated fluorescence vs absorbance at excitation wavelength was sketched for the compound of interest and a standard (fluorescein in 0.1 M NaOH coumarin 343 in EtOH as additional standard for fluorescein). The resulting experimental points were fit into linear regression with intercept = 0 and coefficients  $a$  obtained from this fit were used to calculate fluorescence QY in comparison to the standards (fluorescein in 0.1 M of NaOH – QY = 0.925 [333], quinine sulphate in 0.05 M  $\text{H}_2\text{SO}_4$  – QY = 0.546 [334], coumarin 343 in EtOH – QY = 0.63 [335]); refractive indexes used: CPB/PB buffer solutions –  $n_x = 1.335$ , 0.1 M NaOH – approx.  $n_{ST} = 1.33$  like water, 0.05 M  $\text{H}_2\text{SO}_4$  -  $n_{ST} = 1.34$ , ethanol -  $n_{ST} = 1.36$ ) with the use of equation in the **Figure 36**. All graphs and results of calculations are in the **Supplementary data**.

$$\Phi_X = \Phi_{ST} \left( \frac{Grad_X}{Grad_{ST}} \right) \left( \frac{\eta_X^2}{\eta_{ST}^2} \right)$$

**Figure 36.** Equation for calculation of fluorescence quantum yield.  $\Phi_X$  – fluorescence quantum yield of examined fluorophore;  $\Phi_{ST}$  – fluorescence quantum yield of standard fluorophore;  $Grad_X$  - gradient from the plot of integrated fluorescence intensity vs absorbance of examined fluorophore;  $Grad_{ST}$  – gradient from the plot of integrated fluorescence intensity vs absorbance of standard fluorophore,  $\eta_X$  – refractive index for sample solution,  $\eta_{ST}$  - refractive index for standard solution.

### 3.3.2. $pK_a$ calculation

Citrate phosphate buffer (CPB) solutions were prepared by mixing 0.1 M of citric acid solution, 0.2 M solution of dibasic sodium phosphate, diluted to a total 100mL and adjusted to the desired pH (4.0, 5.0, 6.0, respectively). Phosphate buffer (PB) solutions were prepared by mixing 0.2 M solution of monobasic sodium phosphate and 0.2 M solution of dibasic sodium phosphate, diluted to a total 200 mL and adjusted to the desired pH (6.0, 7.0, 7.5, 8.0, respectively). The stock solution of **SOLpH1** or **SOLpH2** was added to buffer at different pH, and the final concentration both for **SOLpH1** and **SOLpH2** was 20  $\mu$ M. The absorption spectrum and fluorescence emission spectrum were gathered. The excitation for **SOLpH1** was 435 nm and for **SOLpH2** 390 nm. The maximum emission for **SOLpH1** was 600 and for **SOLpH2**, 550 nm. The emission gathered for **SOLpH1**: 475-700 nm, **SOLpH2**: 430-700 nm. The experiment was repeated in triplicates.  $pK_a$  value of **SOLpH1** was obtained by linear regression analysis of the fluorescence titration curve to fit the equation:  $pK_a - pH = \log[(I_{max} - I)/(I - I_{min})]$ , where  $I$  is the fluorescence intensity at 600 or 615 nm at different pH values (CPB: 5, 6; PB: 6, 7.5),  $I_{max}$  and  $I_{min}$  are the fluorescence intensity measured at pH 4.0 and 8.0 at 600 or 615 nm, respectively. The  $pK_a$  values were derived from the plot pH vs  $\log[(I_{max} - I)/(I - I_{min})]$  and averaged to obtain the final  $pK_a$  value of the probe **SOLpH1**.  $pK_a$  value for **SOLpH2** was prepared with analogous method, with  $I$  as fluorescence intensity at 550 nm at mentioned above pH values,  $I_{max}$  and  $I_{min}$  are the fluorescence intensity measured at pH 4.0 and 8.0 at 550 nm, respectively.

### 3.3.3. Interference to pH detection

10 mM stock solutions of various salts in MiliQ water, HEPES 100 mmol (pH=7.5) or ACN were prepared, to check their interference with the fluorescence of **SOLpH1** and **SOLpH2**. MiliQ solutions and HEPES 100 mmol pH=7.5 solutions contained salts:  $LiNO_3$ ,  $KNO_3$ ,  $KI$ ,  $NaNO_3$ ,  $Na_2SO_4$ ,  $NaCl$ ,  $Na_2CO_3$ ,  $Mg(NO_3)_2$ ,  $MgCl_2 \cdot 6H_2O$ ,  $Ca(NO_3)_2 \cdot 4H_2O$ ,  $Cu(NO_3)_2 \cdot 3H_2O$ ,  $Ni(NO_3)_2 \cdot 6H_2O$ ,  $Cd(NO_3)_2 \cdot 4H_2O$ ,  $Ga(NO_3)_3 \cdot XH_2O$ ,  $Cd(NO_3)_2 \cdot 4H_2O$ ,  $Co(NO_3)_2 \cdot 6H_2O$ ,  $PbNO_3$ ,  $Hg(NO_3)_2 \cdot H_2O$ ,  $Zn(NO_3)_2 \cdot 6H_2O$ ,  $ZnBr_2$ ,  $Mn(NO_3)_2 \cdot 4H_2O$ ,  $AgNO_3$ ,  $Al(NO_3)_3 \cdot 9H_2O$ ,  $Na_3PO_4$ ,  $Na_2HPO_4 \cdot 7H_2O$ ,  $NaH_2PO_4 \cdot H_2O$ ,  $K_2PtCl_4$ ,  $FeCl_3$  anh. or  $FeCl_3 \cdot 6H_2O$ ,  $FeSO_4 \cdot 7H_2O$ ,  $(NH_4)_2Fe(SO_4)_2 \cdot 6H_2O$ ,  $NH_4OAc$ , ammonium citrate dibasic,  $NaOAc$ , trisodium citrate  $\cdot H_2O$ , citric acid. ACN was a solvent for  $Cu(CH_3CN)_4BF_4$  only. The measurement concentration of **SOLpH1** was 20  $\mu$ M, and the concentration of interferent were 200  $\mu$ M (1 to 10) or 2 mM (1 to 100), while concentration of **SOLpH2** was 15  $\mu$ M and of interferents – respectively 150  $\mu$ M (1 to 10) or 1.5 mM (1 to 100). The control experiment only had probe **SOLpH1** or **SOLpH2**. The excitation for

**SOLpH1** was 435 nm, for **SOLpH2** 390 nm and the width of the excitation slit and the emission slit were both 5 nm. The emission gathered for **SOLpH1**: 475-700 nm, **SOLpH2**: 430-700 nm. The experiment was repeated in triplicates.

#### 3.3.4. Polarity changes sensing

Sensitivity for polarity changes was checked with a set of solutions with changing ratio dioxane:water (10:0, 9:1, 8:2, 7:3, 6:4, 1:1, 4:6, 3:7, 2:8, 1:9, 0:10, respectively). Stock solution of **SOLpH1** or **SOLpH2** was prepared in DMSO and later diluted in prepared dioxane:water solutions. Final concentration of the fluorophores in the obtained solutions was kept at 20  $\mu\text{M}$  for **SOLpH1** and 15  $\mu\text{M}$  for **SOLpH2**. The effect of polarity changes on the excitation and emission spectrum was investigated as well with a set of solvents (direct dissolving of compounds in the solvents): a) for **SOLpH1**: DCM, THF, dioxane, acetone, EtOH, DMF, ACN, MeOH, DMSO, CPB pH=4, MiliQ water, PBS, PB pH=7.5, Tris 100 mmol pH=7.4, HEPES 100 mmol pH=7.5; b) for **SOLpH2**: dioxane, acetone, DMSO, MeOH, ACN, DMF, EtOH, MiliQ water, PB pH=7.5, PBS, Tris 100 mmol pH=7.4, CPB pH=4, HEPES 100 mmol pH=7.5. The excitation for **SOLpH1** was 435 nm and for **SOLpH2** 390 nm. The emission gathered for **SOLpH1**: 475-700 nm, **SOLpH2**: 430-700 nm. The experiment was repeated in duplicates.

#### 3.3.5. Viscosity changes sensing

Sensitivity for viscosity changes was investigated with a set of glycerol:water solutions with ratios ranging 9:1, 8:2, 7:3, 6:4, 1:1, 4:6, 3:7, 2:8, 1:9, 0:10, respectively. Stock solution of **SOLpH1** and **SOLpH2** were prepared in DMSO and diluted in prepared glycerol:water solutions. Final concentration of the fluorophores in the obtained solutions was kept at 20  $\mu\text{M}$  for **SOLpH1** and 15  $\mu\text{M}$  for **SOLpH2**. The probe **SOLpH1** was excited at 435 nm and **SOLpH2** at 390 nm. The emission gathered for **SOLpH1**: 475-700 nm, **SOLpH2**: 430-700 nm. The experiment was repeated in duplicates.

### 3.4. Cellular experiments

#### 3.4.1. Human cell culture and fluorescent live-cell imaging

HEK293T and A549 cells were cultured in DMEM high glucose medium containing 10% fetal bovine serum, 1% L-glutamine and 1% penicillin-streptomycin at 37 °C and 5% CO<sub>2</sub>. Then, 7.5 × 10<sup>5</sup> cells/mL were evenly spread in a 35/10 mm cell culture dish with 4 compartments. After culture for 48h, the medium was discarded and the fresh medium containing **SOLpH1** (2.5 μM) or **SOLpH2** (15 μM) was added for 15 minutes. The old medium was discarded again, the wells were washed with PBS three times, and FluoroBrite™ DMEM high glucose was added. Finally, imaging was performed under a confocal microscope. For the co-localization of organelles, HEK293T or A549 cells were cultured in the same way as the imaging experiment with MitoTracker Deep Red FM and LysoTracker Deep Red. Blue channel: Ex. 405 nm, Em. 430-495 nm; Green channel: Ex. 405 nm, Em. 500-639 nm; Red channel: Ex. 645 nm, Em. 655-750. The control group was HEK293T or A549 cells treated only with DMSO. The fixed concentration of DMSO in all experiments was 1%. The imaging was performed with an inverted confocal microscope inside a micro-environmental gas chamber (5% CO<sub>2</sub>, 10% O<sub>2</sub>). The image acquisition settings were optimized by providing the excitation light from a Blue/UV diode continuous laser 50mW 405 nm with mild intensity (15-20%) during imaging for **SOLpH1** and **SOLpH2**, as well as pulsed White Light Laser Excitation System (White Light Laser; 470-670 nm) during imaging for trackers used for colocalization experiments (20%). The same settings were applied for lambda scan measurements, with detection 435-750 nm range, 10 nm detection band width and 7.33 nm λ-detection stepsize. The images were processed and the colocalization analysis performed by using Fiji [336].

#### 3.4.2. pH-dependent fluorescent live-cell imaging

HEK293T cells were cultured in DMEM high glucose medium containing 10% fetal bovine serum, 1% L-glutamine and 1% penicillin-streptomycin at 37 °C and 5% CO<sub>2</sub>. Then, 7.5 × 10<sup>5</sup> cells/mL were evenly spread in a 35/10 mm cell culture dish with 4 compartments. After culture for at least 48h, the medium was discarded and the fresh medium containing **SOLpH1** (7.5 μM) or **SOLpH2** (15 μM) was added for 15 minutes. The old medium was discarded again, the wells were washed with PBS three times, and Britton-Robinson 40 mmol buffer was added for 30 min incubation (pH=5.0, 6.0, 7.5 or 8.0). Finally, imaging was performed under a confocal microscope without change of cell medium, inside a micro-environmental gas chamber (5% CO<sub>2</sub>, 10% O<sub>2</sub>), with blue channel: Ex. 405 nm, Em. 430-495 nm; green channel: Ex. 405 nm, Em. 500-639 nm. The control group was HEK293T cells treated only with DMSO. The fixed concentration of DMSO in all experiments was 1%. The image acquisition settings were optimized by providing the excitation light from a Blue/UV diode continuous laser 50mW 405 nm with mild intensity (15-20%) during imaging for **SOLpH1** or **SOLpH2**. The same settings were applied for lambda scan measurements, with detection 435-750 nm range, 10 nm detection band width and 5 nm λ-detection stepsize. The images were processed by using Fiji [336].



### 3.5. hCAII *in vitro* experiments

#### 3.5.1. Labeling experiments of the probe SOLpH1-Tos and SOLpH1-Bz for hCAII

Stock solution of 10 mM **SOLpH1-Tos** was prepared in DMSO. A commercial solution of human carbonic anhydrase II in 20 mM Tris buffer pH=7.5 (with 150 mM NaCl) was diluted to 10  $\mu$ M with use of 100 mM HEPES pH=7.3. Probe solution was added to protein solution to obtain 3 samples in 1.5 mL Eppendorf tubes: 1) control 10  $\mu$ M protein solution, no probe; 2) protein:probe, 1:2 (10  $\mu$ M to 20  $\mu$ M protein:probe); 3) protein:probe, 1:10 (10  $\mu$ M to 100  $\mu$ M protein:probe). The total concentration of DMSO was 1% (v/v). All reaction mixtures were mixed gently with use of a pipette and incubated at 37°C for 48 h. After the incubation, samples from all tubes were separately diluted with sodium bicarbonate 50 mM solution for digestion. Afterward, 1.5  $\mu$ L of the dithiothreitol (DTT) solution (0.1 M) was added to the samples, which were subsequently incubated at 95°C for 5 min. After cooling down and centrifuging, 3  $\mu$ L of iodoacetamide (IAA) solution (0.1 M) was added to the samples. The samples were incubated in darkness for 20 min and centrifuged. The last step was addition of trypsin 1X (2  $\mu$ L) and incubation for 16 h before the final analysis of obtained peptides during digestion process.

In the second experiment, two stock solutions of **SOLpH1-Tos** and **SOLpH1-Bz** were prepared in DMSO. A commercial solution of hCAII in 20 mM Tris buffer pH=7.5 (with 150 mM NaCl) was diluted to 10  $\mu$ M with use of 100 mM HEPES pH=7.5. Probe solution was added to protein solution to obtain 3 samples in 1.5 mL Eppendorf tubes: 1) 10  $\mu$ M protein solution, no probe; 2) protein:probe **SOLpH1-Tos**, 1:2 (10  $\mu$ M to 20  $\mu$ M protein:probe); 3) protein:probe **SOLpH1-Bz**, 1:2 (10  $\mu$ M to 20  $\mu$ M protein:probe). The total concentration of DMSO was 1%. All reaction mixtures were incubated at 37°C for 46 h. After the incubation, 16  $\mu$ L samples from all tubes were separately diluted with sodium bicarbonate 50 mM solution. Afterward, 1.5  $\mu$ L of the dithiothreitol (DTT) solution (0.1 M) was added to the samples, which were subsequently incubated at 95°C for 5 min. After cooling down and centrifuging, 3  $\mu$ L of iodoacetamide (IAA) solution (0.1 M) was added to the samples. The samples were incubated in darkness for 20 min and centrifuged. The last step was addition of trypsin 1X (2  $\mu$ L) and incubation for 16 h before the final analysis of obtained peptides during digestion process.

#### 3.5.2. pH-dependent emission of the SOLpH1-Tos labeled to hCAII

After confirmation of labeling of hCAII protein in the previous step, the non-digested protein sample (straight after incubation at 37°C for 48h as described in **3.5.1**) was dialyzed against HEPES buffer (100 mM, pH=7.5) with a Slide-A-Lyzer MINI Dialysis Device (10000 MWCO) (Thermo Scientific). The protein sample was loaded on HiLoad 16/60 Superdex 200 column equilibrated with 10 mM HEPES buffer pH 7.0 and purified by size-exclusion chromatography. Protein fractions were collected and sample concentrated using Amicon Ultra-15 (10000 MWCO) centrifuge filter. The final protein concentration was determined by measuring the absorbance at 280 nm using molar absorption coefficients of 54,000  $M^{-1} cm^{-1}$  [337]. The protein stock solution was diluted with a set of buffers: CPB pH=4.0, 5.0, 6.0; PB pH=6.0, 7.0, 7.5, 8.0 and 100 mM HEPES buffer pH=7.5. The final concentration of the protein was 5.2  $\mu$ M in each well (based on the previous estimation with use of molar absorption coefficient).

The samples were excited at 430 nm. The emission gathered: 470-700 nm (5 nm step); the absorbance was collected in the range: 300-700 nm (10 nm step). The experiment was repeated in triplicates.

### 3.5.3. Evaluation of the enzymatic activity of hCAII labeled with SOLpH1-Tos

The **SOLpH1-Tos**-labeled hCAII samples measured for pH-dependent emission were further analyzed for the enzymatic activity with Carbonic Anhydrase (CA) Activity Assay Kit (Colorimetric). The product of reaction, nitrophenol, was used for standard curve preparation. 0, 4, 8, 12, 16 and 20  $\mu\text{L}$  of 20 mM nitrophenol standard were added into series of wells (in triplicate), the volumes were adjusted to 100  $\mu\text{L}$ /well with CA Assay Buffer and the absorbance was measured at 405 nm in an end-point mode. The experiment was repeated in duplicates.

The samples with estimated protein concentration 5.2  $\mu\text{M}$ , in buffers: CPB 4.0, 6.0; PB 6.0, 7.5 and 100 mM HEPES pH=7.5 were further used as test samples together with a control sample (non-labeled hCAII, non-digested) from the incubation step. The latter was diluted with CA Assay Buffer from 10  $\mu\text{M}$  to 5.2  $\mu\text{M}$  before the final measurement. For the final measurements, 1, 2, 5 and 10  $\mu\text{L}$  (in duplicates) of all test samples were diluted to 95  $\mu\text{L}$  final volume with CA Assay Buffer. CA Assay Buffer (95  $\mu\text{L}$ ) was used as a background control. A commercial solution of hCAII in 20 mM Tris buffer pH=7.5 (with 150 mM NaCl) was diluted to 5.2  $\mu\text{M}$  (with CA Assay Buffer); 10  $\mu\text{L}$  of the obtained solution was diluted to 95  $\mu\text{L}$  as a positive control sample (no Acetazolamide, inhibitor of hCAII) and negative control sample (with 2  $\mu\text{L}$  of the 20 mM inhibitor solution). 5  $\mu\text{L}$  of the hCAII substrate solution, nitrophenol ester was added to all samples just before measurement. The absorbance of the samples was measured at 405 nm in a kinetic mode for 1 h at RT for the product of reaction, nitrophenol. The experiment was repeated in duplicates.

To assess the enzymatic activity, two time points ( $t_1$  and  $t_2$ ) within the linear range of the plot were selected, and the corresponding absorbance values ( $A_1$  and  $A_2$ ) were recorded. The change in absorbance over time ( $\Delta A/\Delta t$ ) was then calculated. A nitrophenol standard curve was plotted to determine the slope ( $\Delta A/\text{nmol}$ ). If the substrate background control reading was significant, it was subtracted from the sample reading. To calculate the specific CA activity of the sample, the absorbance change of the negative control ( $\Delta \text{ANC}$ ) was subtracted from that of the sample ( $\Delta \text{AS}$ ) using the equation shown in the **Figure 37**.

$$\text{Serum Specific CA Activity} = \frac{B \times D \times 1000}{\Delta t \times V} \left( \frac{mU}{ml} \right)$$

**Figure 37.** The equation for specific CA activity of tested samples. B – released nitrophenol in sample based on the standard curve slope (nmol); D – dilution Factor (D = 1 when samples are undiluted); 1000 – 1000  $\mu\text{L}$ ;  $\Delta t$  – reaction time (min); V – tested sample volume ( $\mu\text{L}$ ).

## 4. Results and discussion

### 4.1. Multianalyte polarity/viscosity/pH probe based on SBD (SOLpH1)

#### 4.1.1. Design of SOLpH1

The structure of the first probe **SOLpH1** (**Figure 38**) consists of a few crucial parts, where each of them play important role in the design and the expected function of the molecule. These design details are in the upcoming paragraphs.

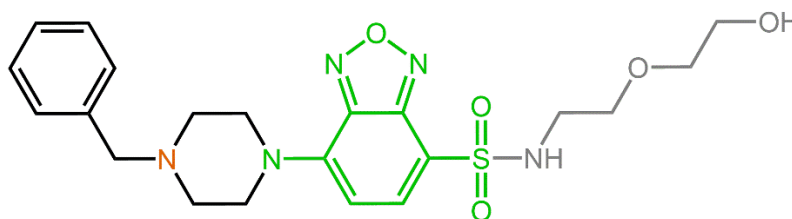


**Figure 38.** Structure of the probe **SOLpH1**. The fluorophore part is marked with green color, pH-sensor with orange and PEG linker (potential place of further derivatization) with gray one.

The structure of the probe is based on 4-sulfonamide 2,1,3-benzoxadiazole fluorophore (SBD, **Figure 39**, left). Similarly to 4-nitro-2,1,3-benzoxadiazole (NBD, **Figure 39**, right), another widely used fluorophore of this class, SBD and NBD, both have extraordinary optical properties convenient for imaging purposes, such as high quantum yields, biocompatibility, emission wavelengths (energies) shifted towards red [185]. Moreover, they were introduced into therapeutics structures or used for studies of cellular uptake, where no noticeable changes of cellular functions were observed [338, 339] suggesting high biocompatibility. Additionally, they were proven to be sensitive to polarity of environment, what makes them ideal for polarity-changes sensing for *in vitro* and *in cellulo* applications [46]. NBD derivatives were used as direct probes for protein labeling, as they tend to be reactive in para- position to nitro-group. The withdrawing effect of  $-\text{NO}_2$  group results in tendency for nucleophilic attack at position 1 [340–343]. In comparison, sulfonamide group at position better stabilizes the whole molecule and SBD is expected to be less prone to nucleophilic attack at position 4 [278].

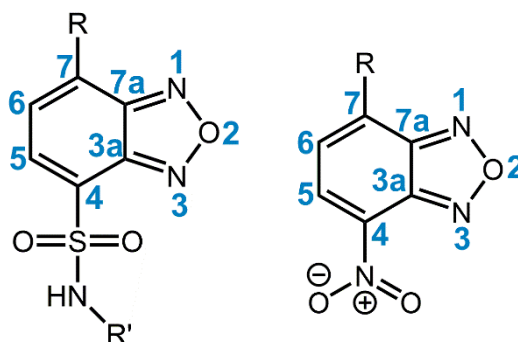
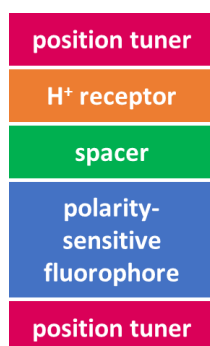
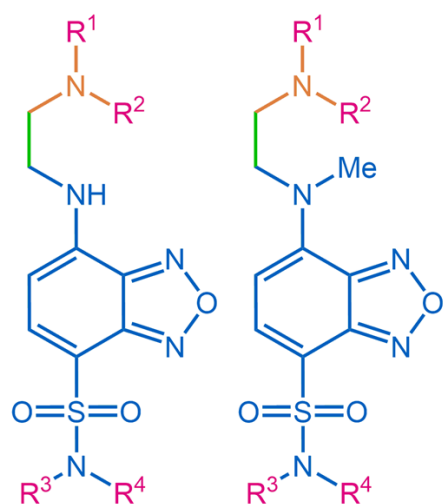


**Figure 39.** Structures of 4-sulfonamide 2,1,3-benzoxadiazole (SBD, left) and 4-nitro-2,1,3-benzoxadiazole (NBD, right) with numbered atoms in molecules. R, R' – any substituent.

Inspired by the design of previously reported pH responsive probes based on NBD [344, 345] in my work SBD scaffold (instead of NBD) was furnished with benzyl-piperazine part at position 1. The first amine group in piperazine, which is directly attached to SBD phenyl ring, has a nitrogen lone electron pair (**green**-marked nitrogen atom in the piperazine ring, **Figure 39**) engaged in  $\pi$ -conjugated system (partial double bond character of C-N bond [346]). At the same time, the lone electron pair on the other nitrogen group in the ring (**orange**-marked nitrogen atom in the piperazine ring, **Figure 39**) is available for PeT quenching [344]. Alternatively, two other mechanisms are considered as well, with non-radiative decay through a non-fluorescent TICT or PICT (planar intramolecular charge transfer) [345, 346].

The **orange**-marked amine motif is more prone for protonation than the **green**-marked one, that should subsequently mask the lone pair minimizing or even potentially eliminating any quenching effect and allowing for SBD fluorescence. This gives the **SOLpH1** a unique property to be fluorescent only upon the decrease in surrounding pH, i.e. higher concentration (activity) of protons (e.g. intracellular one). It is worth to highlight that certain SBD derivatives (**Figure 40**) were successfully introduced as *in vitro* sensors of proton concentration and polarity changes in 5 nm distance, around spherical micelles in water, mimicking in a simplified way lipid monolayer structure [252, 253]. The detailed mechanism of pH-sensing for similar molecules is described in subchapter **1.1.4**.

Last but not least, a short PEG-like linker may balance the hydrophobicity of the rest of the molecule **SOLpH1** to ensure its sufficient aqueous solubility critical for practical applications. PEG linkers are in fact commonly used to increase the solubility of the molecules, due to the presence of many oxygen atoms, intertwined with methylene groups. Moreover, their presence may minimize non-specific interactions between molecule bearing a PEG linker and proteins or even lipid membranes [168, 169]. The flexibility of those linkers makes them possible to interact both with polar solvents (with oxygen atoms outside and creating of hydrogen bonds), as well as non-polar ones (twisting of the chain may result in exposition of methylene groups instead). PEG dual nature resembles the behavior of micelles, which are similarly able to interact with many different solvents. Therefore, polyethylene glycol chains are frequently used to create micelle-like structures [167]. Moreover, terminal hydroxyl group of PEG linker may be a place of attachment for additional functionalities, something critical for designing more advanced probes based on this fluorophore, which was used in the probe **SOLpH1-Tos**.



R <sup>1</sup>	R <sup>2</sup>	R <sup>3</sup> , R <sup>4</sup>		
		Me, Me	Me, <sup>n</sup> Oc	<sup>n</sup> Oc, <sup>n</sup> Oc
CH <sub>2</sub> COO <sup>-</sup>	CH <sub>2</sub> COO <sup>-</sup>	1	10	19
CH <sub>2</sub> COO <sup>-</sup>	Et	2	11	20
H	H	3	12	21
CH <sub>2</sub> CH <sub>2</sub> OH	CH <sub>2</sub> CH <sub>2</sub> OH	4	13	22
CH <sub>2</sub> CH <sub>2</sub> OCH <sub>2</sub> CH <sub>2</sub>		5	14	23
Me	Me	6	15	24
H	Et	7	16	25
CH <sub>2</sub> COOMe	Et	8	17	26
Et	Et	9	18	27
Me	Me	28	30	32
Et	Et	29	31	33

**Figure 40.** The SBD derivatives, which were successfully introduced to *in vitro* studies for nanoscaled environmental mapping around spherical micelles mimicking lipid monolayer. The sequence of 1→9, 10→18, and 19→27 is determined by the log*P* (n-octanol/water partition coefficient) value of the corresponding amine (R<sup>1</sup>R<sup>2</sup>NH). Adapted from [252, 253].

#### 4.1.2. Synthesis and characterization of SOLpH1

The synthesis of **SOLpH1** probe was started with aromatic electrophilic substitution at position 7 of the 4-chloro-2,1,3-benzoxadiazole to form the intermediate **1** [279] (**Figure 41**). The reaction is selective towards the *para*-position, while the *ortho*-product is not formed possibly due to the steric hindrance at position 6 relative to 4. In this step, the chlorosulfonic acid molecules react between themselves to form a strong electrophile, SO<sub>2</sub>Cl with a formal positive charge on sulfur atom. The latter gets attacked by the electrons in the aromatic benzene ring of benzoxadiazole. According to the possible resonance structures, even though chlorine atom at the position 7 should direct substituent to both *ortho*- and *para*-positions, only a *para*-product is formed. As a result of further acidic proton elimination, substitution in *para*-position occurs with regeneration of the aromatic benzene ring (**Figure 42**).

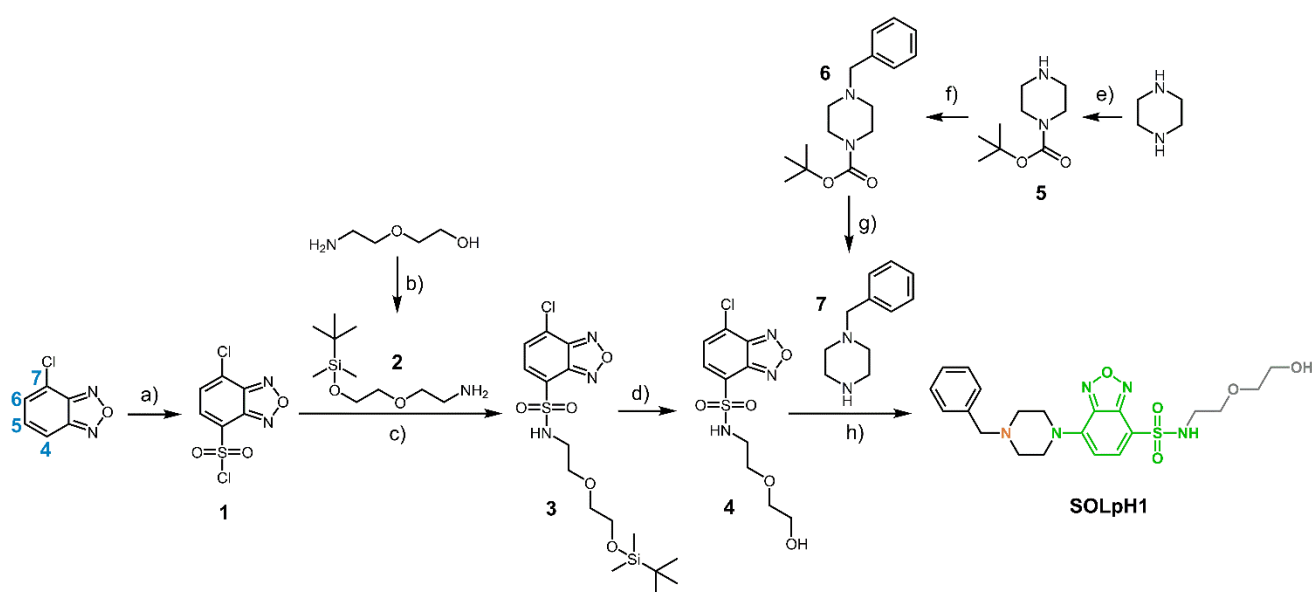


**Figure 41.** Synthetic pathway leading to the **SOLpH1** probe: a) chlorosulfonic acid, 3 h, 120°C, 81%; b) *tert*-butyldimethylsilyl chloride, imidazole, DCM, RT, 20 h, 57%; c) Et<sub>3</sub>N, DCM, 24 h, RT, 54%; d) 3M HCl in MeOH, 2 h, RT, quant.; e) di-*tert*-butyl dicarbonate, *tert*-butanol, NaOH 2M solution, 1 h, RT, 69%; f) benzyl bromide, Et<sub>3</sub>N, ACN, RT, 65%; TFA, DCM, RT, 1 h, quant.; g) Et<sub>3</sub>N, ACN, 80°C, 24 h, 59%. The first substrate, 4-chloro-2,1,3-benzoxadiazole, has its atoms partially numbered to track the substitutions described in the text. The fluorophore part is marked with green color (with orange-marked nitrogen as pH-sensor) and PEG linker with grey one.

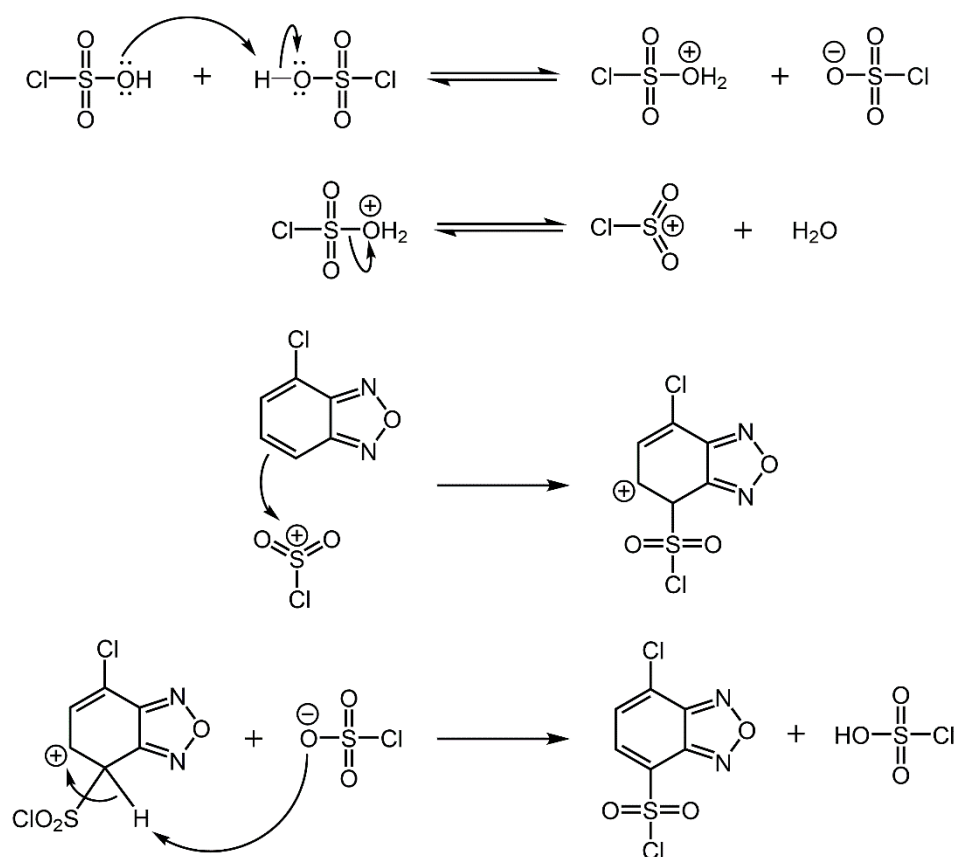


**Figure 42.** Schematic presentation of a simplified mechanism of the first step of the **SOLpH1** probe synthesis. The detailed description is included in the text.

After a few hours of stirring at temperature close to the boiling point of chlorosulfonic acid, which was both reagent and solvent of the reaction, the mixture had to be slowly and carefully poured onto ice. Interestingly, sulfonation is considered a reversible reaction, however due to high excess of chlorosulfonic acid and minimal amount of water in the reaction mixture, the equilibrium is significantly pushed towards the products of reaction. The pouring onto ice step cooled down the reaction mixture, where high excess of acid was exothermically decomposed into hydrochloric acid and sulfuric acid, to facilitate further work-up of reaction (extraction and aqueous layer neutralization), as chlorosulfonic acid is more toxic than products of its decomposition. To conduct the next step, 2-(2-aminoethoxy)ethanol had to be protected at the hydroxyl group site. *tert*-Butyldimethylsilyl (*t*BDMS) protecting group was selected as previously reported [323] due to its sufficient stability in the conditions of the next reaction step with simultaneous relative facility of deprotection and accessibility of deprotection agents [347]. The unprotected linker may have led to a mixture of two different products, one with sulfonamide group formed from amine group and the other one with sulfonate ester one from hydroxyl group. The latter was preliminary confirmed in the other test reaction performed, where intermediate **1** (**Figure 41**) was mixed together with 33% dimethylamine in EtOH and as a result two different products were formed: sulfonamide and ethyl ester one. Interestingly, compound **2** (**Figure 41**) showed rare and therefore diagnostic negative chemical shift values for protons from two methyl groups in the protecting group, typical for methyl(ene) motifs directly connected to silicon, that are shielded stronger than in

tetramethylsilane (the usual internal standard used in NMR). Due to a high electrophilicity of the sulfonic chloride, the substitution occurred primarily on this functional motif, yielding novel compound **3** (**Figure 41**), a sulfonamide derivative intermediate in 54% isolated yield. Even though both chlorine atoms (position 7 of SBD derivative and chlorosulfonic group at position 4) may have been substituted with the amine linker **2** (**Figure 41**), the time and temperature of reaction occurred to be crucial (30 minutes of stirring) to ensure reaction selectivity as previously reported for similar type of compounds [279]. After the removal of the silyl protective group with use of 3M HCl in methanol to obtain compound **4**, another electrophilic center of SBD was substituted, this time with compound **6**, benzylpiperazine. Intermediate **6** was previously obtained from compound **5** [326] in the reaction between BOC-piperazine **5**, protected through mono-substitution with *tert*-butyloxycarbonyl protecting group, and benzyl bromide. The piperazine mono-protection method to yield **5** was reported previously [325], using the byproduct of the reaction (*tert*-butanol from *tert*-butyl dicarbonate) as solvent, creating an equilibrium during the process, which results in a relatively high yield of the mono-substitution reaction (69%). The reaction mixture after coupling of compounds **4** and **6** was purified by flash column chromatography and preparative thin layer chromatography yielding a new SOLpH1 probe in the overall yield of 6.5% over 8 steps. The structures of novel compounds that were not previously reported (intermediate compounds **3**, **4** and the final probe **SOLpH1**) were confirmed structurally by <sup>1</sup>H NMR, <sup>13</sup>C NMR and HRMS analyses.



### 4.1.3. Optical properties of SOLpH1

Absorption spectra of **SOLpH1** collected in aqueous citrate-phosphate buffer (CPB) at pH 4.0 revealed maximum absorption at 420 nm, making it suitable for confocal imaging with both 405 and potentially also 488 nm excitation lasers (data for the second excitation wavelength not included) with emission maximum at 600 nm (**Figure 43**). In the PB buffer at pH=8.0 the values were shifted 10-15 nm towards red part of visible spectrum ( $\lambda_{exc/em}=435/615$  nm). The possibility of excitation with 488 nm makes it compatible with biological cellular applications, markedly eliminating the risk of UV-induced phototoxicity. The values of excitation and emission of the **SOLpH1** are comparable to values presented in the literature for similar SBD derivatives in aqueous media [**DBD-IA** with  $\lambda_{exc/em}=452/616$  nm in water [252] and **ATMND-DBD** with  $\lambda_{exc/em}=451/615$  nm in a solution buffered to pH 7.0 (10 mM sodium cacodylate) and containing NaCl (100 mM) and EDTA (1.0 mM, water/ethanol 97.2:2.8 (**Figure 43**)] [348].

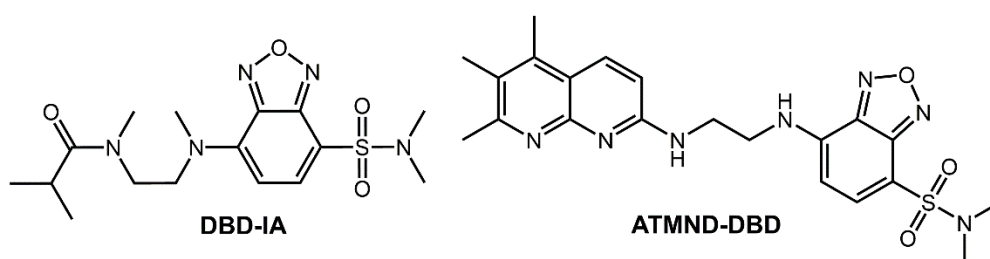


**Figure 43.** The structures of the probes with similar core structures and optical properties to the probe **SOLpH1**: DBD-IA (left, [252]) and ATMND-DBD (right, [348]).

Clear separation of absorption (420 nm) and emission maxima (600 nm) in the same experimental conditions (**Figure 44**) ( $7143\text{ cm}^{-1}$  in CPB buffer pH=4.0) demonstrates large Stokes shifts typical for this class of fluorophore, minimizing potential self-quenching. Another advantage of significant Stokes shift is a possibility of multiplexing with variable other dyes of similar excitation that often exhibit much less red-shifted emission maxima.

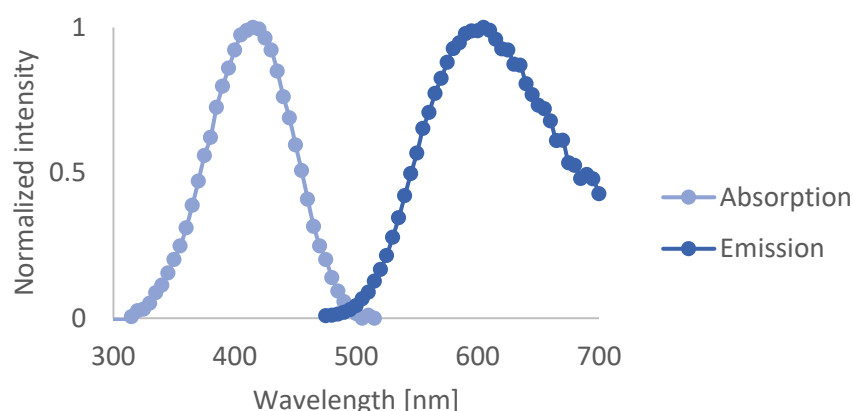


**Figure 44.** Absorption (left) and emission (right;  $\lambda_{exc}=435$  nm) spectra of **SOLpH1** (50  $\mu\text{M}$ ) in CPB buffer at pH=4. Absorbance was measured at 10 nm steps, the emission at 5 nm steps. The final concentration of DMSO was kept at 1%. Experimental data points, averaged over 3 repeats ( $n = 3$ ) were connected with a line, which is there as a guideline for eyes to obtain a visual effect of the continuous line.

The calculated relatively low quantum yield (**Table 1**) of the probe in CPB pH=4.0 (QY=0.206) and PB pH=7.5 (QY=0.026) buffers is typical for fluorophores with significant Stokes shifts [349]. Furthermore, as suggested in the subchapter 4.1.5, the probe **SOLpH1** is sensitive to viscosity changes, therefore the non-viscous aqueous media may have affected the quantum yield value. The more viscous medium (e.g. glycerol) is expected to provide a higher QY as was observed for other viscosity-sensitive sensors (examples: [212, 215]). It is worth to highlight that there is a significant difference between the fluorescence quantum yield in CPB pH=4.0 and PB pH=8.0, where QY for the lower pH is circa 8 times higher proving a pH sensitivity of the probe's emission. Similar difference was observed in a literature for the other pH-responsive probes (examples: [237, 350, 351]). All this combined indicates that local concentration of protons around the **SOLpH1** affects the probe's optical properties as well. The relatively low values of QY contributed to the final values of brightness that are order of magnitude lower than the standards used (**Table 1**).

Importantly for practical applications, the probe presented linearity of response to changing concentrations in the range of 50  $\mu\text{M}$  - 2  $\mu\text{M}$  (extrapolated to 0  $\mu\text{M}$  concentration) (**Figure 45**) that fits the range of concentrations of the **SOLpH1** used in other analytical and biological tests described in the upcoming subchapters.

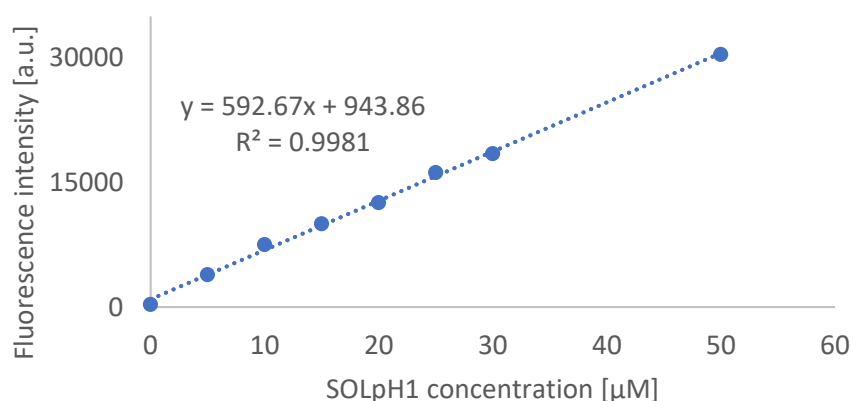


**Figure 45.** Linear plot of various **SOLpH1** concentrations fluorescence intensity at 600 nm in CPB buffer at pH=4,  $\lambda_{\text{exc}}=435$  nm. The emission was measured at 10 nm steps. The final concentration of DMSO was kept at 1%. The experimental data points were averaged over 3 repeats (n=3).

**Table 1.** Values of extinction coefficients, fluorescence quantum yields and brightness of standards (quinine sulphate, coumarin 343, fluorescein) and the probe **SOLpH1**. The final concentration of DMSO was kept at 1%. The experimental data was averaged over 3 repeats (n=3).

Compound	Solvent	Calculated extinction coefficient $\epsilon_{\lambda}$ [ $\text{cm}^{-1} \text{M}^{-1}$ ]	Calculated fluorescence quantum yield $\Phi_x$	Literature fluorescence quantum yield	Brightness $B_{\lambda}$
					$B_{430}=18900$
<b>Coumarin 343</b>	EtOH	$\epsilon_{405}=30000$	0.637	0.63 [335]	$B_{430}=20790$
		$\epsilon_{430}=33000$			$B_{475}=15939$
		$\epsilon_{475}=25300$			
<b>Fluorescein</b>	0.1M NaOH	$\epsilon_{475}=21700$	0.915	0.925 [333]	$B_{475}=20072.5$
<b>SOLpH1</b>	CPB pH=4	$\epsilon_{405}=8450$	0.206	-	$B_{405}=1740.7$
		$\epsilon_{430}=8710$			$B_{430}=1794.3$
		$\epsilon_{475}=2440$			$B_{475}=502.6$
<b>SOLpH1</b>	PB pH=7.5	$\epsilon_{405}=5800$	0.026	-	$B_{405}=150.8$
		$\epsilon_{430}=7950$			$B_{430}=206.7$
		$\epsilon_{475}=5060$			$B_{475}=131.6$

#### 4.1.4. Fluorescence response of SOLpH1 to pH

In order to understand the mechanism of fluorescence response of the **SOLpH1**, the hypothesized behavior of the molecule upon excitation can be analyzed using Jablonski diagram (**Figure 46**), as it was suggested for similar fluorescent scaffolds [344–346]. The most popular mechanism used for explanation of the fluorescence of SBD (and NBD) derivatives is PeT, photoinduced electron transfer [252, 344, 345, 352]. In this approximation, upon excitation the electron density on the fluorophore initially in ground state HOMO orbital (highest occupied molecular orbital) is excited to higher energy state, LUMO (Lowest Unoccupied Molecular Orbital – before excitation). Subsequently, upon relaxation the electron returns to the ground state with emission of fluorescence. The design of the **SOLpH1** is based on the existence of free electron pair on a piperazine nitrogen of aliphatic tertiary amine motif that is at higher energy than a ground state of the HOMO (but a lower energy than LUMO) of the fluorophore. In the consequence, upon excitation of the fluorophore, high energy electron density from piperazine in direct proximity of the SBD fluorophore (but not being a part of a conjugated  $\pi$  system), enables PeT effect to occur. This hinders a radiative relaxation of the SBD fluorophore back to its ground state, significantly decreasing the fluorescence intensity. However, as lone electron pair on the same nitrogen may get protonated at low pH, it makes it “not available” (lower energy) for PeT and alleviates inhibition leading to significant increase of fluorescent signal [353, 354]. The mechanism of this pH-dependent change in fluorescence of **SOLpH1** results in higher intensity upon decrease in pH. The expected PeT-based mechanism of pH-sensing by the probe was presented in the **Figure 46**. Modulating the pKa of amine group participating in the PeT effect provides possibility of adjusting the properties of the scaffold to one’s purposes, e.g. to physiological, intracellular pH range [353, 354].

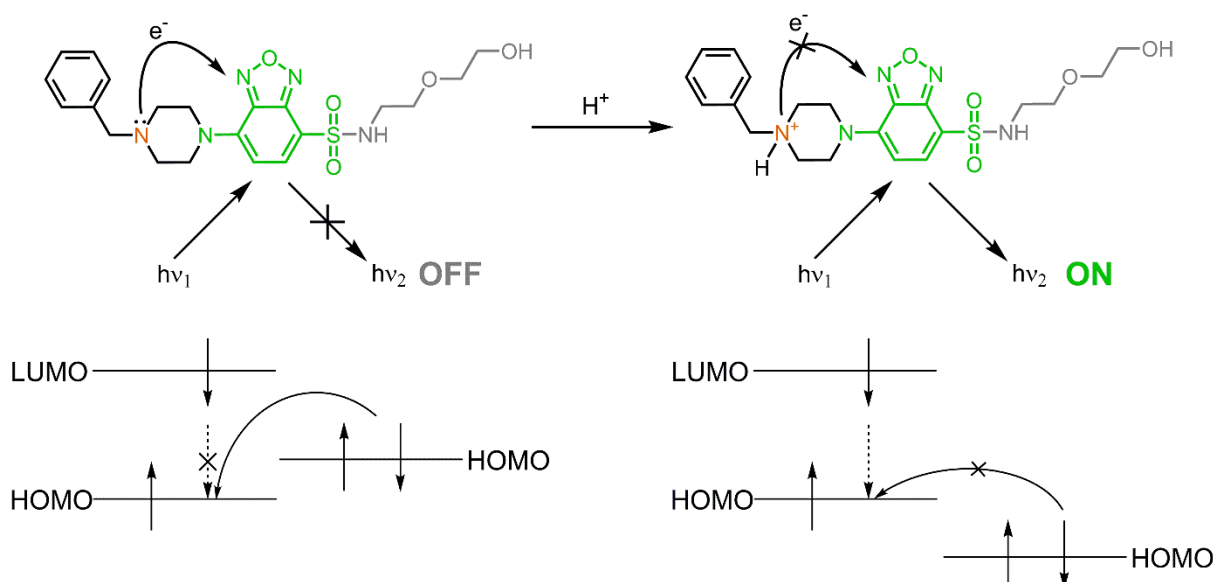


**Figure 46.** The expected PeT-mechanism of pH sensing for the probe **SOLpH1**. HOMO – highest occupied molecular level; LUMO – lowest unoccupied molecular level;  $h\nu$  – quantum of light. The fluorophore part is marked with green color, pH-sensor with orange one and PEG linker with gray one.

As it was already mentioned in the subchapter 4.1.1., even though the nitrogen lone pair of the SBD is in direct connection with benzene ring and presents partial double bond character of C-N bond [346], two other mechanisms are suggested to contribute for SBD-based (or NBD-based) scaffolds. The first one was presented in detail in the subchapter 1.3.3., TICT-involved, non-radiative deactivation processes in molecular rotors (quenching by rotation) [345, 346]. The last mechanism, planar intramolecular charge transfer (PICT) is based on an opposite orientation of two rotating parts of an excited molecule, in comparison to TICT [345, 346] (**Figure 47**). The PICT model proposes an ICT structure with enhanced double bond character between the D and A moieties (C–N bond in NR), leading to a partial positive charge on the amino group and a quinoidal resonance structure [355]. However, the TICT and PICT mechanisms were mostly considered for molecules bearing only one nitrogen atom, in a direct connection to SBD/NBD, suggesting that mechanism of more complex molecules, like the **SOLpH1**, fluorescence inhibition/increase may be based on more than one mechanism [346]. Additionally, the experimental results of pH sensitivity support the dominant role of the PeT-based mechanism.

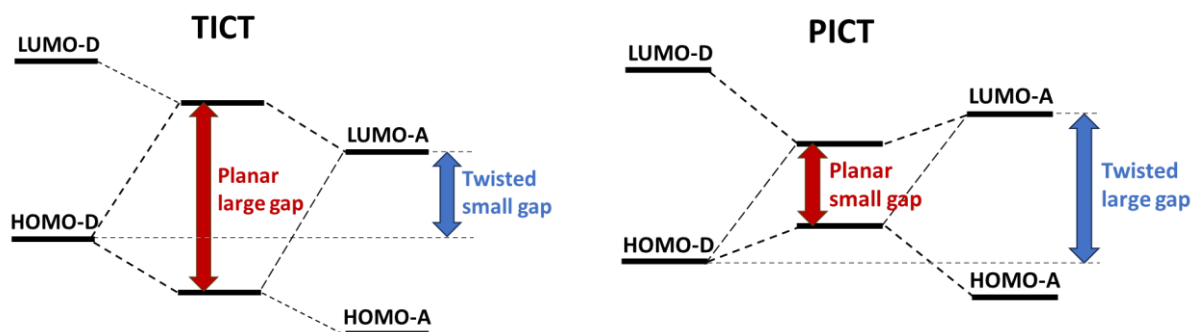


**Figure 47.** Conceptual illustration on how orbitals interactions determine the energy gap of twisted (left) or planar state (right). A – acceptor; D – donor; TICT – twisted intramolecular charge transfer; PICT – planar intramolecular charge transfer; HOMO – highest unoccupied molecular orbital; LUMO – lowest unoccupied molecular orbital; LUMO-A / LUMO-D – LUMO of acceptor or donor; HOMO-A / HOMO-D – HOMO of acceptor or donor. Adapted from [355].

The pH-sensing properties were confirmed in experiments performed in buffers of different pH. Citrate phosphate buffer (pH: 4.0, 5.0, 6.0) and phosphate buffer (6.0, 7.0, 7.5, 8.0) were used as media of choice. Both buffering systems showed increase of fluorescence with decreasing pH values (**Figure 48**). The near-identical value of the fluorescence intensity for both CBP and PB at pH 6 suggests that it is indeed a pH and not the chemical nature of the buffer that is responsible for the fluorescence intensity change. The peak emission intensity at pH=4 was approximately 14 times higher than in pH=8 (**Figure 48**, right) with a subtle shift in the wavelength of maximum emission from 600 nm at pH=4 to 615 nm at pH=8 (**Figure 105**). The absorbance measurement presented pH-dependence as well (**Figure 107**), with similar shift to the emission spectra. Notably, the highest absorbance was observed for low pH (4-5), the lowest for pH=6 and pH 7-8 the middle values.

The  $pK_a$  of the **SOLpH1** calculated as an average of values obtained separately from emission at 600 nm for pH=4 and at 615 nm for pH=8 (**Figure 49**) is  $6.4, \pm 0.2$ , well within biologically-relevant pH range making it suitable for intracellular applications. Simply put, the  $pK_a$  value indicates the pH range ( $\pm 1.5$  pH units corresponding to a three orders of magnitude difference in proton concentration) over which a probe alters its optical properties (or charge), making it valuable for sensing applications [94].

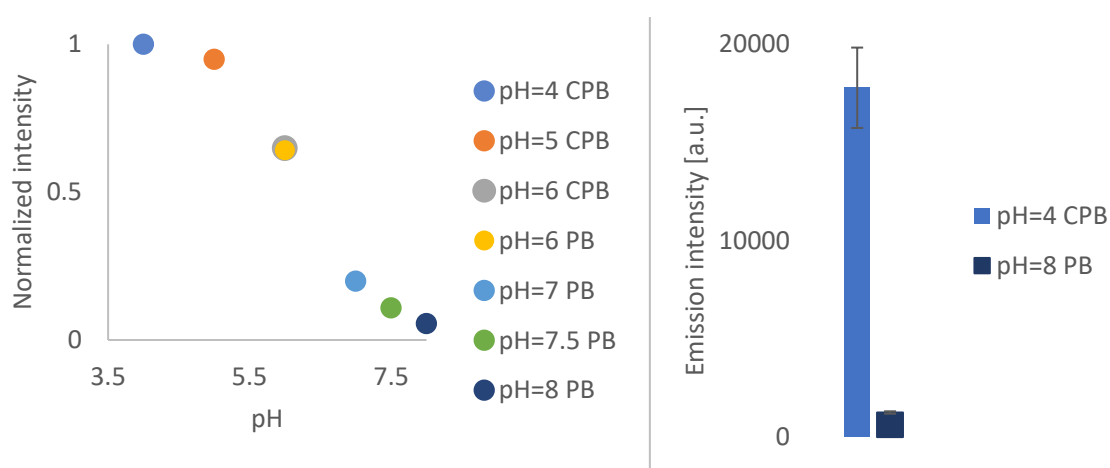


**Figure 48.** (left) The pH response for the **SOLpH1** (20  $\mu$ M) of fluorescence at 600 nm,  $\lambda_{exc}=435$  nm: pH response curve. Experimental data points were averaged over 2 repeats ( $n=2$ ). (right) Direct comparison of emission intensity at 600 nm for CPB pH=4.0 and PB pH=8.0. Error bars represent standard error of mean of 2 measurements. CPB – citrate phosphate buffer; PB – phosphate buffer. The emission was measured at 5 nm steps. The final concentration of DMSO was kept at 1%. The values were normalized to the highest value of emission at 600 nm for CPB pH=4.0.

It is important to keep in mind, that even though the calculated value for the probe was based on experiments with 150-200 mM ion concentration (CPB or PB buffers), once it enters the cell, the local microenvironment may differ, affecting the probe's properties (including  $pK_a$ ). The possible shift of  $pK_a$  value may be altered by local effects/differences in ionic strength, binding of probes to proteins or other charged moieties (non-specific interactions) or even local temperature [94]. It was reported that increasing the ionic strength from 0.01 to 3 M can shift the  $pK_a$  by up to 1.2 units [356]. In spite of this reported change regarded tremendous change in ionic strength, it is expected that the intracellular pH sensitivity of the **SOLpH1** may slightly differ from the one determined *in vitro*.

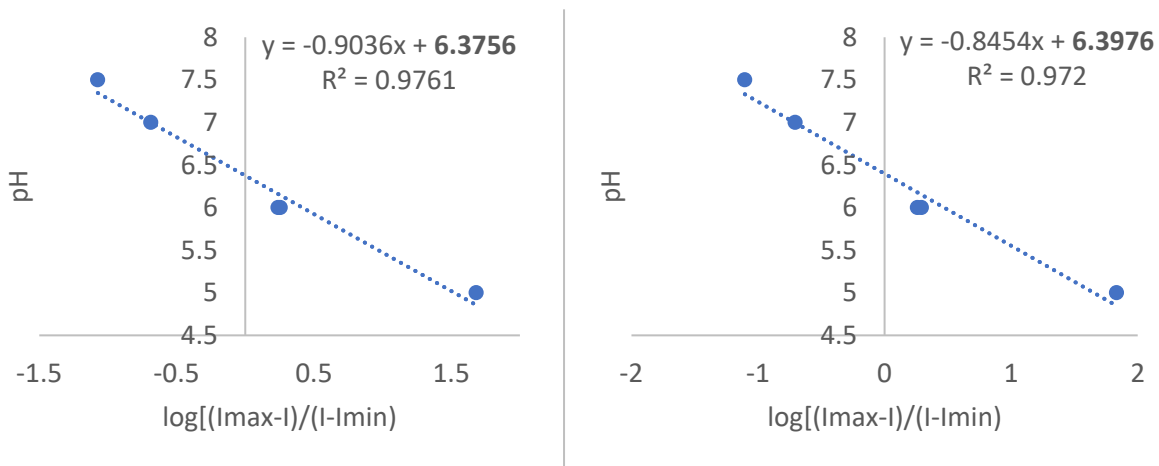


**Figure 49.** Plot of pH vs  $\log[(I_{\max}-I)/(I-I_{\min})]$ , where  $I$  is the observed fluorescence intensity of the **SOLpH1** (20  $\mu\text{M}$ ) at 600 (left)/615 (right) nm,  $\lambda_{\text{exc}}=435$  nm. The y-intercept is the  $\text{p}K_{\text{a}}$  value ( $6.37 \pm 0.17$  for 600 nm;  $6.39 \pm 0.18$  for 615 nm) of an equilibrium between the protonated and non-protonated forms of the **SOLpH1**. The final  $\text{p}K_{\text{a}}$  value was calculated as an average of both values:  $6.4 \pm 0.2$ .

#### 4.1.5. Polarity-sensing properties of SOLpH1

Polarity sensitivity of the **SOLpH1** was evaluated by studying the fluorescence of the probe in dioxane:water mixtures (**Figure 50**) as well as in a set of solvents (DCM to water-based solutions; **Figure 51**). 1439  $\text{cm}^{-1}$  shift of emission maximum towards red was observed between the probe's response in pure dioxane (565 nm) vs pure MiliQ water making it potentially sufficient to explore in a ratiometric type of sensing (615 nm) (**Table 2**). While polarity of different pure solvents was thoroughly characterized [357], analysis and characterization of binary mixtures (including dioxane:water mixtures) pose a challenge when it comes to homogeneity [358], acid dissociation constants, hydrogen-bonding interactions etc. [359]. Even though dioxane:water mixtures may differ on microscopical level, dioxane is still considered as fully miscible with water (despite negligible polarity) and does not form aggregates with its molecules (due to lack of H-bond donor sites).

One of the most reliable and important parameter scales used for characterization of polarity of binary mixtures (with themselves or pure solvents) is an empirical Reichardt polarity parameter measured with an indicator betaine B30 (2,6-diphenyl-4-(2,4,6-triphenyl-1-pyridinio)-phenolate,  $E_T(30)$ ), where molar transition energy is measured for each medium [54, 359–361]. The  $E_T(30)$  values for all used dioxane:water mixtures were calculated with use of two equations:  $E_T(30) = 2997.5 N_{av,x} + 2.123$  for mixtures with  $N_{av,x} < 0.015 \text{ mol/cm}^3$  (1,4-dioxane-rich section) and  $E_T(30) = 398,8 N_{av,x} + 40.42$  for  $N_{av,x} > 0.015 \text{ mol/cm}^3$  (water-rich section), where  $N_{av,x}$  – average molar concentration (x – water) [360]. The relative polarity for dioxane:water mixtures  $E_T^N$  was calculated with an equation:  $E_T^N = (E_T(30) - 30.7) / 32.4$  [54]. The values for all solvents presented in the **Table 3** were derived from the literature [357, 362].

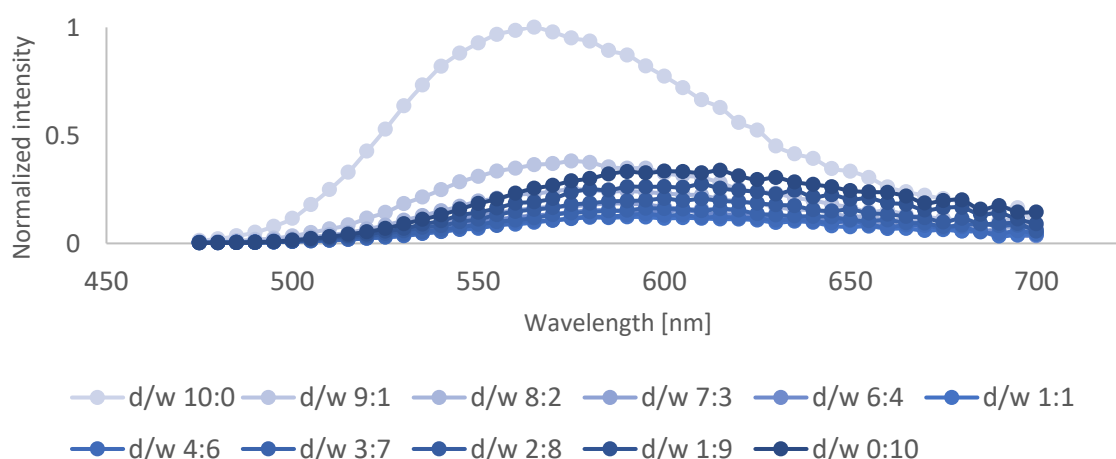


**Figure 50.** Fluorescence spectra of the **SOLpH1** (20  $\mu\text{M}$ ) in dioxane:water mixtures with changing ratio,  $\lambda_{exc}=435 \text{ nm}$ . d – dioxane; w – water. The emission was measured at 5 nm steps. The final concentration of DMSO was kept at 1%. Experimental data points, averaged over 2 repeats ( $n = 2$ ) were connected with a line, which is there as a guideline for eyes to obtain a visual effect of the continuous line.



**Table 2.** The optical properties of the **SOLpH1** (20  $\mu$ M) in various dioxane:water mixtures. The final concentration of DMSO was kept at 1%.  $E_T(30)$  – empirical Reichardt polarity parameter measured with an indicator B30 [360];  $\lambda_{em}$  – maximum of emission spectrum;  $\lambda_{em-max}$  intensity – fluorescence intensity of the maximum emission wavelength. Relative total fl. Intensity – sum of emission given for chosen dioxane:water mixtures, where values were normalized to the highest value (for pure dioxane). The  $E_T(30)$  value was calculated with use of two equations:  $E_T(30) = 2997.5 N_{av,x} + 2.123$  for mixtures with  $N_{av,x} < 0.015$  mol/cm<sup>3</sup> (1,4-dioxane-rich section) and  $E_T(30) = 398,8 N_{av,x} + 40.42$  for  $N_{av,x} > 0.015$  mol/cm<sup>3</sup> (water-rich section), where  $N_{av,x}$  – average molar concentration (x – water) [360]. The relative polarity  $E_T^N$  was calculated with an equation:  $E_T^N = (E_T(30) - 30.7) / 32.4$  [54]. (n=2)

Dioxane % in water	Polarity $E_T(30)$ [360] [kcal/mol]	Relative polarity $E_T^N$ [54]	$\lambda_{em}$ [nm]	$\lambda_{em}$ [cm <sup>-1</sup> ]	$\lambda_{em-max}$ intensity [a.u.]	Relative total fl. intensity
100%	37.1	0.197	565	17700	20791	1
90%	40.2	0.293	580	17240	7495.5	0.379
80%	46.0	0.472	575	17390	4963.5	0.256
70%	46.6	0.490	590	16950	3706.5	0.191
60%	47.3	0.513	590	16950	2996	0.160
50%	48.1	0.538	595	16810	2717	0.148
40%	49.5	0.580	595	16810	2779	0.146
30%	51.1	0.629	600	16670	3231.5	0.178
20%	53.5	0.705	600	16670	4646	0.261
10%	57.1	0.815	610	16390	5328	0.298
0%	62.5	0.982	615	16260	6865	0.381

The 20  $\mu$ M solutions of the **SOLpH1** probe in various solvents or buffers additionally confirmed the first results obtained in the dioxane:water mixtures, with even bigger shift of 1921 cm<sup>-1</sup> between DCM (550 nm) and water-based solutions (MiliQ water and chosen buffers – 595 to even 615 nm) (**Figure 51**). The relative fluorescence intensity values (**Table 3**, last column) confirm the conclusions derived from dioxane:water experiments, where the more non-polar medium, the higher emission of the probe **SOLpH1**. The high value of emission for CPB at pH=4.0 is considered as exception, as based on the description in the subchapter **4.1.4**, the **SOLpH1** probe should present a significant increase of emission at low pH values. The latter provides an additional explanation about a relatively high emission in MiliQ water in comparison to the other aqueous media (buffers), as the pH value of such a water is estimated to be 7.0 [363].

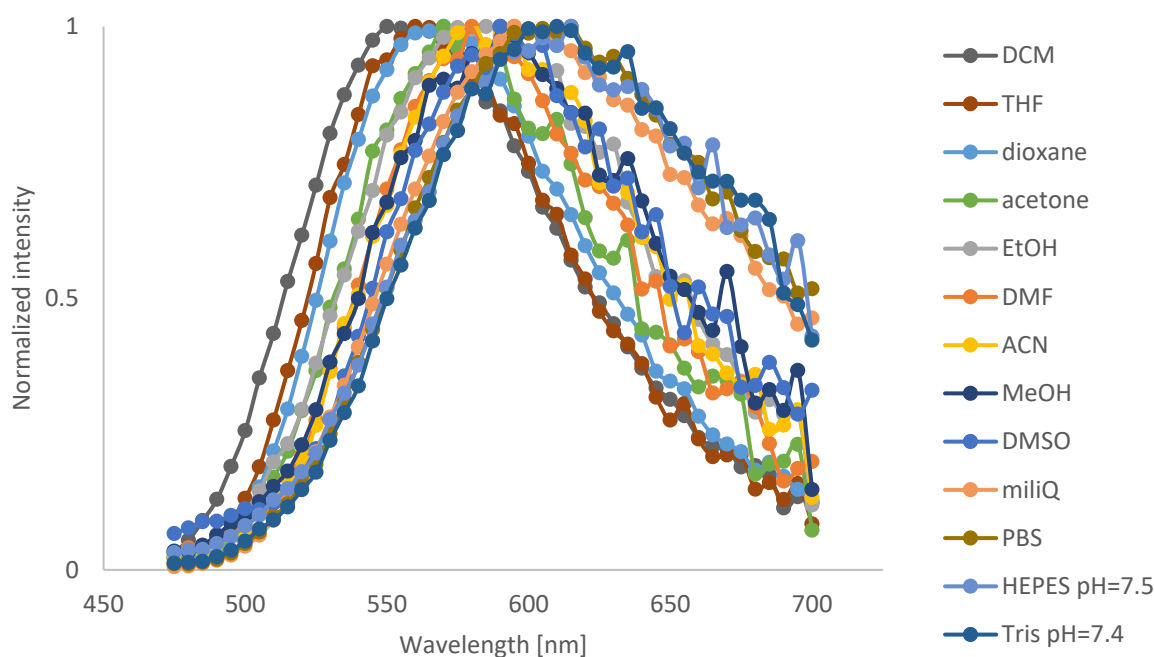


**Figure 51.** Fluorescence spectra of the **SOLpH1** (20  $\mu\text{M}$ ) in various solvents/solutions,  $\lambda_{\text{exc}}=435$  nm. The values were normalized to the highest value of emission for DCM at 550 nm. The emission was measured at 5 nm steps. The final concentration of DMSO was kept at 1%. Experimental data points, averaged over 2 repeats ( $n = 2$ ) were connected with a line, which is there as a guideline for eyes to obtain a visual effect of the continuous line.

**Table 3.** The optical properties of the **SOLpH1** (20  $\mu\text{M}$ ) in various solvents or buffers.  $E_{\tau}(30)$  – empirical Reichardt polarity parameter [362];  $E_T^N$  – relative polarity;  $\lambda_{\text{exc}}$  – maximum of excitation spectrum;  $\lambda_{\text{exc}}$  – maximum of excitation in a chosen solvent or buffer;  $\lambda_{\text{em}}$  – maximum of emission in a chosen solvent or buffer (in nm or  $\text{cm}^{-1}$ );  $\lambda_{\text{em-max}}$  – maximum of emission spectrum value in a chosen medium (solvent or buffer); Relative total fl. Intensity – sum of emission given for chosen solvent or buffer, where values were normalized to the highest value (for CPB pH=4.0). To simplify the analysis, the relative polarity for all aqueous-based media was decided to be 1.0 as for water. ( $n=2$ )

Solvent or buffer	Polarity $E_{\tau}(30)$ [362] [kcal/mol]	Relative polarity $E_T^N$ [357]	$\lambda_{\text{exc}}$ [nm]	$\lambda_{\text{em}}$ [nm]	$\lambda_{\text{em}}$ [ $\text{cm}^{-1}$ ]	$\lambda_{\text{em-max}}$ intensity [a.u.]	Relative total fl. intensity
DCM	41.1	0.309	420	550	18180	19572.5	0.388
THF	37.4	0.207	440	560	17860	7679	0.142
Dioxane	36.0	0.164	435	570	17540	17210.5	0.323
Acetone	42.2	0.355	445	570	17540	2183	0.042
Ethanol	51.9	0.654	435	585	17090	2652	0.056
DMF	43.8	0.386	455	580	17240	3185.5	0.060
Acetonitrile	46.0	0.46	450	595	16810	1707.5	0.034
Methanol	55.5	0.762	440	590	16950	1200.5	0.025
DMSO	45.0	0.444	445	590	16950	2478	0.049
CPB pH=4.0	63.1	1.0	420	595	16810	46076	1
MiliQ water	63.1	1.0	420	595	16810	7894	0.172
PBS pH=7.4	63.1	1.0	430	615	16260	3464	0.077
Tris pH=7.4	63.1	1.0	435	610	16390	2433	0.054
PB pH=7.5	63.1	1.0	435	615	16260	6224	0.140
HEPES pH=7.5	63.1	1.0	430	615	16260	2639	0.059

Interestingly, it may be observed that larger bathochromic shift is observed for fluorescence band maximum (550 to 615 nm, which corresponds to  $1921\text{ cm}^{-1}$  of a difference) than for absorption (420 to 455 nm, which is equal to  $1831\text{ cm}^{-1}$  difference) (**Table 3**). The detailed correlation of changes between the total fluorescence emission to wavenumber and to Reichardt polarity parameter was presented in the **Figure 52** for dioxane:water mixtures (top) and different solvents/buffers (bottom). It was observed that behavior of dioxane:water mixture changes at  $0.015\text{ mol/cm}^3$  average molar concentration  $N_{av,x}$  of water, between 70% and 80% of dioxane in water [360]. Indeed, both mixtures present decrease in the integrated emission and wavenumber (energy of emission). Further increase of the dioxane percentage causes a gradual decrease in emission until it reaches 30% of water. There, the increasing amount of water (70% and more) may inhibit PeT-based quenching process through protonation, resulting in a gradual fluorescence increase closely to the level of emission presented by dioxane:water 9:1 mixture (only 0.6% of a difference).

In the **Figure 52**, bottom panel, demonstrates that in general, DCM and polar aprotic solvents (dioxane, THF, acetone) lead to a higher emission intensity for probe **SOLpH1**, a known phenomenon described previously in the literature [278]. At the same time, in the solvents, which are polar and protic (EtOH, MeOH, MilliQ water) the probe presents a decrease in intensity and energy (longer wavelength) of emission. The reason for the latter, i.e. lower emission intensity at longer wavelength (lower energy difference between the excited and ground state) is due to an increased probability of non-radiative relaxation the closer the excited and ground states are (according to the so called “energy gap law”) [364–366]. The decrease in the energy gap between the excited and a ground state is, in turn, a consequence of the stronger interaction between the solvent and usually the excited state (stronger stabilization) than with the ground state. Finally, the strength of interaction between the solvent and the excited state increases (stabilization increases and energy gap decreases) the more similar they are to each other in terms of the type of interactions they can engage in.

With this in mind, the deeper analysis of the trends in the changes in energies of emission in different solvents (wavelength – orange dots on the **Figure 52**, bottom panel) reveals the existence of three distinct linear trends (unlike in the case of dioxane-water mixtures with one linear trend of decreasing the energy of emission with increasing Reichardt polarity, **Figure 52**, top panel). Interestingly, these trends are not following Reichardt polarity, but instead seem to correlate better with the ability of solvents to form hydrogen bonds. This suggests that hydrogen bonding dominates interaction between the solvent and the excited state of the fluorophore and the stronger it is, the stronger the stabilization of the excited state and the lower the intensity of fluorescence.

The results of the polarity-dependent experiments give insights into the probable mechanism of the sensitivity of **SOLpH1** fluorescence to those fluctuations. At first the probe gets excited and goes through intramolecular charge transfer (ICT), where lone electron pair from electron-donating piperazine group (the one directly connected to SBD core) travels within the  $\pi$ -conjugated system to electron-withdrawing sulfonamide group. The charge separation creates a strong dipole and the more polar the solvent is (as EtOH, MeOH or aqueous solutions), the more the solvent is able to stabilize the excited state of the probe. The more stabilized the excited state of the **SOLpH1** is, the more towards red emission shifted is its fluorescence and the lower emission (unless the low pH of a medium inhibits PeT-based quenching) [204, 367].

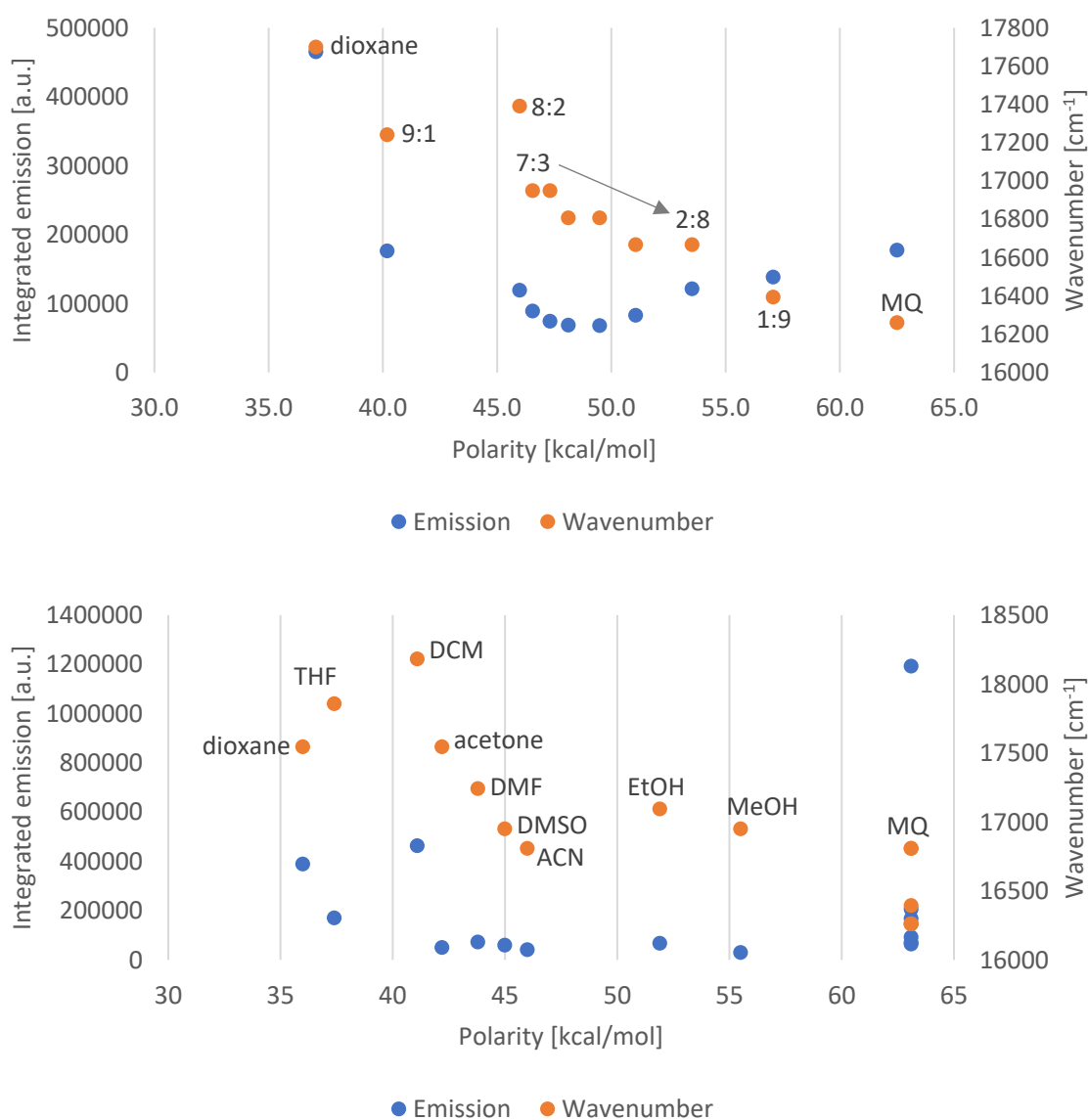


**Figure 52.** Plot representing correlation between total intensity (sum) of fluorescence emission for the probe **SOLpH1** (20  $\mu$ M) vs wavenumber and Reichardt polarity parameter: in dioxane:water mixtures (top; mixtures from 6:4 to 3:7 are omitted and represented by an arrow to increase the graph readability) and different solvents or buffers (bottom; aqueous-based solvents names are omitted to increase the graph readability). ACN – acetonitrile, MeOH – methanol, MQ – MilliQ water, EtOH – ethanol.

Additionally, the experiments with set of various solvents confirmed that the probe is soluble in both organic and inorganic media with extremely different properties, without need of use of DMSO as additive – from non-polar aprotic solvent like DCM towards polar protic solvent as water or water-based solvents (buffer solutions). This might be due to its rather amphiphilic nature thanks to the introduction of the PEG-like linker onto a less polar pH-sensitive motif. This opens possibility to use the probe **SOLpH1** in live-cell imaging experiments without need of preparation of DMSO-based stock solutions.

#### 4.1.6. Viscosity-sensing properties of SOLpH1

Sensitivity of the probe **SOLpH1** to changes in environment viscosity was examined with glycerol:water mixtures, with changing ratio of both solvents (**Figure 53**). About twelve times higher emission was observed in 9:1 mixture glycerol:water in comparison to pure water, with minimal change in the wavelength of the emission maximum (**Table 4**). The resulting plot between integrated emission for all the mixtures and viscosity values was fit to the logarithmic trendline and indicates possible logarithmic relationship between the compared variables (**Figure 54**, top). Such relationship was observed in the literature for other viscosity-sensitive probes [368, 369]. As shown in the **Figure 54**, bottom, two separate linear trends emerge when logarithms of emission intensity and viscosity are plotted against each other. At low glycerol percentage (viscosity increase between values 1-3.72 cP), the polarity-sensing properties of the probe **SOLpH1** may be dominant as reported for similar probes [212], resulting in a first visible linear trends. Once glycerol becomes a dominant solvent in a set of mixtures (over 50%), the other trend with a lower slope can be observed between logarithm of emission and logarithm of viscosity in a range of 6-219 cP. Similar behavior was observed for molecules sensitive to both polarity and viscosity changes [368, 370, 371]. The results of the polarity and viscosity experiments for the probe **SOLpH1** could suggest justification of both PeT and TICT-based mechanism of fluorescence, highly dependent on the probe's microenvironment, as it was previously described in detail in the subchapter **4.1.4**. Thus, the possible mechanism of **SOLpH1** sensitivity to viscosity changes may involve decrease in the rate of the movement (e.g. rotations) of the labile parts of the molecule (e.g. piperazine motif) in more viscous environment, as the C-N bond between aromatic and piperazine part of the probe has only a partial double bond character (subchapter **4.1.4**).

A pure glycerol was not used as a solvent due to its high viscosity, which prevented homogenous probe distribution, crucial for such experiments. The latter was confirmed experimentally (lack of reproducibility in subsequent results). Apart from the mentioned above mechanistic insights, the rotation of piperazine motif may affect the rigidity of the fluorescent scaffold and an orientation of the electron-donating aniline-like motif required for the ICT and subsequent fluorescence. Another contributor to the signal intensity might also be a lower polarity index of glycerol vs water (0.812 vs 1 [372]), which, as discussed in the subchapter **4.1.5**., correlates with the higher fluorescence intensity of probe's emission. The difference in polarity, however, is rather minor in comparison to the water vs dioxane (1 vs 0.164) to induce significant changes in the wavelength of emission maximum (color of fluorescence). The fluctuations of color did not show any clear tendency with change of glycerol:water ratio. The minor changes from 590 to 605 nm,  $420 \text{ cm}^{-1}$ , where observed fluctuations may have appeared due to 5-nm-step of analysis (affecting the error value) or change of medium polarity (glycerol vs water; more probable) (**Table 4**, 3<sup>rd</sup> and 4<sup>th</sup> column).

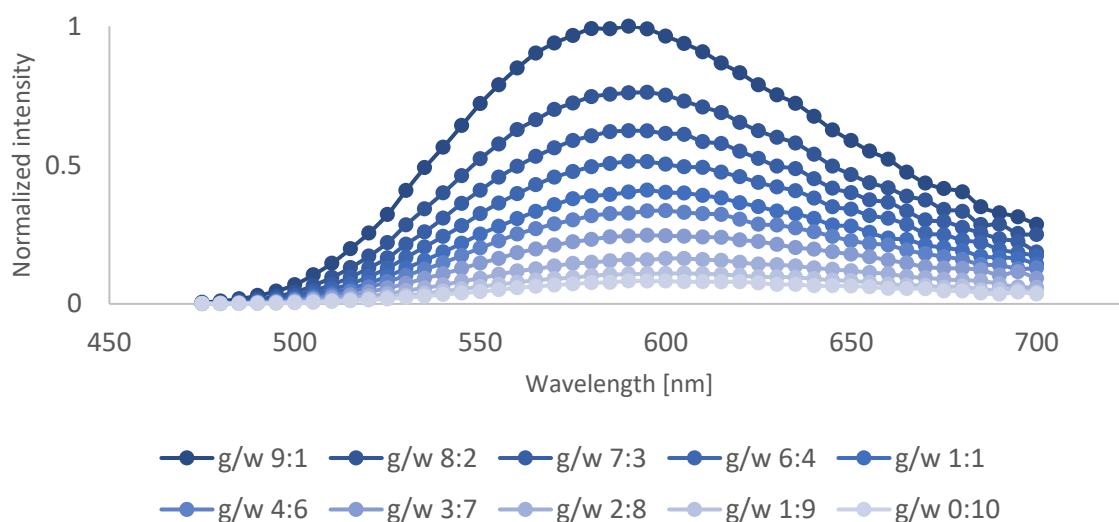


**Figure 53.** The **SOLpH1** probe presents an increase of fluorescent signal with increasing medium viscosity. Fluorescence spectra of the **SOLpH1** (20  $\mu\text{M}$ ) in glycerol:water mixtures with changing ratio,  $\lambda_{\text{exc}}=435$  nm. g – glycerol; w – water. The values were normalized to the highest value of emission in a glycerol:water 9:1 ratio mixture. The emission was measured at 5 nm steps. The final concentration of DMSO was kept at 1%. Experimental data points, averaged over 2 repeats ( $n = 2$ ) were connected with a line, which is there as a guideline for eyes to obtain a visual effect of the continuous line.

**Table 4.** The optical properties of the **SOLpH1** (20  $\mu\text{M}$ ) in various glycerol:water mixtures. The final concentration of DMSO was kept at 1%.  $\lambda_{\text{em}}$  – maximum of emission for a chosen glycerol:water mixture (in nm or  $\text{cm}^{-1}$ );  $\lambda_{\text{em-max}}$  – maximum of emission spectrum value in a chosen glycerol:water mixture; Total fl. Intensity – sum of emission given in a chosen glycerol:water mixture; Relative total fl. intensity – sum of emission given in a chosen solvent or buffer, where values were normalized to the highest value (for glycerol:water mixture 9:1). ( $n=2$ )

Glycerol % in water	Dynamic viscosity at 20°C [373] [cP=mPa·s]	$\lambda_{\text{em}}$ [nm]	$\lambda_{\text{em}}$ [ $\text{cm}^{-1}$ ]	$\lambda_{\text{em-max}}$ intensity [a.u.]	Total fl. intensity	Relative total fl. intensity
90%	219.0	590	16950	70792	1782763.5	1
80%	60.1	595	16810	53913	1366402	0.766
70%	22.5	590	16950	44125	1117834.5	0.627
60%	10.8	590	16950	36315	918215	0.515
50%	6.00	595	16810	28991.5	730424	0.410
40%	3.72	600	16670	23757.5	603280.5	0.338
30%	2.50	595	16810	17462	452007	0.254
20%	1.76	605	16530	11577	295423	0.166
10%	1.31	605	16530	7783.5	200884.5	0.113
0%	1.005	590	16950	5856.5	151299.5	0.085

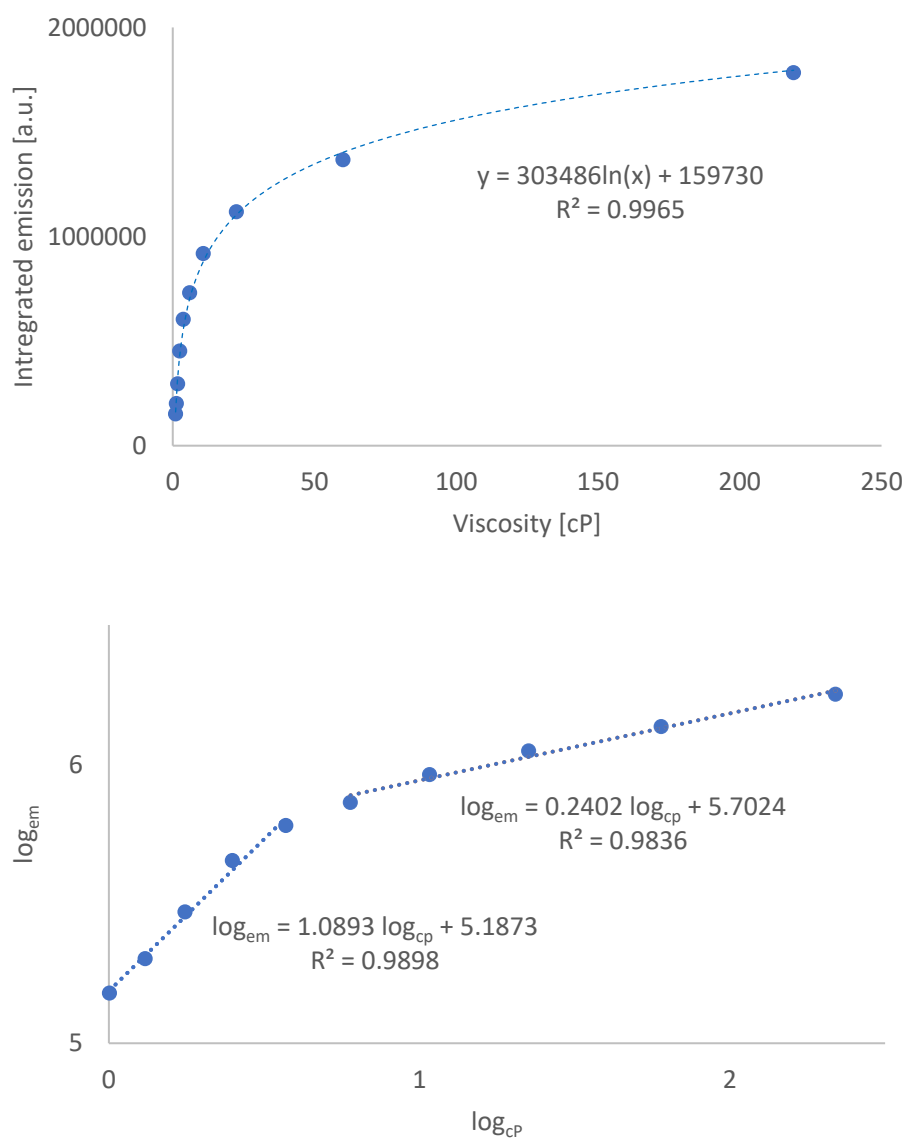


**Figure 54.** Plotting of the total intensity (sum) of the fluorescence emission of the probe **SOLpH1** (20  $\mu$ M) as a function of the viscosity parameter for glycerol:water mixtures (top) and plotting of the  $\log_{em}$  as a function of the  $\log_{cp}$  (bottom).  $\log_{em}$  – logarithm of the integrated emission of the probe **SOLpH1**;  $\log_{cp}$  – logarithm of the viscosity of glycerol:water mixtures (bottom).



#### 4.1.7. The effects of other biologically-relevant analytes

Interference of various metal ions and their salts with emission of **SOLpH1** was also investigated (**Figures 55, 56, 57**). The choice of tested interfering ions was based on the ingredients of mixtures used for all analyses (e.g. ingredients of buffers: citrate anion, phosphate anions), possible biologically-relevant analytes (composing the *in cellulo* environment, e.g. Na<sup>+</sup>, K<sup>+</sup>, Mg<sup>2+</sup>, Ca<sup>2+</sup>, Fe<sup>2+</sup>, Zn<sup>2+</sup>) as well as possible toxic metal ions (e.g. Cd<sup>2+</sup> or Pb<sup>2+</sup> which can enter biological systems and/or analytic solutions from exposure to commercial additives to plastic consumables and possible contaminants [374, 375]). The analytes were tested at two different concentrations (100 times and 10 times higher concentration than the **SOLpH1**). The choice of two ratios could provide an additional perspective to influence of individual ions or compounds on the observed fluorescent signal. Careful examination of interferent effect is important for reliable interpretation of observed fluorescent responses in all of the performed experiments and inform data analysis in the future.

HEPES buffer pH=7.5 or Milli-Q water were used to prepare all aqueous solutions and ACN was used to dissolve one salt, Cu(CH<sub>3</sub>CN)<sub>4</sub>BF<sub>4</sub>, a stable complex of Cu(I). HEPES buffer pH (7.5) was chosen with a value close to the average *in cellulo* one and its concentration (100 mM) to ensure its sufficient buffering capacity, even for high concentrations of ions. All salts available from commercial sources were of analytical grade. The salts most sensitive to oxidation process were weighed on the same day [Cu(CH<sub>3</sub>CN)<sub>4</sub>BF<sub>4</sub>, FeSO<sub>4</sub>, (NH<sub>4</sub>)<sub>2</sub>FeSO<sub>4</sub>], prepared (dissolved) just before measurement and measured separately from the rest of salts. The most of chosen metal salts were used in a form of highly soluble nitrates, if possible, to separate possible additional effect of anion difference between samples (to simplify the comparison). If nitrate of a chosen salt was not available, other anions were used. To better account for the effect of anions, a few salts were used with the same common cation (as in case of sodium: NaCl, Na<sub>2</sub>CO<sub>3</sub>, Na<sub>2</sub>SO<sub>4</sub>, Na<sub>3</sub>PO<sub>4</sub>, magnesium: MgCl<sub>2</sub>, Mg(NO<sub>3</sub>)<sub>2</sub> or potassium: KNO<sub>3</sub>, KI). All the experiments were conducted with settings optimal for the **SOLpH1** in a chosen solvent or buffer: i) for ACN:  $\lambda_{exc}=425$  nm and  $\lambda_{em}=565$  nm; ii) for HEPES buffer pH=7.5:  $\lambda_{exc}=430$  nm and  $\lambda_{em}=605$  nm; iii) for MiliQ water:  $\lambda_{exc}=430$  nm and  $\lambda_{em}=600$  nm. A slightly basic pH of the buffer resulted in formation of hydroxide or oxides in case of a few examples [FeCl<sub>3</sub>, FeSO<sub>4</sub>, (NH<sub>4</sub>)<sub>2</sub>Fe(SO<sub>4</sub>)<sub>2</sub>, Cu(NO<sub>3</sub>)<sub>2</sub>, Zn(NO<sub>3</sub>)<sub>2</sub>, AgNO<sub>3</sub>, Pb(NO<sub>3</sub>)<sub>2</sub>] during the preparation of samples, thus the analysis was not possible and the data could not be included in the final graph. The rest of the salts were therefore tested with use of aliquots dissolved in MiliQ water and afterward diluted with 100 mM HEPES pH=7.4.

The deeper analysis of the effects of the metal ions reveals that there was some trend in the increasing of the fluorescence of the probe in the presence of additional metal ions, but the effect was not specific to any particular metal and also of minimal to no statistical significance (**Figures 55, 56**). This suggests that the effects might be caused by generic changes in the properties of the solution in the presence of additional ions of any type (e.g. ionic strength / polarity / viscosity) rather than the specific metal-probe interactions. The results present that the probe **SOLpH1** is selective to pH changes as expected.

At higher concentrations of basic counterions like  $\text{CO}_3^{2-}$  and acids like citrate the fluorescence of the probe changes as observed also in the case of changing pH of solution and is dependent on the concentration of the added acid/base indicating that the buffering solution of HEPES is not sufficient to maintain stable pH (**Figure 55**). This result points out at the importance of the right balancing of the correct buffer composition for particular experiments and while relatively obvious and yet frequently underestimated even in bioanalytical work.

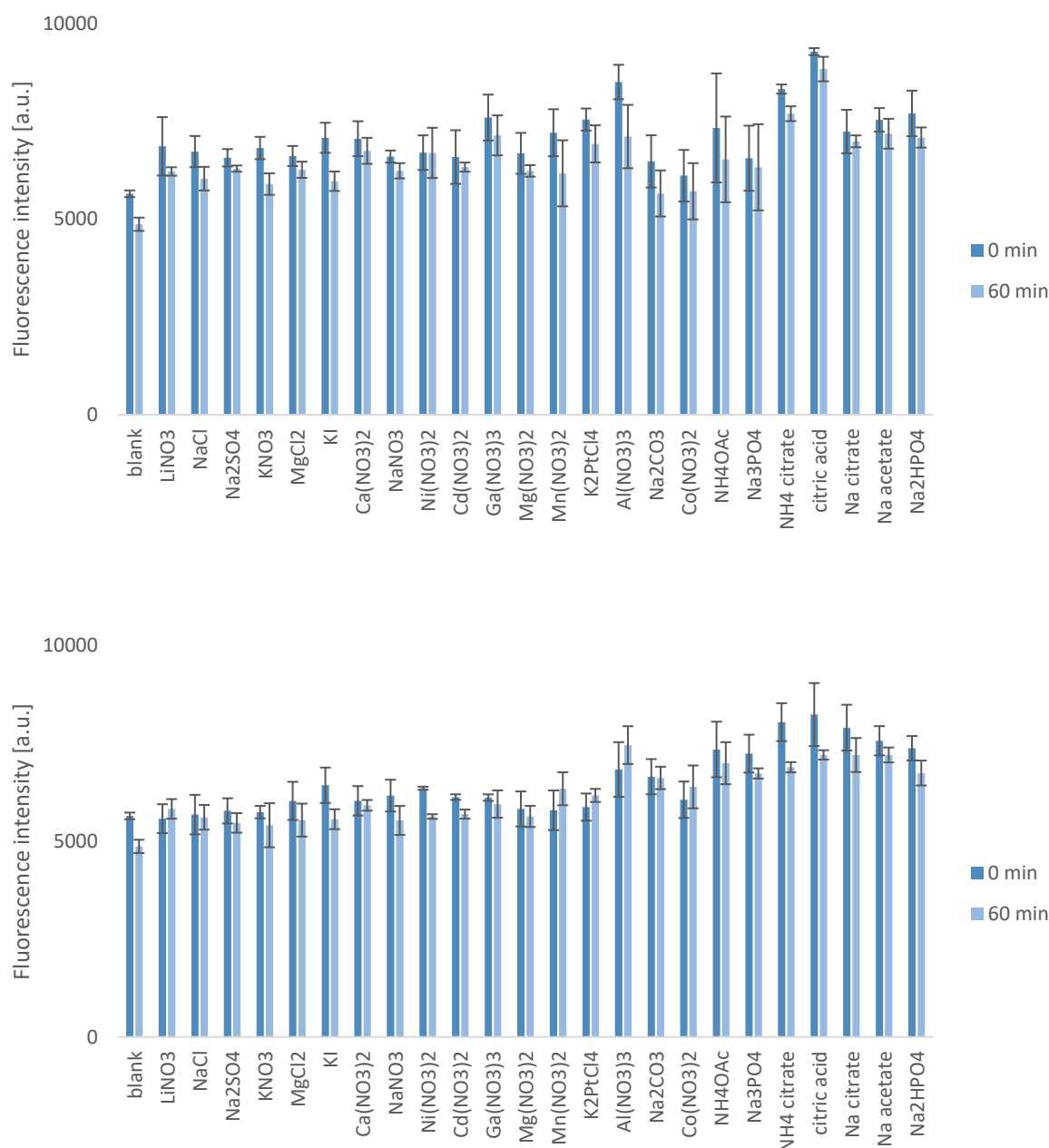


**Figure 55.** Interference tests of fluorescence intensity signal of **SOLpH1** (20  $\mu\text{M}$ ) at 605 nm with presence of different compounds ratio probe:salt 1:100 (top) and 1:10 (bottom) in 100mM HEPES pH=7.5. The final concentration of DMSO was kept at 0.5%.  $\lambda_{\text{exc}}=430$  nm,  $\lambda_{\text{em}}=605$  nm. Experimental data points were averaged over 3 repeats ( $n = 3$ ).

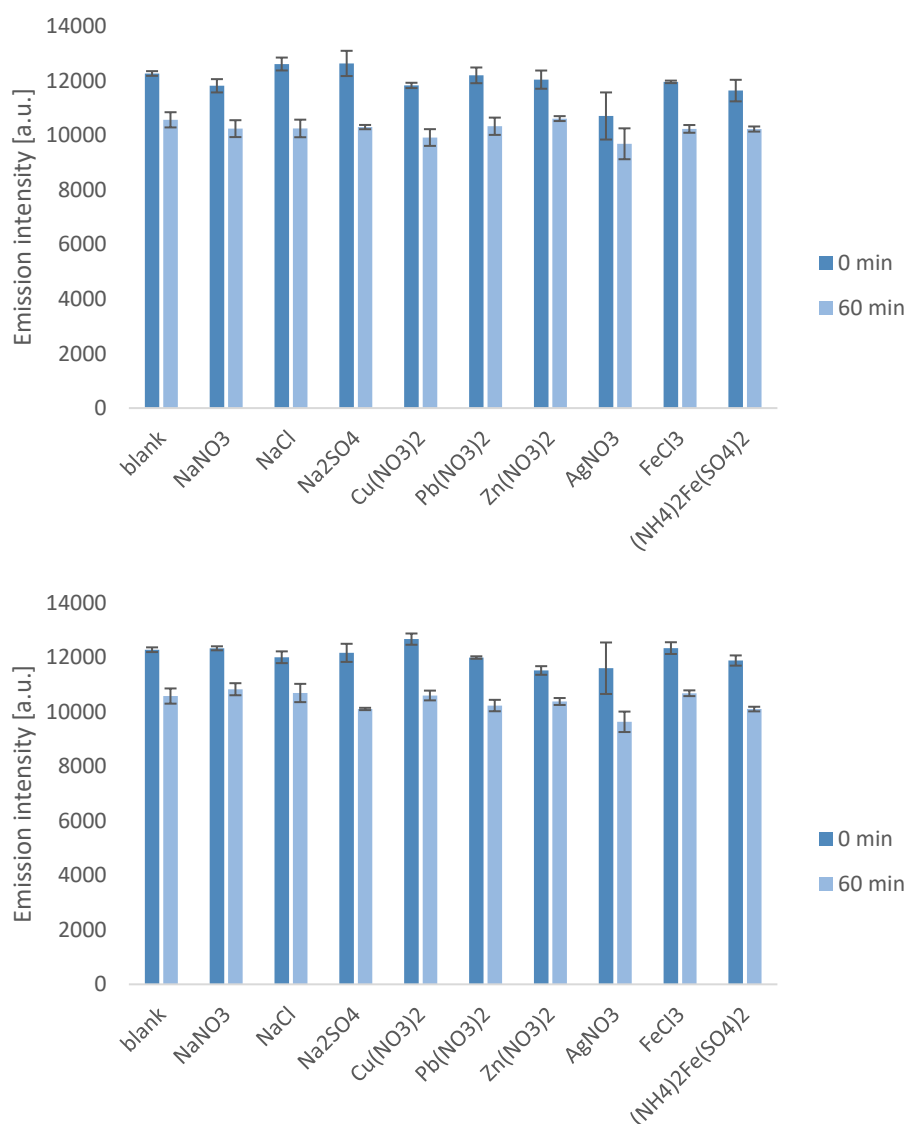


**Figure 56.** Interference tests of fluorescence intensity signal of the **SOLpH1** (20 μM) with presence of salts prepared in MiliQ aliquots 1:10 (top) and 1:1 (bottom) and diluted in 100 mM HEPES 7.4. The final concentration of DMSO was kept at 0.5%.  $\lambda_{exc}=430$  nm,  $\lambda_{em}=650$  nm. Experimental data points were averaged over 3 repeats ( $n = 3$ ).

The response of the probe **SOLpH1** to the presence of Cu(I) in ACN, in a form of a complex  $Cu(CH_3CN)_4BF_4$ , is presented in the **Figure 57**. Both in 1:10 and 1:100 of a probe:salt ratios, the emission signal significantly increases (in comparison to the blank samples). This is in line with the previous observations of pH-responsive probes that might show the binding tendency towards other cations as they do towards protons. However, since the experiments had to be conducted in ACN (to provide further stability of Cu(I)), the aprotic and relatively non-competitive nature of acetonitrile as solvent means that electrostatic interactions like the ones expected between the probe and the cation, are far stronger than they would be in a much more competitive aqueous media, let alone those with other ions in it. Therefore, even if in organic solvents Cu(I) may create stable interactions with **SOLpH1** that leads to the increase in fluorescence, none of this interaction would be expected to “survive” in the aqueous and much more competitive media of buffered solutions, let alone biological matrix.

In addition, because copper ions' estimated concentration in human cells is  $10^{-18}$ – $10^{-13}$  [376], which is billion times less than the probe's concentration used for experiments, no effects in biological systems are expected. Nevertheless, it is worth keeping in mind that the local concentration of ions (including Cu(I)) as well as the nature of the microenvironment may differ from the average values in a crowded intracellular environment with multiple processes occurring at the same.

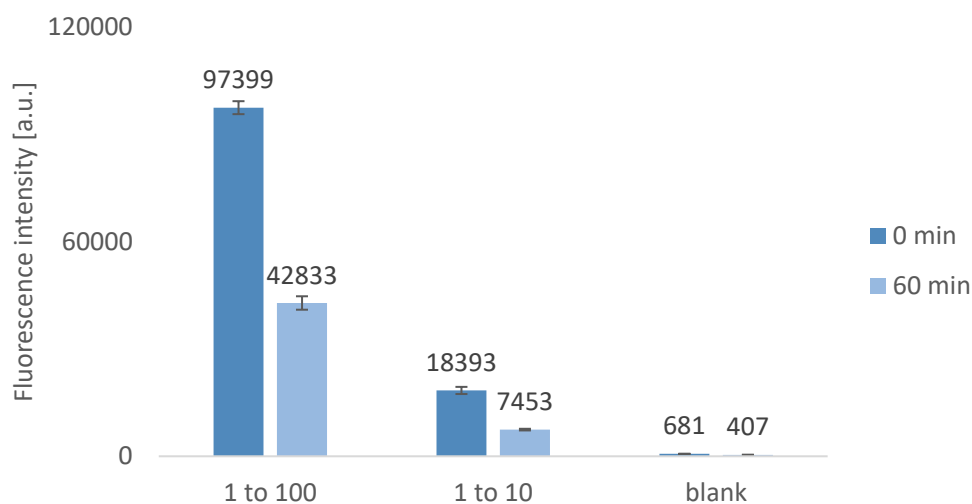


**Figure 57.** Graph presenting the response of the probe **SOLpH1** to different concentrations of Cu(I) in form of complex Cu(CH<sub>3</sub>CN)<sub>4</sub>BF<sub>4</sub> in ACN in ratio 1:10 and 1:100.  $\lambda_{exc}$ =425 nm;  $\lambda_{em}$ =565 nm. (n=3)

#### 4.1.8. Cellular localization of SOLpH1

To look into the intracellular localization of the probe **SOLpH1**, confocal imaging experiments with two cell lines were conducted. HEK293T cell line (human embryonic kidney 293T cells) line that is used in biological studies as proxy / model of a healthy line. Those cells have been purchased from commercial sources and are a variant of the HEK293 cells but transfected with a plasmid that expresses a temperature-sensitive variant of the SV40 large T antigen [377]. HEK293T cells have more advantageous growth kinetics than HEK293 cell line [377]. The cancerous cell line of choice was A549, adenocarcinomic human alveolar basal epithelial cells isolated from lung tissue that is commonly used in biological experiments around understanding of mechanisms of disease and testing therapies. It is squamous in structure and functions in the diffusion of substances across the alveoli in the lungs [378].

Before the imaging experiments, both cell lines were cultured in the supplemented high glucose version of Dulbecco's Modified Eagle's Serum (DMEM) at 37 °C, 5% CO<sub>2</sub> and passaged at least 2 times (after defrosting of cell banks) to stabilize the cell culture. Two days before the imaging experiment,  $7.5 \times 10^5$  cells/mL were evenly spread in a 35/10 mm cell culture dish with 4 compartments. Just before the imaging, the DMEM high glucose medium was discarded and the fresh medium containing **SOLpH1** (2.5 μM) or organelle tracker of choice (MitoTracker Deep Red FM at 0.1 μM or LysoTracker Deep Red at 75 nM) was added for 15 min incubation. One well per each dish was used as control one, only with DMSO added. The DMSO concentration was kept at 1%. After the incubation, cell medium was discarded, the wells washed 3 times with phosphate buffer saline (PBS) and the Fluorobrite™ DMEM high glucose was added. The latter medium is a special version of a normal DMEM medium, without an additional pH-sensor, phenol red. The Fluorobrite™ DMEM has 90% lower background fluorescence than that emitted by standard phenol red-free DMEM. Therefore, it simply lacks visual representation of pH change of solution, which is usually not needed in case of co-localization experiments and is a suitable choice for fluorescence imaging purposes.

The trackers of organelles, i.e. MitoTracker Deep Red FM (MTDR) and LysoTracker Deep Red (LTDR), were chosen from a wide array of commercially available organelle-specific cell-permeable probes. Both of them were chosen based on the optical properties, to emit in the deep red part of visible spectrum (not to overlap with emission of the probe **SOLpH1**). The first one, MTDR ( $\lambda_{exc}=644$  nm;  $\lambda_{em}=665$  nm [379]), covalently binds mitochondrial proteins by reacting with free mercaptan of cysteine residues, allowing staining of mitochondrial membrane potential independent of membrane potential [380]. LTDR on the other hand consists of a fluorophore linked to a weak base that is only partially protonated at neutral pH and typically concentrates in spherical, acidic organelles (lysosomes or late endosomes [381]). Its optical properties are similar to the MTDR, with  $\lambda_{exc}=647$  nm and  $\lambda_{em}=668$  nm.

The imaging was performed under an inverted confocal microscope. As the 405 nm laser was chosen for the imaging experiments, three different emission channels were monitored to separate the emission of naturally occurring intracellular chromophores from the emission of the **SOLpH1**. The blue channel ( $\lambda_{exc}=405$  nm and  $\lambda_{em}=430-495$  nm) accounted for largely autofluorescence of the cells, the green channel ( $\lambda_{exc}=405$  nm and  $\lambda_{em}=500-639$  nm) was aimed at collecting the bulk of the fluorescence of the probe but with potential contribution from autofluorescence and the far red channel ( $\lambda_{exc}=645$  nm and  $\lambda_{em}=655-670$  nm) was set up to fit into the optical properties of MTDR and LTDR:  $\lambda_{exc}=645$  nm and  $\lambda_{em}=655-670$  nm. The image acquisition settings were optimized by providing the excitation light from a Blue/UV diode continuous laser 50mW 405 nm with mild intensity (15-20%) during imaging for **SOLpH1**, as well as pulsed White Light Laser Excitation System (White Light Laser; 470-670 nm) during imaging for trackers used for colocalization experiments (20%). All channels are schematically presented in the **Figure 58**.

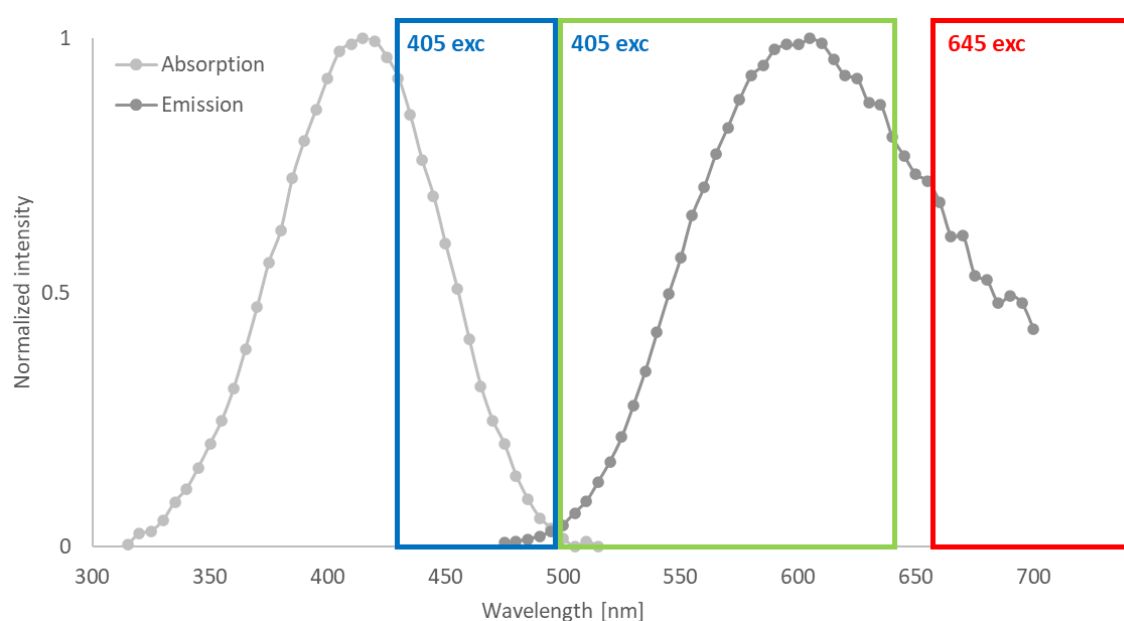


**Figure 58.** Schematic representation of excitation wavelengths and channel ranges during confocal imaging for the **SOLpH1** for cell lines HEK293T and A549. Presented absorption and emission spectra of the probes were collected in citrate phosphate buffer (CPB) buffer at pH=4.0. The values were normalized to the highest value of emission in CPB pH=5.0. The emission was measured at 5 nm steps. The final concentration of DMSO was kept at 1%. Experimental data points from the absorption and emission experiments with the probe in conditions described above were connected with a line, which is there as a guideline for eyes to obtain a visual effect of the continuous line. Color of the rectangle symbolizes the gathered emission color.

One well was imaged in 5 different fields of view (FoV) with so-called Z-scans, with 5 different steps of 1  $\mu\text{m}$  each, scanned from top to bottom of samples. The image size was set to: 246.03 x 246.03  $\mu\text{m}$ . The chosen FoVs were possibly distant from each other, to prevent accidental photobleaching of both the probe **SOLpH1** and organelle trackers. After all FoV images were ready, 3 lambda scans for each well were performed at different FoVs, with settings as for green channel ( $\lambda_{\text{exc}}=405$  nm, 10 nm width of detection band and 7.33 nm  $\lambda$ -detection stepsize). Lambda scan allows to scan samples within a chosen range, similarly to the emission spectrum performed with use of standard spectrofluorometer. However, the final result are images of the ROI every few nanometers, depending on the choice of a user. The images were processed and the colocalization analysis performed by using Fiji [336].

The emission intensity of both **SOLpH1**-incubated and control samples (DMSO, 1%, v/v) was calculated to be statistically significant (Student's *t*-test,  $p < 0.05$ ) (**Figure 59**, left). Similarly, the difference between ratios of green channel ( $\lambda_{\text{exc}}=405$  nm and  $\lambda_{\text{em}}=500-639$  nm) to blue channel ( $\lambda_{\text{exc}}=405$  nm and  $\lambda_{\text{em}}=430-495$  nm) presented statistical significance ( $p < 0.05$ ). Interestingly, the probe showed 1.4-fold higher ratio between green and blue channel in the cancerous A549 cell line, in comparison to healthy HEK293T one (**Figure 59**, right). As it was described in the subchapter **1.2.4.**, cancerous cell lines may differ in pH from healthy cells, sometimes low microenvironment pH (6.5–6.8) is considered a typical cancer hallmark of carcinogenesis [382]. Moreover, it was suggested that cancer cell line may be more viscous in comparison to non-cancerous cell line [383, 384]. Both biomarkers may have contributed to the increased signal in the A549 (cancerous) cell line and presents a perspective of possible future distinction between healthy and cancer cells.

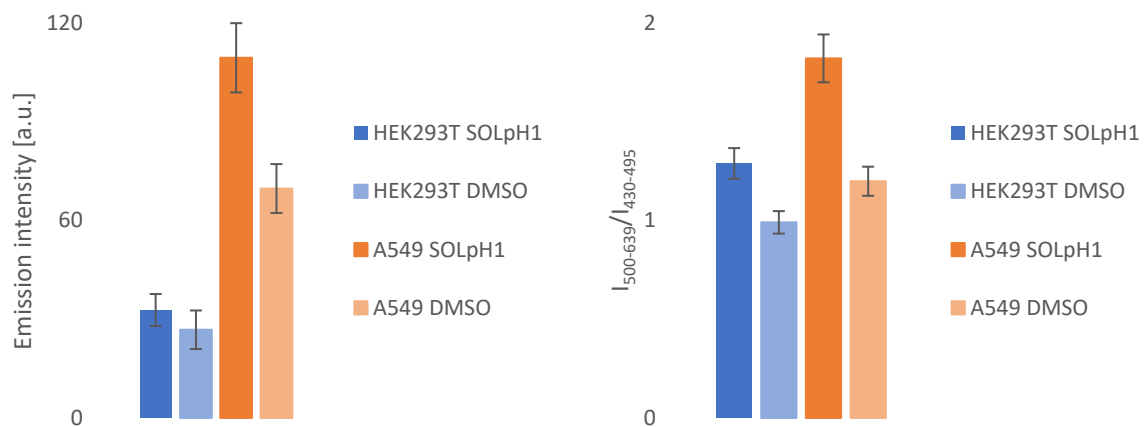


**Figure 59.** (left) Mean intensities of images from Z-scans in green channel of A549 cells incubated with **SOLpH1** (2.5  $\mu\text{M}$ ) compared with values observed for control sample (DMSO, 1%, v/v). The differences between the **SOLpH1**-incubated samples and control ones (DMSO only, 1%, v/v) is statistically significant ( $p < 0.05$ ). (right) The probe **SOLpH1** presents 1.4-fold higher ratio between the green channel (500–639 nm) to blue channel (430–495 nm) in cancerous cell line A549 in comparison to the healthy HEK293T cells. The differences between the **SOLpH1**-incubated samples and control ones (DMSO only, 1%, v/v) is statistically significant ( $p < 0.05$ ).  $\lambda_{\text{exc}}=405$  nm,  $\lambda_{\text{em}}=500-639$  nm. Error bars represent standard error of mean of 20 measurements. DMSO – 1% DMSO, v/v, control sample; SOLpH1 – sample with **SOLpH1**, 2.5  $\mu\text{M}$ .

The lambda scans gathered for HEK293T and A549 cell lines incubated with the **SOLpH1** indicate that the emission of the probe inside this cancerous cell line corresponds to the emission in dichloromethane (DCM,  $\lambda_{em-max}=550$  nm) (**Table 3**). The maximum emission value was observed to be at  $\sim 552$  nm in HEK293T and A549 cells. A preliminary additional conclusion would be to assume that an average intracellular polarity in both cell lines is around 41.1 kcal/mol, as in DCM. Interestingly, the analysis of lambda scans gathered for all samples resulted in a not expected observation of partial emission spectrum coming from both the LysoTracker Deep Red and Mito Tracker Deep Red excited at 405 nm (**Figure 60**, bottom). While available spectra provided by producers of the used trackers confirm a possibility of observation of such signals with excitation at 405 nm for the LysoTracker Deep Red, no such results are reported for the MitoTracker Deep Red.

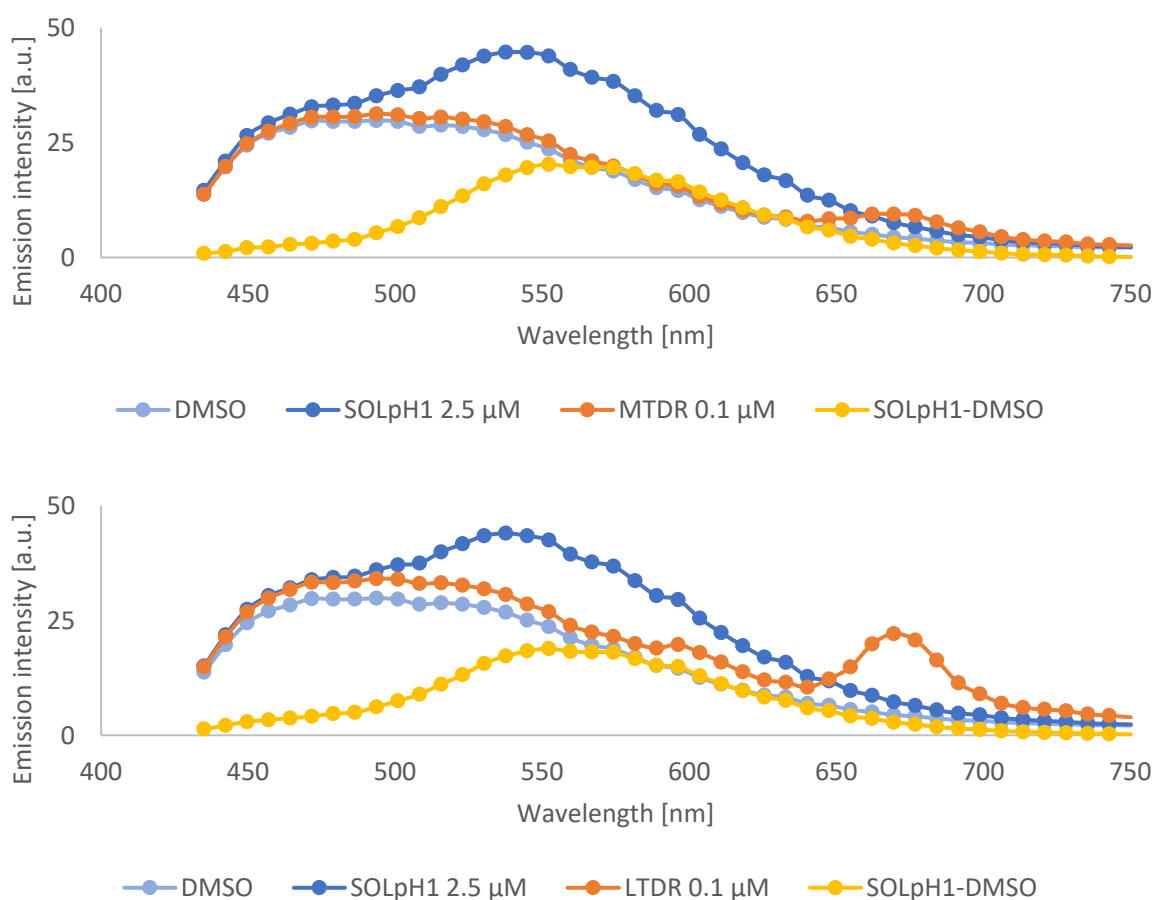


**Figure 60.** Results of lambda scans for A549 cells incubated with **SOLpH1** probe (2.5  $\mu$ M) with MitoTracker Deep Red FM (0.1  $\mu$ M) (top) and LysoTracker Deep Red (75 nM) (bottom). The emission was measured at 7.33 nm steps. The final concentration of DMSO was kept at 1%. Spectra were connected with a line, which is there as a guideline for eyes to obtain a visual effect of the continuous line.  $\lambda_{exc}=405$  nm,  $\lambda_{em}=435-750$  nm. DMSO – emission curve obtained for control samples; SOLpH-DMSO – emission curve for the probe **SOLpH1** calculated from subtraction of values gathered for DMSO (control) from values for SOLpH1 only. (n=3)



The colocalization coefficient was calculated to be 0.575 for the **SOLpH1**/MitoTracker Deep Red FM (MTDR) and 0.436 for the **SOLpH1**/LysoTracker Deep Red (LTDR) in HEK293T cells. Higher values of the coefficient were calculated for cancerous cell line A549, 0.561 for MTDR and 0.434 for LTDR (average of 20 repeats for both cell lines). Notably, the average values are comparable for both cell lines. The linear relationship between gray levels in two images (understood as intensity of emission), one channel with the **SOLpH1** intensity and the other one with the MitoTracker Deep Red FM or the LysoTracker Deep Red, suggests no clear correlation (no co-localization with lysosomes or mitochondria), with higher coverage (more than 50%) of areas, where mitochondria are located (**Figure 61, 62**). The latter is especially visible in the **Figure 62**, bottom, where the periphery of multiple cells is green-colored only, suggesting the presence of the **SOLpH1** and lack of LTDR. The results show that the **SOLpH1** is not fully transported towards lysosomes or mitochondria, even though pH-sensors may have tendency to be transported into these organelles [385]. It suggests that the probe **SOLpH1** may be used as a general pH-sensor in different compartments of cells.

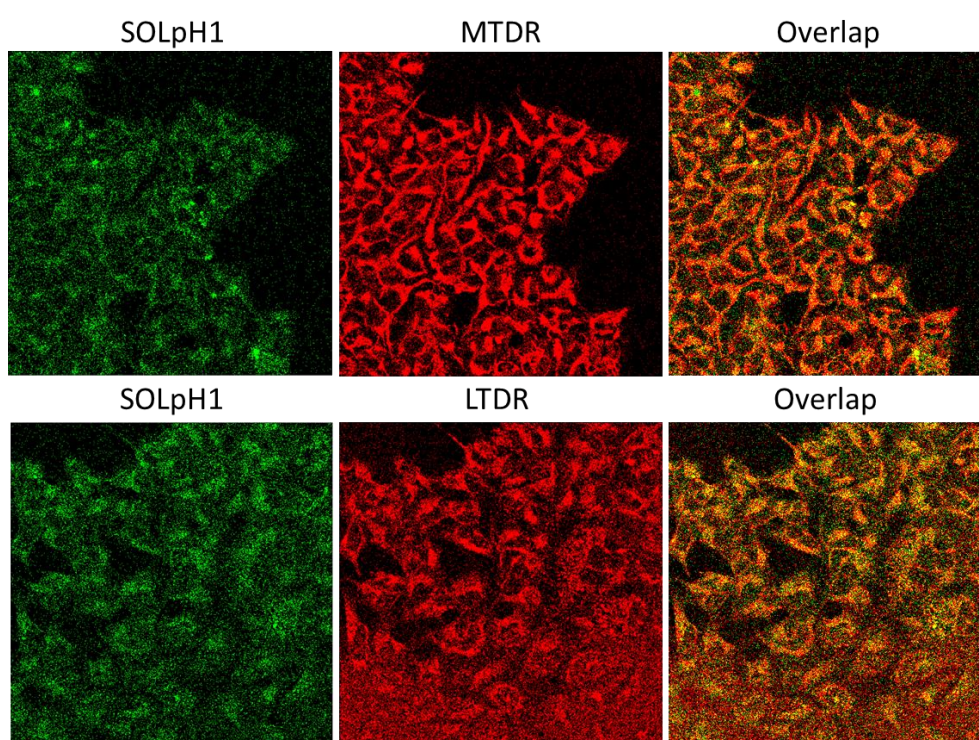


**Figure 61.** Confocal images for the: (top) **SOLpH1** 2.5  $\mu\text{M}$  /MitoTracker Deep FM 0.1  $\mu\text{M}$  (MTDR) in HEK293T cell line; (bottom) for the **SOLpH1** 2.5  $\mu\text{M}$ /LysoTracker Deep Red 75 nM (LTDR) in HEK293T cell line. Such measurement was repeated 10 times, the provided images and plots are for images with values closest to the average ones. Green channel (**SOLpH1**):  $\lambda_{\text{exc}}=405$  nm,  $\lambda_{\text{em}}=500-639$  nm; red channel (MTDR/LTDR):  $\lambda_{\text{exc}}= 645$  nm,  $\lambda_{\text{em}}=655-750$  nm. The yellow color presents an overlap between the two channels. Images size: 246.03 x 246.03  $\mu\text{m}$ .

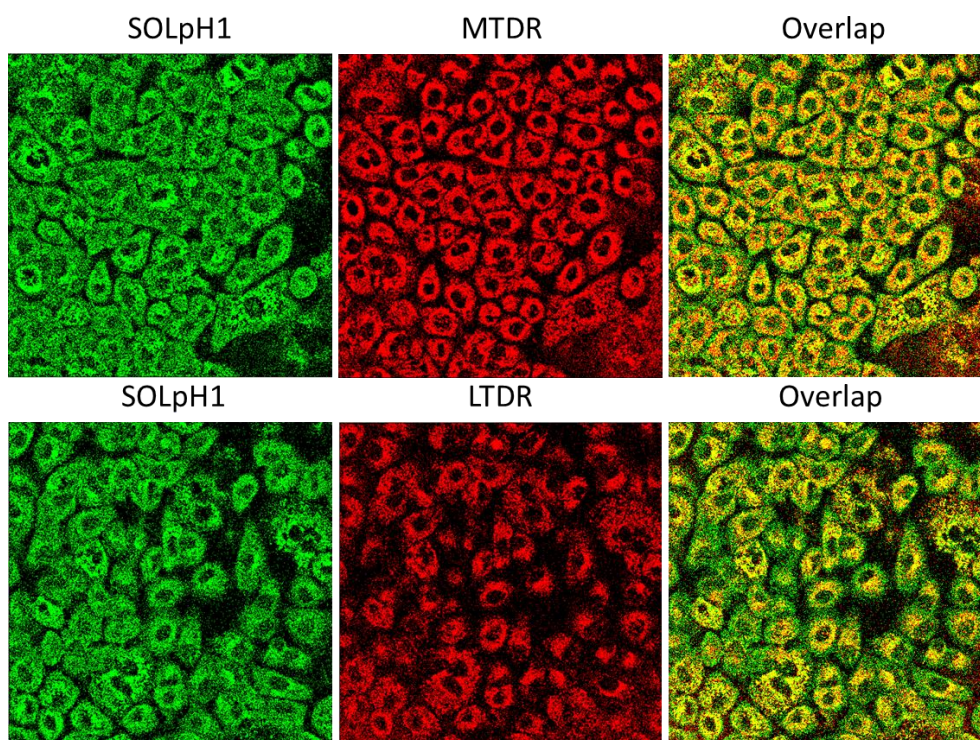


**Figure 62.** Confocal images for the: (top) **SOLpH1** 2.5  $\mu\text{M}$  /MitoTracker Deep Red 0.1  $\mu\text{M}$  (MTDR) in A549 cell line; (bottom) for the **SOLpH1** 2.5  $\mu\text{M}$ /LysoTracker Deep Red 75 nM (LTDR) in A549 cell line. Such measurement was repeated 10 times, the provided images and plots are for images with values closest to the average ones. Green channel (**SOLpH1**):  $\lambda_{\text{exc}}=405$  nm,  $\lambda_{\text{em}}=500-639$  nm; red channel (MTDR/LTDR):  $\lambda_{\text{exc}}= 645$  nm,  $\lambda_{\text{em}}=655-750$  nm. The yellow color presents an overlap between the two channels. Images size: 246.03 x 246.03  $\mu\text{m}$ .

#### 4.1.9. Intracellular pH-detection by SOLpH1

The **SOLpH1** probe was able to show intracellular pH changes inside non-cancerous (healthy) cells. The cells were cultured accordingly to the description presented in the subchapter **4.1.8**. The choice of the Britton-Robinson (B-R) buffer was based on the discussion in the subchapter **1.3.4**, about buffer working ranges (wide working range of B-R buffer). Before the imaging, human embryonic kidney 293T (HEK293T) cells were firstly incubated in cell DMEM HG medium with the **SOLpH1** (7.5  $\mu\text{M}$ ) for 15 minutes, for the probe to be transported/absorbed inside of the cells. Secondly, after triple wash with 40 mM Britton-Robinson (B-R) buffer of choice, cells were incubated for 30 minutes more with buffer only. During that time, the intracellular pH was expected to create equilibrium between inside and outside of the cells [223–225]. Afterward, imaging without change of imaging medium was conducted, inside a micro-environmental gas chamber (5%  $\text{CO}_2$ , 10%  $\text{O}_2$ ). Similarly to the co-localization tests (subchapter **4.1.8**), for each well 5 different fields of view (FoV) were analyzed with use of Z-scans and 3 different fields of view of interest with lambda scans.

Data collected from Z-scans and lambda scans was analyzed with use of Fiji [336]. From each 5 images gathered for one FoV (Z-scans) in the green channel ( $\lambda_{\text{exc}}=405 \text{ nm}$ ,  $\lambda_{\text{em}}=500\text{-}639 \text{ nm}$ ), the one with highest mean intensity was chosen (i.e. brightest plan of the cells). Then, it was analyzed with use of prepared Macro (background correction/subtraction, auto local threshold and selection of the data for final analysis) and mean intensity was again measured. All measurements from 5 Z-scans for control samples (1% DMSO, v/v) and from 10 Z-scans for **SOLpH1** (7.5  $\mu\text{M}$ ) were averaged and the results, for each pH value separately, are summarized in the **Figure 63**, left. The obtained data was analyzed with use of Student's *t*-test, for direct comparison of a statistical significance of changes between control samples for each pH (DMSO only) and experimental ones for each pH (7.5  $\mu\text{M}$  **SOLpH1**). The outcomes suggest a statistically significant difference in fluorescence intensity for cells in pH=5.0 and pH=6.0 ( $p<0.05$ ) over non-probe control, while for pH=7.5 and pH=8.0 there is lack of thereof ( $p>0.05$ ). The **SOLpH1** sensing properties are additionally presented with lambda scans curves (**Figure 64**, top) together with the spectra after subtracting a spectrum of control (DMSO, 1%, v/v) from spectrum of the given pH for samples containing the **SOLpH1** (7.5  $\mu\text{M}$ ) (**Figure 64**, bottom).

All images gathered from lambda scans were analyzed separately (change of threshold to include in intensity calculation only pixels in a RANGE from 1 to 255 /max/) and gathered to create data for each emission scan. For each pH value, the 3 curves obtained from control samples (1% DMSO, v/v) and 6 curves from **SOLpH1** (7.5  $\mu$ M) samples were averaged and the results are presented in the **Figure 63**, right. The direct comparison of data obtained for control and **SOLpH1** samples, for each pH value separately, resulted in the conclusion with agreement to the one for lambda scan analyses. A statistically significant difference is observed for pH=5.0 and pH=6.0 ( $p < 0.05$ ), whereas for the rest of pH values (7.5; 8.0) it is not a case ( $p > 0.05$ ). Importantly, intracellular spectra (lambda scans) with a probe and at pH 5.0 and 6.0 show a shift in maximum emission intensity (approx. 550 nm) in comparison to autofluorescence (i.e. with no probe in cells – emission max. at approx. 520 nm) confirming that the majority of the pH-dependent fluorescence comes from the probe.

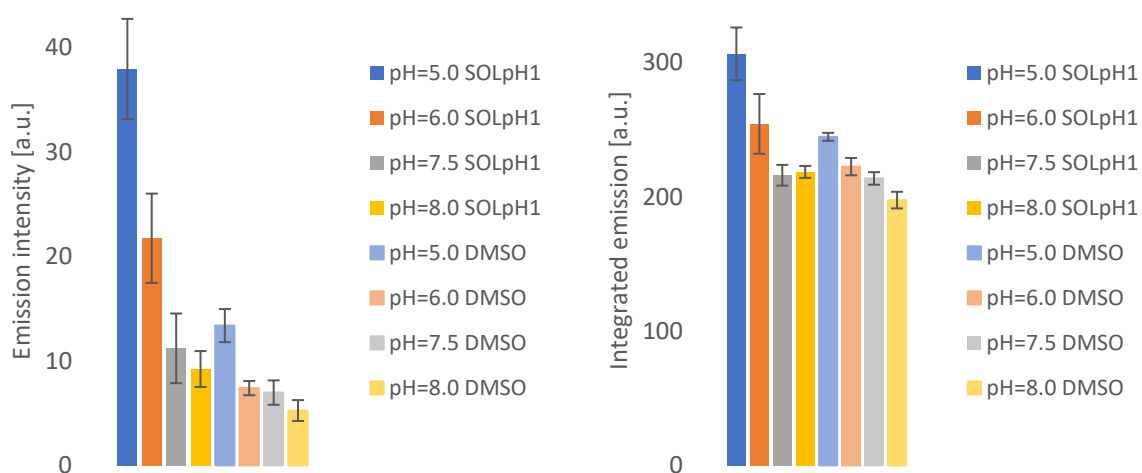
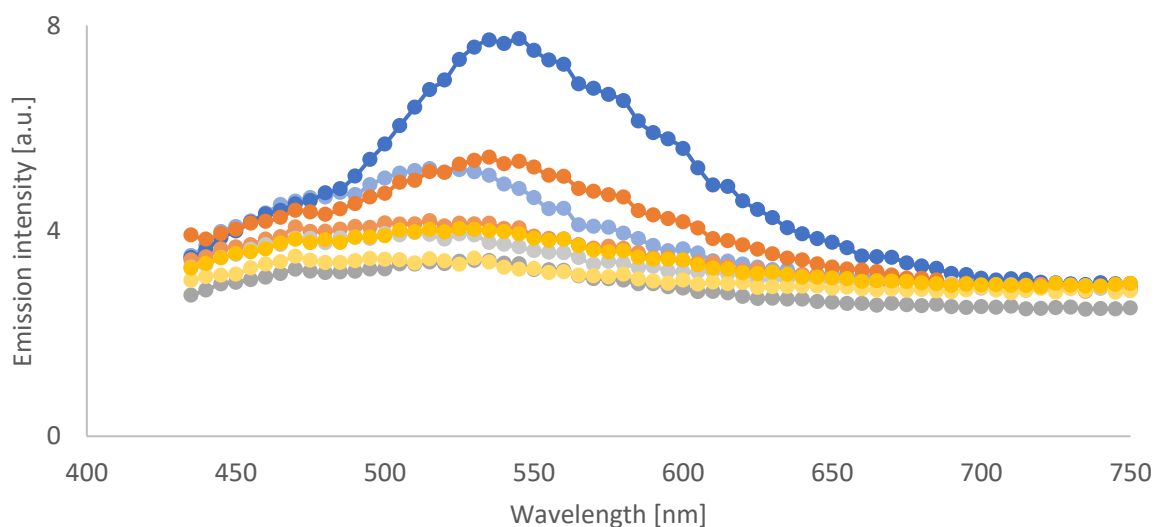
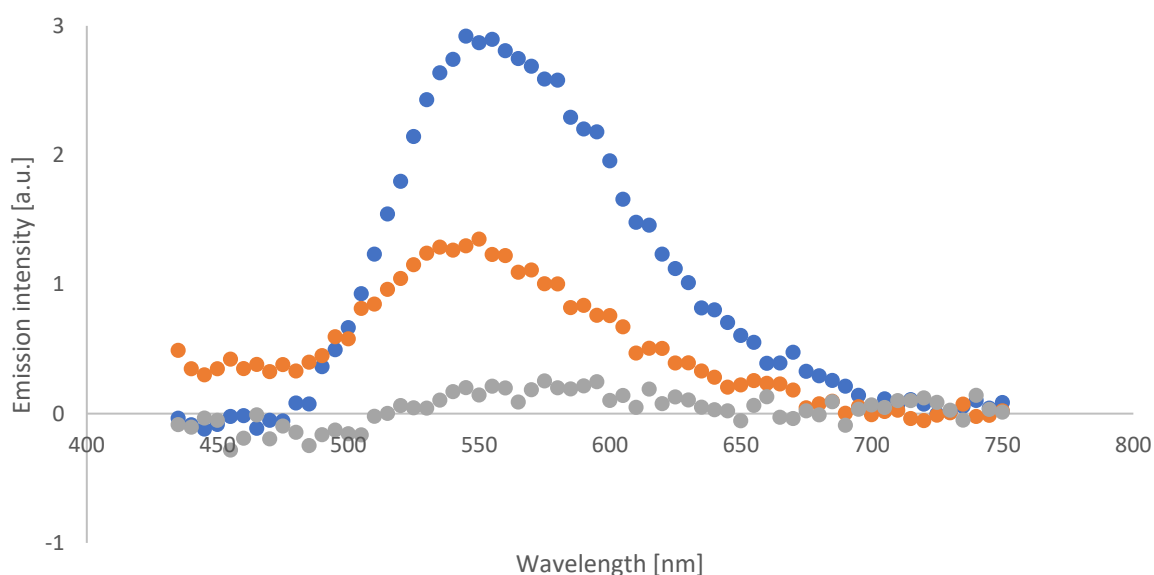


**Figure 63.** The **SOLpH1** probe presents the highest integrated lambda scan emission in HEK293T cells incubated for 30 min with buffer of low pH (pH=5.0, Britton-Robinson buffer 40 mM). Increase of pH causes a decrease in a fluorescent response of the probe. (left) Mean intensities of images from Z-scans in green channel of HEK293T cells incubated in Britton-Robinson 40 mM buffers of different pH values (5.0, 6.0, 7.5, 8.0) for **SOLpH1** (7.5  $\mu$ M) compared with values observed for control sample (DMSO, 1%, v/v). (right) Mean integrated emission intensities gathered from lambda scans in green channel of HEK293T cells incubated in Britton-Robinson 40 mM buffers of different pH values (5.0, 6.0, 7.5, 8.0) for **SOLpH1** (7.5  $\mu$ M) compared with values observed for control samples (DMSO, 1%, v/v). B-R – Britton-Robinson 40 mM buffer of chosen pH; DMSO – 1% DMSO, v/v, control sample; SOLpH1 – sample with **SOLpH1**, 7.5  $\mu$ M.  $\lambda_{exc}$ =405 nm,  $\lambda_{em}$ =500-639 nm (green channel). Error bars represent standard error of mean of 6 measurements (left), and 5 or 10 (right).



● DMSO pH=5.0    ● SOLpH1 pH=5.0    ● DMSO pH=6.0    ● SOLpH1 pH=6.0  
● DMSO pH=7.5    ● SOLpH1 pH=7.5    ● DMSO pH=8.0    ● SOLpH1 pH=8.0



● pH=5.0    ● pH=6.0    ● pH=7.5

**Figure 64.** (top) Lambda scans of HEK293T cells incubated with **SOLpH1** (7.5  $\mu\text{M}$ ) probe in the Britton-Robinson 40 mM buffers of different values (5.0, 6.0, 7.5, 8.0). The emission was measured at 10 nm steps. The final concentration of DMSO was kept at 1%. Experimental data points, averaged over 3 or 6 repeats, were connected with a line, which is there as a guideline for eyes to obtain a visual effect of the continuous line. (bottom) Spectra after subtracting an average spectrum of control (DMSO, 1%, v/v) from average spectrum of the given pH for samples containing the **SOLpH1** (7.5  $\mu\text{M}$ ).  $\lambda_{\text{exc}}=405$  nm,  $\lambda_{\text{em}}=435\text{-}750$  nm. DMSO – emission curve obtained for control samples (DMSO only, 1%); SOLpH1 – lambda scans for samples containing the probe **SOLpH1** (7.5  $\mu\text{M}$ ).  $\lambda_{\text{exc}}=405$  nm,  $\lambda_{\text{em}}=500\text{-}639$  nm (green channel). Images size: 246.03 x 246.03  $\mu\text{m}$ .

#### 4.1.10. Summary and discussion

The **SOLpH1** probe has its absorption and emission maximums in citrate phosphate buffer (CPB) pH=4.0 at 420/600 nm and at 435/615 nm for PB pH=8.0, with linearity in emission vs concentration in a wide range (5-50  $\mu$ M). The absorption and emission spectra are practically separate with significant Stokes shifts, which minimizes the self-quenching risk. The possibility of excitation of the probe with 488 nm laser makes it compatible with confocal imaging for biological cellular applications, markedly eliminating the risk of UV-induced phototoxicity. The wavelengths of excitation and emission of the **SOLpH1** are comparable to the values presented in the literature for similar SBD derivatives in aqueous media:  $\lambda_{exc/em}=410/585$  nm in water [252];  $\lambda_{exc/em}=451/615$  nm in a solution buffered to pH 7.0 (10 mM sodium cacodylate) and containing NaCl (100 mM) and EDTA (1.0 mM, water/ethanol 97.2:2.8) [348]. Additionally, the **SOLpH1** probe showed pH-dependent fluorescence with 14-time increase of emission between citrate phosphate buffer pH=4.0 and phosphate buffer pH=8.0. The  $pK_a$  of the probe was calculated to be around 6.4, which is within biologically relevant pH range, making it suitable for *in vitro* experiments purposes.

Further examination of **SOLpH1** probe's environment-sensitive properties revealed a significant bathochromic shift in the wavelength of the emission maximum between two most extreme solvents or solutions (DCM vs aqueous-based media 65 nm,  $1921\text{ cm}^{-1}$ ). Interestingly, the more non-polar the solvent was, the higher emission was observed. The probe **SOLpH1** response to viscosity changes was clear, the more viscous environment, the higher emission (12.5 times increase). There was no noteworthy interference of any ions in HEPES buffer pH=7.5. Finally, the probe **SOLpH1** was proved to be cell permeable (non-cancerous HEK293T and cancerous cell line A549) and colocalization experiments did not suggest any preference of the probes towards mitochondria or lysosomes, even though pH-sensing probes may present such tendency [385, 386]. Interestingly, a significant difference in signal between the cancerous cell line and healthy one was observed (suggestion of possible distinction of healthy and cancerous cell lines in the future). Furthermore, the probe **SOLpH1** was successfully validated as suitable sensor of intracellular pH-changes in the HEK293T cell line. There was a clear difference between the control cells (DMSO only, 1%, v/v) and the ones incubated with the **SOLpH1**, both in low pH 40 mM Britton-Robinson buffer (pH=5.0 and slightly lower emission for pH=6.0), while buffers of higher pH (pH=7.5 and pH=8.0) led to no statistically significant difference in the emission intensity in comparison to control.

There are only two literature examples of probes responsive to polarity and pH changes [387, 388] whereas sensitive to viscosity and pH changes are more numerous [389–394]. Nevertheless, the high response to pH changes was usually investigated with extreme pH values (1-2 or 10-12) [390–392, 394], not applicable into cellular environment, therefore the increase in the range pH=4.0-8.0 is in fact lower and presents the **SOLpH1** response to pH values as a moderate one, with favorable  $pK_a$  for cellular purposes among all the viscosity/pH and polarity/pH probes.

The probes sensitive to both polarity and viscosity changes occur in even greater number of examples in the literature [65, 249, 391, 395–399]. Considering viscosity- and polarity-sensitivity of known probes, **SOLpH1** presents medium values for polarity-

responsiveness in terms of the spectral emission wavelength shift and moderate increase of fluorescence emission with viscosity fluctuations (from water to water/glycerol 1:9; with slight change of emission intensity maximum). Notably, the lower polarity and higher viscosity (molecular crowding), the higher value of emission intensity is shown by the **SOLpH1**. Such a tendency is presented by the most of molecules sensing changes in both physicochemical parameters [247–249] and presents **SOLpH1** as a good candidate for investigation of viscosity/polarity fluctuations. The latter may come as especially attractive in case of interaction of the probe with a protein. It was previously reported for a few environment-sensitive SBD-based probes that the closer to the proteins active site (non-polar residues and more bulky nanoenvironment), the higher signal was observed [209, 277, 278, 280]. Therefore, the **SOLpH1** may be considered as an interesting candidate for covalent labeling studies of proteins.

To the best of our knowledge, there are only four [400, 401] probes sensitive to all three changes: in pH, viscosity and polarity with only one of them used in biological applications; all are based on the core of indolenine. The first three presented probes have  $pK_a$  value respectively 9.3-9.4 and 11.6-11.8, depending on the structure (working pH ranges: 10.3–12.7 and 8.3–10.5) making them incompatible with pH sensing in biologically-relevant ranges [400]. In the set of solvents [MeOH, n-butanol, ethylene glycol, glycerol, chloroform, PBS pH=7.4, complex with bovine serum albumin (BSA)] only 8-18 nm shift was observable upon change from non-polar to polar media, which is significantly smaller to the range presented by **SOLpH1**. Similarly to the probe **SOLpH1**, the absorption and emission maxima were found to be almost independent on the solvent viscosity (shift <5 nm). Even though those three indolenine derivatives present interesting properties, they were not introduced *in cellulo*, what highlights the utility of **SOLpH1**. The last example, **BSJD**, remains the only environment triple-sensing probe introduced *in cellulo* and *in vivo* [401]. While it is mainly described as a molecule sensitive to pH and polarity changes (spiropyran isomerization between open/close form, in a response to both parameter changes), its emission increases with increasing viscosity as well (80 times increase from pure water to 90% glycerol in water). Despite the favorable viscosity-sensing properties of **BSJD**, **SOLpH1** presents superior properties for polarity-based response with significantly higher sensitivity and higher signal in non-polar solvents (in contrast to **BSJD**). Therefore, **SOLpH1** still remains a single triple-sensing labeling candidate for potential fluorogenic labeling proteins.

All things considered, **SOLpH1** is:

- a first probe presenting responsiveness to all three parameters in its microenvironment: pH, viscosity and polarity, with such significant solvatochromic shift of maximum emission (in comparison to other similar molecules),
- with  $pK_a$  value in biologically relevant pH range, that was successfully introduced into non-cancerous and cancerous cell lines (the other were introduced to none or macrophage one),
- with ability to present intracellular pH-imaging in a non-cancerous cell line and
- preference towards non-polar environment, where the latter makes it an excellent candidate for protein labeling studies.

## 4.2. Multianalyte polarity/viscosity/pH probe based on naphthalimides (SOLpH2)

### 4.2.1. Design of SOLpH2

The structure of the second probe, **SOLpH2** (**Figure 65**), was based on well characterized fluorophore with a library of derivatives, 1,8-naphthalimide. 1,8-Naphthalimides are commonly used due to their biocompatibility, photostability, chemical stability, high quantum yields and large Stokes shifts [402]. Due to the structure of their core, there is a possibility of multiple different substituents on the aromatic part, giving a unique opportunity to adjust molecule's properties to one's purposes. Core of the **SOLpH2** probe (green color in the **Figure 65** with black-marked *N*-butyl linker) was previously synthesized and characterized [186]. It was proved to be sensitive to polarity changes, which resulted in substantial shift of its emission maximum in more polar solvents and made it potentially excellent for our purposes of ratiometric sensing of polarity changes. The probe **SOLpH2** is additionally equipped with a piperazine ring as a pH-sensitive moiety elongated with a short PEG linker for improved solubility in a wider range of media.

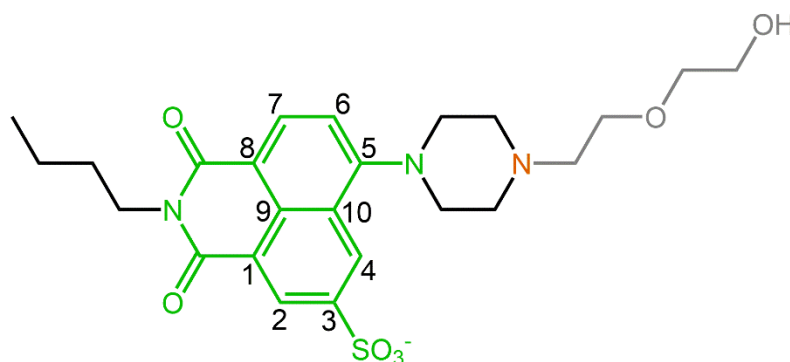


**Figure 65.** Structure of the probe **SOLpH2**. The fluorophore part is marked with green color, pH-sensor with orange and PEG linker (potential place of further derivatization) with gray one. Atoms of the naphthalimide scaffold were numbered to present multiple substitution possibilities.

In detail, substitution of the main 1,8-naphthalimide core with sulfonate group largely contributed to its polarity-sensing properties and high solubility in protic polar solvents. Moreover, such derivatization is widely used to increase solubility of various molecules in polar solvents like water (examples: [403–405]). Short glycol methylene linker plays similar role to sulfonate group in the **SOLpH2**, increasing the general solubility in a wide range of protic and aprotic polar solvents and possibly minimizing non-specific interactions with other molecules. The last part, piperazine ring, was inserted to the structure to provide the **SOLpH2** with pH-responsive property (**Figure 65**, orange-marked atom as pH-sensing part). The mechanism of its pH-responsiveness is related to the one presented for the probe **SOLpH1** and will be discussed in detail in the subchapter **4.2.4**.



#### 4.2.2. Synthesis and characterization of SOLpH2

The synthesis of the probe **SOLpH2** starts with the conversion of 1,8-naphthalic anhydride into a diimide derivative (**8**) (**Figure 66**). The mechanism includes nucleophilic attack of the lone pair from n-butylamine on the electrophilic center at carbonyl group, what results in a temporary opening of the non-aromatic ring. The other carbonyl group is attacked next in an intramolecular fashion, resulting in formation of a diimide derivative, intermediate **8**. This reaction is well known and its literature yield tends to have quite high values (68 to 95%) [406–408]. Nevertheless, possible presence of residual water in n-butylamine as well as in EtOH, which greatly absorbs water, caused the formation of a possible hydrolysis byproduct of the reaction: dicarboxylic acid (data not included), significantly decreasing the yield of the first step. This competing side reaction is rarely discussed in the literature in the context of diimide formation (example: [409]) (**Figure 67**).

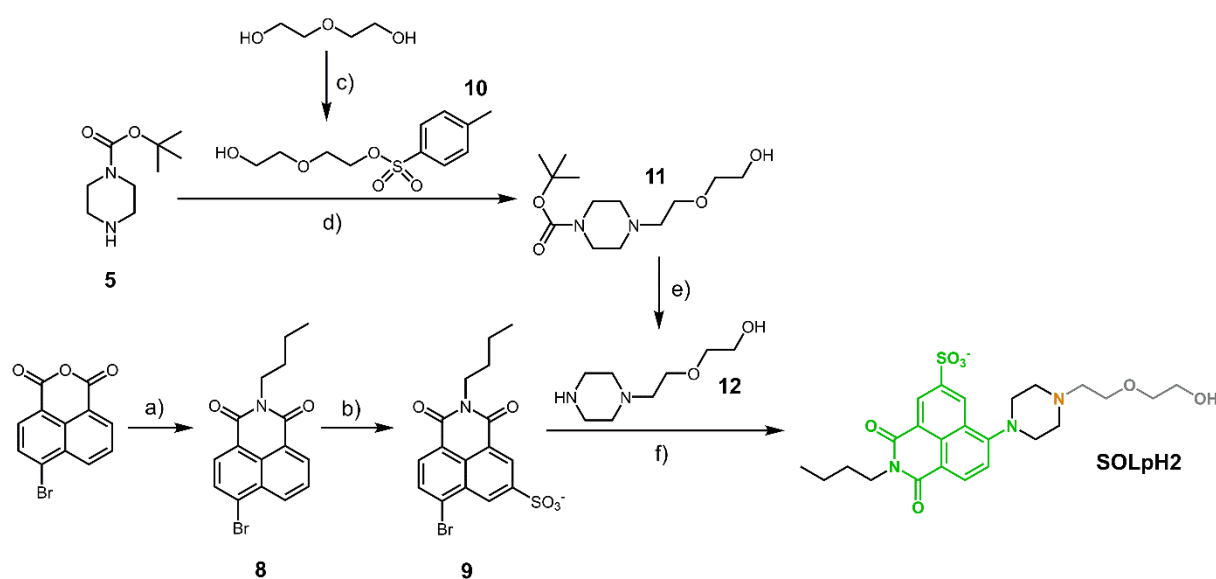


**Figure 66.** Synthetic pathway leading to the **SOLpH2** probe: a) n-butylamine, anh. EtOH, 78°C, Ar, 24 h, 23%; b) oleum, 90°C, 3 h, 65% (mixture of 2 regioisomers); c) tosyl chloride, Ag<sub>2</sub>O, KI, 3 h, 0°C, DCM, 65%; d) KI, K<sub>2</sub>CO<sub>3</sub>, ACN, 80°C, 22 h, 75%; e) TFA, DCM, RT, quant.; f) DMSO, 90°C, 24 h, 22%. The fluorophore part is marked with green color (with orange-marked nitrogen as pH-sensor) and PEG linker with gray one.

In the next step, oleum (aka. fuming sulfuric acid) was selected as a reagent for sulfonation of the aromatic ring. Both oleum ingredients, sulfuric acid and sulfur oxide (VI), are crucial for the reaction leading to *in situ* formation of sulfonium ion, which reacts with the naphthalene scaffold, resulted in the production of two regioisomers, where the desired one was marked as compound **9** (**Figure 68**). The products were readily recognized on <sup>1</sup>H NMR spectrum due to differing multiplets in downfield region of the spectra (aromatic peaks). Interestingly, different attempts of the reaction led to varying ratio of both regioisomers (from nearly 90% of the desired regioisomer with a substitution at position 6 of naphthalene scaffold to nearly 50:50 ratio of both regioisomers). Moreover, longer time of reaction than recommended in the literature [186] (3 hours) resulted in a range of by-products coming from a multiple substitution of the naphthalene part of the molecule (data not included).

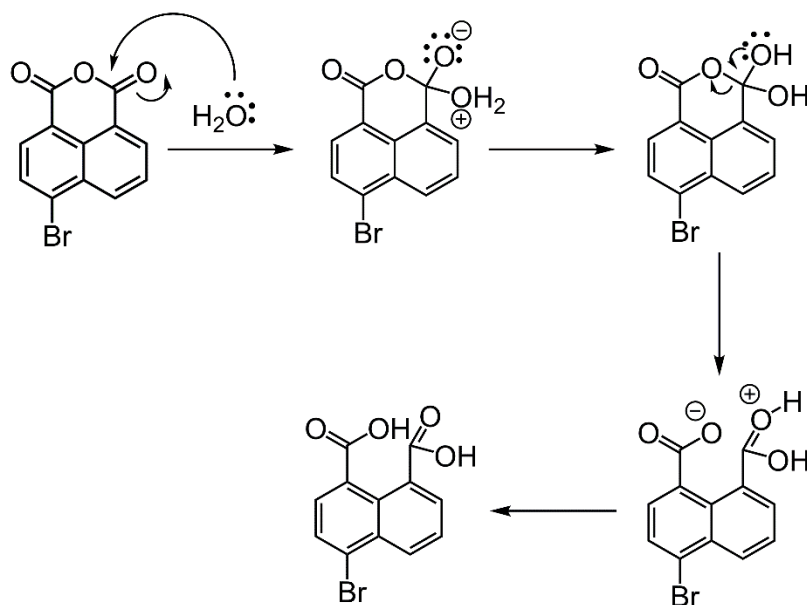


**Figure 67.** A simplified mechanism of dicarboxylic acid byproduct formation from 4-bromo-1,8-naphthalic anhydride at the first step of synthetic pathway (in presence of residual water) [409].

For the last step of the synthetic pathway (**Figure 66**), compound **12** was obtained by deprotection of compound **11**. Compound **11** was formed in a reaction between already mentioned compound **5** and compound **10**, which had to be previously derivatized in asymmetric tosylation reaction. The latter is another interesting example for mono-substitution of a symmetric molecule (as compound **5**), in this instance with use of two catalysts: silver(I) oxide and potassium iodide [410]. After both sulfonic derivatives of naphthalimides (one of them compound **9**) and compound **12** were ready to be used, the last step leading to **SOLpH2** was completed in DMSO solvent. In the literature such a direct bromine substitution with amine derivative is conducted in a range of solvents, as well as with use of different catalysts [411–413]. The most popular method for piperazine insertion is the use of 2-methoxy-ethanol as a solvent [414–416]. However, this solvent is extremely toxic, known to cause damage to the immune system, thymus or even fertility, so another reported method [329] was selected. After derivatization of compound **9**, the separation of the final product (**SOLpH2**) from the other regioisomer occurred to be time-consuming, requiring flash and preparative TLC purification steps, that despite multiple optimization attempts affected the final isolated yield of the last step of the fluorophore synthesis (22% with 3.1% final isolated yield over 3 steps). All the structures were confirmed by  $^1\text{H}$  and  $^{13}\text{C}$  NMR techniques. A novel compound, the **SOLpH2**, was additionally analyzed with HRMS, which confirmed the atomic composition of the product.

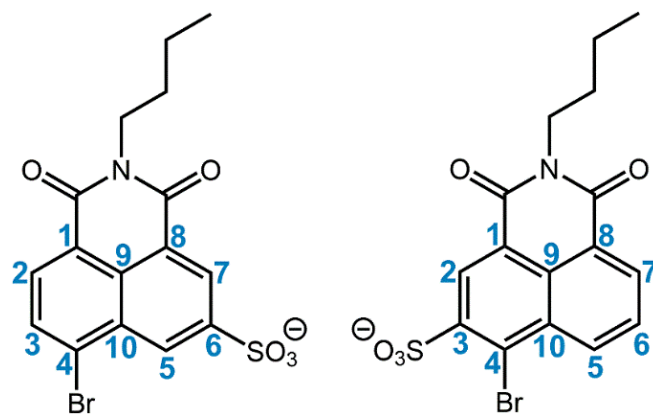


**Figure 68.** Structures of two products of the second step in the **SOLpH2** synthesis, sulfonation of intermediate **8** at position 6 to obtain compound **9** (left) and another regioisomer (right).

### 4.2.3. Optical properties of SOLpH2

The **SOLpH2** exhibits a maximum of absorption at 390 nm in CPB buffer at pH=4.0, suitable for fluorescence microscopy imaging with 405 nm excitation laser. Excitation in UV part of the electromagnetic spectrum may pose a challenge in case of live-cell applications, resulting in high background signal coming from fluorophore species naturally occurring inside cells (autofluorescence). The emission maximum of the **SOLpH2** was 550 nm in CPB buffer at pH=4.0, thus Stokes shift was estimated to be  $7459\text{ cm}^{-1}$ , promising for *in cellulo* applications by enabling separation of autofluorescence that exhibits lower Stokes shift (**Figure 69**). In contrast to the previously described **SOLpH1**, the **SOLpH2** does not present shift of emission maximum between extreme pH values tested (pH=4.0 and pH=8.0). The wavelengths of excitation and emission maxima of the **SOLpH2** are comparable to values presented in the literature for similar 1,8-naphthalimide derivatives in aqueous media [186, 417–420]. Additionally, both absorption and emission spectra are relatively narrow (in comparison to other organic fluorophores), which is a generally preferred feature for fluorescent probes (possibility of multiplexing). This and large Stokes shifts mean, the overlap of the absorption and emission spectra is minimal limiting any potential auto-excitation and/or self-quenching. The probe's fluorescence was linearly dependent on the concentration of the probe at least in the range of 5  $\mu\text{M}$  to 20  $\mu\text{M}$  (extrapolated to 0  $\mu\text{M}$  concentration) covering the range of concentrations used in all future analytical experiments (**Figure 70**).

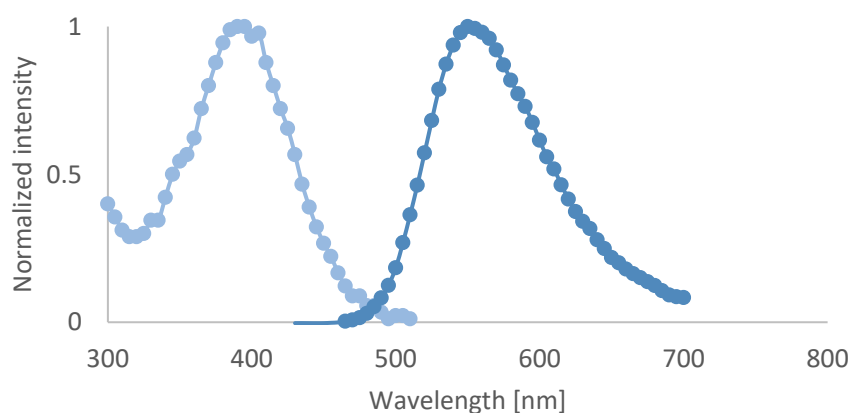


**Figure 69.** Absorption (left) and emission (right;  $\lambda_{\text{exc}}=390\text{ nm}$ ) spectra of the **SOLpH2** (20  $\mu\text{M}$ ) in CPB buffer at pH=4.0. The final concentration of DMSO was kept at 1%. Experimental data points, averaged over 3 repeats ( $n = 3$ ) were connected with a line, which is there as a guideline for eyes to obtain a visual effect of the continuous line

**Table 5.** Values of extinction coefficients, fluorescence quantum yields and brightness of standards (quinine sulphate, coumarin 343, fluorescein) and the probe **SOLpH1**. The final concentration of DMSO was kept at 1%. The experimental data was averaged over 3 repeats (n=3).

Compound	Solvent	Calculated extinction coefficient $\epsilon_\lambda$ [ $\text{cm}^{-1} \text{M}^{-1}$ ]	Calculated fluorescence quantum yield $\Phi_x$	Literature fluorescence quantum yield	Brightness $B_\lambda$
<b>Coumarin 343</b>	EtOH	$\epsilon_{405}=30600$	0.91	0.63 [335]	$B_{405}=19278$
<b>Quinine sulphate</b>	0.05 M $\text{H}_2\text{SO}_4$	$\epsilon_{350}=4400$	0.38	0.546 [334]	$B_{350}=2402.4$
		$\epsilon_{380}=900$			$B_{350}=491.4$
<b>SOLpH2</b>	CPB pH=4.0	$\epsilon_{405}=2000$	0.333	-	$B_{380}=666$
		$\epsilon_{430}=3780$			$B_{350}=1258.7$
		$\epsilon_{475}=4050$			$B_{405}=1348.7$
<b>SOLpH2</b>	PB pH=7.5	$\epsilon_{350}=1380$	0.029	-	$B_{350}=40$
		$\epsilon_{380}=2730$			$B_{380}=79$
		$\epsilon_{405}=3550$			$B_{405}=103$

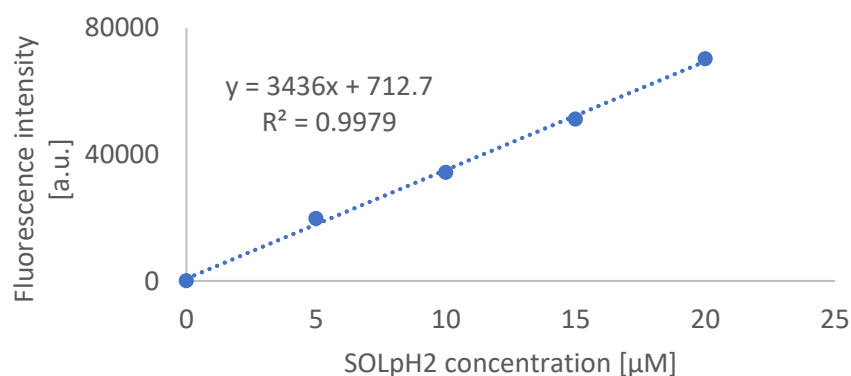


**Figure 70.** Linear plot of various **SOLpH2** concentrations fluorescence intensity at 550 nm in CPB buffer at pH=4.0,  $\lambda_{\text{exc}}=390$  nm. The emission was measured at 10 nm steps. The final concentration of DMSO was kept at 1%. The experimental data points were averaged over 3 repeats (n=3).

#### 4.2.4. Fluorescence response of SOLpH2 to pH

The pH-sensing properties of **SOLpH2** were confirmed in *in vitro* experiments with use of citrate phosphate buffer CPB and phosphate buffer PB of different pH. These studies showed increase of emission intensity with decreasing pH values (**Figure 71**). The emission difference between pH=4.0 to pH=8.0 for the probe **SOLpH2** is nearly 13 times higher for lower pH (**Figure 71**, right; direct comparison of maximum emission at 550 nm). No significant shift in the wavelength of emission maximum was observed (**Figure 106**), in contrast to the results obtained for the probe **SOLpH1** (**Figure 105**). Interestingly however, despite a lack of change in emission wavelength, such change is observed in the wavelength of the maximum of absorption ( $950\text{ cm}^{-1}$ , i.e. 390 nm in CPB pH=4.0 and 405 nm in buffers of pH=7.4-7.5). Moreover, the change of absorbance value is observed as well, with similar tendency to the emission spectra – the highest values for the lowest pH (4-6) and the lowest for the highest pH (7-8) (**Figure 108**).

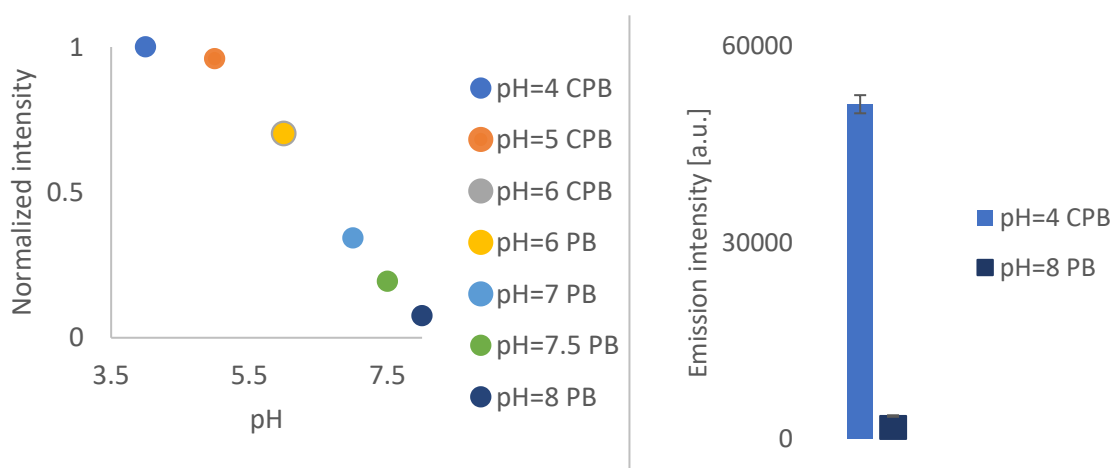


**Figure 71.** (left) The pH response curve for the **SOLpH2** (15  $\mu\text{M}$ ) of fluorescence at 550 nm,  $\lambda_{\text{exc}}=390$  nm: pH response curve. Experimental data points were averaged over 2 repeats ( $n=2$ ). (right) Direct comparison of emission intensity at 550 nm for CPB pH=4.0 and PB pH=8.0. Error bars represent standard error of mean of 2 measurements. CPB – citrate phosphate buffer; PB – phosphate buffer. The emission was measured at 5 nm steps. The final concentration of DMSO was kept at 1%. The values were normalized to the highest value of emission at 550 nm for CPB pH=4.0.

Fluorescence response of the probe **SOLpH2** to pH changes were used for calculation of  $pK_a$  of the molecule. A calculated  $pK_a$  of **SOLpH2** is  $6.5 \pm 0.1$ , which remains in biologically-relevant range and makes it suitable for intracellular purposes (**Figure 72**). The obtained value is slightly closer to the value of physiological pH than the  $pK_a=6.4 \pm 0.2$  of the probe **SOLpH1** (**Figure 49**). It is worth to keep in my mind that the intracellular  $pK_a$  value for the probe may slightly differ from the one obtained in *in vitro* experiments though [94] due to a change in the physicochemical properties of the media.

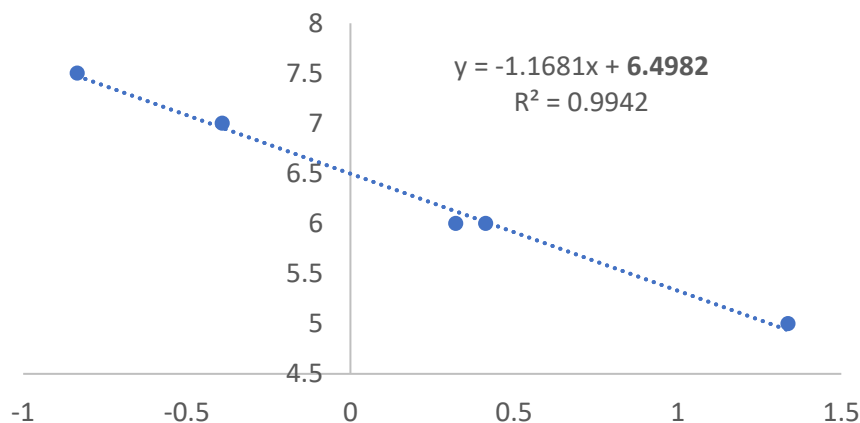


**Figure 72.** Plot of pH vs  $\log[(I_{\max}-I)/(I-I_{\min})]$ , where  $I$  is the observed fluorescence intensity of the **SOLpH2** (20  $\mu\text{M}$ ) at 550 nm,  $\lambda_{\text{exc}}=390$  nm. The y-intercept is the  $\text{pK}_a$  value ( $6.5 \pm 0.1$ ) of equilibrium between the protonated and non-protonated forms of the **SOLpH2**.

The **SOLpH2** sensitivity to environment changes is based on analogous mechanism as in case of the probe **SOLpH1**, through inhibition of PeT [353] and/or TICT [246]. In general, as shown above, once the probe gets protonated, the increase in fluorescence is observed. TICT mechanism of fluorescence in this molecule is most probably based on rotation of piperazine ring; once the molecule is excited, the gained energy is lost in the ring movements (quenching when the movement is non restricted) or emitted in a form of fluorescence (radiative relaxation pathway preferred when the movement is restricted). Upon a protonation of the piperazine's nitrogen from aliphatic amine, a boat conformation of the piperazine ring might be preferred via an intramolecular hydrogen bonding between the two nitrogen atoms of the piperazine, leading to movement restriction and increased fluorescence. An alternative (or additional) mechanism for pH sensing by **SOLpH2** can be based on PeT phenomenon. This one is presented in the **Figure 73**. Through this mechanism, a protonation of piperazine leads to a stabilization of a lone pair on the nitrogen atom (orange-marked in the **Figure 73**) by engaging it into covalent bond with proton and making it not available for photoelectron transfer and eliminating quenching (increased fluorescence). Both of the above-mentioned mechanisms could be occurring simultaneously, and while fluorescence intensity changes might point at PeT process, the shift in the wavelengths of the maximum absorption at different pH (but not emission) may suggest a change in the stable conformation of the molecule in the ground state.

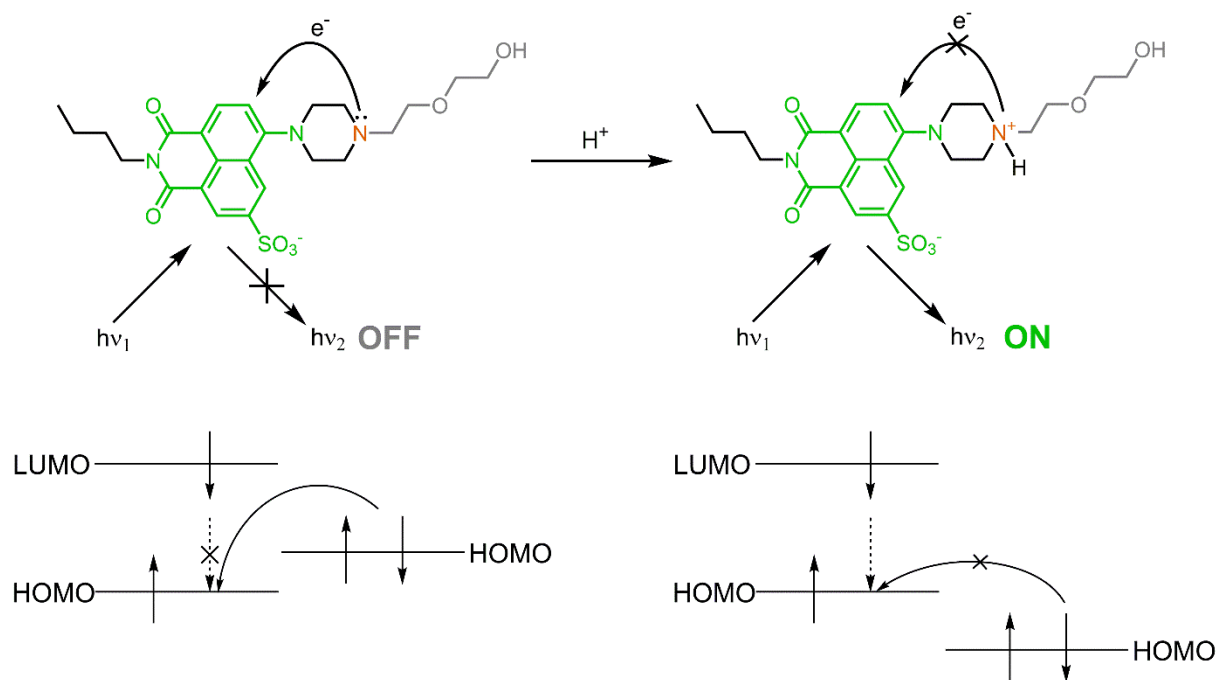


**Figure 73.** The expected PeT-based mechanism of pH sensing for the probe **SOLpH2**. HOMO – highest occupied molecular level; LUMO – lowest unoccupied molecular level;  $h\nu$  – quantum of light. The fluorophore part is marked with green color, pH-sensor with orange one and PEG linker with gray one.



#### 4.2.5. Polarity-sensing properties of SOLpH2

Polarity-sensitivity of the **SOLpH2** probe were evaluated by dissolving the probe in dioxane:water mixtures (**Figure 74**) as well as set of solvents (DCM to water-based solutions; **Figure 75**). 1049 cm<sup>-1</sup> shift of emission maximum towards red was observed between the probe's fluorescence emission maximum in pure dioxane (520 nm) and pure MiliQ water (550 nm) (**Table 6**). Interestingly, the most favorable conditions to obtain the highest fluorescence intensity are a mixture of dioxane:water with 20% of dioxane (53.5 kcal/mol for polarity value).

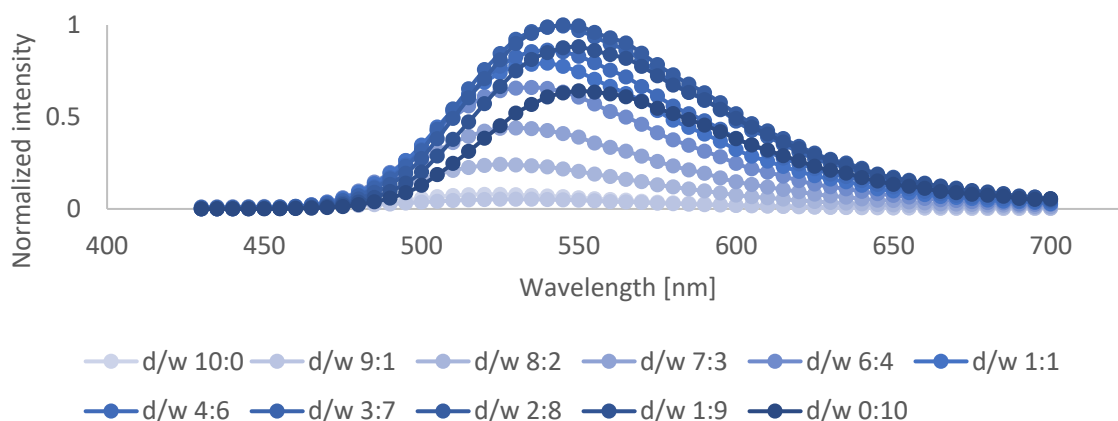


**Figure 74.** Fluorescence spectra of the **SOLpH2** (15 μM) in dioxane:water mixtures with changing ratio,  $\lambda_{exc}=390$  nm. d – dioxane; w – water. The emission was measured at 5 nm steps. The final concentration of DMSO was kept at 1%. Experimental data points, averaged over 2 repeats (n = 2) were connected with a line, which is there as a guideline for eyes to obtain a visual effect of the continuous line.

**Table 6.** The optical properties of the **SOLpH2** (15 μM) in various dioxane:water mixtures. The final concentration of DMSO was kept at 1%.  $E_T(30)$  – empirical Reichardt polarity parameter measured with an indicator B30 [360];  $\lambda_{em}$  – maximum of emission spectrum;  $\lambda_{em-max}$  intensity – fluorescence intensity of the maximum emission wavelength. Relative total fl. Intensity – sum of emission given for chosen dioxane:water mixtures, where values were normalized to the highest value (for pure dioxane). The  $E_T(30)$  value was calculated with use of two equations:  $E_T(30) = 2997.5 N_{av,x} + 2.123$  for mixtures with  $N_{av,x} < 0.015$  mol/cm<sup>3</sup> (1,4-dioxane-rich section) and  $E_T(30) = 398,8 N_{av,x} + 40.42$  for  $N_{av,x} > 0.015$  mol/cm<sup>3</sup> (water-rich section), where  $N_{av,x}$  – average molar concentration (x – water) [360]. The relative polarity  $E_T^N$  was calculated with an equation:  $E_T^N = (E_T(30) - 30.7) / 32.4$  [54]. (n=2)

Dioxane % in water	Polarity $E_T(30)$ [360] [kcal/mol]	Relative polarity $E_T^N$ [54]	$\lambda_{em}$ [nm]	$\lambda_{em}$ [cm <sup>-1</sup> ]	$\lambda_{em-max}$ intensity [a.u.]	Relative total fl. intensity
100%	37.1	0.197	520	19230	5217	0.072
90%	40.2	0.293	525	19050	3461	0.059
80%	46.0	0.472	525	19050	15997.5	0.231
70%	46.6	0.490	530	18870	28972.5	0.423
60%	47.3	0.513	535	18690	43484	0.641
50%	48.1	0.538	540	18520	52155	0.770
40%	49.5	0.580	540	18520	56789.5	0.846
30%	51.1	0.629	545	18350	65475	0.986
20%	53.5	0.705	545	18350	65874.5	1
10%	57.1	0.815	550	18180	58050	0.889
0%	62.5	0.982	550	18182	42241.5	0.659

The measurements of the spectra of 15  $\mu\text{M}$  solutions of **SOLpH2** in various solvents additionally confirmed the results observed for dioxane:water mixtures, with shift of  $1049\text{-}1236\text{ cm}^{-1}$  between the energy of emission maximum in dioxane (515-520 nm) and water-based solutions (MiliQ water and chosen buffers, 550 nm, **Figure 75**). The probe **SOLpH2** does not show any significant difference in emission wavelengths between different aqueous-based solutions (buffers), with 5 nm max difference (as in case of the **SOLpH1** probe) (**Table 7**), but their absorption maxima change with pH (see subchapter **4.2.3.**). Subsequently, highest intensity of fluorescence can in generally be observed in aqueous media, but in those, a large difference between the intensities occurs between different buffers, most probably due to an overwhelming influence of protonation/deprotonation equilibria on the emission intensity as discussed in subchapter **4.2.3.**

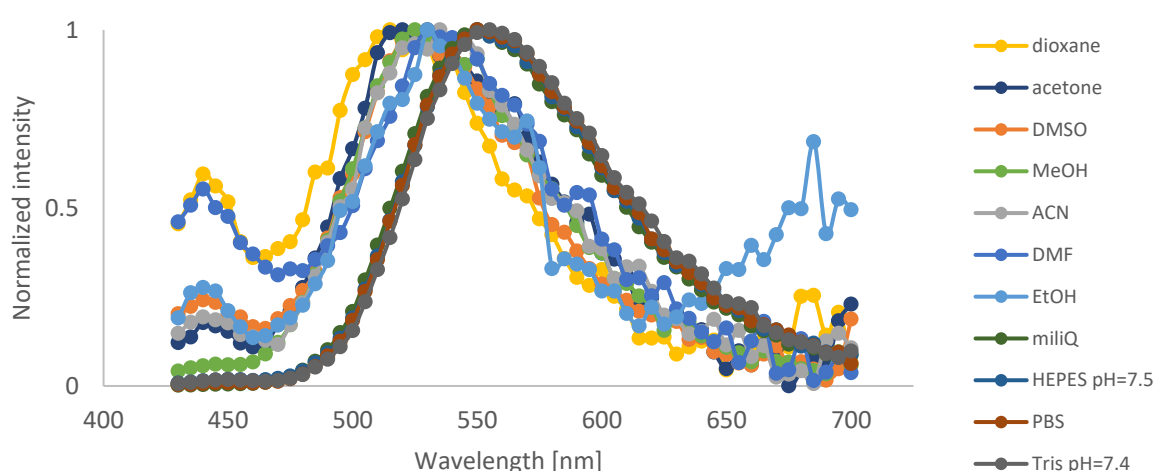


**Figure 75.** Fluorescence spectra of the **SOLpH2** (15  $\mu\text{M}$ ) in various solvents/solutions,  $\lambda_{\text{exc}}=390\text{ nm}$ . The values were normalized to the highest value of emission for dioxane at 515 nm. The emission was measured at 5 nm steps. The final concentration of DMSO was kept at 1%. Spectra were connected with a line, which is there as a guideline for eyes to obtain a visual effect of the continuous line. ( $n=2$ )

Detailed correlation of changes between the total fluorescence emission intensity to wavenumber and to Reichardt polarity parameter was presented in the **Figure 76** for dioxane:water mixtures (top) and different solvents/buffers (bottom). As it was previously mentioned in the subchapter **4.1.5.**, it was observed that behavior of dioxane:water mixture changes at  $0.015\text{ mol/cm}^3$  average molar concentration  $N_{\text{av},x}$  of water, between 70% and 80% of dioxane in water [360]. Indeed, from 80% to 20% of dioxane in water the emission gradually increases. Notably, dissolution of the **SOLpH2** in pure water provides a result similar to the 70% of dioxane in water mixture. Interestingly, **SOLpH1** discussed in subchapter **4.1.5** presented a different behavior with much less pronounced decrease in the wavenumber. More importantly, **SOLpH2** exhibited an initial logarithmic decrease in intensity of fluorescence between pure dioxane and dioxane:water 50:50 followed by modest linear increase from dioxane:water 50:50 to pure water (**Figure 51**). This behavior of **SOLpH2** of increasing emission intensity with longer wavelengths (lower wavenumbers) is relatively unique (is opposite to most other fluorophores) and might indicate change in the dominant mechanism of fluorescence upon changes in polarity.

**Table 7.** The optical properties of the **SOLpH2** (15  $\mu\text{M}$ ) in various solvents or buffers.  $E_T(30)$  – empirical Reichardt polarity parameter [362];  $E_T^N$  – relative polarity;  $\lambda_{\text{exc}}$  – maximum of excitation spectrum;  $\lambda_{\text{em}}$  – maximum of emission in a chosen solvent or buffer (in nm or  $\text{cm}^{-1}$ );  $\lambda_{\text{em-max}}$  – maximum of emission spectrum value in a chosen medium (solvent or buffer); Relative total fl. Intensity – sum of emission given for chosen solvent or buffer, where values were normalized to the highest value (for CPB pH=4.0). To simplify the analysis, the relative polarity for all aqueous-based media was decided to be 1.0 as for water. (n=2)

Solvent or buffer	Polarity $E_T(30)$ [362] [kcal/mol]	Relative polarity $E_T^N$ [357]	$\lambda_{\text{exc}}$ [nm]	$\lambda_{\text{em}}$ [nm]	$\lambda_{\text{em}}$ [ $\text{cm}^{-1}$ ]	$\lambda_{\text{em-max}}$ intensity [a.u.]	Relative total fl. intensity
Dioxane	36.0	0.164	405	515	19420	179	0.005
Acetone	42.2	0.355	415	520	19230	320.5	0.008
DMSO	45.0	0.444	415	530	18870	437	0.011
Methanol	55.5	0.762	390	525	19050	1144	0.027
Acetonitrile	46.0	0.46	410	535	18690	305	0.008
DMF	43.8	0.386	425	530	18870	298.5	0.009
Ethanol	51.9	0.654	415	530	18870	199	0.006
MiliQ water	63.1	1.0	400	550	18180	13788	0.335
HEPES pH=7.5	63.1	1.0	405	550	18180	5350	0.131
PBS pH=7.4	63.1	1.0	400	550	18180	6428	0.157
Tris pH=7.4	63.1	1.0	405	555	18180	3084	0.076
PB pH=7.5	63.1	1.0	405	550	18180	7039	0.167
CPB pH=4	63.1	1.0	390	550	18180	40873.5	1

The analyses of the **Figure 76**, bottom, additionally highlight the significance of solvent/solution polarity in emission increase of the **SOLpH2**. Interestingly, a trend of decreasing wavenumber (increasing wavelength of maximum emission) with increasing polarity is disturbed for **SOLpH2** by behavior in EtOH and MeOH. Both of those solvents exhibit higher polarity than acetonitrile, as defined by  $E_T(30)$ , but lead to shorter maximum emission wavelengths (higher wavenumbers, i.e. energy of emission). This might be attributed to a relatively less stabilizing interactions with excited state vs ground state of the **SOLpH2** by EtOH and MeOH than ACN. Indeed, a susceptibility of the **SOLpH2** to form hydrogen bonds already in the ground state (as suggested also by longer absorption wavelengths with little-to-no emission wavelength change upon protonation) might mean that EtOH and MeOH as hydrogen donors might stabilize the ground state and excited state similarly well. On the other hand, ACN as aprotic dipolar solvent might have preference for excited state interaction over ground state, effectively leading to a decrease in the gap between ground and excited state and decrease in the emission energy/wavenumber (increase in emission wavelength) in comparison to EtOH and MeOH.

Due to their contrary response to polarity of solutions, both the **SOLpH1** and the **SOLpH2** used in one sample may present mutually complementary properties. The probe **SOLpH2** showed limited solubility in less polar solvents (DCM, THF), possibly to simultaneous presence of short ethylene glycol linker and especially sulfonate group. Therefore, while solubilization in apolar solvents might require a co-solvent, it might be hoped that no DMSO as co-solvent will be needed if dissolution in water (more polar solvent) is attempted.

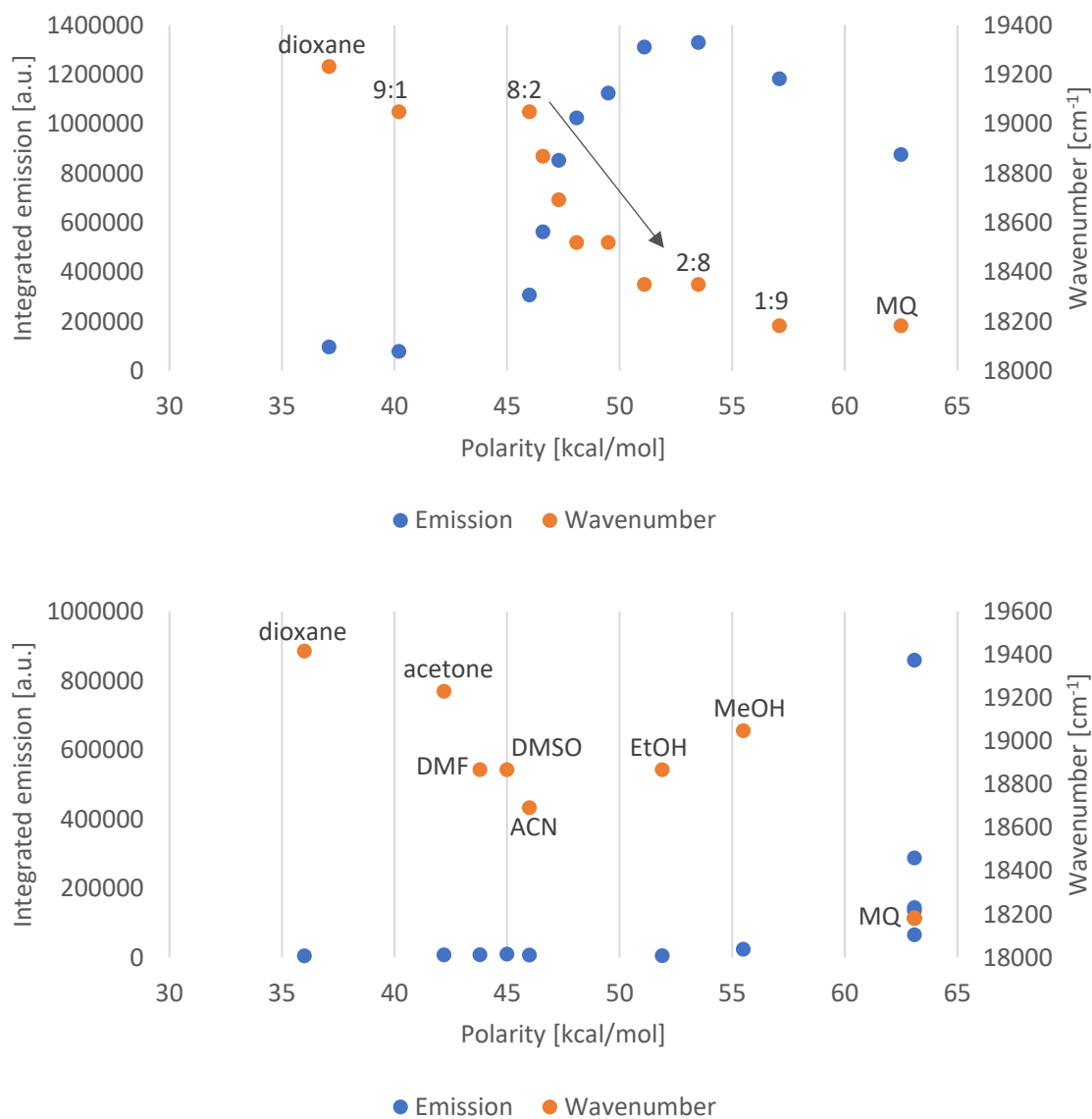


**Figure 76.** Plot representing correlation between total intensity (sum) of fluorescence emission for the probe **SOLpH2** (15  $\mu$ M) vs wavenumber and Reichardt polarity parameter: in dioxane:water mixtures (top; mixtures from 7:3 to 3:7 are omitted and represented by an arrow to increase the graph readability) and different solvents or buffers (bottom; aqueous-based solvents names are omitted to increase the graph readability). ACN – acetonitrile; MeOH – methanol; MQ – MiliQ water; EtOH – ethanol.

#### 4.2.6. Viscosity-sensing properties of SOLpH2

Sensitivity of the probe **SOLpH2** to changes in environment viscosity was examined with glycerol:water mixtures, with changing ratio of both solvents (**Figure 77**). Pure glycerol was not used as a solvent due to its high viscosity (lack of repeatability in subsequent experiments). The influence of changing viscosity on the probe emission (the dynamic range) was definitely lower than in case of the probe **SOLpH1**. There was no significant change of emission maximum observed between difference ratio of glycerol:water mixture (maximum 5 nm shift as a result of a slightly different polarity between mixtures is within the experimental error, **Table 8**). The emission intensity for glycerol:water 9:1 was 1.66 times higher than pure MiliQ water (vs >11 times for **SOLpH1**, subchapter 4.1.6.). The rest of glycerol:water mixtures gave comparable values, with glycerol:water 7:3 as the highest one (1.8 times higher than pure water). Main conclusion of the presented measurements would be that **SOLpH2** molecule behavior is significantly less affected by changes of viscosity in its surroundings than the **SOLpH1** molecules.

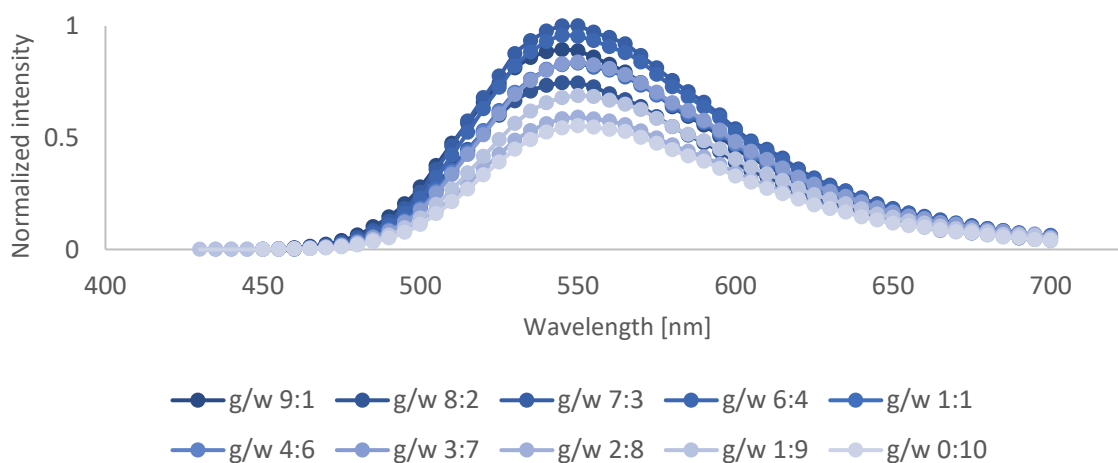


**Figure 77.** Fluorescence spectra of the **SOLpH2** (15  $\mu\text{M}$ ) in glycerol:water mixtures with changing ratio,  $\lambda_{\text{exc}}=390$  nm. g – glycerol; w – water. The values were normalized to the highest value of emission in a glycerol:water 7:3 ratio mixture. The emission was measured at 5 nm steps. The final concentration of DMSO was kept at 1%. Experimental data points, averaged over 2 repeats ( $n = 2$ ) were connected with a line, which is there as a guideline for eyes to obtain a visual effect of the continuous line.

**Table 8** summarizes values for dynamic viscosity for all mixtures glycerol:water together with optical response of the probe **SOLpH2** to viscosity changes: the maximum wavelength of emission  $\lambda_{\text{em}}$ , the intensity of fluorescence at the maximum  $\lambda_{\text{em-max}}$ , total fluorescence intensity and relative total fluorescence intensity (normalized to the highest signal for glycerol:water 7:3 ratio mixture). The plot of the integrated emission as a function of the viscosity, the **Figure 78** left part, presents pseudo-logarithmic increase of the **SOLpH2** emission with the solution viscosity between 1-22.5 cP. Once glycerol percentage exceeds 70%, a sudden decrease in emission is observed, followed by a partial increase for 9:1 glycerol:water mixture. Plotting of the same values in logarithm scale present none or only a slightly positive linear correlation (**Figure 78**, right) in contrast to the **SOLpH1** for which the correlation was much stronger and biphasic.

**Table 8.** The optical properties of the **SOLpH2** (15  $\mu\text{M}$ ) in various glycerol:water mixtures. The final concentration of DMSO was kept at 1%.  $\lambda_{\text{em}}$  – maximum of emission for a chosen glycerol:water mixture (in nm or  $\text{cm}^{-1}$ );  $\lambda_{\text{em-max}}$  – maximum of emission spectrum value in a chosen glycerol:water mixture; Total fl. Intensity – sum of emission given in a chosen glycerol:water mixture; Relative total fl. intensity – sum of emission given in a chosen solvent or buffer, where values were normalized to the highest value (for glycerol:water mixture 7:3). (n=2)

Glycerol % in water	Dynamic viscosity at 20°C [373] [cP=mPa·s]	$\lambda_{\text{em}}$ [nm]	$\lambda_{\text{em}}$ [ $\text{cm}^{-1}$ ]	$\lambda_{\text{em-max}}$ intensity [a.u.]	Total fl. intensity	Relative total fl. intensity
90%	219.0	545	18350	72188	1474237	0.894
80%	60.1	545	18350	60212	1230452.5	0.746
70%	22.5	550	18180	80764	1649685	1
60%	10.8	545	18350	77319.5	1576481.5	0.956
50%	6.00	550	18180	67272.5	1372724.5	0.832
40%	3.72	550	18180	67499	1380101	0.837
30%	2.50	550	18180	67600	1383559	0.839
20%	1.76	550	18180	47697.5	981078.5	0.595
10%	1.31	550	18180	55533.5	1148190.5	0.695
0%	1.005	550	18180	44644	925681	0.561

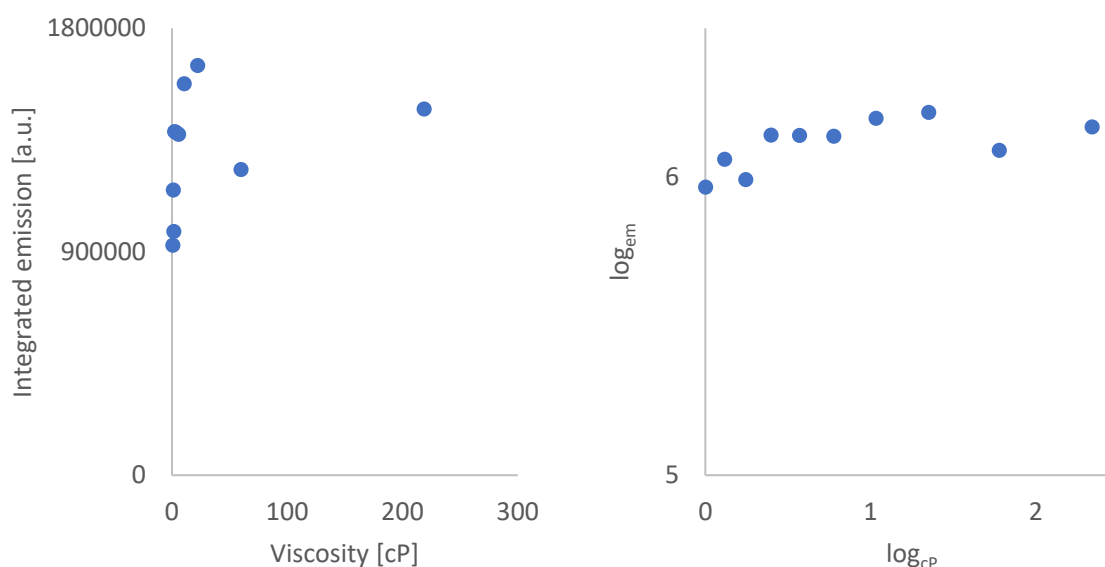


**Figure 78.** Plotting of the total intensity (sum) of the fluorescence emission of the probe **SOLpH2** (15  $\mu\text{M}$ ) as a function of the viscosity parameter for glycerol:water mixtures (top) and plotting of the  $\log_{\text{em}}$  as a function of the  $\log_{\text{cp}}$  (bottom).  $\log_{\text{em}}$  – logarithm of the integrated emission of the probe **SOLpH2**;  $\log_{\text{cp}}$  – logarithm of the viscosity of glycerol:water mixtures (bottom).

#### 4.2.7. The effects of other biologically-relevant analytes

Interference of various metal ions and their salts with emission signal of the **SOLpH2** was investigated (**Figure 79, 80, 81**) in a similar way to the investigations carried out for **SOLpH1** (subchapter 4.1.7.). The chosen interferents consisted of possible biologically relevant analytes, ingredients of buffers used for the other experiments as well as toxic interferents (additives to plastic laboratory equipment). The experiments were conducted at two different ratios the **SOLpH2**:analyte, 1 to 10 and 1 to 100. All solutions were aqueous-based, with 100 mM HEPES (**Figure 79, 80**). Additionally, to look into the interference of Cu(I), its stable complex,  $\text{Cu}(\text{CH}_3\text{CN})_4\text{BF}_4$ , was separately prepared in ACN (**Figure 81**). The salts most sensitive to oxidation process were weighed on the same day ( $\text{Cu}(\text{CH}_3\text{CN})_4\text{BF}_4$ ,  $\text{FeSO}_4$ ,  $(\text{NH}_4)_2\text{FeSO}_4$ ), prepared (dissolved) just before measurement and measured separately from the rest of salts. Whenever possible, the selected metal salts were used in the form of highly soluble nitrates to minimize any potential effects from variations in anions between samples, thereby simplifying comparisons. If the nitrate form of a particular salt was unavailable, salts with other anions were used. To further explore the impact of different anions, different salts of the same cations were tested (e.g., for sodium:  $\text{NaCl}$ ,  $\text{Na}_2\text{CO}_3$ ,  $\text{Na}_2\text{SO}_4$ ,  $\text{Na}_3\text{PO}_4$ ; for magnesium:  $\text{MgCl}_2$ ,  $\text{Mg}(\text{NO}_3)_2$ ; or for potassium:  $\text{KNO}_3$ ,  $\text{KI}$ ). For the salts presenting lower solubility in HEPES buffer ( $\text{FeCl}_3$ ,  $\text{FeSO}_4$ ,  $(\text{NH}_4)_2\text{Fe}(\text{SO}_4)_2$ ,  $\text{Cu}(\text{NO}_3)_2$ ,  $\text{Zn}(\text{NO}_3)_2$ ,  $\text{AgNO}_3$ ,  $\text{Pb}(\text{NO}_3)_2$ ), additional measurements with use of the MiliQ aliquots and further dilution with HEPES buffer was conducted (**Figure 80**). All experiments were conducted under conditions optimized for **SOLpH2** in the chosen solvent or buffer: i) for ACN:  $\lambda_{\text{exc}}=385$  nm and  $\lambda_{\text{em}}=510$  nm; ii) for HEPES buffer at pH 7.5:  $\lambda_{\text{exc}}=405$  nm and  $\lambda_{\text{em}}=550$  nm; iii) for Milli-Q water:  $\lambda_{\text{exc}}=405$  nm and  $\lambda_{\text{em}}=550$  nm.

Similarly to the **SOLpH1** response, the **SOLpH2** presents some fluctuations of the fluorescent signal in presence of different analytes, but the effect is not specific to any metal and it remains within 20% change in comparison to the control that is mostly statistically insignificant (**Figure 79, 80**). The observed subtle effects might be caused by individual changes in ion strength, polarity or viscosity, but their magnitude can be neglected in practical considerations. Therefore, it can be concluded that **SOLpH2** while presenting excellent pH-sensitivity, its fluorescence is not affected by other biologically-relevant analytes promising a reliability in pH sensing in even complex intracellular environment.

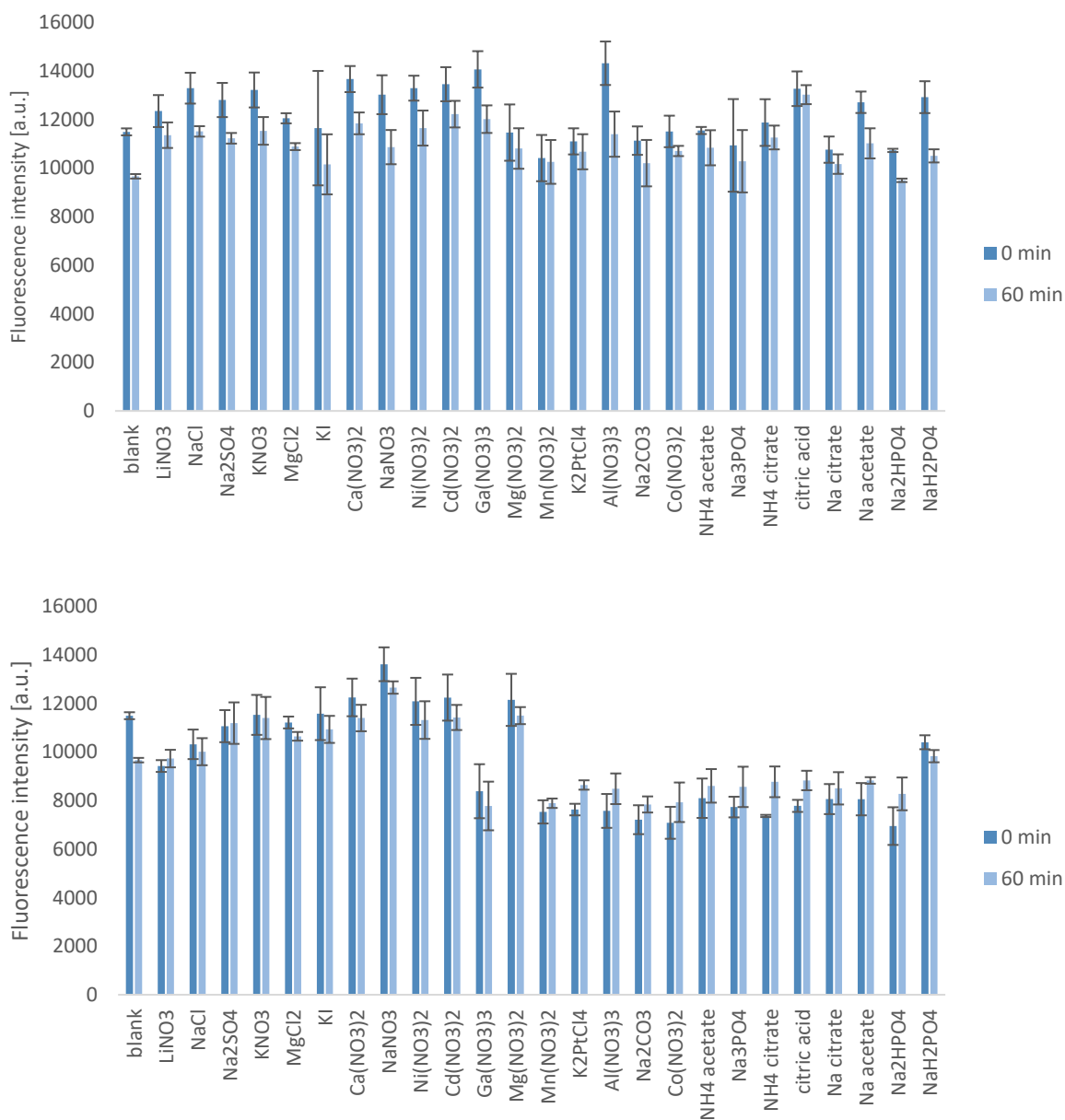


**Figure 79.** Interference tests of fluorescence intensity signal of the **SOLpH2** (15  $\mu$ M) with presence of different compounds ratio probe:salt 1:100 (top) and 1:10 (bottom) in 100mM HEPES pH=7.5. The final concentration of DMSO was kept at 0.5%.  $\lambda_{exc}$ =405 nm,  $\lambda_{em}$ =550 nm. Error bars represent standard error of mean of 3 measurements.



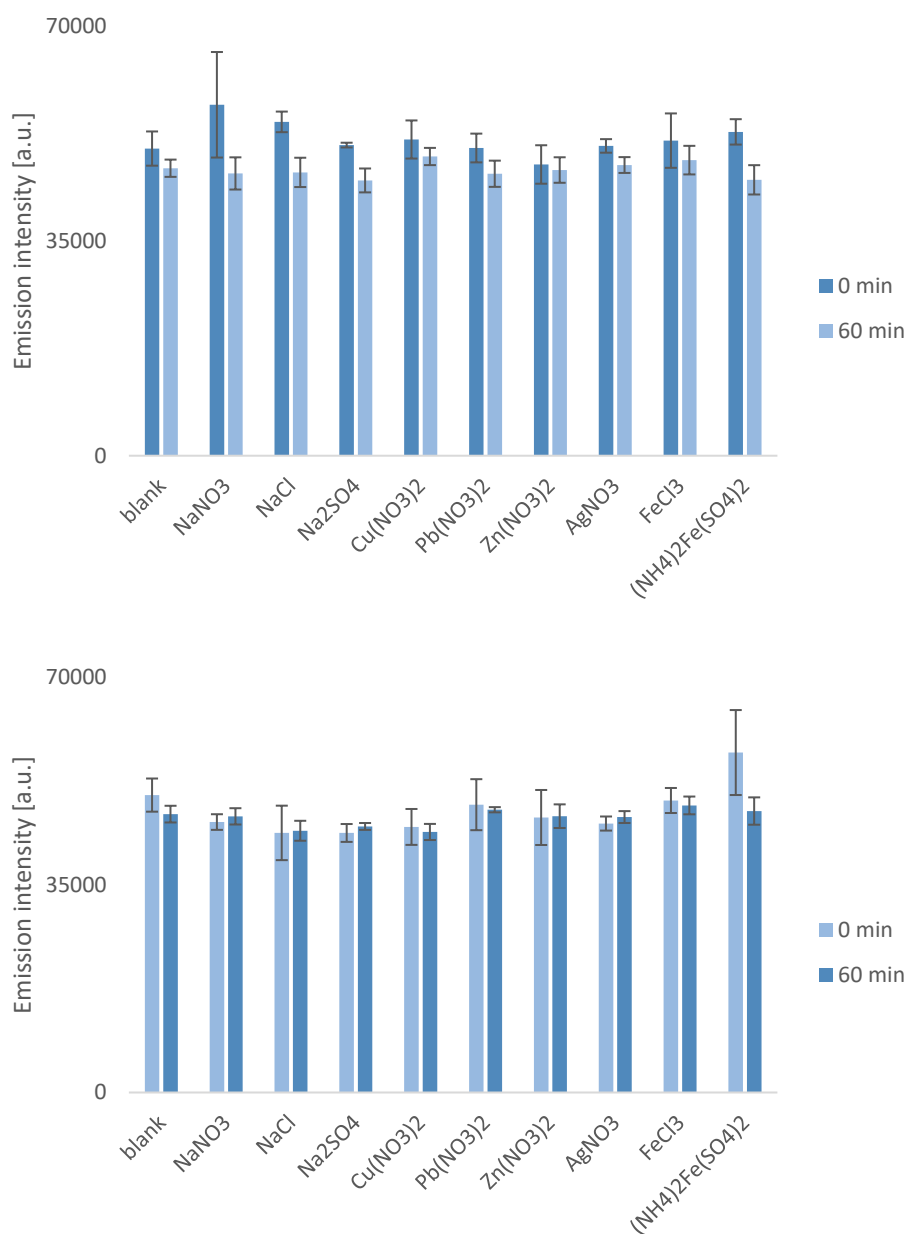


**Figure 80.** Interference tests of fluorescence intensity signal of the **SOLpH2** (15  $\mu\text{M}$ ) with presence of salts prepared in MiliQ aliquots 1:10 (top) and 1:1 (bottom) and diluted in 100 mM HEPES 7.4. The final concentration of DMSO was kept at 0.5%.  $\lambda_{\text{exc}}=405$  nm,  $\lambda_{\text{em}}=550$  nm. Error bars represent standard error of mean of 3 measurements.

The probe **SOLpH2**'s response to the presence of Cu(I) in acetonitrile (ACN), where the copper is in the form of the complex  $\text{Cu}(\text{CH}_3\text{CN})_4\text{BF}_4$ , is illustrated in the **Figure 81** and remains largely similar to **SOLpH1**. When tested with probe-to-salt ratios of 1:10 and 1:100, the emission signal shows a significant increase compared to blank samples. This behavior aligns with previous findings that pH-responsive probes may also exhibit binding tendencies towards other cations similarly to how they interact with protons. However, since these experiments were conducted in ACN to maintain the stability of Cu(I), the solvent's aprotic and relatively non-competitive nature enhances electrostatic interactions between the probe and the cation making these interactions much stronger than they would be in more competitive solvents like aqueous solutions (especially those containing multiple ions). As a result, although Cu(I)

may form stable interactions with **SOLpH2** in organic solvents, these interactions are unlikely to persist in aqueous, more competitive environments such as buffered solutions or biological matrices. Furthermore, the estimated concentration of copper ions in human cells is between  $10^{-18}$  and  $10^{-13}$  M [376], which is several orders of magnitude lower than the probe concentration used in these experiments. Consequently, no effects are anticipated in biological systems. Nevertheless, it is important to consider that local ion concentrations (including Cu(I)) and the microenvironment's characteristics may differ from average values in the crowded intracellular environment where multiple processes occur simultaneously.

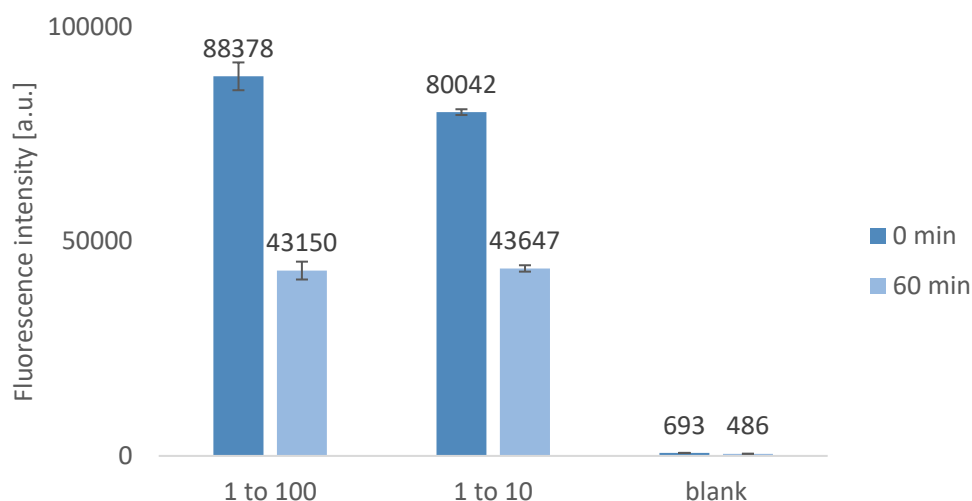


**Figure 81.** Graph presenting the response of the probe **SOLpH2** to different concentrations of Cu(I) in form of complex  $\text{Cu}(\text{CH}_3\text{CN})_4\text{BF}_4$  in ACN in ratio 1:10 and 1:100.  $\lambda_{\text{exc}}=385$  nm;  $\lambda_{\text{em}}=510$  nm. Error bars represent standard error of mean of 3 measurements.

#### 4.2.8. Cellular localization of SOLpH2

To determine if the **SOLpH2** is localized in mitochondria or lysosomes, co-localization fluorescence imaging experiments were conducted. The A549 cell line was cultured according to the description presented in the subchapter **4.1.8.** for the **SOLpH1** imaging. Just before the imaging, DMEM high glucose medium was exchanged for the one containing the **SOLpH2** probe (15  $\mu\text{M}$ ) and/or tracker of choice (MitoTracker Deep Red FM MTDR 0.1  $\mu\text{M}$  or LysoTracker Deep Red LTDR 75 nM) for 15-minute incubation. One well per each dish was used as control one, only with DMSO added (1%, v/v). The DMSO concentration was kept at 1% (v/v) for all wells. The cell medium was discarded, triple was with PBS and imaging in the Fluorobrite™ DMEM conducted. As the division for channels for the **SOLpH1** imaging was based on the ranges of typical cell autofluorescence and both probes have neighboring spectra, same settings were used for the imaging of the **SOLpH2**:

- First scan: gathering emission of the probe **SOLpH2** and partially autofluorescence (green channel,  $\lambda_{\text{exc}}=405$  nm and  $\lambda_{\text{em}}=500-639$  nm),
- Second scan: gathering emission from before the green channel (blue channel,  $\lambda_{\text{exc}}=405$  nm and  $\lambda_{\text{em}}=430-495$  nm) and
- Third scan: connected directly with optical properties of MTDR and LTDR (red channel,  $\lambda_{\text{exc}}=645$  nm and  $\lambda_{\text{em}}=655-670$  nm).

The Blue/UV diode power was kept at 15-20%, while a pulsed White Light Laser at 20% power intensity. The chosen excitation wavelengths and schematic presentation of the gathered emission ranges are presented in the **Figure 82.**

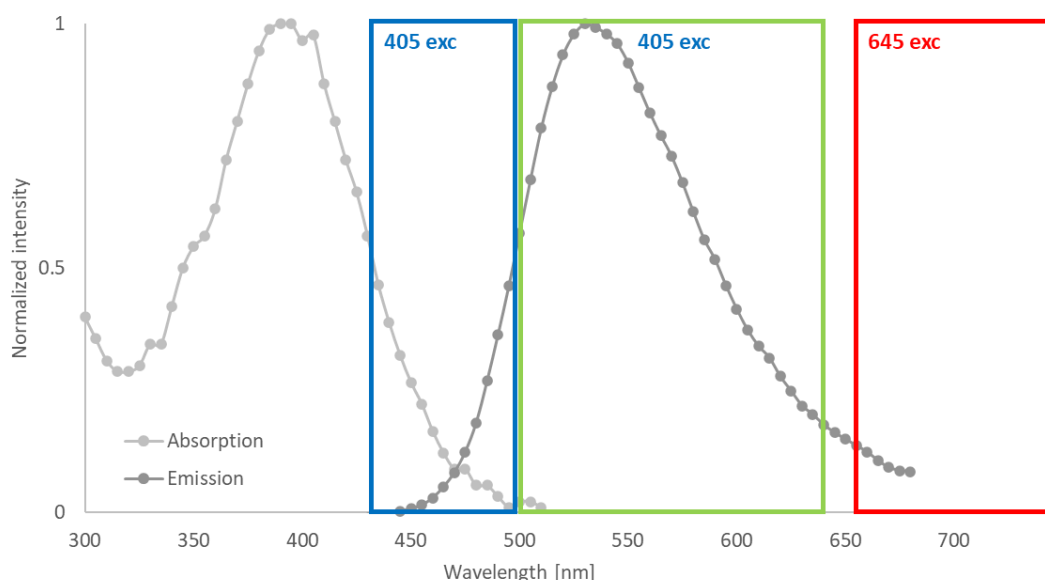


**Figure 82.** Schematic representation of excitation wavelengths and channel ranges during confocal imaging for the **SOLpH2** for cell line A549. Presented absorption and emission spectra of the probes were collected in citrate phosphate buffer (CPB) buffer at pH=4.0. The values were normalized to the highest value of emission in CPB pH=5.0. The emission was measured at 5 nm steps. The final concentration of DMSO was kept at 1%. Experimental data points, averaged over 3 repeats ( $n = 3$ ) were connected with a line, which is there as a guideline for eyes to obtain a visual effect of the continuous line. Color of the rectangle represents the gathered emission color.

Five images were taken from each well in 5 distinct fields of view (FoV) using Z-scans with 5 steps within a 1.0  $\mu\text{m}$  Z-volume and 246.03 x 246.03  $\mu\text{m}$  image size, scanning from top to bottom of the samples. After imaging all FoV, 3 lambda scans per well were performed, using green channel settings ( $\lambda_{\text{exc}}=405$  nm and  $\lambda_{\text{em}}=500-639$  nm). Lambda scans, which capture images across the emission spectrum, were conducted with a 10 nm detection bandwidth and a 7.33 nm step size. The images were processed, and colocalization analysis was conducted using Fiji [336].

Difference between average value of Z-scan for **SOLpH2**-incubated samples and control ones (DMSO only, 1%, v/v) was not statistically significant (Student's *t*-test,  $p>0.05$ ) (**Figure 83**, left). Similarly, the average values of ratio between the green channel ( $\lambda_{\text{exc}}=405$  nm and  $\lambda_{\text{em}}=500-639$  nm) and blue channel ( $\lambda_{\text{exc}}=405$  nm and  $\lambda_{\text{em}}=430-495$  nm) did not present statistically significant difference ( $p>0.05$ ) (**Figure 83**, right). Therefore, it is suspected that the probe was not absorbed by cells during the performed incubation (15 min) or is in its off-state at physiological pH value (PeT-based process).

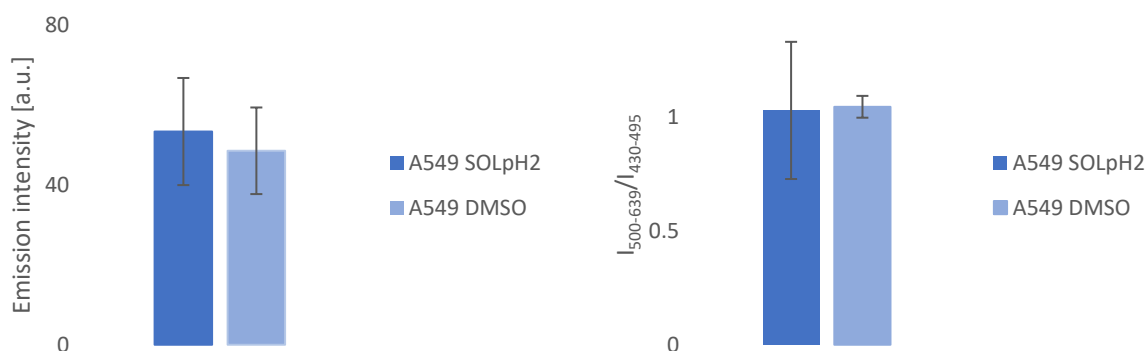


**Figure 83.** (left) The **SOLpH2**-incubated samples and control ones (DMSO only, 1%, v/v) does not present statistically significant difference ( $p>0.05$ ). (right) The **SOLpH2**-incubated samples and control ones (DMSO only, 1%, v/v) does not present statistically significant difference ratio between the green channel ( $\lambda_{\text{exc}}=405$  nm and  $\lambda_{\text{em}}=500-639$  nm) to blue channel ( $\lambda_{\text{exc}}=405$  nm and  $\lambda_{\text{em}}=430-495$  nm) in cancerous A549 cell line ( $p>0.05$ ). Error bars represent standard error of mean of 20 measurements.

The intensity of lambda scans for the **SOLpH2** samples at physiological pH was hardly perceptible, at the level of background (naturally occurring autofluorescence) or even below (**Figure 84**). While it may be suggested that the probe **SOLpH2** did not penetrate the cells and was washed out from the cell medium, its cellular membrane permeability was confirmed in the next subchapter (pH-dependent *in cellulo* experiments, subchapter 4.2.9). In conclusion, the co-localization was not determined due to the **SOLpH2** off state at physiological pH value, with lower pH value as a possibility of future co-localization experiments.

The top graph in the **Figure 84** may suggest that the difference between samples containing **SOLpH2** comes from the probe's emission; the subtraction of values gathered for the experiment samples and control ones does not confirm it, as its shape clearly corresponds to the autofluorescence coming from A549 cells. Moreover, the pH-dependent experiments in the subchapter **4.2.9.** present that the **SOLpH2** is in its turn-off state at physiological pH (7.4-7.5), thus its emission was too dim and not significantly visible without external decreasing of intracellular pH (incubation with buffer of lower than physiological pH) in the co-localization measurements. The presence of a small peak with a maximum at ~670 nm additionally confirms the conclusion from the subchapter **4.1.8.** that MitoTracker Deep Red FM emits in this region with 405 nm excitation (what is not mentioned in the product datasheet from the producer) (**Figure 84**, top).

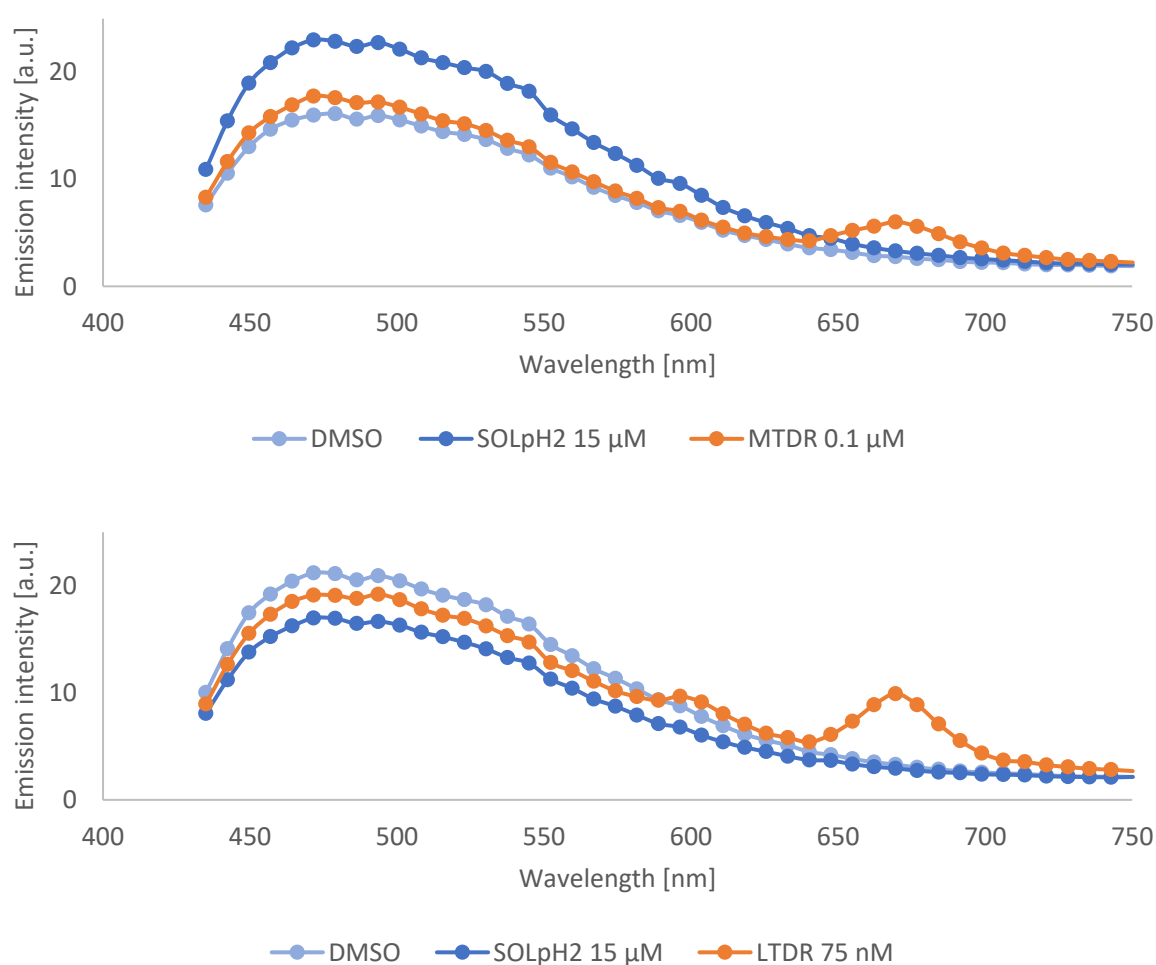


**Figure 84.** Results of lambda scans for A549 cells incubated with **SOLpH2** probe (15 μM) with MitoTracker Deep Red FM (0.1 μM) (top) and LysoTracker Deep Red (75 nM) (bottom). The emission was measured at 7.33 nm steps. The final concentration of DMSO was kept at 1%. Experimental data points, averaged over 3 repeats (n = 3) were connected with a line, which is there as a guideline for eyes to obtain a visual effect of the continuous line.  $\lambda_{exc}=405$  nm,  $\lambda_{em}=435-750$  nm. DMSO – emission curve obtained for control samples; SOLpH2-DMSO – emission curve for the probe **SOLpH2**-incubated samples calculated from subtraction of values gathered for DMSO (control) from values for **SOLpH2**-incubated only.

#### 4.2.9. Intracellular pH-detection by SOLpH2

To monitor the **SOLpH2** ability to show acidic intracellular environment in HEK293T cell line, experiments at two different pH values were conducted: 5.0 and 7.5 (40 mM Britton-Robinson buffer). The cells were cultured accordingly to the description presented in the subchapter **4.1.8**. The first step of incubation was 15 minute one with 15  $\mu\text{M}$  **SOLpH2** solution in DMEM high glucose, the medium was next discarded, cells washed 3 times with B-R buffer of chosen pH and incubated in this buffer (30 min). Five images were captured from each well across 5 distinct fields of view (FoVs) using Z-scans, each with 5 steps covering a Z-volume of 1.0  $\mu\text{m}$  and an image size of 246.03 x 246.03  $\mu\text{m}$ , scanning from the top to the bottom of the samples. Following the imaging of all FoVs, 3 lambda scans were performed per well using green channel settings ( $\lambda_{\text{exc}} = 405 \text{ nm}$  and  $\lambda_{\text{em}} = 500\text{-}639 \text{ nm}$ ) in different FoVs. The latter were recorded with a detection bandwidth of 10 nm and a step size of 5 nm.

Intensities of fluorescence between pH=5.0 and pH=7.5 with and without probe were compared (Figure 86). The results of Z-scan analysis are in the left part of the **Figure 86**. Data obtained from lambda scans was integrated separately for each pH value and the results are presented in the **Figure 86**, right. These reveal that fluorescence intensity increases when moving from pH = 7.4 to pH = 5.0 for both Z-stack based-images and lambda-scans and that the increase is statistically significant (Student's *t*-test with confidence interval of  $p < 0.01$ ). Additionally, the fluorescence intensity was significantly higher in the presence of the probe vs no-probe control in pH=5.0, but not in pH=7.5 proving a truly off-on response. This is particularly important, since it demonstrates that increase in the intensity of fluorescence comes with high probability from the change in the sensed parameter and not from changes in probes concentrations and the signal is therefore largely independent from probe's accumulation. Interestingly, results in **Figure 86** demonstrate that lowering pH leads also to increase in autofluorescence (comparing signal without a probe at two different pH). This, together with *in vitro* sensitivity of **SOLpH2** to polarity and viscosity, suggests that potential contribution of these other environmental changes to the observable fluorescence signal change from **SOLpH2** at pH=5.0 might also be considered.

Lambda scans at lower pH allowed also for determination of wavelength of maximum emission of **SOLpH2**, which in cells is estimated to be around 535 nm (**Figure 87**, top). This wavelength would suggest that general/average polarity of the intracellular environment has polarity similar to the one obtained in ACN measurements, in parallel to the conclusions stemming from the maximum emission wavelength in cells for **SOLpH1** probe. Interestingly, results of the lambda scans for the probe **SOLpH2** occurred to be sensitive enough to provide us with direct confirmation of turn-on properties of the fluorophore.

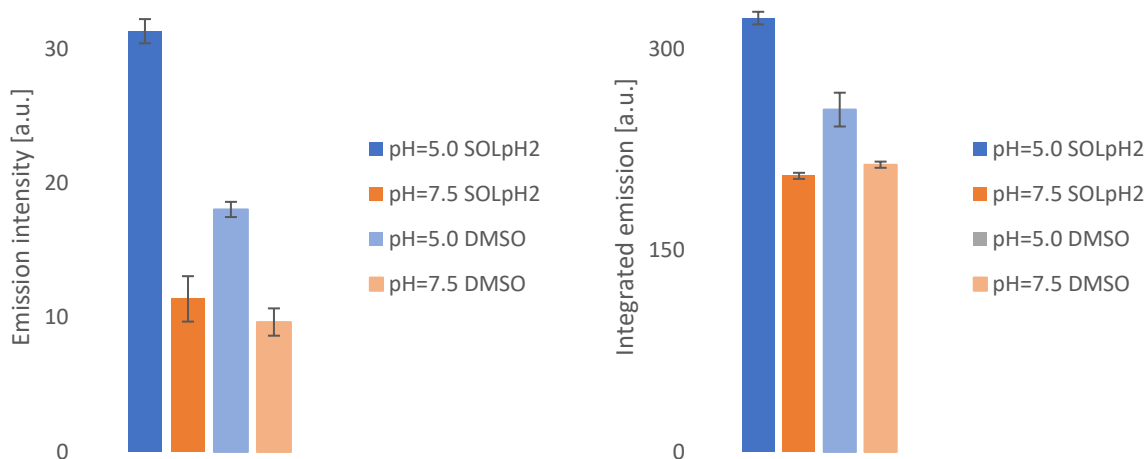


**Figure 85.** The **SOLpH2** probe presents higher emission in HEK293T cells incubated for 30 min with buffer of low pH (pH=5.0, Britton-Robinson buffer 40 mM). Increase of pH causes a decrease in a fluorescent response of the probe. (left) Mean intensities of images from Z-scans in green channel of HEK293T cells incubated in Britton-Robinson 40 mM buffers of different pH values (5.0, 6.0, 7.5, 8.0) for **SOLpH2** (15  $\mu$ M) compared with values observed for control sample (DMSO, 1%, v/v). (right) Mean integrated emission intensities gathered from lambda scans in green channel of HEK293T cells incubated in Britton-Robinson 40 mM buffers of different pH values (5.0, 6.0, 7.5, 8.0) for **SOLpH2** (15  $\mu$ M) compared with values observed for control samples (DMSO, 1%, v/v). B-R – Britton-Robinson 40 mM buffer of chosen pH; DMSO – 1% DMSO, v/v, control sample; SOLpH2 – sample with **SOLpH2**, 15  $\mu$ M.  $\lambda_{exc}$ =405 nm,  $\lambda_{em}$ =500-639 nm (green channel). Error bars represent standard error of mean of 6 measurements (left), and 5 or 10 (right).

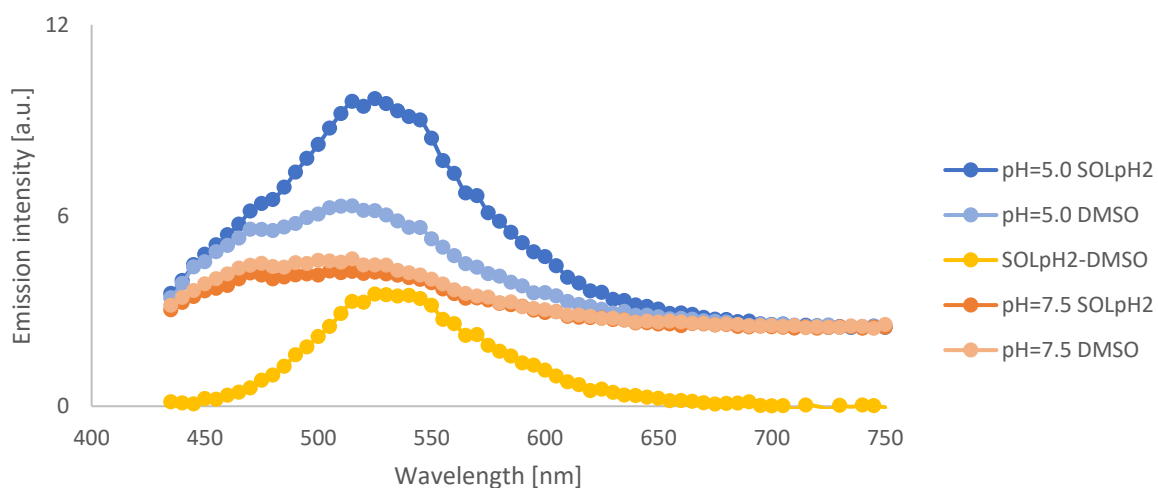


**Figure 86.** Fluorescence spectrum from lambda scan of HEK293T cells incubated with the **SOLpH2** (15  $\mu$ M, 15 min) and Britton-Robinson 40 mmol buffer pH=5 vs pH=7.5 (30 min).  $\lambda_{exc}$ =405 nm,  $\lambda_{em}$ =435-750 nm. The values were normalized to the highest value of emission in CPB pH=5.0. The emission was measured at 5 nm steps. The final concentration of DMSO was kept at 1% (v/v). Experimental data points, averaged over 3 repeats (n = 3) were connected with a line, which is there as a guideline for eyes to obtain a visual effect of the continuous line. DMSO – emission curve obtained for control samples; SOLpH2-DMSO – emission curve for the probe **SOLpH2**-incubated samples calculated from subtraction of values gathered for DMSO (control) from values for **SOLpH2**-incubated only; B-R – Britton-Robinson buffer.

#### 4.2.10. Summary and discussion

The conducted experiments confirmed the expected properties of the novel fluorophore structure, **SOLpH2**. The **SOLpH2** probe has its absorption and emission maximums in citrate phosphate buffer (CPB) pH=4.0 at 390/530 nm. The probe presented 13-time increase of fluorescence from phosphate buffer (PB) pH=8.0 to CPB pH=4.0. Interestingly, 15-20 nm shift of absorption spectrum maximum was observed, with no shift of emission maximum within this pH range. The calculated  $pK_a$  of the **SOLpH2** is 6.5, within biologically relevant values, and makes the probe suitable for intracellular experiments. The probe's environment-sensing properties were examined with dioxane:water mixtures (maximum 1049  $\text{cm}^{-1}$  shift) and various solvents & buffers (maximum 1236  $\text{cm}^{-1}$ ). Interestingly, the **SOLpH2** behavior was opposite to the **SOLpH1**, with the highest emission intensity in water or aqueous-based solutions and lowest in non-polar ones (perspective of simultaneous using both of them, as they partially present complementary properties). The dynamic range for viscosity-induced changes for probe **SOLpH2** was lower than for the **SOLpH1**, without clear turn-on or turn-off effect, showing it is less sensitive to viscosity than **SOLpH1**. The ion interference studies in the 100 mM HEPES pH=7.5 presented no drastic changes in emission for any of wide range of investigated salts. Notably, the **SOLpH2** was successfully proved for intracellular turn-on pH-changes monitoring, between pH=5.0 and pH=7.5 and showed reliable turn-on response with negligible fluorescence in a dark state, ensuring reliability of pH sensing and its independence or probes concentration/accumulation.

The direct comparison of the properties between the **SOLpH1** and the **SOLpH2** will be provided in the subchapter 4.3.1. Therefore, the current discussion will focus on the naphthalimide-based sensors for environment (pH, viscosity, polarity).

Multiple 1,8-naphthalimide-based pH-probes are described in the literature [180, 236, 421–424], with one of them presenting additional viscosity-sensing properties [246] and one triple-sensing ones [425]. The compound **3**, as the first example of dual-sensing 1,8-naphthalimide based probe, is a molecule getting excited at 394 nm at pH=4, with similar dynamic range of viscosity sensing [246] as the **SOLpH2**. The triple sensing probe **7** was described as a dual-sensing one, pH- and viscosity-sensing, however experiments in various solvents proves its polarity responsiveness as well [425]. Based on a high-efficient FRET system, the compound **7** was able to change its emission between chloroform (abs/em 362/498) and EtOH (abs/em 360/523) for 960  $\text{cm}^{-1}$ . The fluorescent response to pH changes was shown as a 4-fold increase between pH=10 and 5, while 6-fold increase was observed between pure glycerol and the less viscous glycol solution [425]. All things considered, the probe **SOLpH2** has superior properties in comparison to a triple-sensing naphthalimide-based probe **7**, comparable to the dual-sensing compound **3** and moderate to the rest of probes described in the subchapter 4.1.10.

Last but not least, since the **SOLpH2** has similar characteristics to the **SOLpH1**, in reference to the subchapter 4.1.10. about the pH/polarity/viscosity sensing probes, it may be concluded that the **SOLpH2** is the second probe with triple responsiveness to microenvironment, with  $pK_a$  value close to the intracellular pH one, successfully introduced into healthy and cancerous cell lines, with ability to present intracellular pH-imaging (turn-on response to pH changes inside non-cancerous cells).



### 4.3. Ligand-directed affinity labeling probe (SOLpH1-Tos)

#### 4.3.1. Design of SOLpH1-Tos

The aim of this subchapter was to develop a dual-function molecular tool that would be able to covalently attach to the protein of interest without affecting its activity and subsequently enable monitoring of changes in the local pH in a reliable way while attached to the protein. The desired probe would therefore be composed of an appropriate **fluorescent scaffold responsive to pH**, decorated with the **reactive linker** that would recruit probe to the protein of interest and subsequently react with the protein to form covalent bond between the protein and the probe without affecting its activity (**Figure 87**).

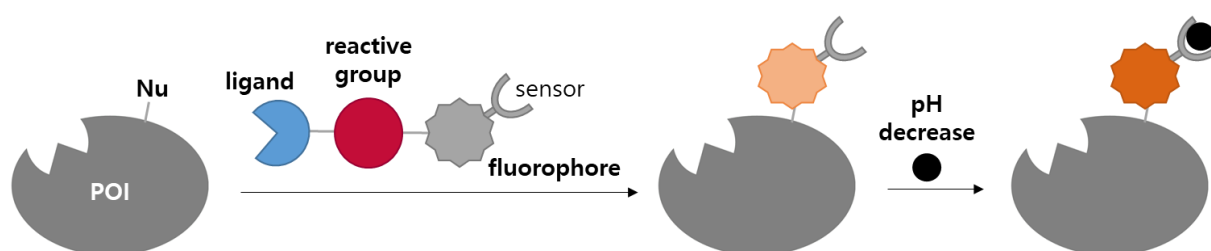


**Figure 87.** Schematic presentation of the structure and mechanism of labeling/response of the designed probe. POI – protein of interest; Nu – nucleophilic amino acid in close proximity to the POI active site; ligand – reversible ligand of POI. Ligand of the probe is marked with blue, reactive group with red and turn-on form of fluorophore by orange color. The gray color of fluorophore represents its turn-off state, dim orange color represents fluorophore state at physiological pH and dark orange color at decreased pH.

The selection of the **fluorescent scaffold responsive to pH** was made between the two pH and environment-sensitive fluorescent probes **SOLpH1** and **SOLpH2** described before in this thesis in chapters **4.2.** and **4.3.** In order to enable reliable detection of pH upon covalent attachment to the protein of interest, the fluorescent scaffold should exhibit:

- a) a unique change in fluorescence signal upon changes in the pH in biologically relevant range (pH 5.0 to pH 7.4-7.5),
- b) enable distinguishing between the protein bound and free probe (for this design, it was to be achieved by exploring the known change in polarity and/or viscosity upon protein binding) and
- c) be biocompatible and exhibit biologically favorable fluorescent properties.

When selecting appropriate fluorescent scaffold for the construction of the desired probe, multiple parameters that correlate with the requirements above, have been evaluated. Firstly, the synthetic access to **SOLpH1** was more direct with higher overall yields and more facile purifications. More importantly, however, it should be pointed out that both probes were able to report on the change in the cellular pH by statistically significant change in fluorescence intensity as well as spectral profile, making them both potentially suitable for intracellular pH sensing applications. When looking closely into their optical properties, however, some significant differences can be observed *in vitro* that can prove particularly important when covalent protein labelling followed by pH sensing is concerned. These are summarized and discussed below (**Table 9**).

**Table 9.** Comparison of the properties of probes **SOLpH1** and **SOLpH2**.  $\lambda_{exc}/\lambda_{em}$  – maximum of excitation and emission in citrate phosphate buffer at pH=4.0;  $\Delta\lambda_{em}$  – maximum Stokes shift observed for polarity-sensing studies.

	<b>SOLpH1</b>	<b>SOLpH2</b>
<b>Synthetic yield</b>	25.8%	3.1%
<b>Number of steps</b>	4 steps	3 steps
$\lambda_{exc}$ [nm]	420 (CPB pH=4.0)	395 (CPB pH=4.0)
$\lambda_{em}$ [nm]	600 (CPB pH=4.0)	550 (CPB pH=4.0)
$\Delta\lambda_{em}$ [cm <sup>-1</sup> ]	7143 cm <sup>-1</sup> (CPB pH=4.0)	7134 cm <sup>-1</sup> (CPB pH=4.0)
<b>Extinction coefficient <math>\epsilon</math></b>	pH=4.0 CPB:	pH=4.0 CPB:
<b>Quantum yield QY</b>	$\epsilon_{405} = 8450$	$\epsilon_{405} = 2000$
<b>Brightness B</b>	QY = 0.206	QY = 0.333
	$B_{405} = 1740.7$	$B_{405} = 1348.7$
	pH=7.5 PB:	pH=7.5 PB:
	$\epsilon_{405} = 5800$	$\epsilon_{405} = 1380$
	QY = 0.026	QY = 0.029
	$B_{405} = 150.8$	$B_{405} = 103$
<b>Color shift in pH <i>in vitro</i></b>	15 nm (821 cm <sup>-1</sup> )	0 nm
<b>Color shift in pH <i>in cellulo</i></b>	30 nm (941 cm <sup>-1</sup> )	-
<b>pK<sub>a</sub></b>	6.4 ± 0.2	6.5 ± 0.1
<b>Color shift in polarity</b>	1439 cm <sup>-1</sup>	1236 cm <sup>-1</sup>
<b>Intensity shift in polarity</b>	DCM/dioxane > aqueous-based	Dioxane < aqueous-based
<b>Color shift in viscosity</b>	10 nm (420 cm <sup>-1</sup> )	5 nm (167 cm <sup>-1</sup> )
<b>Intensity shift in viscosity</b>	glycerol > water	Glycerol:water 7:3 highest

Firstly, relative fluorescent properties of the two probes were compared. The **SOLpH1** has wavelengths of excitation and emission maxima shifted more towards red range of the visible spectrum and exhibits higher Stokes shifts, that makes it more biocompatible allowing for a better separation of the signal from autofluorescence. It has also been shown, that **SOLpH1** can be used to study pH in cells at lower probes concentration than **SOLpH2** (but this might differ significantly once fluorescent scaffold is decorated with the linker of different physical properties).

Secondly, **SOLpH1** exhibited larger intensity and color changes in response to changes in polarity and viscosity than **SOLpH2**. This increases the probability of observing desirable changes in spectral properties (even potentially ratiometric in the case of **SOLpH1** thanks to larger shifts in wavelengths of absorption and emission maxima) upon covalent protein attachment (that usually changes effective local polarity and/or rotational flexibility around the probe). That would allow for more reliable identification of the protein labelling event and distinguishing between covalently attached and free probes.

When comparing the pH responsiveness of the probes, even though **SOLpH1** exhibits lower (11.5-fold) change in brightness between pH 4.0 and pH 7.5 than **SOLpH2** (13-fold change), the change of pH is accompanied by higher change in wavelength of maximum absorbance and emission for the first probe (respectively  $\Delta\lambda_{\text{abs}}=15$  nm,  $\Delta\lambda_{\text{em}}=15$  nm and  $\Delta\lambda_{\text{abs}}=15$  nm,  $\Delta\lambda_{\text{em}}=0$  nm for **SOLpH1** and **SOLpH2**). Therefore, combined shift of emission together with intensity change might more reliably quantify pH in a ratiometric manner when using **SOLpH1**.

Taking all of these aspects into consideration, **SOLpH1** has superior properties that promise to better fulfil the requirements of the fluorescent scaffold of the dual function tool for protein labelling and subsequent monitoring of local pH.

The design of **the linker part** is based on ligand-driven proximity labelling technology formulated by Hamachi group [308] that used it for covalent labelling of proteins but mainly with non-responsive fluorescent tags. In this thesis we extend it to development of responsive probe that can be covalently attached to the protein target for potential measurement of changes (pH) in local microenvironment. The main function of the linker was to:

- a) enable an effective recruitment of the probe to the protein of interest (POI), which in the case of this thesis was carbonic anhydrase as a model enzyme involved in a range of diseases, responsible for pH homeostasis and with already validated labelling with ligand-driven proximity labelling technology (reversible protein ligand),
- b) be relatively stable in cellular environment but react with nucleophilic residues on the surface of the protein of interest when brought to its proximity, enabling orders of magnitude more efficient labelling of bound protein of interest over other target (reactive group) and
- c) appropriate separation and orientation of the elements of the probe, in particular:
  - a. separation of the ligand and reactive group to ensure a right positioning of the reactive motif in relation to nucleophiles on protein surface when bound to POI
  - b. maintaining an optimal distance between the reactive group (and subsequent point of covalent attachment to the protein) and fluorophore to not sterically hinder the reaction between protein's nucleophile and probes reactive motif but also to ensure as close as possible proximity of the fluorophore to the protein surface after labelling.

To meet these criteria, the following design has been selected. In order to effectively introduce the probe to the protein of interest, the fluorescent moiety is connected with a short linker with the reactive group, originally already included in the **SOLpH1** molecule. From a whole array of possible reactive groups, tosylate/tosyl one was selected, for it proved

to be able to label histidine (His) amino acid at human carbonic anhydrase II (hCAII) active site [308]. The reactive group is further connected to benzenesulfonamide ligand, which is able to selectively interact with the active site of hCAII, as a ligand for zinc cofactor, present in the active site. This interaction brings the probe in a close proximity to the site of labeling (His). Finally, since the linker connected to the **SOLpH1** is short the probe may land close to the active site (as discussed and confirmed later in the **subchapter 4.3.3.**) and in closer proximity to the protein surface. The closer the probe to the surface of the protein the more effective the changes in the environment polarity and / or rotational flexibility of the probe and possibly the higher fluorescence change of the **SOLpH1** upon binding [426].

The detailed description of the affinity-based technology was provided in the **subchapter 1.4.4.** and the next **subchapter 4.3.3.** will focus on the studies with use of the synthesized probe, **SOLpH1-Tos**. Taking into consideration the aspects discussed above, the final design of the **SOLpH1-Tos** probe is presented on the figure below (**Figure 88**, top). Since additional linker elements added to the **SOLpH1** fluorescent scaffold to obtain **SOLpH1-Tos** probe has no optically active elements, the optical properties of the fluorophore, and at the same time the whole molecule, should remain nearly identical as in the case of the original molecule, the **SOLpH1**, at least before protein labelling. For analytical studies of selectivity of the probe, a control compound **SOLpH1-Bz** (**Figure 88**, bottom) was synthesized as well. Absence of the affinity ligand (sulfonamide), crucial for the interaction with hCAII, should result in the lack of ligand-protein reversible complex and thus less efficient labeling of the POI.

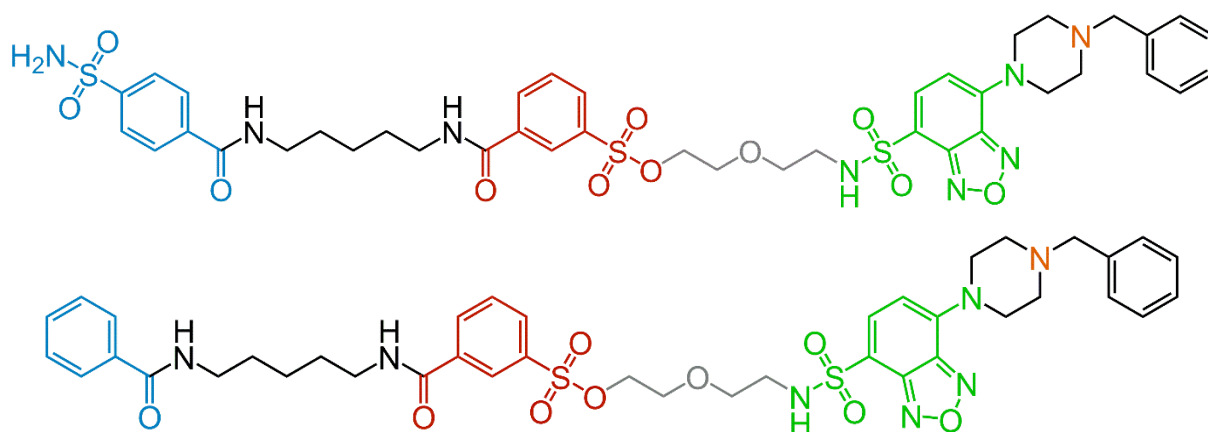


**Figure 88.** Structure of the probe **SOLpH1-Tos** (top) and control compound **SOLpH1-Bz** (bottom). The fluorophore part (**SOLpH1**) is marked with green color, reactive group with red one, ligand for human carbonic anhydrase II (hCAII) with blue one and PEG linker with gray one.

#### 4.3.2. Synthesis and characterization of SOLpH1-Tos and SOLpH1-Bz

The first two approaches to the synthesis of the probe **SOLpH1-Tos** (compound **15**) were conducted traditionally – in solution. Despite comprehensive description in the literature sources, insertion of the reactive group into one of the precursors of the final probe significantly complicated all the steps, including purification (**Figure 89**). The reactive group tended to decompose (hydrolyze) during the purification as well as each of the synthesis steps into product of its reaction (sulfonic acid) even with trace amounts of water, as it was observed in a few synthesis and purification steps (**Figure 90**). To prevent further complication and possible loss of the fluorophore intermediate, **SOLpH1**, a different approach was assumed.

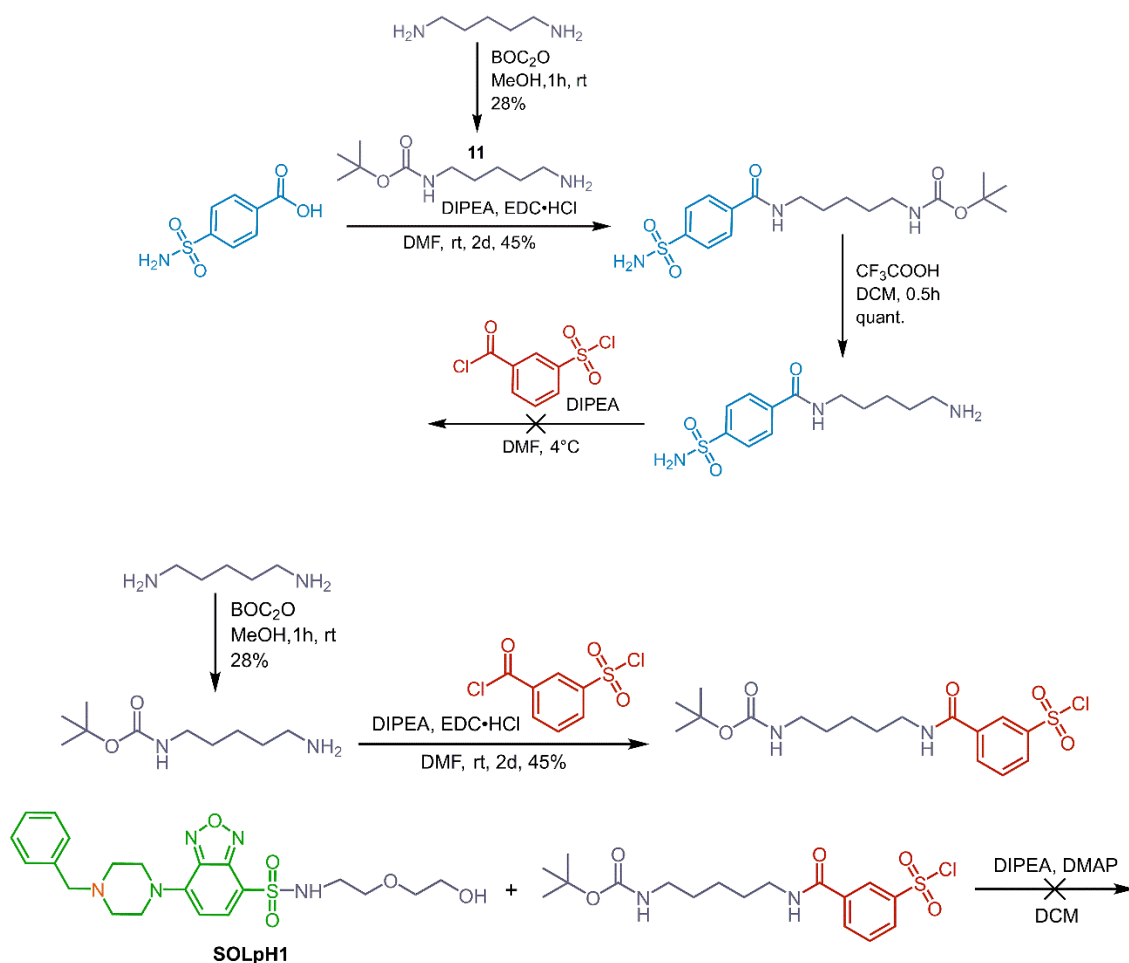


**Figure 89.** Presentation of the first two approaches to synthesis of an affinity-labeling probe. The crossed arrow represents the step, where problems with substrate and product stability highly affected the synthesis process, what resulted in switch to solid-phases synthesis method (resin). The fluorophore part (**SOLpH1**) is marked with green color (with orange-marked nitrogen as pH-sensor), reactive group with red one, ligand for human carbonic anhydrase II (hCAII) with blue one and PEG linker with gray one.

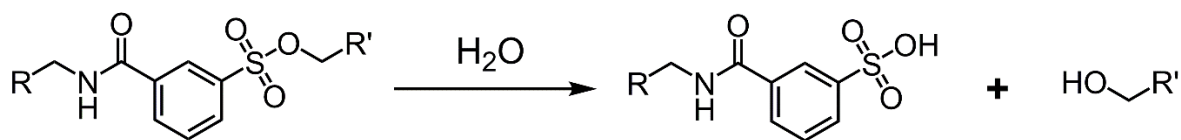


**Figure 90.** Schematic representation of hydrolysis reaction of molecules bearing tosyl/tosylate reactive group. Tosylate-containing compounds are estimated to hydrolyze only at 10%, in buffer aqueous conditions at 37°C within 48 h. Prepared based on [308]. R, R' – substituent groups.

Solid-phase synthesis on resin of affinity-based labeling probes bearing tosylate reactive group was inspired by previous report [308], where 2-chlorotrityl chloride resin was used as medium for attaching nearly all building blocks. Moreover, Wang resin (*p*-benzyloxybenzyl alcohol resin), was also used in another literature report and we decided to attempt the synthesis according to that latter protocol [330]. To test this method, firstly two model compounds were successfully obtained and characterized (**Figure 91**) that prompted us to attempt this synthetic approach also to the synthesis of the final probe.

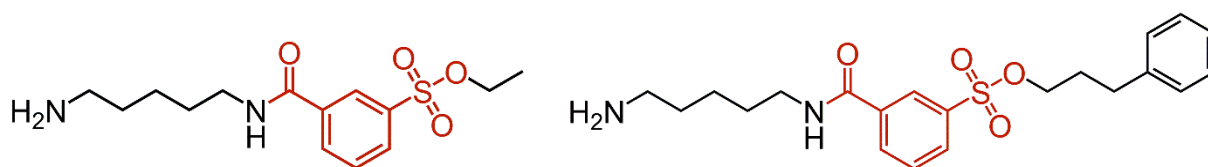


**Figure 91.** Structures of two model compounds, where solid synthesis method was checked before trial with the **SOLpH1** introduction to the method. Reactive group part is marked with red color.

The first step of the target probe synthesis (**SOLpH1-Tos**) is activation of the Wang resin. Addition of *p*-nitrophenyl chloroformate with the use of a strong base, collidine (2,4,6-trimethylpyridine) resulted in overnight formation of an active ester (**Figure 92**, a i)). The use of collidine instead of pyridine possibly prevented some undesired, side reactions. The active ester undergoes attack with 1,5-diaminopentane (cadaverine) in the presence of *N,N*-diisopropylethylamine (DIPEA) and a carbamate bond is formed between resin and cadaverine within approximately 16 hours (**Figure 92**, a ii)). For the next step, DCM as a solvent had to be additionally dried, because the substrate for this reaction, 3-(chlorosulfonyl)benzoyl chloride is extremely unstable in the presence of any moisture. The reagent decomposes easily over time in commercially received bottle into its acid derivative (similarly to the decomposition presented in the **Figure 90**). Furthermore, to prevent the decomposition of the obtained product, the introduction of the tosylate reactive group (**Figure 92**, b)) has to be instantly followed by the reaction with the last substrate, the **SOLpH1** (**Figure 92**, c), introduction of the **SOLpH1**). The possibly elongated time of this step may result in partial decomposition of the obtained derivative, lowering the chances of successful and high-yield insertion of the **SOLpH1** fluorophore. After all the steps, cleavage of compound **13** from Wang resin was conducted (**Figure 92**, d i)). With use of crude cleavage mixture, two different products were formed in reaction with a proper *N*-hydroxysuccinimide active ester. The compound **14** (active ester) was used to obtain **SOLpH1-Tos**, while the compound **15**

(active ester) to obtain **SOLpH1-Bz** (**Figure 92**, d) ii) for both final compounds). The solid phase approach has undoubtedly another additional advantage – **SOLpH1** DCM solution used for last step was recovered and with one step of purification most of the non-reacted fluorophore scaffold was obtained unaffected. The final reaction mixtures containing compounds **SOLpH1-Tos** and **SOLpH1-Bz** were purified by flash column chromatography and preparative thin layer chromatography, in the estimated overall yield 8% over 5 steps for **SOLpH1-Tos** and **SOLpH1-Bz**. The structures of novel compounds that were not previously reported (**SOLpH1-Tos**, **SOLpH1-Bz**) were confirmed structurally with  $^1\text{H}$  NMR,  $^{13}\text{C}$  NMR and HRMS analyses.

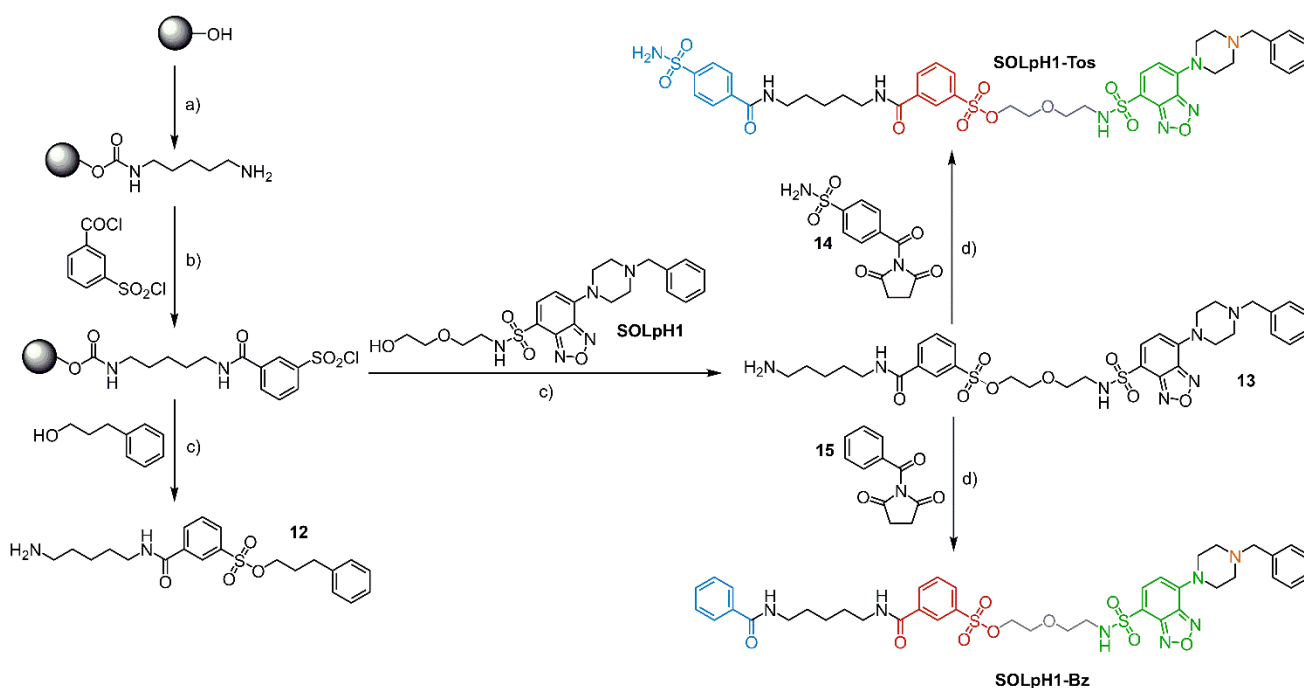


**Figure 92.** Synthetic pathway leading to the test compound **12**, **SOLpH1-Tos** probe and control compound **SOLpH1-Bz**: a) i) *p*-nitrophenyl chloroformate, collidine, DCM, RT, 9 h; ii) 1,5-diaminopentane, DIPEA, DMF, RT, 16 h; c) DIPEA, DCM, RT, 2h; d) i) 50% TFA/TES in DCM, RT, 2h (quant. for all 3 compounds); ii) DIPEA, DMF, 1h (8% both for **SOLpH1-Bz** and **SOLpH1-Tos**). The fluorophore part is marked with green color (with orange-marked nitrogen as pH-sensor), reactive group with red one, ligand for human carbonic anhydrase II (hCAII) with blue one and PEG linker with gray one.

#### 4.3.3. Labeling experiments of human carbonic anhydrase II

To confirm if the prepared probe could effectively label the protein of interest (carbonic anhydrase II, hCAII) incubation experiments between the probe and hCAII at 37°C were conducted. The **SOLpH-Tos** stock solution was prepared in DMSO. The commercial solution of hCAII in 20 mM Tris buffer pH=7.5 (with 150 mM NaCl) was diluted to the final concentration of 10 µM with use of 100 mM HEPES pH=7.3. Three samples were prepared for incubation and further analysis:

- 1) Control sample (10 µM hCAII protein solution, no probe added),
- 2) 1 to 2 ratio of hCAII to the probe **SOLpH1-Tos** (10 µM : 20 µM, protein:probe) and
- 3) 1 to 10 ratio of hCAII to the probe **SOLpH1-Tos** (10 µM : 100 µM, protein:probe).

The total concentration of DMSO was 1%. All reaction mixtures were mixed gently with use of a pipette and incubated at 37°C for 48 h. After this time, small aliquotes from all tubes were separately diluted with sodium bicarbonate 50 mM solution (digestion buffer). Afterward, 1.5 µL of the dithiothreitol (DTT) solution (0.1 M) was added to all of the samples, which were subsequently incubated at 95°C for 5 min; DTT is used to reduce disulfide bonds in proteins and peptides. After cooling down and centrifuging, 3 µL of iodoacetamide (IAA) solution (0.1 M) was added to the samples; IAA is an alkylating agent, covalently binding with cysteine residues, for a protein not to form disulfide bonds. The samples were incubated in darkness for 20 min (IAA is unstable and light sensitive) and centrifuged. The last step was an addition of protease (2 µL) and incubation for 16 h before the final analysis of the obtained peptides. From a wide array of proteases available for such experiments, trypsin was chosen. Trypsin is an enzyme from a family of serine proteases and predominantly cleaves protein at the C-terminal side (carboxylic acid side): lysine, arginine and (arguably) proline [427, 428]. Moreover, it is considered an endopeptidase, which was clearly observed in the result of the digestion analysis – the cuts were observed within the polypeptide chain and not at the terminal amino acids. As its function is dependent on the temperature of the surroundings, the incubation and digestion process were conducted at the temperature of human organism (37°C). The second approach to the experiment included use of the control compound, **SOLpH1-Bz** in ratio protein:probe 1:2.

The schematic representation of labeling process is shown in the **Figure 93**. As a result of *quasi*-intramolecular reaction between the probe and hCAII, the probe **SOLpH1** should be covalently attached to the surface of hCAII, while the ligand for the protein and reacted reactive group are considered a by-product of the reaction. The analysis of the hCAII samples after digestion was conducted by Dr. Łukasz Marczak, PhD, and Aleksander Strugała, MSc BEng, from the Laboratory of Mass Spectrometry at the Institute of Bioorganic Chemistry, Polish Academy of Sciences. The first part of the analysis was based on the direct observation and comparison of chromatograms of all samples (**Figure 94**). The preliminary conclusion was that in both experiment samples (2, 3) presence of an additional peak was noted (marked with **blue** color), in contrast to the control sample (1). The control sample main peak is as well present in the sample 2 & 3, with a lower retention time and of lower “intensity”, just before the peak marked with **blue** color.



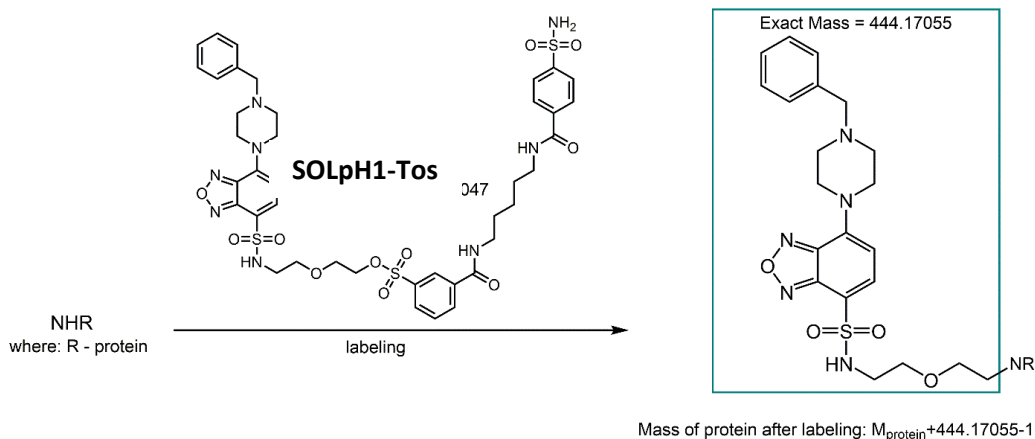


**Figure 93.** Schematic presentation of human carbonic anhydrase II (hCAII) labeling, including the expected mass of the product of hCAII single labeling. NHR – -NH- group from histidine labeled with the probe **SOLpH1-Tos**, where -R- is a protein labeled (hCAII);  $M_{\text{protein}}$  – protein mass (estimated to be 29.3-30 kDa, depending on the isoform or modification).

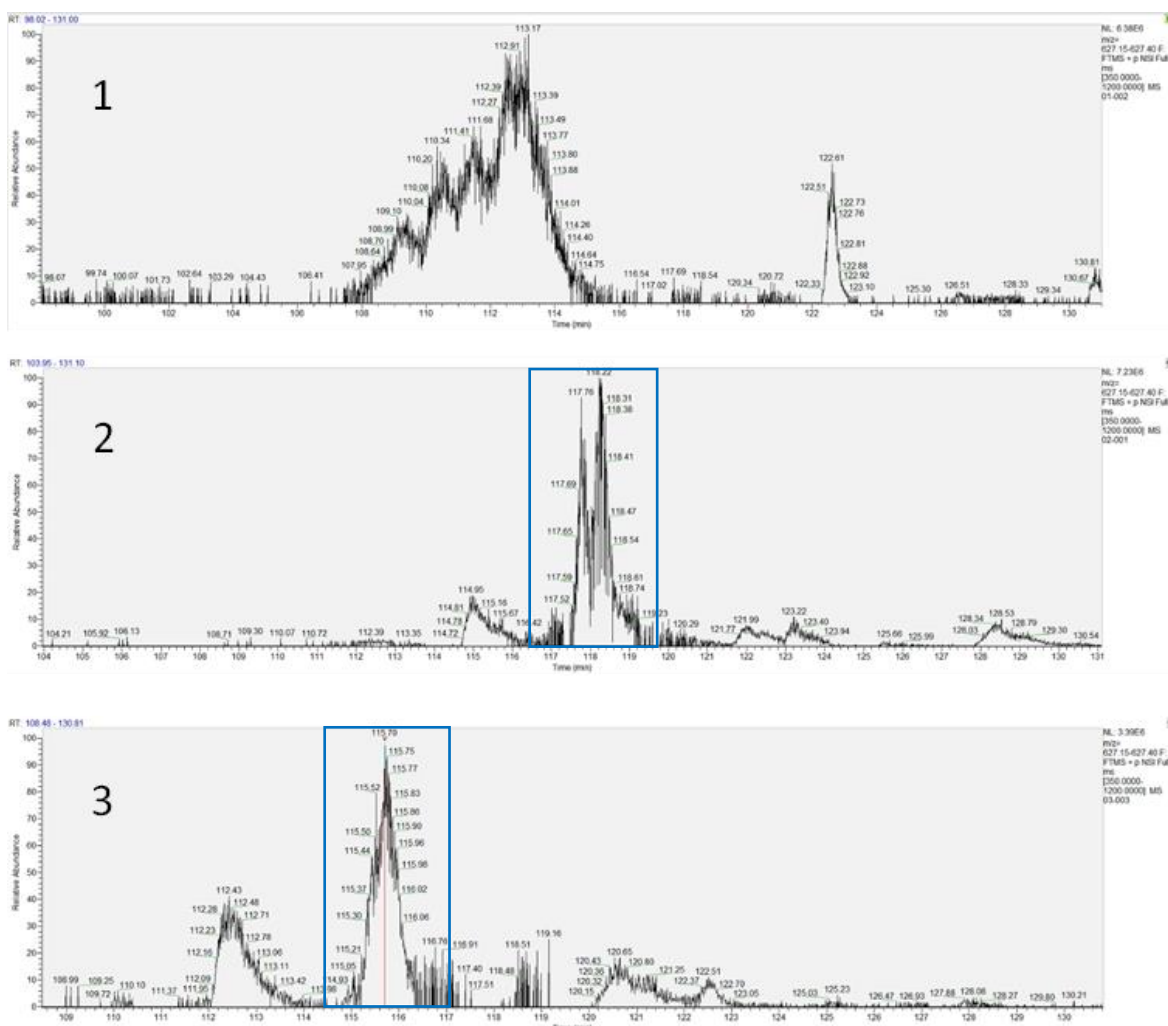


**Figure 94.** Presentation of MS/MS chromatogram results from 3 samples analyzed after incubation hCAII/SOLpH1-Tos: 1) control sample with hCAII protein only (10  $\mu\text{M}$ ); 2) sample, where ratio of protein and the probe **SOLpH1-Tos** to protein was 1:2 (10  $\mu\text{M}$ : 20  $\mu\text{M}$ ); 3) sample, where ratio of protein and the probe **SOLpH1-Tos** to protein was 1:10 (10  $\mu\text{M}$ : 100  $\mu\text{M}$ ). The control sample does not have **peak** at time 115-118 min, which included data about labeling with the probe **SOLpH1-Tos**.

To analyze all the data gained from labeling process, lysis and then mass spectrometry, Mascot search engine data was used. The Mascot employs a probabilistic scoring algorithm for protein identification that was derived from the MOWSE (Molecular Weight Search) algorithm [429]. Analysis usually requires choice of taxonomy of the sample (restricting the choice to certain species or group of species; here: *Homo sapiens*), choice of protein being analyzed (hCAII) and the protease, which was used for protein sample lysis (trypsin). The results of the digestion data analysis are presented in the **Figure 95**. In the figure, the bottom sequence marked in red are sequence parts, which were successfully identified in the sample, while the marked with black color were not (i.e. 83% of sequence was successfully detected and assigned). The numbers on the left present the number of the first amino acid in the sequence in each line. Notably, within one long, red-colored part of the sequence in the **Figure 95**, a few peptides were identified, for example the peptide, which sequence is presented in the **Figure 96**, top, ILNNGHAFNVEFDDSQDK (from Ile59 to Lys76).

## Protein View

Match to: CAH2\_HUMAN Score: 109 Expect: 2.5e-007  
 Carbonic anhydrase 2 OS=Homo sapiens GN=CA2 PE=1 SV=2

Nominal mass ( $M_r$ ): 29285; Calculated pI value: 6.87

NCBI BLAST search of [CAH2\\_HUMAN](#) against nr

Unformatted [sequence string](#) for pasting into other applications

Taxonomy: [Homo sapiens](#)

Fixed modifications: Carbamidomethyl (C)

Variable modifications: Acetyl (N-term), Oxidation (M)

Cleavage by Trypsin: cuts C-term side of KR unless next residue is P

Number of mass values searched: 193

Number of mass values matched: 57

Sequence Coverage: 83%

Matched peptides shown in **Bold Red**

```

1  MSHHWGYGKH NGPEHWHKDF PIKGERQSP VDIDTHTAKY DPSLKPLSVS
51  YDQATSLRIL NNGHAFNVEF DDSQDKAVLK GGPLDGTYRL IQFHFWGSL
101 DGQGSEHTVD KKKYAAELHL VHWNTKYGDF GKAVQQPDGL AVLGIFLKV
151 SAKPGLQKVV DVLDSIKTKG KSADFTNFDP RGLLPESLDY WYTPGSLTTP
201 PLLECVTWIV LKEPISVSSE QVLKFRKLNF NGEGEPEELM VDNWRPAQPL
251 KNRQIKASFK
  
```

**Figure 95.** Mascot software search engine analysis result of labeling experiments of the probe **SOLpH1-Tos** towards hCAII protein. Red labeled amino acids are the amino acids, which were identified and successfully assigned to the human carbonic anhydrase II sequence, while the black ones were not found. The final percentage of amino acids identified and assigned is 83%.

Tandem mass spectrometry (MS/MS) analysis of the chromatogram peaks presented in the **Figure 94** resulted in identification of the peptide sequence assignment to the fragment, which contained mass of the probe **SOLpH1**, as a fragment of the probe **SOLpH1-Tos**, which should be connected to a selected peptide as a result of the labeling (**Figure 96**, top). Tosyl reactive group, according to the literature, has labeling preferences towards a few different amino acids: His (H), Tyr (Y), Glu (E), Asp (D), Cys (C) [430]. At the same time, a part of the peptide (ILNNGHAFNVEFDDSQDK) presented in the **Figure 96**, middle (VEFDDSQ), was proved not to contain any labeled with the **SOLpH1** amino acid. In the rest of this peptide within the identified sequence (ILNNGHAFNVEFDDSQDK) there is only one amino acid from this set: His (H), which finally confirms the labeling on His64 (the amino acid marked with a red color in the sequence: ILNNG**H**AFNVEFDDSQDK).

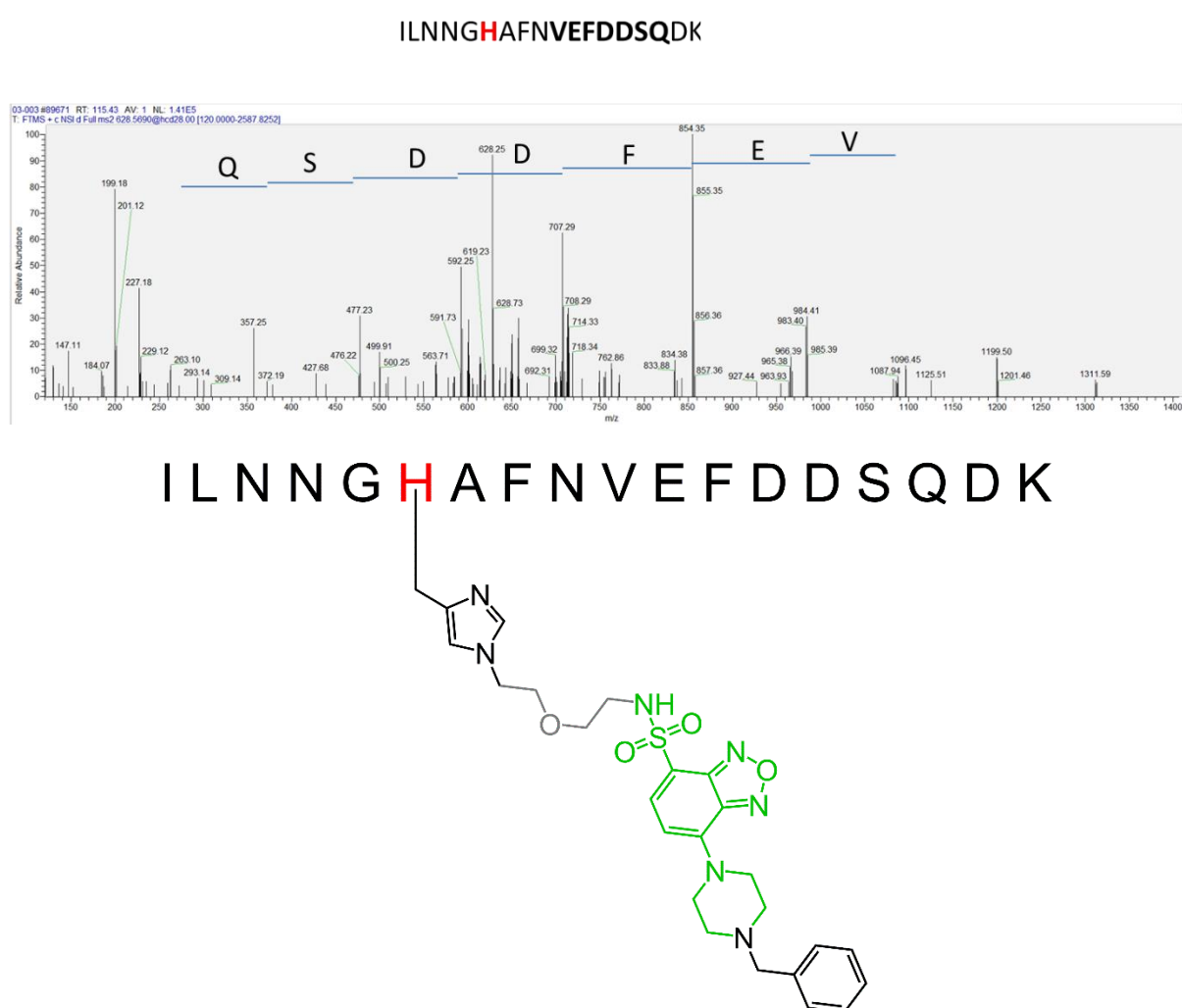


**Figure 96.** (Top) Presentation of the peptide sequence identification (ILNNGHAFNVEFDDSQDK, Ile59 to Lys76), where histidine labeling of the probe **SOLpH1-Tos** was confirmed. (Middle) MS/MS spectrum for the part of the peptide (QSDDFEV), which was proved not to be modified, covering the sequence from Val68 to Gln74. (Bottom) The labeling happened at the other part of the **ILNNGHAFNVEFDDSQDK** peptide, His64.

All things considered, the labeling experiments of human carbonic anhydrase II (hCAII) with SOLpH1-Tos proved to be successful. His64 was confirmed to be the labeled site. At the same time, lack of labeling in case of the control compound SOLpH1-Bz was observed. The latter additionally confirms the crucial role of reversible hCAII ligand in the *quasi*-intramolecular labeling reaction. A report by Tsukiji et al. indicated His3 as the labeled position, also with Tos-based probe [308]. Previously reported 3D structure of the hCAII [431] showed that both His residues are located in a close proximity to each other (**Figure 97**). That difference might stem from a difference in the structure between the previously reported one [308] and the one proposed by this work (different fluorophore). The use of SBD-based molecule (instead of the reported coumarin-based one [308]) may have required potentially alternative conformational arrangement of the whole probe at the entrance to the active site, resulting in the different availability of the reactive tosylate group for a nucleophilic attack of amino-acid residues at the protein surface. Additionally, the process may have been affected by local fluctuations of ion concentration. While the previously reported study was conducted with the HEPES buffer 50 mM pH=7.2, the SOLpH1-Tos labeling experiments were conducted in a mixture of commercial Tris buffer 20 mM HCl pH=7.2 and freshly prepared HEPES buffer 50 mM pH=7.3. All of these factors may have affected and created new non-covalent interactions between the fluorophore, enzyme substrates, zinc ion in the active site or amino acids around it.

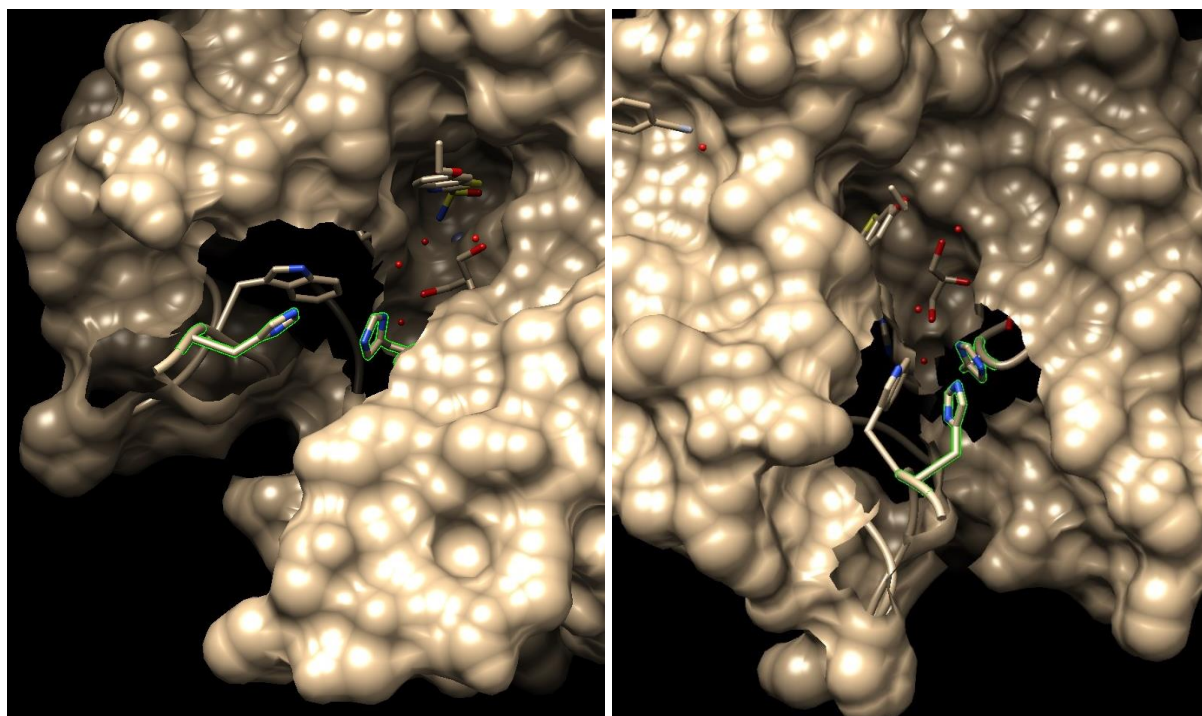


**Figure 97.** Visual representation of histidines labeled with SOLpH1-Tos labeling vs in Tsukiji et al work [308] with use of the previously reported hCAII 3D structure [431]. Both histidines are located at the entrance of the active site of the protein and are highlighted with a thin green line. The images were obtained with use of UCSF Chimera program [432].

#### 4.3.4. pH-dependent emission of SOLpH1 labeled to hCAII

The rest of the experiment sample used for incubation and labeling studies (sample 2, subchapter 4.3.3.) were used to investigate the properties of the labeled fractions of the protein. To do so, they were directly subjected to purification (from the rest of non-reacted probed as well as the products of its hydrolysis) and further experiments. Notably, they were not digested to ensure that human carbonic anhydrase II keeps its enzymatic activity.

All the purification processes were conducted at 4°C, to minimize the effect of temperature on the protein sample. The purification process started with a dialysis against HEPES buffer (100 mM, pH=7.5) to remove small molecule impurities and exchange buffers. Then, the protein sample was purified with use of size-exclusion chromatography, which separates ingredients of the sample by their size that correlates usually with their mass. The column was equilibrated with HEPES buffer 7.0, around physiological pH to stabilize the protein and with molarity sufficient for the process (not to clog the column). The protein fractions containing the desired protein sample were collected and concentrated. The final protein concentration was determined by measuring the absorbance at 280 nm using molar absorption coefficients of 54,000 M<sup>-1</sup> cm<sup>-1</sup> [337] and it was estimated to be ~27 μM. This purified sample was used for the investigation of the fluorescence of the probe when attached to the protein of interest (this subchapter) and also to investigate its activity upon labelling (subchapter 4.3.5).

To look into the pH-sensing properties of the **SOLpH1** connected to hCAII protein, the protein stock solution was diluted with a set of buffers: CPB pH=4.0, 5.0, 6.0; PB pH=6.0, 7.0, 7.5, 8.0 and 100 mM HEPES buffer pH=7.5. The final concentration of the protein was estimated to be 5.2 μM in each well. All the sample were excited at 430 nm (wavelength optimal for aqueous-based solutions for the **SOLpH1**) and emission was gathered for a range 470-700 nm, with 5 nm step. The absorption data for all samples was collected as well (300-700 nm, 10 nm step). The experiment was repeated in triplicates. The results of the emission measurements are presented in the **Figures 98, 99**. To increase the quality and readability of data, the background coming from use of phosphate-based buffers (observed here and previous experiments conducted in CPB/PB as well) was not subtracted for the presented graphs. All data was measured at t=0, 30 and 60 min (**Figure 99**, top).

The subtraction of the values obtained for the background and the data obtained from the **SOLpH-1**-labeled hCAII resulted in estimation of the maximum emission in CPB at pH=4.0 to be 580-590 nm. The obtained wavelength value is a higher than the value obtained for an average intracellular polarity in the HEK293T and A549 cells at physiological pH (~7.4) in the subchapter 4.1.8 (41.1 kcal/mol, ~550 nm). Moreover, 580-590 nm would correspond to the values obtained for solvents DMF, EtOH, MeOH, DMSO (subchapter 4.1.5.), estimating the average polarity at the entrance of the hCAII active site to be within the range 43.8-45 kcal/mol.

The data obtained for the set of buffers with various pH (4.0-8.0) presents that the **SOLpH1** covalently labeled to hCAII is able to sense general pH changes in the solution (**Figure 98**, top). The comparison of data collected for the solutions at t=0 and t=30 min shows a gradual increase in signal in CPB pH=4.0 (5.6%) within 30 min and certain fluctuations of signal. After

60 min incubation, the emission at pH=4.0 decreases by 8.6% and it is visible that the emission values seem to gradually decrease (especially for the lower pH values) and the differences between all of the curves are reduced in time (flattening or less clear separation of the spectra).

Moreover, with isolation and direct comparison of data obtained separately for the CPB pH=4.0 (background and sample containing **SOLpH1**-hCAII) and for the PB pH=8.0 (background and sample containing **SOLpH1**-hCAII as well) additionally confirm an ability of the **SOLpH1** to sense acidic environment in close proximity to the labeled hCAII (**Figure 99**, top) with the statistically significant difference in the intensities and maximum emission wavelength in pH=4.0 vs pH=8.0 with a probe or controls without a probe (**Figure 99**, bottom). Nevertheless, it has to be noticed, that intensities are significantly lower than in a buffered solutions with free probe, potentially indicating partial labelling and/or changes in brightness upon labelling. Another possible explanation can also be a strong buffering capacity of the protein residues around the probe that, at least locally, leads to higher-than-expected pH even if the bulk is acidic. This hypothesis however, requires much deeper analysis, but it demonstrates a possibility of asking a completely new questions with this type of previously virtually inexistent probes.

These experiments further confirm a successful labelling of the hCAII with the probe and more importantly demonstrate that the fluorophore can sense changes in the pH even when attached to the protein of interest that is a key property for the successful application in cells.

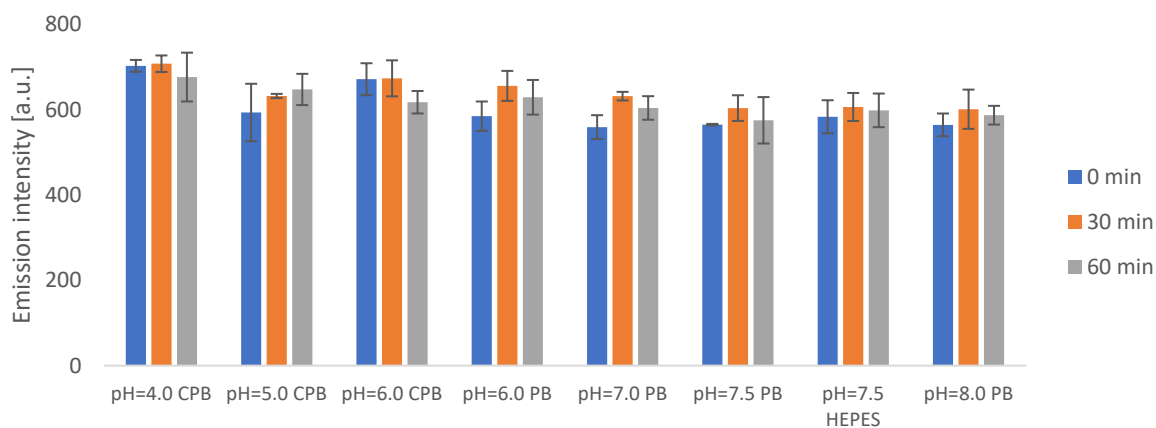


**Figure 98.** (top) The emission of **SOLpH1**-labeled human carbonic anhydrase II at 0, 30 and 60 min measured at 540 nm. (bottom) Direct comparison of integrated emission values for the control (DMSO only, 0.5%, v/v) and experiment samples (**SOLpH1**-labeled hCAII) for pH=4.0 CPB and pH=8.0 PB. The emission was measured at 5 nm steps. The final concentration of DMSO was kept at 0.5%. Experimental data points were averaged over 3 repeats.  $\lambda_{exc}=430$  nm. CPB – citrate phosphate buffer; PB – phosphate buffer.

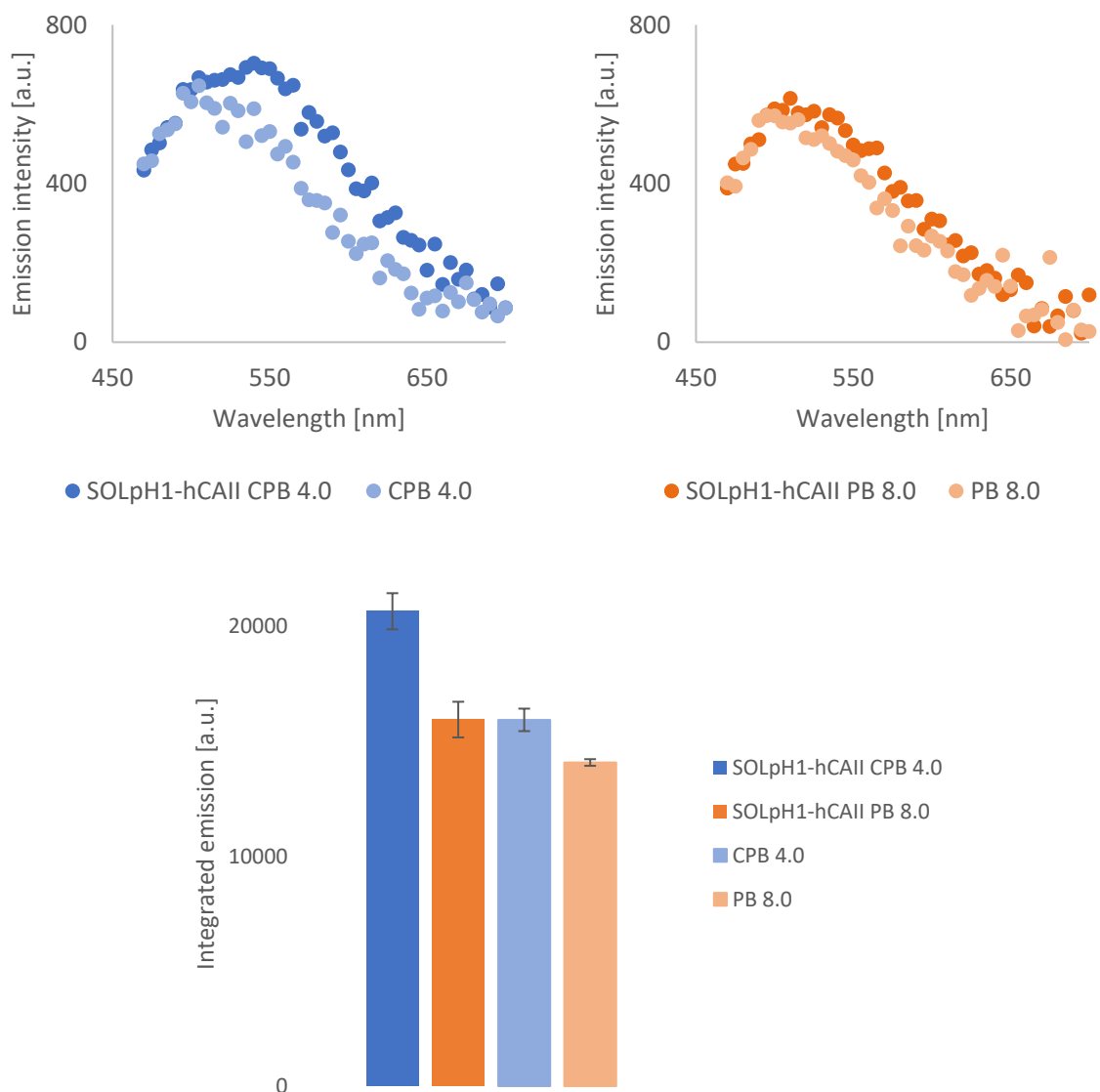


**Figure 99.** (top) Direct comparison of the spectra of the **SOLpH1-hCAII** in CPB pH=4.0 (left) and PB pH=8.0 (right) at 0 min. (bottom) Comparison of integrated emission for experiment samples (**SOLpH1-hCAII** labeled) and control ones (DMSO, 0.5%, v/v) for pH=4.0 and pH=8.0. Both differences at pH=4.0 and 8.0 control vs experiment samples are statistically significant ( $p < 0.05$ ). The emission was measured at 5 nm steps. The final concentration of DMSO was kept at 0.5%. Experimental data points were averaged over 3 repeats.  $\lambda_{exc}=430$  nm,  $\lambda_{em}=470-700$  nm. SOLpH1-hCAII – human carbonic anhydrase labeled with the probe **SOLpH1-Tos**. CPB – citrate phosphate buffer; PB – phosphate buffer.

#### 4.3.5. Evaluation of the enzymatic activity of hCAII labeled with SOLpH1-Tos

One of the big advantages of the ligand-driven proximity labeling outside of the active site of the protein is enable a retention of protein function after labeling. Therefore, to determine if the enzymatic activity of human carbonic anhydrase II was compromised by its labeling, the enzymatic activity assay (Carbonic Anhydrase Activity Assay Kit) was conducted. The analyzed samples included:

- 1) Samples used for pH-dependent experiments (CPB 4.0, 6.0; PB 6.0, 7.5 and 100 mM HEPES pH=7.5; cc. 5.2  $\mu$ M) from the subchapter **4.3.4.** and
- 2) Control sample from the subchapter **4.3.3.** (diluted to cc. 5.2  $\mu$ M with CA Assay Buffer).

All samples were non-digested (to keep the anhydrase's enzymatic activity). Firstly, the product of the reaction detected in this assay kit was used to prepare the standard curve. The volumes of 20 mM nitrophenol standard: 0, 4, 8, 12, 16 and 20  $\mu$ L were added into series of wells (in triplicate), the volumes were adjusted to 100  $\mu$ L/well with CA Assay Buffer and the absorbance was measured at 405 nm in an end-point mode. As a result, the standard curve was prepared for further determination of the analyzed samples' enzymatic activity (**Figure 100**). It is worth mentioning that while **SOLpH1-Tos** (in a form of **SOLpH1** labeled to hCAII) exhibits absorption at 405 nm, the relative amount of the probe (within single digit micromolar) is 2 or 3 orders of magnitude lower than the concentration of nitrophenol and has also significantly lower extinction coefficients than expected from nitrophenol, making the probe's absorbance a minor contribution.

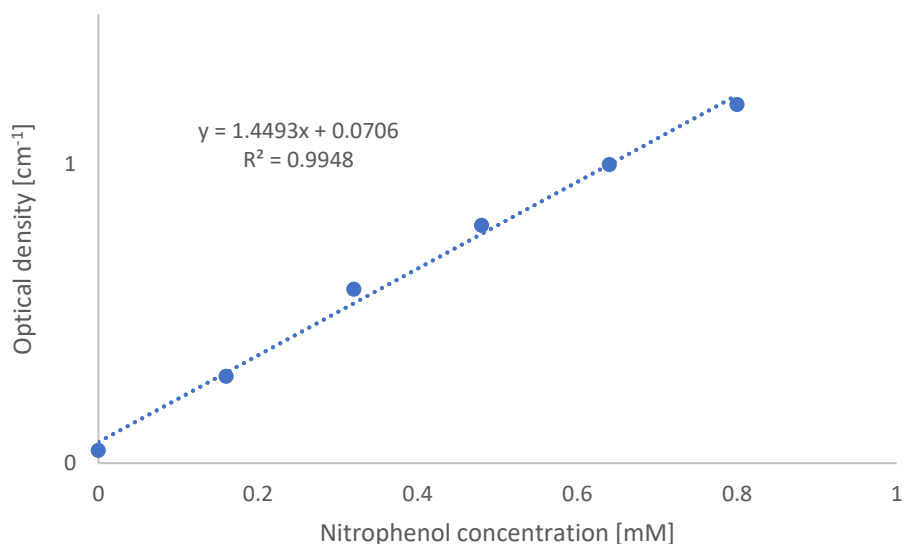


**Figure 100.** The standard curve of nitrophenol, product of reaction between human carbonic anhydrase and nitrophenol ester. The absorbance was gathered with an end-point mode, at 405 nm. Experimental data points were averaged over 3 repeats.



After all samples were ready, with estimated concentration of the protein of 5.2  $\mu\text{M}$ , for the final measurements, 1, 2, 5 and 10  $\mu\text{L}$  (in duplicates) of all test samples (samples 1 & 2) were diluted to 95  $\mu\text{L}$  volume with CA Assay Buffer. Commercially available sample of hCAII in 20 mM Tris buffer pH=7.5 (with 150 mM NaCl) was used as a positive control and negative control; 10  $\mu\text{L}$  of the obtained solution was diluted to 95  $\mu\text{L}$  as a positive control sample (no Acetazolamide, inhibitor of hCAII) and negative control sample (with 2  $\mu\text{L}$  of the 20 mM inhibitor solution). The absorbance of all the samples was measured at 405 nm in a kinetic mode for 1 h at RT (for absorbance of the product of reaction, nitrophenol). The experiment was repeated in duplicates. The direct results of the measurements are presented in the **Figure 101**.

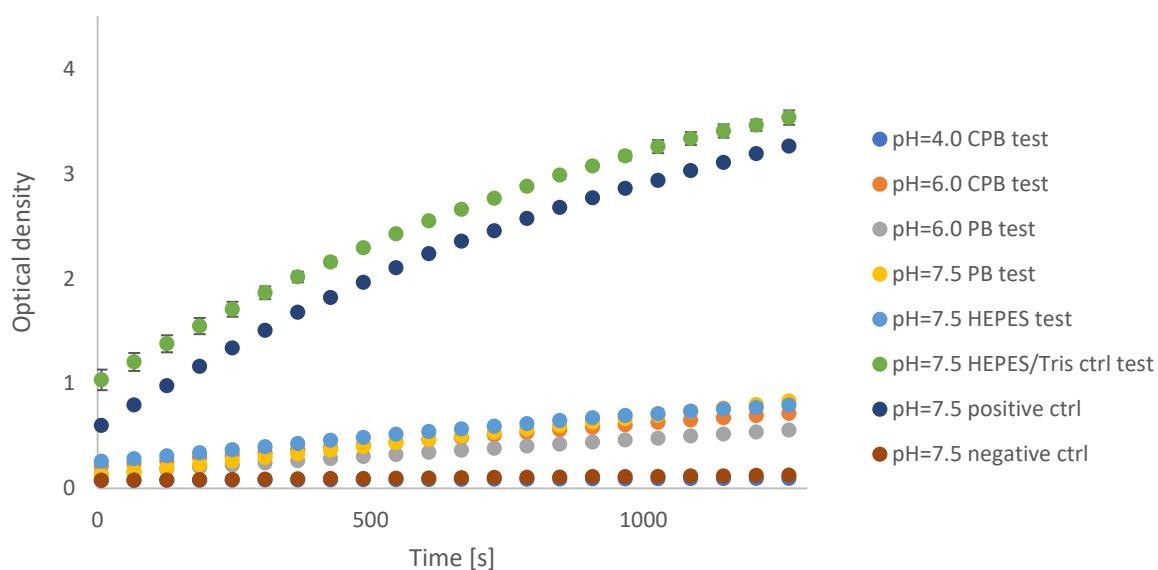


**Figure 101.** The comparison of optical density studies for the tested samples, positive control and negative control. The absorbance was gathered with an end-point mode, at 405 nm. All the compared solutions contained 0.52  $\mu\text{M}$  of each protein sample (10X dilution). Error bars represent standard error of mean of 2 measurements. Positive control – commercially available non-labeled hCAII diluted to 0.52  $\mu\text{M}$  concentration with substrate of hCAII added (nitrophenol ester); negative control - commercially available hCAII diluted to 0.52  $\mu\text{M}$  concentration with substrate of hCAII added (nitrophenol ester) and inhibitor of hCAII (Acetazolamide); CPB – citrate phosphate buffer; PB – phosphate buffer; ctrl – control sample; test – tested samples after pH-measurement studies in the subchapter **4.3.4**.

The analysis of the data combined in the **Figure 101** shows that the control sample used in the subchapter **4.3.3**. (no presence of the **SOLpH1-Tos** probe, no labeling with **SOLpH1**) has the highest enzymatic activity, with values higher even in comparison with the positive control (commercially available, non-labeled hCAII diluted to 0.52  $\mu\text{M}$  concentration with substrate of hCAII added, nitrophenol ester). Since the control sample was equipped with the substrate (nitrophenol ester) earlier than the positive control sample it is highly probable that the difference derives only from a time-delay (the first few time-point measurements were omitted for the first sample because of the addition time of the substrate to the other wells). The results in the **Figure 102** indicate that in fact the freshly prepared non-labeled hCAII solution presented a higher enzymatic rate.

All the test samples (from CPB 4.0, 6.0; PB 6.0, 7.5; HEPES 7.5 – samples used in the subchapter **4.3.4.**) presented decreased activity in comparison to the control positive sample and the one incubated for 48 h at pH=7.5 (**Figure 101, 102**). Especially, conditions of experiments of pH=4.0 in CPB sample occurred to be extremely non-optimal (rate-decreasing) for the hCAII enzymatic activity. The pH=7.5 (both HEPES and PB) **SOLpH1**-hCAII diluted samples presented a reduced activity rate as well. According to the literature, even though His64 is not directly engaged in zinc-binding in hCAII active site, the rate-limiting step involves an intramolecular proton transfer from the zinc-bound water molecule to His64, which acts as a proton shuttle, facilitating proton movement between the metal center and buffer molecules in the reaction medium [110]. Therefore, there are two possible reasons for the inhibited activity of hCAII for the sample diluted from CPB pH=4.0 and partial reduction of the activity pH=7.5 (as the pH is understood as proton activity, which is still relatively high at pH=7.5 in comparison to pH=4.0). The first reason takes into account the labeling of the **SOLpH1** at His64, limiting the activity of the labeled hCAII (lack of possibility of His64 transient protonation). Secondly, since the labeling yield for ligand-directed technology is estimated to reach 75% in 48h [308],  $\frac{1}{4}$  of the sample may have been a non-labeled fraction of hCAII and in fact it may have been inhibited by a decreased solution pH (less at pH=7.5 and more at pH=4.0). Since the product of the activity assay kit did not provide the details about molarity of CA Assay Buffer, it is highly possible that CA Assay Buffer did not overcome the buffering capacity of the diluted CPB pH=4.0 or PB/HEPES pH=7.5 samples. It is expected that the lower pH, the less available is His64 (more protonated His64 of hCAII are in the solution and less of them is available for the proton transfer), significantly slowing down the enzymatic process. Moreover, it was suggested that the His64 conformation is highly dependent on pH of the solution and it rotates away from its active site at low pH (pH=5.7; where it is in fact needed for hCAII enzymatic activity) [433]. The protonation and/or rotation of His64 may have practically inhibited the non-labeled enzyme activity for the pH=4.0 sample and significantly reduced the one at pH=7.5. Therefore, the outcome of pH=4.0 sample analysis is comparable to the one presented by a negative control and the pH=7.5 one presents still reduced activity to the positive control sample, even though the estimated protein concentration was similar to the one used for positive control or the 48h incubated control sample from the subchapter **4.3.3.**

To assess the enzymatic activity, two time points ( $t_1$  and  $t_2$ ) within the linear range of the plot for each tested sample were selected, and the corresponding absorbance values ( $A_1$  and  $A_2$ ) were recorded. The change in absorbance over time ( $\Delta A/\Delta t$ ) was then calculated. With use of the nitrophenol standard curve (**Figure 100**), specific CA activity of the tested samples was determined. The results are presented in the **Figure 102**. The rate for the test samples (CPB 6.0; PB 6.0, 7.5; HEPES 7.5) is not fully compromised in comparison to the positive control. The higher pH of the starting buffer, the more increase is observed in reaction rate. The latter confirms the previous hypothesis of the crucial effect of general sample pH on the hCAII activity and low buffering capacity of the CA Assay Buffer. As labeling of the **SOLpH1-Tos** molecule occurred at His64, it is possible that only the non-labeled form of hCAII present in the test solutions was responsible for the enzymatic activity observed in the **Figure 101** and **102**.

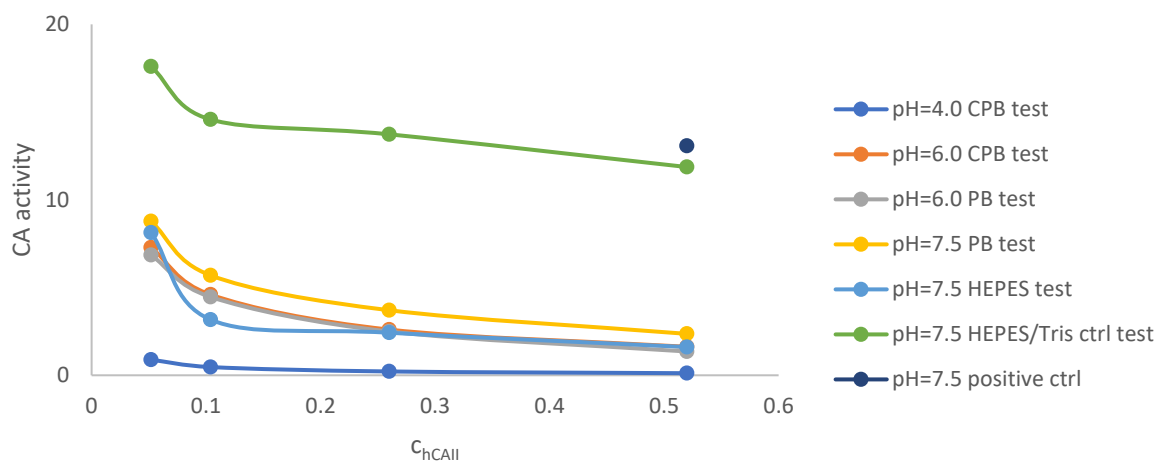


**Figure 102.** The CA activity presented by the tested samples. One unit of CA activity is defined as the amount of enzyme required to catalyze the release of 1  $\mu\text{mol}$  of nitrophenol per minute from the substrate under assay conditions at 25°C.  $c_{hCAII}$  – concentration of hCAII in tested samples; Positive control – commercially available non-labeled hCAII diluted to 0.52  $\mu\text{M}$  concentration with substrate of hCAII added (nitrophenol ester); CPB – citrate phosphate buffer; PB – phosphate buffer; ctrl – control sample; test – tested samples after pH-measurement studies in the subchapter 4.3.4. Calculated values were connected with a line, which is there as a guideline for eyes to obtain a visual effect of the continuous line.

#### 4.4. Summary and discussion

Within the course of work, three novel environment-sensitive probes were designed, synthesized and analyzed. The first two, **SOLpH1** and **SOLpH2**, are pH/polarity/viscosity-responsive molecules, based on SBD and on 1,8-naphthalimide cores, respectively. While both of them exhibit similar optical and intracellular properties, the **SOLpH1** occurred to present superior characteristics (pH-, polarity-, viscosity-sensitivity and use of similar core in the literature for nanoenvironment studies) and was introduced to the final probe structure, **SOLpH1-Tos**. The latter is an affinity-based probe, with ability to label protein of choice, human carbonic anhydrase II, in a close proximity to the enzyme's active site.

The **SOLpH1-Tos** successfully labeled hCAII and as a result the **SOLpH1** probe was covalently introduced into the protein structure at His64 amino acid. After purification of the labeled hCAII, pH-dependent emission studies as well as activity assay for the **SOLpH1**-hCAII were conducted. The first **SOLpH1**-hCAII experiments confirmed the ability of **SOLpH1** to sense pH changes of the surrounding environment. The second study showed that the covalent connection of the **SOLpH1** and His64 may have resulted in a reduction of the hCAII activity. The effect of decreased pH of solution had a similar effect – protonation of His64 disrupts the catalytic mechanism of hCAII.

While the labeling studies and pH-monitoring ones were successful, the consequential inhibition of the hCAII natural activity reduces possibility of monitoring of the natural *in cellulo* activity of hCAII with use of the obtained probe **SOLpH1-Tos**. To empower the technology, introduction of a longer linker between reversible ligand and reactive group could result in labeling of amino acid, which is not at the entrance of the active site, to reduce the disruption of enzyme's native activity. Nevertheless, the **SOLpH1-Tos** is a first pH-sensitive probe covalently connected to the protein of interest, hCAII, without need of the protein genetic modification. This novel probe displays utility in pH-based experiments, and once attached on human carbonic anhydrase II, could provide insight into minor pH changes in immediate proximity to the active site of the enzyme. Such local pH changes may be critical for protein function, potentially crucial to physiological and pathological processes.

## 5. Conclusions and future impact

The doctoral dissertation presented design, synthesis, *in vitro* and *in cellulo* studies of environment-sensitive fluorophores based on two scaffolds: 4-sulfonamide benzo[*c*][1,2,5]oxadiazole (**SOLpH1**; **Figure 103**, top) and 1,8-naphthalimide (**SOLpH2**; **Figure 103**, middle). *In vitro* studies confirmed designed pH-sensitivity of the synthesized probes, as well as their polarity-sensitivity. The obtained molecules additionally showed responsiveness to viscosity changes. Calculated  $pK_a$  of both of them is lower than an average pH present in healthy, non-cancerous cells, thus pH-sensing properties of the probes may be used to observe non-desired fluctuations towards lower pH understood as slight imbalance in cellular homeostasis. pH-sensing properties of both probes **SOLpH1** and **SOLpH2** were studied *in cellulo* with incubation with buffers of chosen pH, where the results indicated that the probe **SOLpH1** presents ratiometric response to pH changes with higher signal in case of lower pH value, while **SOLpH2** presented turn-on response from pH=7.5 (off) to pH=5.0 (on). As the next step, the probe **SOLpH1** was introduced into an affinity-based labeling probe **SOLpH1-Tos** (**Figure 103**, bottom), bearing ligand for protein of choice (human carbonic anhydrase II, hCAII) and reactive group. The *in vitro* labeling experiments of hCAII confirmed the labeling of histidine (His64) at the entrance of active site of the protein. The last synthesized compound is to the best of our knowledge the first pH-sensitive probe for affinity-driven labeling of a protein target without a need of genetically encoded tag.

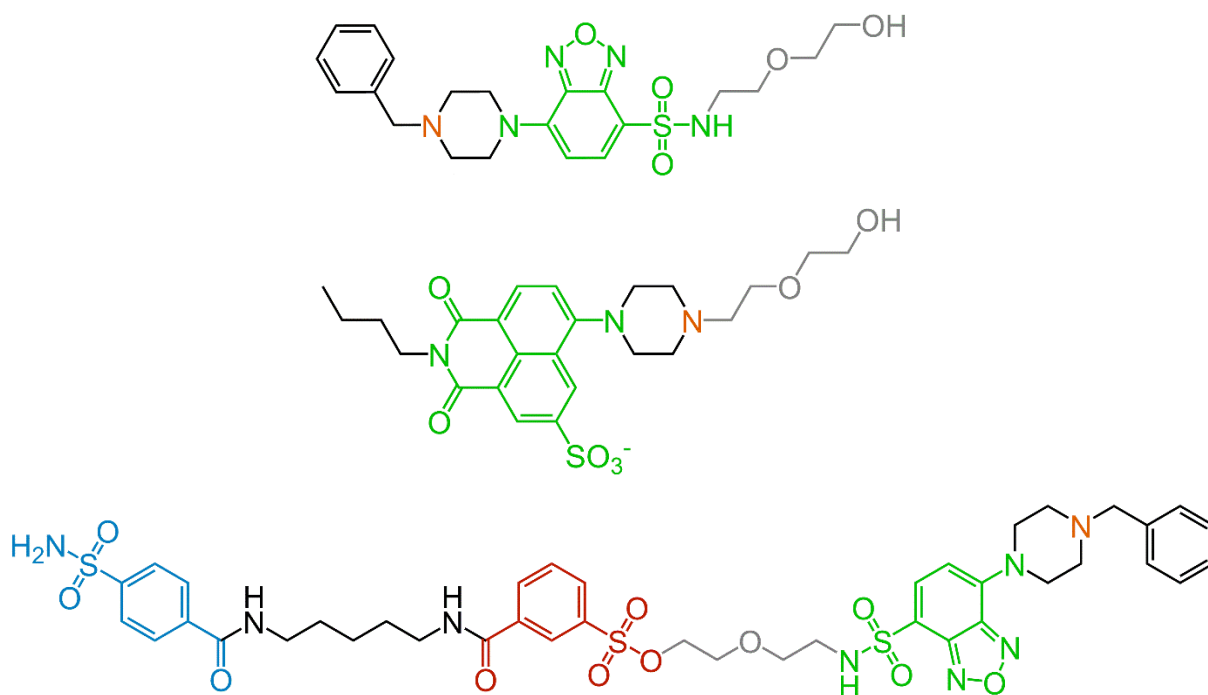


**Figure 103.** The structures of molecules designed, synthesized and studied within the thesis: (top) **SOLpH1**, (middle) **SOLpH2**, (bottom) **SOLpH1-Tos**. The fluorophore part is marked with green color (with orange-marked nitrogen as pH-sensor), reactive group with red one, ligand for human carbonic anhydrase II (hCAII) with blue one and PEG linker with gray one.

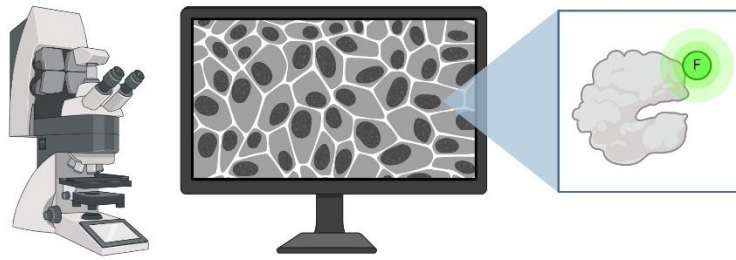
The utility of the obtained pH-probes, **SOLpH1** and **SOLpH2**, lies in their wide solubility in a range of solvents or solutions with various physicochemical properties (very well soluble due to PEG). Notably, the wider solubility range of **SOLpH1** resulted in the ability to determine the average intracellular polarity of both non-cancerous (HEK293T) and cancerous (A549) cells. Moreover, the cellular permeability of **SOLpH1** and **SOLpH2** presents a possibility to monitor the intracellular pH changes, especially in case of **SOLpH1**, which is not fully transported towards lysosomes, with combination of fluorescence imaging techniques (for example FLIM and confocal).

The use of the affinity-based technology presents multiple promising perspectives. One of the biggest advantages of the presented approach is the relatively fast solid-phase-based synthesis of the desired probe without multiple purification steps (otherwise non-avoidable in the traditional synthesis approach). Moreover, in case of rather stable fluorophore scaffolds, re-purification after the final step enables re-use of fluorophore for other syntheses (especially that the fluorophore synthesis is frequently the most time-consuming part).

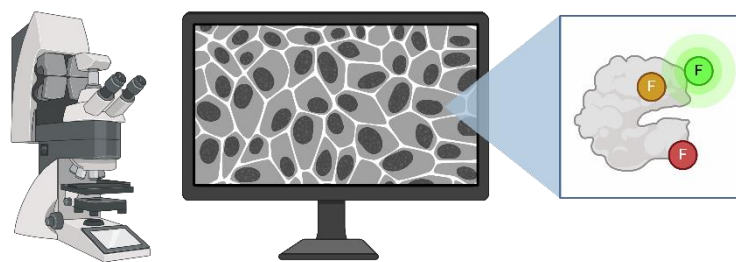
Even though the last probe, **SOLpH1-Tos**, occurred to limit the enzymatic activity of human carbonic anhydrase II, two additional conclusions may be drawn from the results. Firstly, the study confirmed the importance of His64 in the enzyme function, even though it is not considered a direct ligand for zinc ion. Secondly, it opens a possibility of modification of the linker between a hCAII-ligand and reactive group to create a library of ligand-directed probes (to possibly label the amino acids less crucial in the enzymatic activity). This leads to general utility of ligand-directed technology, as each of the probe's part may be exchanged by another one. Such a library could include a set of analogous probes with differing reporter part (fluorophore). These reporters ideally would not have overlapping absorption and emission spectra, be close to near-infrared (NIR) window and would enable monitoring of different sites of one chosen protein (to look into microenvironment around the active site). Use of super-resolution techniques (STED, MINIFLUX – both available in our laboratory) for fluorescence imaging presents a unique perspective to look into microenvironment changes in immediate proximity to the active site, at unprecedented resolution (**Figure 104**). The proteins are a majority of dry weight of cells (and tissues; 68%) and they are a main target of the oxidative damage [434]. Investigation of environment (including pH, with its huge impact on redox processes in amino acid modifications [435]) fluctuations around protein's active site may provide valuable information about natural enzymatic activity as well as malfunctions connected with pathogenesis processes (**Figure 104**). Moreover, the affinity-based approach may be as well successfully used for studies of ligand-protein interactions (even high-throughput ones):

- to identify new ligands for known proteins (new drugs development or studies of side effects of already registered drugs; then instead of fluorophore part, an affinity-based part as a biotin may be introduced to isolate the hits) (**Figure 104**) or
- to identify ligands for proteins with unknown ligands (**Figure 104**) or isolate unknown proteins with use of those ligands, as it is estimated that human body has 80 000 – 400 000 proteins, from where only 18 000 protein-coding genes were identified and the rest of them are considered a so-called dark proteome [436, 437].

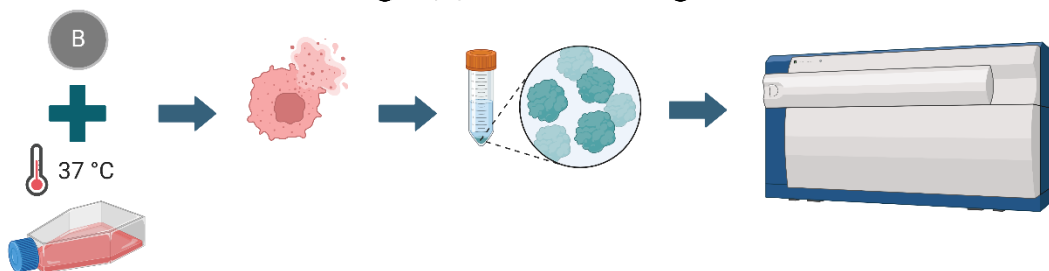
### Monitoring of protein microenvironment



### Monitoring of protein microenvironment at different sites



### Identification of unknown protein target(s) for known ligands



### Identification of unknown ligands for known proteins

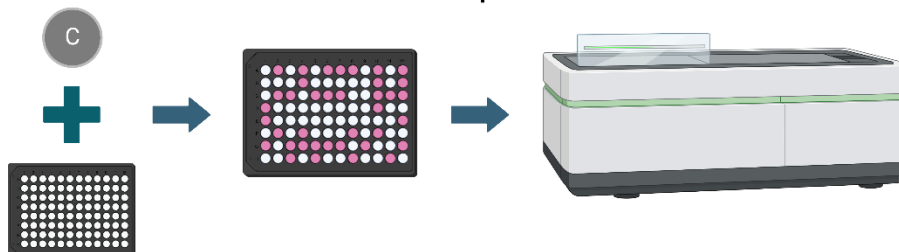


**Figure 104.** Schematic representation of main perspectives for the achievements of the thesis. F – ligand-directed probe with a fluorophore part (different colors symbolize various color emission); B – ligand-directed probe with a biotin part instead of fluorophore; C – ligand-directed probe with click-chemistry handle instead of fluorophore (to enable washing of the samples to get rid of non-reacted probe). Created with BioRender.com.

## 6. Bibliography

1. Wolkenhauer O, Muir A (2011) The complexity of cell-biological systems. *Philos Complex Syst* 10:355–385
2. Haddad LA (2019) Cellular structure and molecular cell biology. Academic Press Inc.
3. Barthes J, Özçelik H, Hindié M, Ndreu-Halili A, Hasan A, Vrana NE (2014) Cell microenvironment engineering and monitoring for tissue engineering and regenerative medicine: The recent advances. *Biomed Res Int* 2014:921905
4. Chaudhuri O, Cooper-White J, Janmey PA, Mooney DJ, Shenoy VB (2020) The impact of extracellular matrix viscoelasticity on cellular behavior. *Nature* 584(1):535–546
5. Diekmann Y, Pereira-Leal JB (2013) Evolution of intracellular compartmentalization. *Biochem J* 449(2):319–331
6. Coleman WB, Tsongalis GJ (2018) Understanding molecular pathogenesis: The biological basis of human disease and implications for improved treatment of human, Second Edi. Elsevier Inc.
7. Schauenburg D, Weil T (2024) Chemical reactions in living systems. *Adv Sci* 11(8):1–22
8. Xie XS, Lu HP (1999) Single-molecule enzymology. *J Biol Chem* 274(23):15967–15970
9. Berrones-Reyes JC, Vidyasagar CC, Muñoz Flores BM, Jiménez-Pérez VM (2018) Luminescent molecules of main group elements: Recent advances on synthesis, properties and their application on fluorescent bioimaging (FBI). *J Lumin* 195(August 2017):290–313
10. Wang K, Sun XH, Zhang Y, et al (2019) Characterization of cytoplasmic viscosity of hundreds of single tumour cells based on micropipette aspiration. *R Soc Open Sci* 6(3):181707
11. Larsen DLD, Gaudreault N, Gibbs HC (2023) Reporting reproducible imaging protocols. *STAR Protoc* 4(1):102040
12. Reichardt C (1994) Solvatochromic dyes as solvent polarity indicators. *Chem Rev* 94(8):2319–2358
13. Li M, Fan J, Li H, Du J, Long S, Peng X (2018) A ratiometric fluorescence probe for lysosomal polarity. *Biomaterials* 164:98–105
14. Slakman BL, West RH (2019) Kinetic solvent effects in organic reactions. *J Phys Org Chem* 32(3):1–12
15. Das M, Gogoi AR, Sunoj RB (2022) Molecular insights on solvent effects in organic reactions as obtained through computational chemistry tools. *J Org Chem* 87(3):1630–1640
16. Prezhdo O V., Craig CF, Fialkov Y, Prezhdo V V. (2007) Control of chemical equilibrium by solvent: A basis for teaching physical chemistry of solutions. *J Chem Educ* 84(8):1348–1354
17. Aravindhana R, Hu J, Momeen MU (2023) Role of the solvent polarity on the optical and electronic characteristics of 1-iodoadamantane. *RSC Adv* 13(42):29489–29495
18. Ercelen S, Klymchenko AS, Demchenko AP (2002) Ultrasensitive fluorescent probe for the hydrophobic range of solvent polarities. *Anal Chim Acta* 464(2):273–287
19. Rondan NG, Houk KN, Beak P, Zajdel WJ, Chandrasekhar J, Schleyer P v. R (1981) Dipole stabilization of  $\alpha$ -heteroatom carbanions: Theory and experiment. *J Org Chem* 46(20):4108–4110



20. Beak P, Reitz DB (1978) Dipole-stabilized carbanions: Novel and useful intermediates. *Chem Rev* 78(3):275–316
21. Spange S, Sens R, Zimmermann Y, Seifert A, Roth I, Anders S, Hofmann K (2003) A solvatochromic dye for probing significantly the dipolarity/polarizability of HBD (hydrogen bond donating) environments. *New J Chem* 27(3):520–524
22. Aqvist J, Luecke H, Quioco FA, Warshel A (1991) Dipoles localized at helix termini of proteins stabilize charges. *Proc Natl Acad Sci U S A* 88(5):2026–2030
23. Lockhart DJ, Kim PS (1993) Electrostatic screening of charge and dipole interactions with the helix backbone. *260(5105):198–202*
24. Doyle DA, Cabral M, Pfuetzner RA, Kuo A, Gulbis JM, Cohen SL, Chait BT, Mackinnon R (1998) The structure of the potassium channel: Molecular basis of K<sup>+</sup> conduction and selectivity. *Science* (80- ) 280(April):1–9
25. Noskov SY, Roux B (2006) Ion selectivity in potassium channels. *Biophys Chem* 124(3):279–291
26. Mao B, Pear MR, McCammon JA, Quioco FA (1982) Hinge-bending in L-arabinose-binding protein. The “Venus’s-flytrap” model. *J Biol Chem* 257(3):1131–1133
27. Riera T V., Zheng L, Josephine HR, Min D, Yang W, Hedstrom L (2011) Allosteric activation via kinetic control: Potassium accelerates a conformational change in IMP dehydrogenase. *Biochemistry* 50(39):8508–8518
28. Schwartz SL, Cao C, Pylpenko O, et al (2013) Crystal structure of a SNARE complex involved in synaptic resolution exocytosis at 2.4 Å. *Cell* 6(2):1–8
29. Scales SJ, Yoo BY, Scheller RH (2001) The ionic layer is required for efficient dissociation of the SNARE complex by  $\alpha$ -SNAP and NSF. *Proc Natl Acad Sci U S A* 98(25):14262–14267
30. Sippel KH, Quioco FA (2015) Ion-dipole interactions and their functions in proteins. *Protein Sci* 24(7):1040–1046
31. Yang Z, Cao J, He Y, Yang JH, Kim T, Peng X, Kim JS (2014) Macro-/micro-environment-sensitive chemosensing and biological imaging. *Chem Soc Rev* 43(13):4563–4601
32. Michalet X, Weiss S, Jäger M (2006) Single-molecule fluorescence studies of protein folding and conformational dynamics. *Chem Rev* 106(5):1785–1813
33. Porter CT, Bartlett GJ, Thornton JM (2004) The Catalytic Site Atlas: A resource of catalytic sites and residues identified in enzymes using structural data. *Nucleic Acids Res* 32:129–133
34. Callaway DJE (1994) Solvent-induced organization: A physical model of folding myoglobin. *Proteins Struct Funct Bioinforma* 20(2):124–138
35. Compiani M, Capriotti E (2013) Computational and theoretical methods for protein folding. *Biochemistry* 52(48):8601–8624
36. Pace CN, Shirley BA, McNutt M, Gajiwala K (1996) Forces contributing to the conformational stability of proteins. *Faseb J* 10(1):75–83
37. Sarkar DK, Surpeta B, Brezovsky J (2024) Incorporating prior knowledge to seeds of adaptive sampling molecular dynamics simulations of ligand transport in enzymes with buried active sites. *J Chem Theory Comput* 20:5807–5819
38. Pravda L, Berka K, Svobodová Vařeková R, Sehnal D, Banáš P, Laskowski RA, Koča J, Otyepka M (2014) Anatomy of enzyme channels. *BMC Bioinformatics* 15(1):1–8

39. Escalante DE, Aksan A (2019) Prediction of ligand Transport along hydrophobic enzyme nanochannels. *Comput Struct Biotechnol J* 17:757–760
40. Kaushik S, Marques SM, Khirsariya P, Paruch K, Libichova L, Brezovsky J, Prokop Z, Chaloupkova R, Damborsky J (2018) Impact of the access tunnel engineering on catalysis is strictly ligand-specific. *FEBS J* 285(8):1456–1476
41. Simons K, Toomre D (2000) Lipid rafts and signal transduction. *Nat Rev Mol Cell Biol* 1(1):31–39
42. Munro S (2003) Lipid Rafts: Elusive or Illusive? *Cell* 115(4):377–388
43. Anderson RGW, Jacobson K (2002) Cell biology: A role for lipid shells in targeting proteins to caveolae, rafts, and other lipid domains. *Science* (80- ) 296(5574):1821–1825
44. Mukherjee S, Maxfield FR (2004) Membrane domains. *Annu Rev Cell Dev Biol* 20:839–866
45. Rahimi H, Salehiabar M, Charmi J, et al (2020) Harnessing nanoparticles for the efficient delivery of the CRISPR/Cas9 system. *Nano Today* 34:100895
46. Qin X, Yang X, Du L, Li M (2021) Polarity-based fluorescence probes: properties and applications. *RSC Med Chem* 12(11):1826–1838
47. Butler MT, Wallingford JB (2017) Planar cell polarity in development and disease. *Nat Rev Mol Cell Biol* 18(6):375–388
48. Shao T, Liu T, Liu H, Zhang M, Shen Y, Gao A, Tian X, Zhang Q, Wu J, Tian Y (2019) Identification of fatty liver disease at diverse stages using two-photon absorption of triphenylamine-based BODIPY analogues. *J Mater Chem B* 7(23):3704–3709
49. Wang H, Dong M, Wang H, Huang F, Li P, Zhang W, Zhang W, Tang B (2021) Ultrasensitive and ratiometric two-photon fluorescence imaging of Golgi polarity during drug-induced acute kidney injury. *Chem Commun* 57(47):5838–5841
50. Wan W, Zeng L, Jin W, et al (2021) A solvatochromic fluorescent probe reveals polarity heterogeneity upon protein aggregation in cells. *Angew Chemie - Int Ed* 60(49):25865–25871
51. Biswas S, Baruah M, Shil A, Sarkar S, Ali M, Samanta A, Bhuniya S (2023) Polarity-driven two-photon fluorescent probe for monitoring the perturbation in lipid droplet levels during mitochondrial dysfunction and acute pancreatitis. *ACS Sensors* 8(10):3793–3803
52. Javorsky A, Humbert PO, Kvensakul M (2023) Viral manipulation of cell polarity signalling. *Biochim Biophys Acta - Mol Cell Res* 1870(7):119536
53. Xiao H, Li P, Tang B (2021) Recent progresses in fluorescent probes for detection of polarity. *Coord Chem Rev* 427:213582
54. Spange S, Weiß N, Schmidt CH, Schreiter K (2021) Reappraisal of empirical Solvent polarity scales for organic solvents. *Chemistry-Methods* 1(1):42–60
55. Zharkova OM, Morozova YP (2013) Use of fluorescent probes to estimate solvent polarity. *Russ Phys J* 56(3):257–263
56. Kudo K, Momotake A, Kanna Y, Nishimura Y, Arai T (2011) Development of a quinoxaline-based fluorescent probe for quantitative estimation of protein binding site polarity. *Chem Commun* 47(13):3867–3869
57. Momen-Heravi F, Balaj L, Alian S, Trachtenberg AJ, Hochberg FH, Skog J, Kuo WP (2012) Impact of biofluid viscosity on size and sedimentation efficiency of the isolated microvesicles.

Front Physiol (May):1–6

58. Kuimova MK (2012) Mapping viscosity in cells using molecular rotors. *Phys Chem Chem Phys* 14(37):12671–12686
59. Yin J, Huang L, Wu L, Li J, James TD, Lin W (2021) Small molecule based fluorescent chemosensors for imaging the microenvironment within specific cellular regions. *Chem Soc Rev* 50(21):12098–12150
60. Magni A, Bondelli G, Paternò GM, Sardar S, Sesti V, D'Andrea C, Bertarelli C, Lanzani G (2022) Azobenzene photoisomerization probes cell membrane viscosity. *Phys Chem Chem Phys* 24:8716–8723
61. Kashirina AS, López-Duarte I, Kubánková M, Gulín AA, Dudenkova V V., Rodimova SA, Torgomyan HG, Zagaynova E V., Meleshina A V., Kuimova MK (2020) Monitoring membrane viscosity in differentiating stem cells using BODIPY-based molecular rotors and FLIM. *Sci Rep* 10(1):1–12
62. Kubánková M, Summers PA, López-Duarte I, Kiryushko D, Kuimova MK (2019) Microscopic viscosity of neuronal plasma membranes measured using fluorescent molecular rotors: effects of oxidative stress and neuroprotection. *ACS Appl Mater Interfaces* 11(40):36307–36315
63. Mukherjee T, Soppina V, Ludovic R, Mély Y, Klymchenko AS, Collot M, Kanvah S (2021) Live-cell imaging of the nucleolus and mapping mitochondrial viscosity with a dual function fluorescent probe. *Org Biomol Chem* 19(15):3389–3395
64. Quan W, Zhang G, Huang L, Song W, Lin W (2021) A novel fluorescent probe for high-fidelity imaging of mitochondria viscosity changes. *J Mol Liq* 333:115973
65. Silswal A, Kanojiya A, Koner AL (2022) A fluorogenic far red-emitting molecular viscometer for ascertaining lysosomal stress in live cells and *Caenorhabditis elegans*. *Front Chem* 10(March):1–9
66. Liu T, Liu X, Spring DR, Qian X, Cui J, Xu Z (2014) Quantitatively mapping cellular viscosity with detailed organelle information via a designed PET fluorescent probe. *Sci Rep* 4(5418):1–7
67. Yang Z, Fan J, Peng X (2011) Fluorescence ratiometry and fluorescence lifetime (FLIM) imaging: Dual mode imaging cellular viscosity by a single molecular rotor. *JACS* 133:6626–6635
68. Kuimova MK, Botchway SW, Parker AW, Balaz M, Collins HA, Anderson HL, Suhling K, Ogilby PR (2009) Imaging intracellular viscosity of a single cell during photoinduced cell death. *Nat Chem* 1(1):69–73
69. Sun M, Wang T, Yang X, Yu H, Wang S, Huang D (2021) Facile mitochondria localized fluorescent probe for viscosity detection in living cells. *Talanta* 225(November 2020):121996
70. Haidekker MA, Ling T, Anglo M, Stevens HY, Frangos JA, Theodorakis EA (2001) New fluorescent probes for the measurement of cell membrane viscosity. *Chem Biol* 8(2):123–131
71. Wray S (1988) Smooth muscle intracellular pH: Measurement, regulation, and function. *Am J Physiol - Cell Physiol* 254(2):213–225
72. Moolenaar WH (1986) Effects of growth factors on intracellular pH regulation. *Annu Rev Physiol* VOL. 48:363–376
73. Lagadic-Gossman D, Huc L, Lecreur V (2004) Alterations of intracellular pH homeostasis in apoptosis: Origins and roles. *Cell Death Differ* 11(9):953–961

74. Bi Y, Di H, Zeng E, Li Q, Li W, Yang J, Liu D (2020) Reliable quantification of pH variation in live cells using Prussian Blue-caged surface-enhanced Raman scattering probes. *Anal Chem* 92(14):9574–9582
75. Sinning A, Hübner CA (2013) pH and synaptic transmission. *FEBS Lett* 587(13):1923–1928
76. Chen L, Wu L, Yu J, Kuo CT, Jian T, Wu IC, Rong Y, Chiu DT (2017) Highly photostable wide-dynamic-range pH sensitive semiconducting polymer dots enabled by dendronizing the near-IR emitters. *Chem Sci* 8(10):7236–7245
77. Zeng J, Shirihai OS, Grinstaff MW (2020) Modulating lysosomal pH: a molecular and nanoscale materials design perspective. *J Life Sci* 2(4):25–37
78. Casey JR, Grinstein S, Orlowski J (2010) Sensors and regulators of intracellular pH. *Nat Rev Mol Cell Biol* 11(1):50–61
79. Whitten ST, García-Moreno E. B, Hilser VJ (2005) Local conformational fluctuations can modulate the coupling between proton binding and global structural transitions in proteins. *Proc Natl Acad Sci U S A* 102(12):4282–4287
80. Trivedi B, Danforth WH (1966) Effect of pH on the kinetics of frog muscle phosphofructokinase. *J Biol Chem* 241(17):4110–4112
81. Pouysségur J, Franchi A, L'Allemain G, Paris S (1985) Cytoplasmic pH, a key determinant of growth factor-induced DNA synthesis in quiescent fibroblasts. *FEBS Lett* 190(1):115–119
82. Romero MF, Rossano AJ (2019) Acid-base basics. *Semin Nephrol* 39(4):316–327
83. Roos A, Boron WF (1981) Intracellular pH. *Physiol Rev* 61(2):249–514
84. Huang YMM, Kang M, Chang CEA (2014) Switches of hydrogen bonds during ligand-protein association processes determine binding kinetics. *J Mol Recognit* 27(9):537–548
85. Neti SS, Pan JJ, Poulter CD (2018) Mechanistic studies of the protonation-deprotonation reactions for type 1 and type 2 isopentenyl diphosphate:dimethylallyl diphosphate isomerase. *J Am Chem Soc* 140(40):12900–12908
86. Jaworska A, Malek K, Kudelski A (2021) Intracellular pH – Advantages and pitfalls of surface-enhanced Raman scattering and fluorescence microscopy – A review. *Spectrochim Acta - Part A Mol Biomol Spectrosc* 251:119410
87. Czowski BJ, Romero-Moreno R, Trull KJ, White KA (2020) Cancer and pH dynamics: Transcriptional regulation, proteostasis, and the need for new molecular tools. *Cancers (Basel)* 12(10):1–19
88. Schwartz L, Peres S, Jolicoeur M, da Veiga Moreira J (2020) Cancer and Alzheimer's disease: intracellular pH scales the metabolic disorders. *Biogerontology* 21(6):683–694
89. Schwartz L, Peres S, Jolicoeur M, da Veiga Moreira J (2020) Cancer and Alzheimer's disease: intracellular pH scales the metabolic disorders. *Biogerontology* 21(6):683–694
90. Han J, Burgess K (2010) Fluorescent indicators for intracellular pH. *Chem Rev* 110(5):2709–2728
91. Mai H, Wang Y, Li S, Jia R, Li S, Peng Q, Xie Y, Hu X, Wu S (2019) A pH-sensitive near-infrared fluorescent probe with alkaline pKa for chronic wound monitoring in diabetic mice. *Chem Commun* 55(51):7374–7377
92. Stratton SG, Taumoefolau GH, Purnell GE, Rasooly M, Czaplowski WL, Harbron EJ (2017) Tuning

- the pKa of fluorescent rhodamine pH probes through substituent effects. *Chem - A Eur J* 23(56):14064–14072
93. Wang R, Yu C, Yu F, Chen L, Yu C (2010) Molecular fluorescent probes for monitoring pH changes in living cells. *TrAC - Trends Anal Chem* 29(9):1004–1013
  94. Steinegger A, Wolfbeis OS, Borisov SM (2020) Optical sensing and imaging of pH values: Spectroscopies, materials, and applications. *Chem Rev* 120(22):12357–12489
  95. Schniererová K, Janeková H, Joniak J, Putala M, Štacko P, Stankovičová H (2024) pH-responsive aminobenzocoumarins as fluorescent probes for biological acidity. *Chem - A Eur J* 30(28):1–8
  96. Liu S, Hoess P, Ries J (2022) Super-resolution microscopy for structural cell biology. *Annu Rev Biophys* 51:301–326
  97. Yan R, Wang B, Xu K (2019) Functional super-resolution microscopy of the cell. *Curr Opin Chem Biol* 51:92–97
  98. Masullo LA, Szalai AM, Lopez LF, Pilo-Pais M, Acuna GP, Stefani FD (2022) An alternative to MINFLUX that enables nanometer resolution in a confocal microscope. *Light Sci Appl* 11:199
  99. Henry RP (1984) The role of carbonic anhydrase in blood ion and acid-base regulation. *Integr Comp Biol* 24(1):241–251
  100. Lindskog S, Coleman JE (1973) The catalytic mechanism of carbonic anhydrase. *Proc Natl Acad Sci U S A* 70(9):2505–2508
  101. Nocentini A, Supuran CT (2008) Carbonic anhydrases: An overview. *Carbon Anhydrases Biochem Pharmacol an Evergr Pharm Target* (14):603–614
  102. O’Herin CB, Moriuchi YW, Bemis TA, Kohlbrand AJ, Burkart MD, Cohen SM (2023) Development of human carbonic anhydrase II heterobifunctional degraders. *J Med Chem* 66(4):2789–2803
  103. Hazen SA, Waheed A, Sly WS, Lanoue KF, Lynch CJ (1996) Differentiation-dependent expression of CA V and the role of carbonic anhydrase isozymes in pyruvate carboxylation in adipocytes. *FASEB J* 10(4):481–490
  104. Mishra CB, Tiwari M, Supuran CT (2020) Progress in the development of human carbonic anhydrase inhibitors and their pharmacological applications: Where are we today? *Med Res Rev* 40(6):2485–2565
  105. Hassan MI, Shajee B, Waheed A, Ahmad F, Sly WS (2013) Structure, function and applications of carbonic anhydrase isozymes. *Bioorganic Med Chem* 21(6):1570–1582
  106. Lomelino CL, Andring JT, McKenna R (2018) Crystallography and its impact on carbonic anhydrase research. *Int J Med Chem* 2018:1–21
  107. Angeli A, Carta F, Supuran CT (2020) Carbonic anhydrases: Versatile and useful biocatalysts in chemistry and biochemistry. *Catalysts* 10(9):1–11
  108. Krishnamurthy VM, Kaufman GK, Urbach AR, Gitlin I, Gudiksen KL, Weibel DB, Whitesides GM (2008) Carbonic anhydrase as a model for biophysical and physical-organic studies of proteins and protein-ligand binding. *Chem Rev* 108(3):946–1051
  109. Supuran CT (2017) Advances in structure-based drug discovery of carbonic anhydrase inhibitors. *Expert Opin Drug Discov* 12(1):61–88
  110. Lindskog S (1997) Structure and mechanism of carbonic anhydrase. *Pharmacol Ther* 74(1):1–

111. Occhipinti R, Boron WF (2019) Role of carbonic anhydrases and inhibitors in acid–base physiology: Insights from mathematical modeling. *Int J Mol Sci* 20(15):3841
112. Winum JY, Poulsen SA, Supuran CT (2009) Therapeutic applications of glycosidic carbonic anhydrase inhibitors. *Med Res Rev* 29(3):419–435
113. Moviat M, Pickkers P, van der Voort PHJ, van der Hoeven JG (2006) Acetazolamide-mediated decrease in strong ion difference accounts for the correction of metabolic alkalosis in critically ill patients. *Crit Care* 10(1):1–6
114. Whitson JT (2007) Glaucoma: A review of adjunctive therapy and new management strategies. *Expert Opin Pharmacother* 8(18):3237–3249
115. Rheims S, Ryvlin P (2014) Pharmacotherapy for tonic-clonic seizures. *Expert Opin Pharmacother* 15(10):1417–26
116. Burtscher M, Gatterer H, Faulhaber M, Burtscher J (2014) Acetazolamide pre-treatment before ascending to high altitudes: When to start? *Int J Clin Exp Med* 7(11):4378–4383
117. Stadelmann K, Latshang TD, Nussbaumer-Ochsner Y, Tarokh L, Ulrich S, Kohler M, Bloch KE, Achermann P (2014) Impact of acetazolamide and CPAP on cortical activity in obstructive sleep apnea patients. *PLoS One* 9(4):1–8
118. Supuran CT, Fiore A Di, Giuseppina DS (2008) Carbonic anhydrase inhibitors as emerging agents for the treatment of obesity. *Expert Opin Investig Drugs* 13(2):383–392
119. Ruusuvaari E, Li H, Huttu K, Palva JM, Smirnov S, Rivera C, Kaila K, Voipio J (2004) Carbonic anhydrase isoform VII acts as a molecular switch in the development of synchronous gamma-frequency firing of hippocampal CA1 pyramidal cells. *J Neurosci* 24(11):2699–2707
120. De Simone G, Scozzafava A, Supuran CT (2009) Which carbonic anhydrases are targeted by the antiepileptic sulfonamides and sulfamates? *Chem Biol Drug Des* 74(3):317–321
121. Aspatwar A, E.E. Tolvanen M, Ortutay C, Parkkila S (2010) Carbonic anhydrase related protein VIII and its role in neurodegeneration and cancer. *Curr Pharm Des* 16(29):3264–3276
122. Poggetti V, Salerno S, Baglini E, Barresi E, Da Settimo F, Taliani S (2022) Carbonic anhydrase activators for neurodegeneration: An overview. *Molecules* 27:2544
123. Adeva-Andany MM, Fernández-Fernández C, Sánchez-Bello R, Donapetry-García C, Martínez-Rodríguez J (2015) The role of carbonic anhydrase in the pathogenesis of vascular calcification in humans. *Atherosclerosis* 241(1):183–191
124. Noor SI, Jamali S, Ames S, Langer S, Deitmer JW, Becker HM (2018) A surface proton antenna in carbonic anhydrase II supports lactate transport in cancer cells. *Elife* 7:1–31
125. Békés M, Langley DR, Crews CM (2022) PROTAC targeted protein degraders: the past is prologue. *Nat Rev Drug Discov* 21(3):181–200
126. Meldrum NU, Roughton FJW (1933) Carbonic anhydrase. Its preparation and properties. *J Physiol* 80(2):113–142
127. Jabłoński A (1933) Efficiency of anti-stokes fluorescence in dyes. *Nature* 131(3319):839–840
128. Lakowicz JR (2006) Principles of fluorescence spectroscopy, 3rd edition.
129. Kasha M (1950) Characterization of electronic transitions in complex molecules. *Discuss*

Faraday Soc 9:14–19

130. Niko Y, Didier P, Mely Y, Konishi GI, Klymchenko AS (2016) Bright and photostable push-pull pyrene dye visualizes lipid order variation between plasma and intracellular membranes. *Sci Rep* 6(August 2015):1–9
131. Wong KL, Bünzli JCG, Tanner PA (2020) Quantum yield and brightness. *J Lumin* 224(March):117256
132. Franck J, Dymond EG (1926) Elementary processes of photochemical reactions. *Trans Faraday Soc* (21):536–542
133. Wallrabe H, Periasamy A (2005) Imaging protein molecules using FRET and FLIM microscopy. *Curr Opin Biotechnol* 16(1 SPEC. ISS.):19–27
134. Clegg RM, Holub O, Gohlke C (2003) Fluorescence lifetime-resolved imaging: Measuring lifetimes in an image. *Methods Enzymol* 360:509–542
135. Szmackinski H, Lakowicz JR (1995) Fluorescence lifetime-based sensing and imaging. *Sensors Actuators B Chem* 29(1–3):16–24
136. Deshayes S, Divita G (2013) *Fluorescence technologies for monitoring interactions between biological molecules in vitro*, 1st ed. Elsevier Inc.
137. Wychowaniec A, Canyelles i Font F, Khan MA, Gładysz M, Kwiatek D, Kolanowski JŁ (2024) Wieloanalitowe, małowzrostkowe sondy luminescencyjne do symultanicznego wykrywania kilku celów molekularnych w modelach komórkowych. *Postepy Biochem* 70(2):1–23
138. Kolanowski JL, Liu F, New EJ (2018) Fluorescent probes for the simultaneous detection of multiple analytes in biology. *Chem Soc Rev* 47(1):195–208
139. Jun J V., Chenoweth DM, Petersson EJ (2020) Rational design of small molecule fluorescent probes for biological applications. *Org Biomol Chem* 18(30):5747–5763
140. Wang L, Tran M, D’Este E, Roberti J, Koch B, Xue L, Johnsson K (2020) A general strategy to develop cell permeable and fluorogenic probes for multicolour nanoscopy. *Nat Chem* 12(2):165–172
141. Joomyung V. Jun, David M. Chenoweth EJP (2020) Rational design of small molecule fluorescent probes for biological applications. *Org Biomol Chem* 18(30):5747–5763
142. Martin A, Rivera-Fuentes P (2024) A general strategy to develop fluorogenic polymethine dyes for bioimaging. *Nat Chem* 16(1):28–35
143. Keller SG, Kamiya M, Urano Y (2020) Recent progress in small spirocyclic, xanthene-based fluorescent probes. *Molecules* 25:5964
144. Gulati GK, Gulati LK, Kumar S (2021) Recent progress in multi-stimulable photochromic oxazines with their wide-ranging applications. *Dye Pigment* 192(May):109445
145. Sun XY, Liu T, Sun J, Wang XJ (2020) Synthesis and application of coumarin fluorescence probes. *RSC Adv* 10(18):10826–10847
146. Das S, Dey S, Patra S, Bera A, Ghosh T, Prasad B, Sayala KD, Maji K, Bedi A, Debnath S (2023) BODIPY-based molecules for biomedical applications. *Biomolecules* 13:1723
147. Yang Y, Gao F, Wang Y, Li H, Zhang J, Sun Z, Jiang Y (2022) Fluorescent organic small molecule probes for bioimaging and detection applications. *Molecules* 27:8421

148. Kand D, Pizarro L, Angel I, Avni A, Friedmann-Morvinski D, Weinstain R (2019) Organelle-targeted BODIPY photocages: Visible-light-mediated subcellular photorelease. *Angew Chemie - Int Ed* 58(14):4659–4663
149. Shen Q, Wang S, Yang N Di, Zhang C, Wu Q, Yu C (2020) Recent development of small-molecule organic fluorophores for multifunctional bioimaging in the second near-infrared window. *J Lumin* 225(February):117338
150. Tang X, Yang T, Yu D, Xiong H, Zhang S (2024) Current insights and future perspectives of ultraviolet radiation (UV) exposure: Friends and foes to the skin and beyond the skin. *Environ Int* 185(November 2023):108535
151. Gromkowska-Kępką KJ, Puścion-Jakubik A, Markiewicz-Żukowska R, Socha K (2021) The impact of ultraviolet radiation on skin photoaging — review of in vitro studies. *J Cosmet Dermatol* 20(11):3427–3431
152. Moan J, Peak MJ (1989) Effects of UV radiation on cells. *J Photochem Photobiol B Biol* 4(1):21–34
153. Agnez-Lima LF, Melo JTA, Silva AE, et al (2012) DNA damage by singlet oxygen and cellular protective mechanisms. *Mutat Res - Rev Mutat Res* 751(1):15–28
154. Smith KC (1977) Ultraviolet radiation effects on molecules and cells. *Sci Photobiol* 113–142
155. Yu SL, Lee SK (2017) Ultraviolet radiation: DNA damage, repair, and human disorders. *Mol Cell Toxicol* 13(1):21–28
156. Koide Y, Urano Y, Hanaoka K, Terai T, Nagano T (2011) Evolution of group 14 rhodamines as platforms for near-infrared fluorescence probes utilizing photoinduced electron transfer. *ACS Chem Biol* 6(6):600–608
157. Zhang Y, Xu B, Chen H, Fang B, Wang H, Hu L (2021) A red-emitting fluorescent probe for visualizing mitochondrial microviscosity by cell imaging. *Chem Pap* 75(6):2517–2523
158. Wan H, Yue J, Zhu S, et al (2018) A bright organic NIR-II nanofluorophore for three-dimensional imaging into biological tissues. *Nat Commun* 9:1171
159. Smith AM, Mancini MC, Nie S (2009) Second window for in vivo imaging. *Nat Nanotechnol* 4(11):710–711
160. Yu F, Gao M, Li M, Chen L (2015) A dual response near-infrared fluorescent probe for hydrogen polysulfides and superoxide anion detection in cells and in vivo. *Biomaterials* 63:93–101
161. Jiang Y, Jin D, Li Y, Yan X, Chen L (2017) A near-infrared fluorescent probe for rapid and selective detection of hydrosulfide and imaging in live cells. *Res Chem Intermed* 43(5):2945–2957
162. Novo D (2022) A comparison of spectral unmixing to conventional compensation for the calculation of fluorochrome abundances from flow cytometric data. *Cytom Part A* 101(11):885–891
163. Bucevičius J, Kostiuk G, Gerasimaitė R, Gilat T, Lukinavičius G (2020) Enhancing the biocompatibility of rhodamine fluorescent probes by a neighbouring group effect. *Chem Sci* 11(28):7313–7323
164. Van De Linde S, Heilemann M, Sauer M (2012) Live-cell super-resolution imaging with synthetic fluorophores. *Annu Rev Phys Chem* 63:519–540



165. Wang L, Frei MS, Salim A, Johnsson K (2019) Small-Molecule Fluorescent Probes for Live-Cell Super-Resolution Microscopy. *J Am Chem Soc* 141(7):2770–2781
166. Walter ERH, Lee LCC, Leung PKK, Lo KKW, Long NJ (2024) Mitochondria-targeting biocompatible fluorescent BODIPY probes. *Chem Sci* 4846–4852
167. Gill KK, Kaddoumi A, Nazzal S (2015) PEG-lipid micelles as drug carriers: Physiochemical attributes, formulation principles and biological implication. *J Drug Target* 23(3):222–231
168. Sano K, Nakajima T, Kiminori M, Ohuchi Y, Ikegami T (2013) Short PEG-linkers improve the performance of targeted, activatable monoclonal antibody-indocyanine green optical imaging probes. *Bioconjug Chem* 24(5):811–816
169. Zhu H, Hamachi I (2020) Fluorescence imaging of drug target proteins using chemical probes. *J Pharm Anal* 10(5):426–433
170. Zheng Q, Jockusch S, Zhou Z, Blanchard SC (2014) The contribution of reactive oxygen species to the photobleaching of organic fluorophores. *Photochem Photobiol* 90(2):448–454
171. Kong X, Nir E, Hamadani K, Weiss S (2007) Photobleaching pathways in single-molecule FRET experiments. *J Am Chem Soc* 129(15):4643–4654
172. Ha T, Tinnefeld P (2012) Photophysics of fluorescent probes for single-molecule biophysics and super-resolution imaging. *Annu Rev Phys Chem* 63:595–617
173. Chen Y, Jiang H, Hao T, Zhang N, Li M, Wang X, Wang X, Wei W, Zhao J (2023) Fluorogenic reactions in chemical biology: Seeing chemistry in cells. *Chem Biomed Imaging* 1(7):590–619
174. Li C, Tebo AG, Gautier A (2017) Fluorogenic labeling strategies for biological imaging. *Int J Mol Sci* 18(7):1473
175. Kozma E, Kele P (2019) Fluorogenic probes for super-resolution microscopy. *Org Biomol Chem* 17(2):215–233
176. Chen Y, Jiang H, Hao T, Zhang N, Li M, Wang X, Wang X, Wei W, Zhao J (2023) Fluorogenic Reactions in Chemical Biology: Seeing Chemistry in Cells. *Chem Biomed Imaging* 1(7):590–619
177. Lukinavičius G, Reymond L, Umezawa K, Sallin O, D’Este E, Göttfert F, Ta H, Hell SW, Urano Y, Johnsson K (2016) Fluorogenic probes for multicolor imaging in living cells. *J Am Chem Soc* 138(30):9365–9368
178. Le Droumaguet C, Wang C, Wang Q (2010) Fluorogenic click reaction. *Chem Soc Rev* 39(4):1233–1239
179. Ramil CP, Lin Q (2014) Photoclick chemistry: A fluorogenic light-triggered in vivo ligation reaction. *Curr Opin Chem Biol* 21:89–95
180. Yu H, Guo Y, Zhu W, Havener K, Zheng X (2021) Recent advances in 1,8-naphthalimide-based small-molecule fluorescent probes for organelles imaging and tracking in living cells. *Coord Chem Rev* 444:214019
181. Dong HQ, Wei TB, Ma XQ, Yang QY, Zhang YF, Sun YJ, Shi BB, Yao H, Zhang YM, Lin Q (2020) 1,8-Naphthalimide-based fluorescent chemosensors: recent advances and perspectives. *J Mater Chem C* 8(39):13501–13529
182. Xu H, Xiao Y, Liu Y, Sun W (2024) Research progress on naphthalimide fluorescent probes. *Adv Sens Res* 3(2):1–15
183. Fuller AA, Seidl FJ, Bruno PA, Plescia MA, Palla KS (2011) Use of the environmentally sensitive

- fluorophore 4-N,N-dimethylamino-1,8-naphthalimide to study peptoid helix structures. *Biopolymers* 96(5):627–638
184. Wei YF, Zhang XQ, Sun R, Xu YJ, Ge JF (2021) Fluorescent probes based 1,8-naphthalimide-nitrogen heterocyclic for monitoring the fluctuation of mitochondrial viscosity. *Dye Pigment* 194(June):109559
  185. Lavis LD, Raines RT (2008) Bright ideas for chemical biology. *ACS Chem Biol* 3(3):142–155
  186. Leslie KG, Jacquemin D, New EJ, Jolliffe KA (2018) Expanding the breadth of 4-amino-1,8-naphthalimide photophysical properties through substitution of the naphthalimide core. *Chem - A Eur J* 24(21):5569–5573
  187. Frizon TEA, Vieira AA, da Silva FN, et al (2020) Synthesis of 2,1,3-benzoxadiazole derivatives as new fluorophores—combined experimental, optical, electro, and theoretical study. *Front Chem* 8(May):1–14
  188. Liu L, Yao Z, Wang S, Xie T, Wu G, Zhang H, Zhang P, Wu Y, Yuan H, Sun H (2021) Syntheses, biological evaluations, and mechanistic studies of benzo[c][1,2,5]oxadiazole derivatives as potent PD-L1 inhibitors with in vivo antitumor activity. *J Med Chem* 64(12):8391–8409
  189. Telvekar VN, Takale BS (2013) Reaction of oximes of-diketones with diphosphorous tetraiodide for preparation of oxadiazoles and nitriles. *Synth Commun* 43(2):221–227
  190. Kagatkar S, Sunil D (2022) A systematic review on 1,8-naphthalimide derivatives as emissive materials in organic light-emitting diodes. *J Mater Sci* 57(1):105–139
  191. Yue Y, Huo F, Cheng F, Zhu X, Mafireyi T, Strongin RM, Yin C (2019) Functional synthetic probes for selective targeting and multi-analyte detection and imaging. *Chem Soc Rev* 48(15):4155–4177
  192. Dey N, Bhattacharya S (2020) Switchable optical probes for simultaneous targeting of multiple anions. *Chem - An Asian J* 15(12):1759–1779
  193. Mondal P, Schwinn K, Huix-Rotllant M (2020) Impact of the redox state of flavin chromophores on the UV–vis spectra, redox and acidity constants and electron affinities. *J Photochem Photobiol A Chem* 387:112164
  194. Kaur A, New EJ (2019) Bioinspired small-molecule tools for the imaging of redox biology. *Acc Chem Res* 52(3):623–632
  195. Sezgin E, Schneider F, Zilles V, Urbančič I, Garcia E, Waithe D, Klymchenko AS, Eggeling C (2017) Polarity-sensitive probes for superresolution stimulated emission depletion microscopy. *Biophys J* 113(6):1321–1330
  196. Paez-Perez M, Kuimova MK (2024) Molecular rotors: Fluorescent sensors for microviscosity and conformation of biomolecules. *Angew Chemie - Int Ed* 63(6):e202311233
  197. Ye S, Zhang H, Fei J, Wolstenholme CH, Zhang X (2021) A general strategy to control viscosity sensitivity of molecular rotor-based fluorophores. *Angew Chemie - Int Ed* 60(3):1339–1346
  198. Minton AP (2006) How can biochemical reactions within cells differ from those in test tubes? *J Cell Sci* 119(14):2863–2869
  199. Grodowski MS, Veyret B, Weiss K (1977) Photochemistry of flavins. II. Photophysical properties of alloxazines and isoalloxazines. *Photochem Photobiol* 26(4):341–352
  200. Yeow J, Kaur A, Anscomb MD, New EJ (2014) A novel flavin derivative reveals the impact of glucose on oxidative stress in adipocytes. *Chem Commun* 50(60):8181–8184

201. Collot M, Fam TK, Ashokkumar P, Faklaris O, Galli T, Danglot L, Klymchenko AS (2018) Ultrabright and fluorogenic probes for multicolor imaging and tracking of lipid droplets in cells and tissues. *J Am Chem Soc* 140(16):5401–5411
202. Lukinavičius G, Umezawa K, Olivier N, et al (2013) A near-infrared fluorophore for live-cell super-resolution microscopy of cellular proteins. *Nat Chem* 5(2):132–139
203. Ghoneim N, Suppan P (1993) Solvation of TICT\* states in solvent mixtures. *Pure Appl Chem* 65(8):1739–1743
204. Klymchenko AS (2017) Solvatochromic and fluorogenic dyes as environment-sensitive probes: design and biological applications. *Acc Chem Res* 50(2):366–375
205. Uchiyama S, Kimura K, Gota C, Okabe K, Kawamoto K, Inada N, Yoshihara T, Tobita S (2012) Environment-sensitive fluorophores with benzothiadiazole and benzoselenadiazole structures as candidate components of a fluorescent polymeric thermometer. *Chem - A Eur J* 18(31):9552–9563
206. Wu T, Duan L, Yang J, Zhou Y (2023) A multidimensional quantitative fluorescent probe for high-fidelity monitoring of the polarity change in lysosomes during autophagy. *Sensors Actuators B Chem* 393(June):134142
207. Qin X, Yang X, Du L, Li M (2021) Polarity-based fluorescence probes: properties and applications. *RSC Med Chem* 12(11):1826–1838
208. Dutta T, Pal K, Koner AL (2022) Intracellular physical properties with small organic fluorescent probes: recent advances and future perspectives. *Chem Rec* 22:e202200035
209. Deng H, Lei Q, Wang C, et al (2022) A fluorogenic probe for predicting treatment response in non-small cell lung cancer with EGFR-activating mutations. *Nat Commun* 13(1):6944
210. Li Mingrui, Wang Bowei, Liu Jiayi, Zhanga Zizhuo, Chen Ligong, Li Yang YX (2021) Lipid droplet-specific dual-response fluorescent probe for the detection of polarity and H<sub>2</sub>O<sub>2</sub> and its application in living cells. *Anal Chem* 94(27):9732–9739
211. Sasaki S, Drummen GPC, Konishi GI (2016) Recent advances in twisted intramolecular charge transfer (TICT) fluorescence and related phenomena in materials chemistry. *J Mater Chem C* 4(14):2731–2743
212. Haidekker MA, Theodorakis EA (2010) Environment-sensitive behavior of fluorescent molecular rotors. *J Biol Eng* 4:1–14
213. Grabowski ZR, Rotkiewicz K, Rettig W (2003) Structural changes accompanying intramolecular electron transfer: Focus on Twisted Intramolecular Charge-Transfer states and structures. *Chem Rev* 103(10):3899–4031
214. Rettig W (1982) Application of a simplified microstructural solvent interaction model to the solvatochromism of twisted intramolecular charge transfer (TICT) states. *J Mol Struct* 84(3–4):303–327
215. Allen BD, Benniston AC, Harriman A, Rostron SA, Yu C (2005) The photophysical properties of a julolidene-based molecular rotor. *Phys Chem Chem Phys* 7(16):3035–3040
216. Rotkiewicz K, Grellmann KH, Grabowski ZR (1973) Reinterpretation of the anomalous fluorescence of p-N,N-dimethylamino-benzonitrile. *Chem Phys Lett* 19(3):315–318
217. Law KY (1980) Fluorescence probe for microenvironments: anomalous viscosity dependence of the fluorescence quantum yield of p-N,N-dialkylaminobenzylidenemalononitrile in 1-

- alkanols. *Chem Phys Lett* 75(3):545–549
218. Zhang G, Ni Y, Zhang D, Li H, Wang N, Yu C, Li L, Huang W (2019) Rational design of NIR fluorescence probes for sensitive detection of viscosity in living cells. *Spectrochim Acta - Part A Mol Biomol Spectrosc* 214:339–347
  219. Kim HJ, Heo CH, Kim HM (2013) Benzimidazole-based ratiometric two-photon fluorescent probes for acidic pH in live cells and tissues. *J Am Chem Soc* 135(47):17969–17977
  220. Urano Y, Asanuma D, Hama Y, et al (2009) Selective molecular imaging of viable cancer cells with pH-activatable fluorescence probes. *Nat Med* 15(1):104–109
  221. Galindo F, Burguete MI, Vigara L, Luis S V., Kabir N, Gavrilovic J, Russell DA (2005) Synthetic macrocyclic peptidomimetics as tunable pH probes for the fluorescence imaging of acidic organelles in live cells. *Angew Chemie - Int Ed* 44(40):6504–6508
  222. Lee MH, Han JH, Lee JH, Park N, Kumar R, Kang C, Kim JS (2013) Two-color probe to monitor a wide range of pH values in cells. *Angew Chemie - Int Ed* 52(24):6206–6209
  223. Hu Z, Li R, Cui X, Hu C, Chen Z (2023) A pH-sensitive carbonic anhydrase IX-targeted near-infrared probe for fluorescent sensing and imaging of hypoxic osteosarcoma. *Sensors Actuators B Chem* 379(October 2022):133171
  224. Mei H, Gu X, Wang M, Chen J, Yang X, Liu X, Xu K (2022) A tri-response colorimetric-fluorescent probe for pH and lysosomal imaging. *Sensors Actuators B Chem* 370(July):132425
  225. Xia Q, Feng S, Hong J, Feng G (2021) One probe for multiple targets: A NIR fluorescent rhodamine-based probe for ONOO<sup>-</sup> and lysosomal pH detection in live cells. *Sensors Actuators, B Chem* 337(December 2020):129732
  226. Zhan J, Geng C, Hao X, Song W, Li Z, Lin W (2022) A pH-correctable, viscosity-susceptible fluorescent reporter for organellar sulfur dioxide. *Sensors Actuators B Chem* 371(July):132506
  227. Qiu J, Zhong C, Liu M, Xiong X, Gao Y, Zhu H (2022) A tunable pH probe scaffold based on sulfonamide rhodamine and its application in mitochondrial pH research. *Sensors Actuators B Chem* 371(August):132606
  228. Chen S, Ma X, Wang L, Wu Y, Wang Y, Fan W, Hou S (2023) Design and application of lysosomal targeting pH-sensitive  $\beta$ -galactosidase fluorescent probe. *Sensors Actuators B Chem* 379(December 2022):133272
  229. Graven SN, Estrada-O S, Lardy HA (1966) Alkali metal cation release and respiratory inhibition induced by nigericin in rat liver mitochondria. *Proc Natl Acad Sci U S A* 56(2):654–658
  230. Pierzyńska-Mach A, Janowski PA, Dobrucki JW (2014) Evaluation of acridine orange, LysoTracker Red, and quinacrine as fluorescent probes for long-term tracking of acidic vesicles. *Cytom Part A* 85(8):729–737
  231. Rennick JJ, Nowell CJ, Pouton CW, Johnston APR (2022) Resolving subcellular pH with a quantitative fluorescent lifetime biosensor. *Nat Commun* 13:6023
  232. Lin J, Yang K, New EJ (2021) Strategies for organelle targeting of fluorescent probes. *Org Biomol Chem* 19:9339–9357
  233. Sharma P, Gupta N, Kaur S, Kaur S, Ohri P, Parihar RD, Bhalla V, Kumar M (2019) Imaging of lysosomal activity using naphthalimide-benzimidazole based fluorescent probe in living cells. *Sensors Actuators, B Chem* 286(January):451–459

234. Niu G, Zhang P, Liu W, Wang M, Zhang H, Wu J, Zhang L, Wang P (2017) Near-infrared probe based on rhodamine derivative for highly sensitive and selective lysosomal pH tracking. *Anal Chem* 89(3):1922–1929
235. Nguyen VN, Li H (2023) Recent development of lysosome-targeted organic fluorescent probes for reactive oxygen species. *Molecules* 28:6650
236. Zhang Y, Liu Q, Tian T, Xu C, Yang P, Ma L, Hou Y, Zhou H, Gan Y (2024) A buffering fluorogenic probe for real-time lysosomal pH monitoring. *Sensors Actuators B Chem* 399(October 2023):134809
237. Gan J, Chen K, Chang CP, Tian H (2003) Luminescent properties and photo-induced electron transfer of naphthalimides with piperazine substituent. *Dye Pigment* 57(1):21–28
238. Xie Z, Yin B, Shen J, Hong D, Zhu L, Ge J, Zhu Q (2018) A dual functional fluorogenic probe for visualization of intracellular pH and formaldehyde with distinct fluorescence signals. *Org Biomol Chem* 16(25):4628–4632
239. Baan R, Grosse Y, Straif K, et al (2009) A review of human carcinogens--Part F: chemical agents and related occupations. *Lancet Oncol* 10(12):1143–1144
240. Salthammer T (2013) Formaldehyde in the ambient atmosphere: From an indoor pollutant to an outdoor pollutant? *Angew Chemie - Int Ed* 52(12):3320–3327
241. Tsukada YI, Fang J, Erdjument-Bromage H, Warren ME, Borchers CH, Tempst P, Zhang Y (2006) Histone demethylation by a family of JmjC domain-containing proteins. *Nature* 439(7078):811–816
242. Tulpule K, Dringen R (2013) Formaldehyde in brain: An overlooked player in neurodegeneration? *J Neurochem* 127(1):7–21
243. Yu R, Lai Y, Hartwell HJ, Moeller BC, Doyle-Eisele M, Kracko D, Bodnar WM, Starr TB, Swenberg JA (2015) Formation, accumulation, and hydrolysis of endogenous and exogenous formaldehyde-induced DNA damage. *Toxicol Sci* 146(1):170–182
244. Thomas D, Rubio V, Iragavarapu V, Guzman E, Pelletier OB, Alamgir S, Zhang Q, Stawikowski MJ (2021) Solvatochromic and pH-sensitive fluorescent membrane probes for imaging of live cells. *ACS Chem Neurosci* 12(4):719–734
245. Di Paolo G, Kim TW (2011) Linking lipids to Alzheimer's disease: Cholesterol and beyond. *Nat Rev Neurosci* 12(5):284–296
246. Bakov V V., Georgiev NI, Bojinov VB (2022) A novel fluorescent probe for determination of pH and viscosity based on a highly water-soluble 1,8-naphthalimide rotor. *Molecules* 27:7556
247. Wang S, Zhao X, Liu M, Yang L, Yu M, Li Z (2023) A dual-responsive crimson fluorescent probe for real-time diagnosis of alcoholic acute liver injury. *Biosens Bioelectron* 239(May):115596
248. Zan Q, Fan L, Ma L, Yang Q, Zhao K, Huang Y, Dong C, Shuang S (2023) Dual-channel fluorescent probe for simultaneously detecting H<sub>2</sub>S and viscosity/polarity and its application in non-alcoholic fatty liver, tumor tissue, and food spoilage. *Sensors Actuators B Chem* 397(August):134596
249. Qi YL, Wang HR, Kang QJ, Chen LL, Qi PF, He ZX, Yang YS, Zhu HL (2022) A versatile fluorescent probe for simultaneously detecting viscosity, polarity and nitroreductases and its application in bioimaging. *Sensors Actuators B Chem* 352(P2):130989
250. Rawale DG, Thakur K, Adusumalli SR, Rai V (2019) Chemical methods for selective labeling of

- proteins. *European J Org Chem* (40):6749–6763
251. Sahoo H (2012) Fluorescent labeling techniques in biomolecules: A flashback. *RSC Adv* 2(18):7017–7029
  252. Uchiyama S, Iwai K, De Silva AP (2008) Multiplexing sensory molecules map protons near micellar membranes. *Angew Chemie - Int Ed* 47(25):4667–4669
  253. Bissell RA, Bryan AJ, De Silva AP, McCoy CP (1994) Fluorescent PET (photoinduced electron transfer) sensors with targeting/anchoring modules as molecular versions of submarine periscopes for mapping membrane-bounded protons. *J Chem Soc Chem Commun* (4):405–407
  254. Morris R, Black KA, Stollar EJ (2022) Uncovering protein function: From classification to complexes. *Essays Biochem* 66(2):255–285
  255. Thorn K (2017) Genetically encoded fluorescent tags. *Mol Biol Cell* 28(7):848–857
  256. Sletten EM, Bertozzi CR (2011) From mechanism to mouse: A tale of two bioorthogonal reactions. *Acc Chem Res* 44(9):666–676
  257. Lim RKV, Lin Q (2010) Bioorthogonal chemistry: Recent progress and future directions. *Chem Commun* 46(10):1589–1600
  258. Spriestersbach A, Kubicek J, Schäfer F, Block H, Maertens B (2015) Purification of His-tagged proteins. *Methods Enzymol* 559:1–15
  259. Lai YT, Chang YY, Hu L, et al (2015) Rapid labeling of intracellular His-tagged proteins in living cells. *Proc Natl Acad Sci U S A* 112(10):2948–2953
  260. Zhao C, Hellman LM, Zhan X, Bowman WS, Whiteheart SW, Fried MG (2010) Hexahistidine-tag-specific optical probes for analyses of proteins and their interactions. *Anal Biochem* 399(8):237–245
  261. Hoffmann C, Gaietta G, Zürn A, Adams SR, Terrillon S, Ellisman MH, Tsien RY, Lohse MJ (2010) Fluorescent labeling of tetracysteine-tagged proteins in intact cells. *Nat Protoc* 5(10):1666–1677
  262. Aliye N, Fabbretti A, Lupidi G, Tsekoa T, Spurio R (2015) Engineering color variants of green fluorescent protein (GFP) for thermostability, pH-sensitivity, and improved folding kinetics. *Appl Microbiol Biotechnol* 99(3):1205–1216
  263. Stepanenko O, Verkhusha V, Kuznetsova I, Uversky V, Turoverov K (2008) Fluorescent proteins as biomarkers and biosensors: Throwing color lights on molecular and cellular processes. *Curr Protein Pept Sci* 9(4):338–369
  264. Thiel Z, Nguyen J, Rivera-Fuentes P (2020) Genetically encoded activators of small molecules for imaging and drug delivery. *Angew Chemie Int Ed* 59(20):7669–7677
  265. Cranfill PJ, Sell BR, Baird MA, Allen JR, Lavagnino Z, De Gruiter HM, Kremers GJ, Davidson MW, Ustione A, Piston DW (2016) Quantitative assessment of fluorescent proteins. *Nat Methods* 13(7):557–562
  266. Aissa H Ben, Gautier A (2020) Engineering glowing chemogenetic hybrids for spying on cells. *European J Org Chem* 2020(35):5637–5646
  267. Rodriguez EA, Campbell RE, Lin JY, Lin MZ, Miyawaki A, Palmer AE, Shu X, Zhang J, Tsien RY (2017) The growing and glowing toolbox of fluorescent and photoactive proteins. *Trends Biochem Sci* 42(2):111–129

268. Wang M, Da Y, Tian Y (2023) Fluorescent proteins and genetically encoded biosensors. *Chem Soc Rev* 52(4):1189–1214
269. (2003) Directed evolution of O6-alkylguanine-DNA alkyltransferase for efficient labeling of fusion proteins with small molecules in vivo. *Chem Biol* 10(4):313–317
270. Mollwitz B, Brunk E, Schmitt S, Pojer F, Bannwarth M, Schiltz M, Rothlisberger U, Johnsson K (2012) Directed evolution of the suicide protein O 6-alkylguanine-DNA alkyltransferase for increased reactivity results in an alkylated protein with exceptional stability. *Biochemistry* 51(5):986–994
271. Gautier A, Juillerat A, Heinis C, Corrêa IR, Kindermann M, Beaufils F, Johnsson K (2008) An engineered protein tag for multiprotein labeling in living cells. *Chem Biol* 15(2):128–136
272. Los G V, Encell LP, Mcdougall MG, et al (2008) HaloTag: A novel protein labeling technology for cell imaging and protein analysis. *3(6):373–382*
273. Hoelzel CA, Zhang X (2020) Visualizing and manipulating biological processes by using HaloTag and SNAP-Tag technologies. *ChemBioChem* 21(14):1935–1946
274. Bachollet SPJT, Shpinov Y, Broch F, Benaissa H, Gautier A, Pietrancosta N, Mallet JM, Dumat B (2022) An expanded palette of fluorogenic HaloTag probes with enhanced contrast for targeted cellular imaging. *Org Biomol Chem* 20(17):3619–3628
275. Leng S, Qiao QL, Gao Y, Miao L, Deng WG, Xu ZC (2017) SNAP-tag fluorogenic probes for wash free protein labeling. *Chinese Chem Lett* 28(10):1911–1915
276. Cole NB (2013) Site-specific protein labeling with SNAP-tags. *Curr Protoc Protein Sci* 2013(September):30.1.1-30.1.16
277. Liu Y, Miao K, Dunham NP, Liu H, Fares M, Boal AK, Li X, Zhang X (2017) The cation- $\pi$  interaction enables a Halo-Tag fluorogenic probe for fast no-wash live cell imaging and gel-free protein quantification. *Biochemistry* 56(11):1585–1595
278. Zhuang Y De, Chiang PY, Wang CW, Tan KT (2013) Environment-sensitive fluorescent turn-on probes targeting hydrophobic ligand-binding domains for selective protein detection. *Angew Chemie - Int Ed* 52(31):8124–8128
279. Liu TK, Hsieh PY, Zhuang Y De, Hsia CY, Huang CL, Lai HP, Lin HS, Chen IC, Hsu HY, Tan KT (2014) A rapid SNAP-tag fluorogenic probe based on an environment-sensitive fluorophore for no-wash live cell imaging. *ACS Chem Biol* 9(10):2359–2365
280. Liu Y, Fares M, Dunham NP, Gao Z, Miao K, Jiang X, Bollinger SS, Boal AK, Zhang X (2017) AgHalo: A facile fluorogenic sensor to detect drug-induced proteome stress. *Angew Chemie - Int Ed* 56(30):8672–8676
281. Qiao Q, Liu W, Chen J, Zhou W, Yin W, Miao L, Cui J, Xu Z (2017) A naphthalimide-derived fluorogenic probe for SNAP-tag with a fast record labeling rate. *Dye Pigment* 147:327–333
282. Leng S, Qiao Q, Miao L, Deng W, Cui J, Xu Z (2017) A wash-free SNAP-tag fluorogenic probe based on the additive effects of quencher release and environmental sensitivity. *Chem Commun* 53(48):6448–6451
283. Wang C, Song X, Xiao Y (2017) SNAP-tag-based subcellular protein labeling and fluorescent imaging with naphthalimides. *ChemBioChem* 18(17):1762–1769
284. Kolb HC, Finn MG, Sharpless KB (2001) Click chemistry: Diverse chemical function from a few good reactions. *Angew Chemie - Int Ed* 40(11):2004–2021

285. Lang K, Chin JW (2014) Bioorthogonal reactions for labeling proteins. *ACS Chem Biol* 9(1):16–20
286. Yang Y, Yang X, Verhelst SHL (2013) Comparative analysis of click chemistry mediated activity-based protein profiling in cell lysates. *Molecules* 18(10):12599–12608
287. Lang K, Chin JW (2014) Cellular incorporation of unnatural amino acids and bioorthogonal labeling of proteins. *Chem Rev* 114(9):4764–4806
288. Adhikari A, Bhattarai BR, Aryal A, Thapa N, Kc P, Adhikari A, Maharjan S, Chanda PB, Regmi BP, Parajuli N (2021) Reprogramming natural proteins using unnatural amino acids. *RSC Adv* 11(60):38126–38145
289. Horisawa K (2014) Specific and quantitative labeling of biomolecules using click chemistry. *Front Physiol* 5(Nov):1–6
290. Wang W, Uzawa T, Tochio N, et al (2014) A fluorogenic peptide probe developed by in vitro selection using tRNA carrying a fluorogenic amino acid. *Chem Commun* 50(22):2962–2964
291. Wang W, Zhu L, Hirano Y, et al (2016) Fluorogenic enhancement of an in vitro-selected peptide ligand by replacement of a fluorescent group. *Anal Chem* 88(16):7991–7997
292. Graziotto ME, Adair LD, Kaur A, Vérité P, Ball SR, Sunde M, Jacquemin D, New EJ (2021) Versatile naphthalimide tetrazines for fluorogenic bioorthogonal labelling. *RSC Chem Biol* 2(5):1491–1498
293. Shiraiwa K, Cheng R, Nonaka H, Tamura T, Hamachi I (2020) Chemical tools for endogenous protein labeling and profiling. *Cell Chem Biol* 27(8):970–985
294. Amaike K, Tamura T, Hamachi I (2017) Recognition-driven chemical labeling of endogenous proteins in multi-molecular crowding in live cells. *Chem Commun* 53(88):11972–11983
295. Chilamari M, Purushottam L, Rai V (2017) Site-selective labeling of native proteins by a multicomponent approach. *Chem - A Eur J* 23(16):3819–3823
296. Zhou P, Yao J, Hu G, Fang J (2016) Naphthalimide scaffold provides versatile platform for selective thiol sensing and protein labeling. *ACS Chem Biol* 11(4):1098–1105
297. Jaffrey SR, Snyder SH (2001) The biotin switch method for the detection of S-nitrosylated proteins. *Sci STKE* (86):1–10
298. Park CM, Macinkovic I, Filipovic MR, Xian M (2015) Use of the “Tag-Switch” method for the detection of protein S-sulphydration. *Methods Enzymol* 555:39–56
299. Pagano M, Castagnolo D, Bernardini M, et al (2014) The fight against the influenza A virus H1N1: Synthesis, molecular modeling, and biological evaluation of benzofurazan derivatives as viral RNA polymerase inhibitors. *ChemMedChem* 9(1):129–150
300. Liu T, Jiang Y, Liu Z, Li J, Fang K, Zhuang C, Du L, Fang H, Sheng C, Li M (2017) Environment-sensitive turn-on fluorescent probes for p53-MDM2 protein-protein interaction. *Medchemcomm* 8(8):1668–1672
301. Chio CM, Lim CS, Bishop AC (2015) Targeting a cryptic allosteric site for selective inhibition of the oncogenic protein tyrosine phosphatase Shp2. *Biochemistry* 54(2):497–504
302. Kuznetsova A, Klein P, Opatz T (2019) Halogenated 2,1,3-benzoxadiazoles as potential fluorescent warheads for covalent protease inhibitors. *Proceedings* 9(1):54
303. Krzeszewski M, Modrzycka S, Bousquet MHE, Jacquemin D, Drąg M, Gryko DT (2022) Green-



- emitting 4,5-diaminonaphthalimides in activity-based probes for the detection of thrombin. *Org Lett* 24(30):5602–5607
304. Hansen SK, Cancilla MT, Shiao TP, Kung J, Chen T, Erlanson DA (2005) Allosteric inhibition of PTP1B activity by selective modification of a non-active site cysteine residue. *Biochemistry* 44(21):7704–7712
305. Singha M, Roy S, Moirangthem R, Das AK, Basak A (2019) Naphthalimide-based template for inhibitor screening via cross-linking and in-gel fluorescence: A case study against HCA II. *ACS Omega* 4(7):11914–11920
306. Singha M, Roy S, Pandey SD, Bag SS, Bhattacharya P, Das M, Ghosh AS, Ray D, Basak A (2017) Use of azidonaphthalimide carboxylic acids as fluorescent templates with a built-in photoreactive group and a flexible linker simplifies protein labeling studies: Applications in selective tagging of HCAII and penicillin binding proteins. *Chem Commun* 53(97):13015–13018
307. Reddi RN, Resnick E, Rogel A, et al (2021) Tunable methacrylamides for covalent ligand directed release chemistry. *J Am Chem Soc* 143(13):4979–4992
308. Tsukiji S, Miyagawa M, Takaoka Y, Tamura T, Hamachi I (2009) Ligand-directed tosyl chemistry for protein labeling in vivo. *Nat Chem Biol* 5(5):341–343
309. Kabalka GW, Varma M, Varma RS, Srivastava PC, Knapp FF (1986) Tosylation of alcohols. *J Org Chem* 51(12):2386–2388
310. Tamura T, Hamachi I (2019) Chemistry for covalent modification of endogenous/native proteins: From test tubes to complex biological systems. *J Am Chem Soc* 141(7):2782–2799
311. Takaoka Y, Nishikawa Y, Hashimoto Y, Sasaki K, Hamachi I (2015) Ligand-directed dibromophenyl benzoate chemistry for rapid and selective acylation of intracellular natural proteins. *Chem Sci* 6(5):3217–3224
312. Masuda M, Matsuo K, Hamachi I (2019) Ligand-directed N-sulfonyl pyridone chemistry for selective native protein labeling and imaging in live cell. *Methods Mol. Biol. Humana Press Inc.*, pp 203–224
313. Xuan W, Ma JA (2024) Pinpointing acidic residues in proteins. *ChemMedChem* 19(5):e202300623
314. Gonzalez-Valero A, Reeves AG, Page ACS, et al (2022) An activity-based oxaziridine platform for identifying and developing covalent ligands for functional allosteric methionine sites: Redox-dependent inhibition of cyclin-dependent kinase 4. *J Am Chem Soc* 144(50):22890–22901
315. Xin X, Zhang Y, Gaetani M, Lundström SL, Zubarev RA, Zhou Y, Corkery DP, Wu YW (2022) Ultrafast and selective labeling of endogenous proteins using affinity-based benzotriazole chemistry. *Chem Sci* 13(24):7240–7246
316. Lin KY, Hin Lam C, Lin XH, et al (2021) Improved stabilities of labeling probes for the selective modification of endogenous proteins in living cells and in vivo. *Chem - An Asian J* 16(8):937–948
317. Song Y, Xiong F, Peng J, Fung YME, Huang Y, Li X (2020) Introducing aldehyde functionality to proteins using ligand-directed affinity labeling. *Chem Commun* 56(45):6134–6137
318. Adusumalli SR, Rawale DG, Singh U, Tripathi P, Paul R, Kalra N, Mishra RK, Shukla S, Rai V (2018) Single-site labeling of native proteins enabled by a chemoselective and site-selective chemical technology. *J Am Chem Soc* 140(44):15114–15123

319. Kojima H, Fujita Y, Takeuchi R, Ikebe Y, Ohashi N, Yamamoto K, Itoh T (2020) Cyclization reaction-based turn-on probe for covalent labeling of target proteins. *Cell Chem Biol* 27(3):334-349.e11
320. Ojima K, Shiraiwa K, Soga K, Doura T, Takato M, Komatsu K, Yuzaki M, Hamachi I, Kiyonaka S (2021) Ligand-directed two-step labeling to quantify neuronal glutamate receptor trafficking. *Nat Commun* 12(1):831
321. Chan HJ, Lin XH, Fan SY, Ru Hwu J, Tan KT (2020) Rapid and selective labeling of endogenous transmembrane proteins in living cells with a difluorophenyl ester affinity-based probe. *Chem - An Asian J* 15(21):3416–3420
322. Tamura T, Tsukiji S, Hamachi I (2012) Native FKBP12 engineering by ligand-directed tosyl chemistry: Labeling properties and application to photo-cross-linking of protein complexes in vitro and in living cells. *J Am Chem Soc* 134(4):2216–2226
323. Andrews KG, Summers DM, Donnelly LJ, Ross M (2016) Catalytic reductive N-alkylation of amines using carboxylic acids. *Chem Commun* 52(9):1–79
324. Abad JL, Villorbina G, Fabriàs G, Camps F (2004) Synthesis and use of stereospecifically deuterated analogues of palmitic acid to investigate the stereochemical course of the  $\Delta 11$  desaturase of the processionary moth. *J Org Chem* 69(21):7108–7113
325. Biannic B, Bozell JJ, Elder T (2014) Steric effects in the design of Co-Schiff base complexes for the catalytic oxidation of lignin models to para-benzoquinones. *Green Chem* 16(7):3635–3642
326. Morgan BP, Muci A, Lu PP, et al (2010) Discovery of omecamtiv mecarbil the first, selective, small molecule activator of cardiac myosin. *ACS Med Chem Lett* 1(9):472–477
327. Bouzide A, Sauve G (2002) Silver (I) oxide mediated highly selective monotosylation of symmetrical diols. Application to the synthesis of polysubstituted cyclic ethers. *Org Lett* 4(14):2329–2332
328. Hermann T, Hochegger P, Dolensky J, Seebacher W, Saf R, Kaiser M, Mäser P, Weis R (2021) New acyl derivatives of 3-aminofurazanes and their antiplasmodial activities. *Pharmaceuticals* 14(5):1–23
329. Lin J, Graziotto ME, Lay PA, New EJ (2021) A bimodal fluorescence-raman probe for cellular imaging. *Cells* 10(7):1699
330. Cho HJ, Gee HY, Baek KH, Ko SK, Park JM, Lee H, Kim ND, Lee MG, Shin I (2011) A small molecule that binds to an ATPase domain of Hsc70 promotes membrane trafficking of mutant cystic fibrosis transmembrane conductance regulator. *J Am Chem Soc* 133(50):20267–20276
331. Killoran MP, Levin S, Boursier ME, Zimmerman K, Hurst R, Hall MP, Machleidt T, Kirkland TA, Ohana RF (2021) An integrated approach toward nanobret tracers for analysis of GPCR ligand engagement. *Molecules* 26(10):2857
332. Rhys Williams AT, Winfield SA, Miller JN (1983) Relative fluorescence quantum yields using a Computer-controlled luminescence spectrometer. *Analyst* 108(1290):1067–1071
333. Brouwer AM (2011) Standards for photoluminescence quantum yield measurements in solution (IUPAC technical report). *Pure Appl Chem* 83(12):2213–2228
334. Eaton DF (1988) Reference materials for fluorescence measurement. *Pure Appl Chem* 60(7):1107–1114
335. Reynolds GA, Drexhage KH (1975) New coumarin dyes with rigidized structure for flashlamp-

- pumped dye lasers. *Opt Commun* 13(3):222–225
336. Schindelin J, Arganda-Carrera I, Frise E, et al (2009) Fiji - an Open platform for biological image analysis. *Nat Methods* 9(7):676–682
337. Supuran CT, Briganti F, Tilli S, Chegwiddden WR, Scozzafava A (2001) Carbonic anhydrase inhibitors: Sulfonamides as antitumor agents? *Bioorganic Med Chem* 9(3):703–714
338. Stone MRL, Masi M, Phetsang W, Pagès JM, Cooper MA, Blaskovich MAT (2019) Fluoroquinolone-derived fluorescent probes for studies of bacterial penetration and efflux. *Medchemcomm* 10(6):901–906
339. Rohacova J, Marin ML, Miranda MA (2010) Complexes between fluorescent cholic acid derivatives and human serum albumin. A photophysical approach to investigate the binding behavior. *J Phys Chem B* 114(13):4710–4716
340. Song F, Li Z, Li J, Wu S, Qiu X, Xi Z, Yi L (2016) Investigation of thiolysis of NBD amines for the development of H<sub>2</sub>S probes and evaluating the stability of NBD dyes. *Org Biomol Chem* 14(47):11117–11124
341. Wang W, Peng Z, Ji M, Chen J, Wang P (2022) Highly selective fluorescent probe based on AIE for identifying cysteine/homocysteine. *Bioorg Chem* 126(May):105902
342. Taliani S, Simorini F, Sergianni V, et al (2007) New fluorescent 2-phenylindolglyoxylamide derivatives as probes targeting the peripheral-type benzodiazepine receptor: Design, synthesis, and biological evaluation. *J Med Chem* 50(2):404–407
343. Yamaguchi T, Asanuma M, Nakanishi S, Saito Y, Okazaki M, Dodo K, Sodeoka M (2014) Turn-ON fluorescent affinity labeling using a small bifunctional O-nitrobenzoxadiazole unit. *Chem Sci* 5(3):1021–1029
344. Ma Z, Lin Y, Chen H, Du L, Li M (2016) A novel NBD-based pH “on-off” fluorescent probe equipped with the: N-phenylpiperazine group for lysosome imaging. *RSC Adv* 6(104):102773–102777
345. de Almeida RFM, Santos TCB, da Silva LC, Suchodolski J, Krasowska A, Stokowa-Sołtys K, Puchalska M, Starosta R (2021) NBD derived diphenyl(aminomethyl)phosphane – A new fluorescent dye for imaging of low pH regions and lipid membranes in living cells. *Dye Pigment* 184:108771
346. Saha S, Samanta A (1998) Photophysical and dynamic NMR studies on 4-amino-7-nitrobenz-2-oxa-1,3-diazole derivatives: Elucidation of the nonradiative deactivation pathway. *J Phys Chem A* 102(41):7903–7912
347. Greene TW, Wuts PGM (2014) Greene’s protective groups in organic synthesis, 5th editio. Wiley-VCH Verlag
348. Wang CX, Sato Y, Kudo M, Nishizawa S, Teramae N (2012) Ratiometric fluorescent signaling of small molecule, environmentally sensitive dye conjugates for detecting single-base mutations in DNA. *Chem - A Eur J* 18(31):9481–9484
349. Czaplinska B, Malarz K, Mrozek-Wilczkiewicz A, Slodek A, Korzec M, Musiol R (2020) Theoretical and experimental investigations of large stokes shift fluorophores based on a quinoline scaffold. *Molecules* 25(11):2488
350. Drössler P, Holzer W, Penzkofer A, Hegemann P (2002) pH dependence of the absorption and emission behaviour of riboflavin in aqueous solution. *Chem Phys* 282(3):429–439

351. Berezin MY, Kao J, Achilefu S (2009) pH-dependent optical properties of synthetic fluorescent imidazoles. *Chem - A Eur J* 15(14):3560–3566
352. Uchiyama S, Yano K, Fukatsu E, de Silva AP (2019) Precise proton mapping near ionic micellar membranes with fluorescent Photoinduced-Electron-Transfer sensors. *Chem - A Eur J* 25(36):8522–8527
353. Huang R, Yan S, Zheng X, Luo F, Deng M, Fu B, Xiao Y, Zhao X, Zhou X (2012) Development of a pH-activatable fluorescent probe and its application for visualizing cellular pH change. *Analyst* 137(19):4418–4420
354. Myochin T, Kiyose K, Hanaoka K, Kojima H, Terai T, Nagano T (2011) Rational design of ratiometric near-infrared fluorescent pH probes with various pKa values, based on aminocyanine. *J Am Chem Soc* 133(10):3401–3409
355. Haberhauer G, Gleiter R, Burkhart C (2016) Planarized Intramolecular Charge Transfer: A Concept for fluorophores with both large Stokes shifts and high fluorescence quantum yields. *Chem - A Eur J* 22(3):971–978
356. Edmonds TE, Flatters NJ, Jones CF, Miller JN (1988) Determination of pH with acid-base indicators: Implications for optical fibre probes. *Talanta* 35(2):103–107
357. Alimmari A, Božić B, Mijin D, Marinković A, Valentić N, Uščumlić G (2015) Synthesis, structure and solvatochromic properties of some novel 5-aryloxy-6-hydroxy-4-(4-methoxyphenyl)-3-cyano-2-pyridone dyes: Hydrazone-azo tautomeric analysis. *Arab J Chem* 8(2):269–278
358. Schrödle S, Hefter G, Buchner R (2007) Picosecond dynamics and microheterogeneity of water + dioxane mixtures. *J Phys Chem B* 111(21):5946–5955
359. Casassas E, Fonrodona G, de Juan A (1992) Solvatochromic parameters for binary mixtures and a correlation with equilibrium constants. Part I. Dioxane-water mixtures. *J Solution Chem* 21(2):147–162
360. Spange S (2024) Polarity of organic solvent/water mixtures measured with Reichardt's B30 and related solvatochromic probes—A critical review. *Liquids* 4(1):191–230
361. Reichardt C (1979) Empirical parameters of solvent polarity as linear free-energy relationships. *Angew Chemie Int Ed English* 18(2):98–110
362. Reichardt C (1965) Empiric parametres of the polarity of solvents. *Angew Chem, internat Ed* 4(1887):29–40
363. Abbaszadegan A, Sedigh Shams M, Jamshidi Y, Parashos P, Bagheri R (2015) Effect of calcium chloride on physical properties of calcium-enriched mixture cement. *Aust Endod J* 41(3):117–121
364. Benniston AC, Harriman A, Rostron JP (2005) The effect of solvent polarity on the photophysical properties of 4-cyano-(4'-methylthio)diphenylacetylene: A prototypic donor-acceptor system. *Phys Chem Chem Phys* 7(16):3041–3047
365. Casey KG, Onganer Y, Quitevis EL (1992) Effect of solvent polarity on non-radiative processes in xanthene dyes: the acid form of rhodamine B in nitrile solvents. *J Photochem Photobiol A Chem* 64(3):307–314
366. Erker C, Basché T (2022) The energy gap law at work: Emission yield and rate fluctuations of single NIR emitters. *J Am Chem Soc* 144(31):14053–14056
367. Ma J, Sun R, Xia K, Xia Q, Liu Y, Zhang X (2024) Design and application of fluorescent probes to

- detect cellular physical microenvironments. *Chem Rev* 124(4):1738–1861
368. Yin X, Cai Y, Cai S, Jiao X, Liu C, He S, Zeng X (2020) A deep-red fluorescent molecular rotor based on donor-two-acceptor modular system for imaging mitochondrial viscosity. *RSC Adv* 10(51):30825–30831
369. Sun C, Cao W, Zhang W, Zhang L, Feng Y, Fang M, Xu G, Shao Z, Yang X, Meng X (2019) Design of a ratiometric two-photon fluorescent probe for dual-response of mitochondrial SO<sub>2</sub> derivatives and viscosity in cells and in vivo. *Dye Pigment* 171(July):107709
370. Sahoo D, Chakravorti S (2009) Spectra and dynamics of an ionic styryl dye in reverse micelles. *J Photochem Photobiol A Chem* 205(2–3):129–138
371. Yang T, Fang Y, Zhang Q, Wang F, Xu X, Li C (2024) Lipid droplets-targeting multifunctional fluorescent probe and its application in ferroptosis and bioimaging. *Sensors Actuators B Chem* 417(June):136138
372. Reichardt C, Welton T (2010) Solvents and solvent effects in organic chemistry: Fourth Edition. *Solvents Solvent Eff Org Chem Fourth Ed* 549–555
373. Segur JB, Oderstar HE (1951) Viscosity of glycerol and its aqueous solutions. *Ind Eng Chem* 43(9):2117–2120
374. Salmela S, Vuori E (1979) Contamination with cadmium from micropipette tips. *Talanta* 26(2):175–176
375. Olivieri A, Degenhardt OS, McDonald GR, Narang D, Paulsen IM, Kozuska JL, Holt A (2012) On the disruption of biochemical and biological assays by chemicals leaching from disposable laboratory plasticware. *Can J Physiol Pharmacol* 90(6):697–703
376. Tapiero H, Townsend DM, Tew KD (2003) Trace elements in human physiology and pathology. Copper. *Biomed Pharmacother* 57(9):386–398
377. Bae DH, Marino M, Iaffaldano B, et al (2020) Design and testing of vector-producing HEK293T cells bearing a genomic deletion of the SV40 T antigen coding region. *Mol Ther Methods Clin Dev* 18(September):631–638
378. Sundararajan R, Salameh T, Camarillo IG, Ramachandran RP, Natarajan A, Sankaranarayanan K (2014) Irreversible electroporation: a drug-free cancer treatment. Woodhead Publishing Limited
379. Buckman JF, Hernández H, Kress GJ, Votyakova T V., Pal S, Reynolds IJ (2001) MitoTracker labeling in primary neuronal and astrocytic cultures: Influence of mitochondrial membrane potential and oxidants. *J Neurosci Methods* 104(2):165–176
380. Clutton B, ACP A reproducible, objective method using MitoTracker® fluorescent dyes to assess mitochondrial mass in T Cells by flow cytometry. *Cytom Part A* 99 (95)(7 (4)):753 (450–456)
381. Zhitomirsky B, Farber H, Assaraf YG (2018) LysoTracker and MitoTracker Red are transport substrates of P-glycoprotein: implications for anticancer drug design evading multidrug resistance. *J Cell Mol Med* 22(4):2131–2141
382. Hanahan D, Weinberg RA (2011) Hallmarks of cancer: The next generation. *Cell* 144(5):646–674
383. Dessard M, Manneville JB, Berret JF (2024) Cytoplasmic viscosity is a potential biomarker for metastatic breast cancer cells. *Nanoscale Adv* 6(6):1727–1738

384. Webb BA, Chimenti M, Jacobson MP, Barber DL (2011) Dysregulated pH: A perfect storm for cancer progression. *Nat Rev Cancer* 11(9):671–677
385. Yue Y, Huo F, Lee S, Yin C, Yoon J (2017) A review: The trend of progress about pH probes in cell application in recent years. *Analyst* 142(1):30–41
386. Liu Y, Zhang D, Qu Y, Tang F, Wang H, Ding A, Li L (2024) Advances in small-molecule fluorescent pH probes for monitoring mitophagy. *Chem Biomed Imaging* 2(2):81–97
387. Rai R, Bhandari R, Kaleem M, Shraogi N, Patnaik S, Mishra H, Misra A (2024) An imidazole-naphthalimide-based pH-sensitive molecular probe for selective detection of picric acid and cell imaging. *Ind Eng Chem Res* 63(23):10077–10092
388. Chao L, Zhang Q, Ga L, Ai J (2024) Design, synthesis and application of polarity- and pH-sensitive dual-responsive small molecule fluorescent probe for early cancer diagnosis. *Microchem J* 205:111250
389. Wang X, Wang L, Jin T, Sun K, Yang J (2023) pH/Viscosity dual-response fluorescent probes as highly selective tumor visualization tools. *Sensors Actuators B Chem* 375(October 2022):132935
390. Zhu M, Sen, Zhang G, Xu YJ, Sun R, Ge JF (2023) Conjugated structures based on quinazolinones and their application in fluorescent labeling. *Org Biomol Chem* 21(9):1992–2000
391. Luo J, Song C, Chen Y, Liu K (2024) Near-infrared fluorescent probe with pH- and viscosity-switchable performance for the detection of thrombi in live animals and organs. *Chem Biomed Imaging* 2(6):422–431
392. Li L, Guo D, Wang C, et al (2024) Revealing the protective role of mitophagy for liver injury via a promising dual-channel activated fluorescent probe. *Sensors Actuators B Chem* 420(August):136459
393. Zhang X, Huo F, Zhang Y, Yue Y, Yin C (2022) Dual-channel detection of viscosity and pH with a near-infrared fluorescent probe for cancer visualization. *Analyst* 147(11):2470–2476
394. Chen T, Xiang Y, Sang Y, et al (2025) Bioimaging research of a turn-on homodimer fluorescent probes for pH and viscosity: A new turn-on strategy. *J Mol Struct* 1319(P2):139478
395. Zhou Y, Wang Q, Chanmungkalakul S, Wu X, Xiao H, Miao R, Liu X, Fang Y (2024) Fluorogenic rhodamine probes with pyrrole substitution enables STED and lifetime imaging of lysosomes in live cells. *Chem - A Eur J* 30(15):1–7
396. He Y, Yang YH, Chen GY, Li L, Wang LQ, Li LK, Wang JY (2024) A viscosity-sensitive fluorescent probe with a large Stokes shift for monitoring lipid droplets and its application in cell, tobacco leaf, and food detection. *New J Chem* 48(28):12828–12833
397. Jachak M, Khopkar S, Patel K, Patil Y, Shankarling G (2021) Synthesis of novel D- $\pi$ -A chromophores: Effect of structural manipulations on photophysical properties, viscosity and DFT study. *J Mol Struct* 1233:130086
398. Pei S, Li J, Zhang C, Zhang G, Zhou Y, Fan L, Wang W, Shuang S, Dong C (2022) TICT-based microenvironment-sensitive probe with turn-on red emission for human serum albumin detection and for targeting lipid droplet imaging. *ACS Biomater Sci Eng* 8(1):253–260
399. Pei S, Li J, Kang N, Zhang G, Zhang B, Zhang C, Shuang S (2022) Synthesis of a new environment-sensitive fluorescent probe based on TICT and application for detection of human serum albumin and specific lipid droplets imaging. *Anal Chim Acta* 1190:339267

400. Svoiakov RP, Kulyk OG, Hovor I V., Shishkina S V., Tatarets AL (2023) Environment-sensitive indolenine-based hemisquaraine dyes: Synthesis, molecular structure, and spectral properties. *Dye Pigment* 219(August):111612
401. Li ZL, Han GM, Wang K, Lyu JA, Li ZW, Zhu BC, Zhu LN, Kong DM (2024) Multiparameter assessment of foam cell formation progression using a dual-color switchable fluorescence probe. *Anal Chem* 96(18):6968–6977
402. Duke RM, Veale EB, Pfeffer FM, Kruger PE, Gunnlaugsson T (2010) Colorimetric and fluorescent anion sensors: An overview of recent developments in the use of 1,8-naphthalimide-based chemosensors. *Chem Soc Rev* 39(10):3936–3953
403. Darmawan A, Muhtar H, Zakiyyah H, Bima DN (2023) Water soluble Schiff base complexes of 4-aminoantipyrine: Synthesis, characterization, and antibacterial activity. *Polyhedron* 244(August):116607
404. Mansour AM, Radacki K, Shehab OR (2021) Sulfonate improves water solubility and cell selective toxicity and alters the lysozyme binding activity of half sandwich Rh(III) complexes. *Dalt Trans* 50(31):10701–10706
405. Idzik KR, Nödler K, Maier F, Licha T (2014) Efficient synthesis and reaction kinetics of readily water soluble esters containing sulfonic groups. *Molecules* 19(12):21022–21033
406. Chen L, Park SJ, Wu D, Kim HM, Yoon J (2019) A two-photon fluorescent probe for colorimetric and ratiometric monitoring of mercury in live cells and tissues. *Chem Commun* 55(12):1766–1769
407. Zeng X, Zhang X, Zhu B, Jia H, Li Y (2012) A highly selective wavelength-ratiometric and colorimetric probe for cysteine. *Dye Pigment* 94(1):10–15
408. Lim T, Ryoo JY, Jang M, Han MS (2021) Ligand-free Suzuki-Miyaura cross-coupling with low Pd content: rapid development by a fluorescence-based high-throughput screening method. *Org Biomol Chem* 19(5):1009–1016
409. De Barros TC, Filho PB, Loos M, Politi MJ, Chaimovich H, Cuccovia IM (2011) Formation and decomposition of N-alkylnaphthalimides: Experimental evidences and ab initio description of the reaction pathways. *J Phys Org Chem* 24(5):385–397
410. Wang S, Fang W (2011) Design and synthesis of a dual linker for solid phase synthesis of oleanolic acid derivatives. *Molecules* 16(6):4748–4763
411. Fleming CL, Ashton TD, Pfeffer FM (2014) Synthesis of 4-amino substituted 1,8-naphthalimide derivatives using palladium-mediated amination. *Dye Pigment* 109:135–143
412. Sun G, Wei YC, Zhang Z, Lin JA, Liu ZY, Chen W, Su J, Chou PT, Tian H (2020) Diversified excited-state relaxation pathways of donor–linker–acceptor dyads controlled by a bent-to-planar motion of the donor. *Angew Chemie - Int Ed* 59(42):18611–18618
413. Zhou J, Lin X, Ji X, Xu S, Liu C, Dong X, Zhao W, Zhao W (2020) Azetidine-containing heterospirocycles enhance the performance of fluorophores. *Org Lett* 22(11):4413–4417
414. Liu S, Bai H, Sun Q, Zhang W, Qian J (2015) Naphthalimide-based fluorescent photoinduced electron transfer sensors for saccharides. *RSC Adv* 5(4):2837–2843
415. Un HI, Wu S, Huang CB, Xu Z, Xu L (2015) A naphthalimide-based fluorescent probe for highly selective detection of histidine in aqueous solution and its application in in vivo imaging. *Chem Commun* 51(15):3143–3146

416. Zhang PL, Gopala L, Zhang SL, Cai GX, Zhou CH (2022) An unanticipated discovery towards novel naphthalimide corbelled aminothiazoximes as potential anti-MRSA agents and allosteric modulators for PBP2a. *Eur J Med Chem* 229:114050
417. Zhou X, Su F, Hongguang Lu, Senechal-Willis P, Tian Y, Johnson R, Meldrum DR (2012) A FRET-based ratiometric chemosensor for in vitro cellular fluorescence analyses of pH. *Biomaterials* 33(1):171–180
418. Lee MH, Kim JY, Han JH, Bhuniya S, Sessler JL, Kang C, Kim JS (2012) Direct fluorescence monitoring of the delivery and cellular uptake of a cancer-targeted RGD peptide-appended naphthalimide theragnostic prodrug. *J Am Chem Soc* 134(30):12668–12674
419. Lee MH, Park N, Yi C, Han JH, Hong JH, Kim KP, Kang DH, Sessler JL, Kang C, Kim JS (2014) Mitochondria-immobilized pH-sensitive off-on fluorescent probe. *JACS* 136:14136–14142
420. Tian Y, Su F, Weber W, Nandakumar V, Shumway BR, Jin Y, Zhou X, Holl MR, Johnson RH, Meldrum DR (2010) A series of naphthalimide derivatives as intra and extracellular pH sensors. *Biomaterials* 31(29):7411–7422
421. Hu J, Chen Z, Li J, Zhang L, Zhu J, Wang C, Cui L, Zheng K (2024) A novel low-cytotoxicity fluorescent probe applied to monitor pH in vivo and in vitro. *Tetrahedron* 155(March):133917
422. Georgiev NI, Krasteva P V., Bakov V V., Bojinov VB (2022) A highly water-soluble and solid state emissive 1,8-naphthalimide as a fluorescent PET Probe for determination of pHs, acid/base vapors, and water content in organic solvents. *Molecules* 27:4229
423. Dong Y, Xiao H, Xing L, Wu C, Zhou J, Zhou Z, Liu Y, Zhuo S, Li P (2020) Two-photon fluorescence visualization of lysosomal pH changes during mitophagy and cell apoptosis. *Talanta* 209:120549
424. Dong B, Song W, Lu Y, Kong X, Mehmood AH, Lin W (2019) An ultrasensitive ratiometric fluorescent probe based on the ICT-PET-FRET mechanism for the quantitative measurement of pH values in the endoplasmic reticulum (ER). *Chem Commun* 55(72):10776–10779
425. Georgiev NI, Marinova N V., Bojinov VB (2020) Design and synthesis of light-harvesting rotor based on 1,8-naphthalimide units. *J Photochem Photobiol A Chem* 401:112733
426. Moelbert S, Emberly E, Tang C (2004) Correlation between sequence hydrophobicity and surface-exposure pattern of database proteins. *Protein Sci* 13(3):752–762
427. Manea M, Mezo G, Hudecz F, Przybylski M (2007) Mass spectrometric identification of the trypsin cleavage pathway in lysyl-proline containing oligotufsin peptides. *J Pept Sci* 13(4):227–236
428. Rodriguez J, Gupta N, Smith RD, Pevzner PA (2008) Does trypsin cut before proline? *J Proteome Res* 7(1):300–305
429. Pappin DJC, Hojrup P, Bleasby AJ (1993) Rapid identification of proteins by peptide-mass fingerprinting. *Curr Biol* 3(6):327–332
430. Tamura T, Hamachi I (2019) Chemistry for covalent modification of endogenous/native proteins: From test tubes to complex biological systems. *J Am Chem Soc* 141(7):2782–2799
431. Avvaru BS, Kim CU, Sippel KH, Gruner SM, Agbandje-McKenna M, Silverman DN, McKenna R (2010) A short, strong hydrogen bond in the active site of human carbonic anhydrase II. *Biochemistry* 49(2):249–251
432. Pettersen EF, Goddard TD, Huang CC, Couch GS, Greenblatt DM, Meng EC, Ferrin TE (2004)

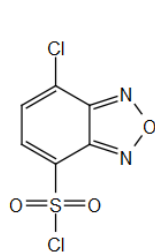


- UCSF Chimera - A visualization system for exploratory research and analysis. *J Comput Chem* 25(13):1605–1612
433. Nair SK, Christianson DW (1991) Unexpected pH-dependent conformation of His-64, the proton shuttle of carbonic anhydrase II. *J Am Chem Soc* 113(25):9455–9458
434. Davies MJ (2003) Singlet oxygen-mediated damage to proteins and its consequences. *Biochem Biophys Res Commun* 305(3):761–770
435. Davies MJ (2016) Protein oxidation and peroxidation. *Biochem J* 473(7):805–825
436. Perdigão N, Heinrich J, Stolte C, et al (2015) Unexpected features of the dark proteome. *Proc Natl Acad Sci U S A* 112(52):15898–15903
437. Perdigão N, Rosa A (2019) Dark proteome database: Studies on dark proteins. *High-Throughput* 8(2):1–30

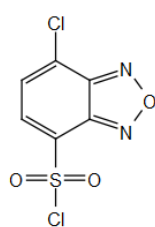
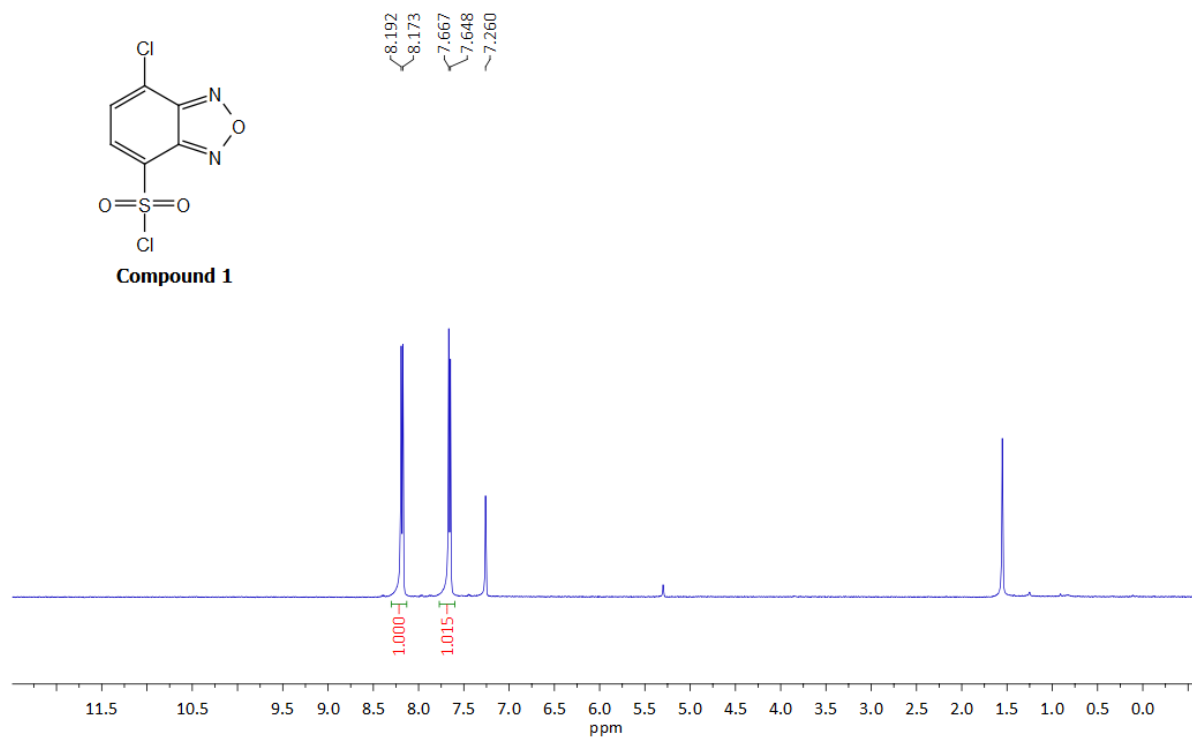
## 7. Supplementary data

### 7.1. $^1\text{H}$ & $^{13}\text{C}$ NMR spectra

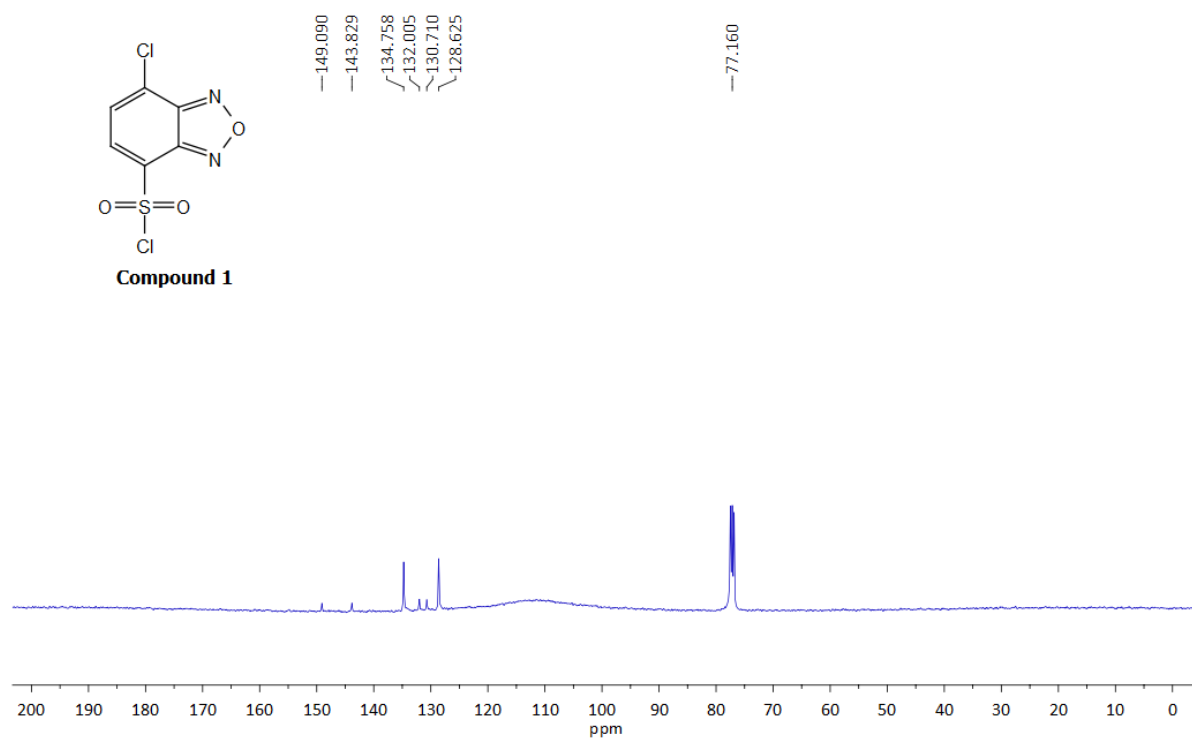
Compound 1:  $^1\text{H}$  NMR (400 MHz) &  $^{13}\text{C}$  NMR (101 MHz)  $\text{CDCl}_3$



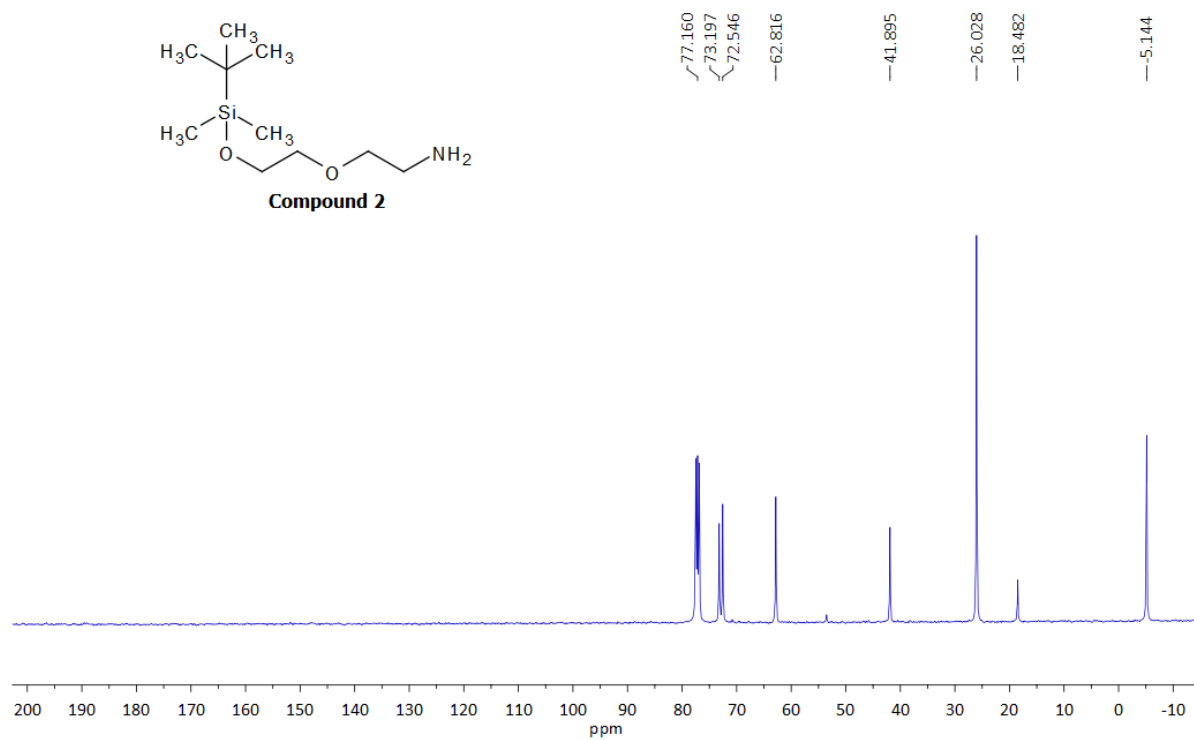
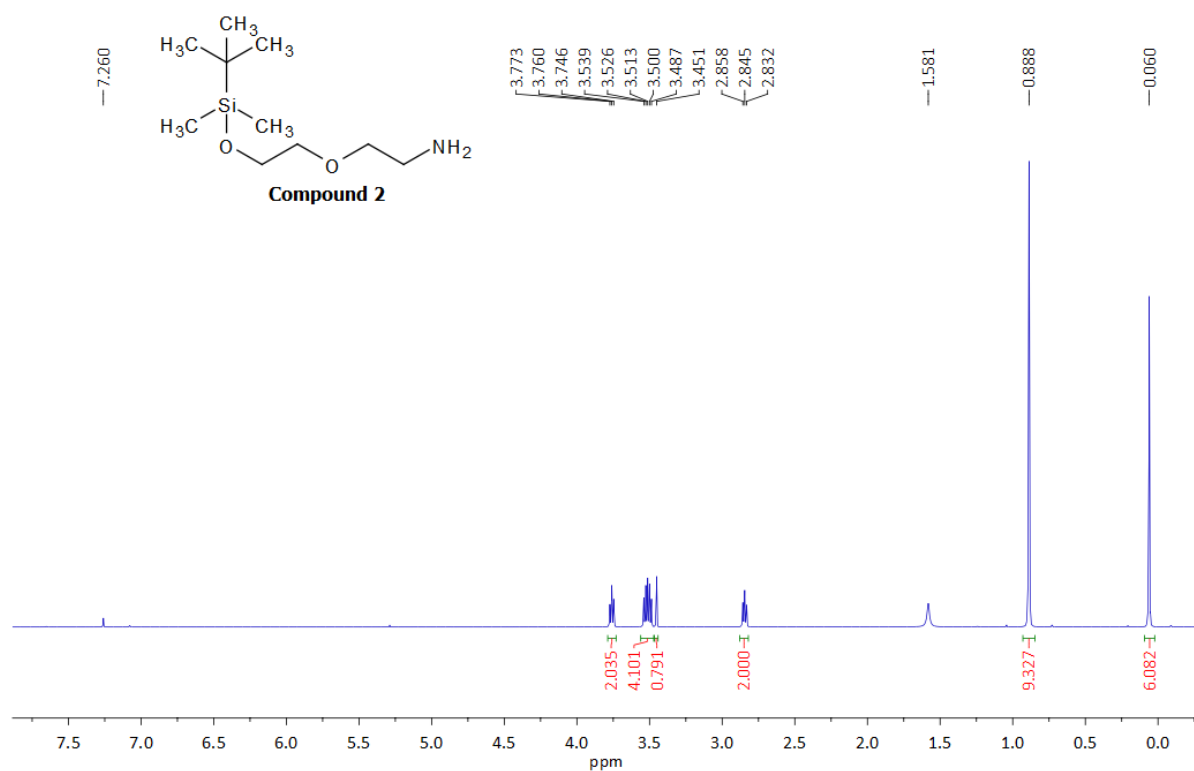
Compound 1



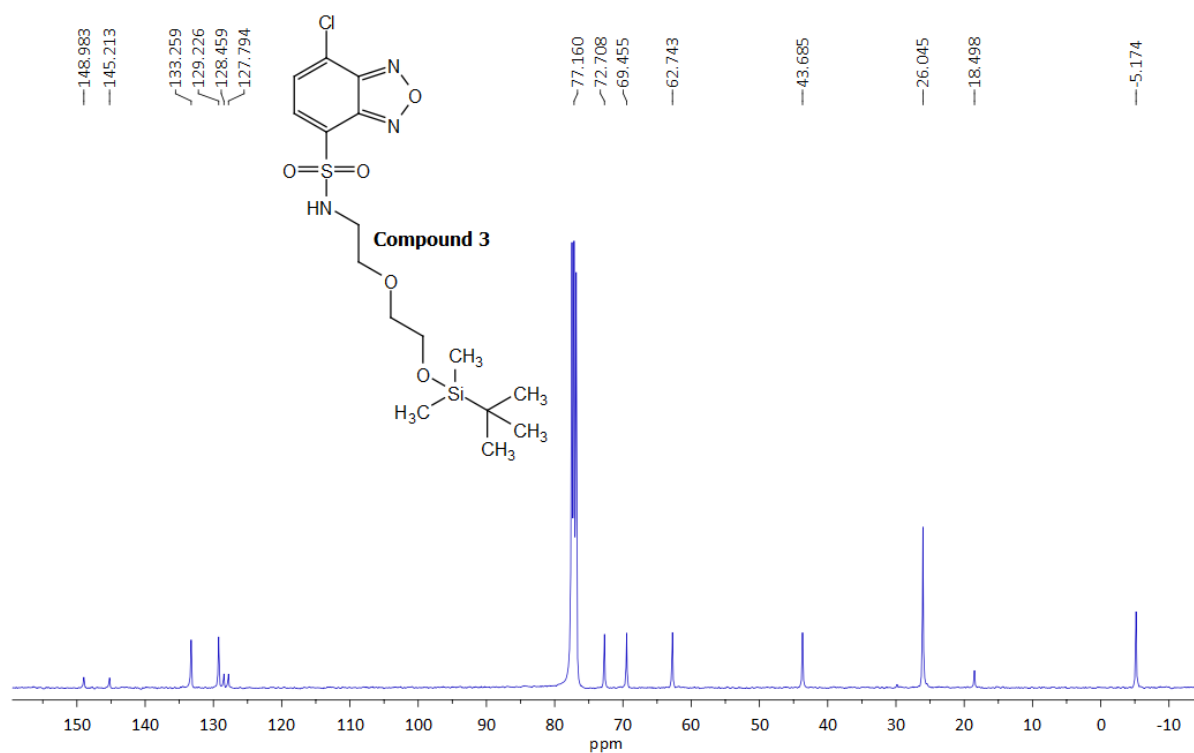
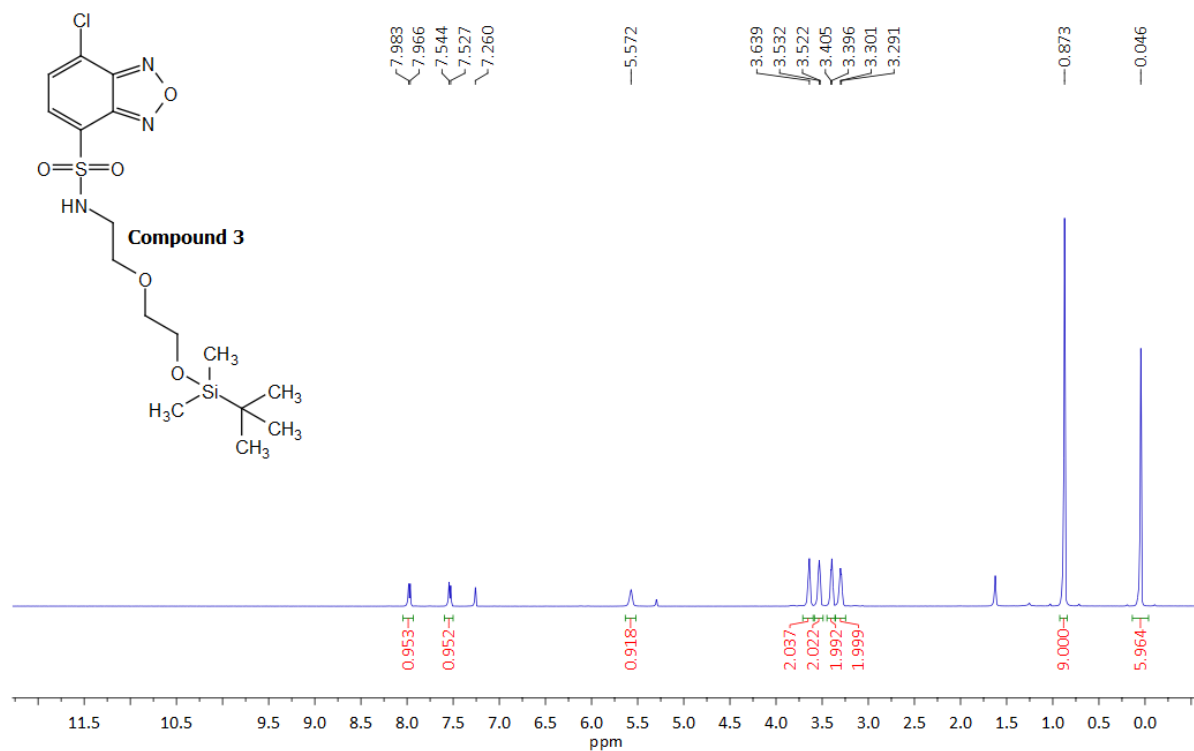
Compound 1



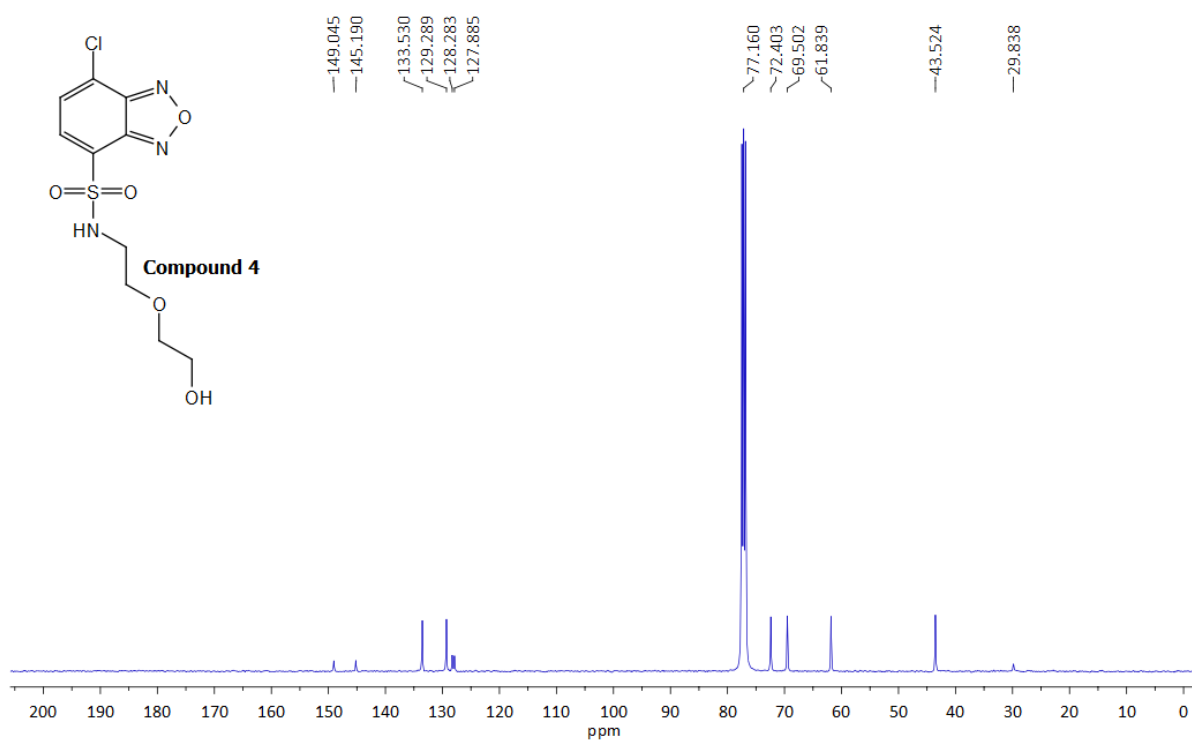
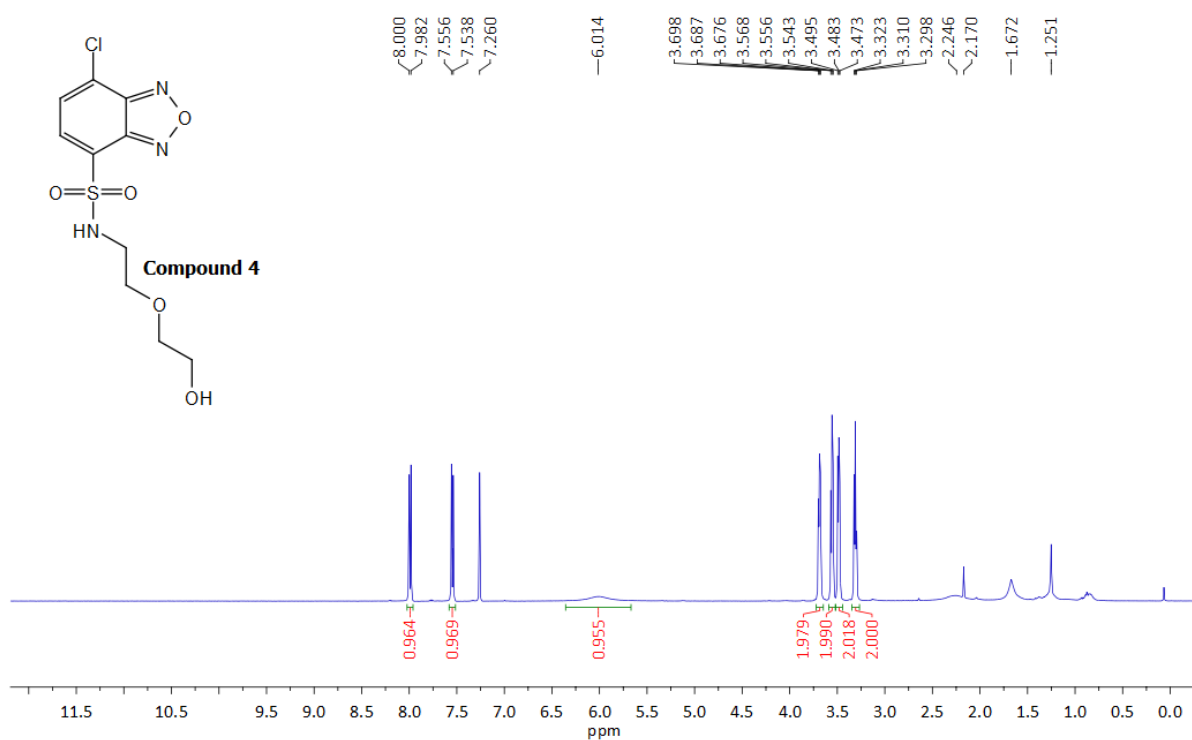
**Compound 2:  $^1\text{H}$  NMR (400 MHz) &  $^{13}\text{C}$  NMR (101 MHz)  $\text{CDCl}_3$**



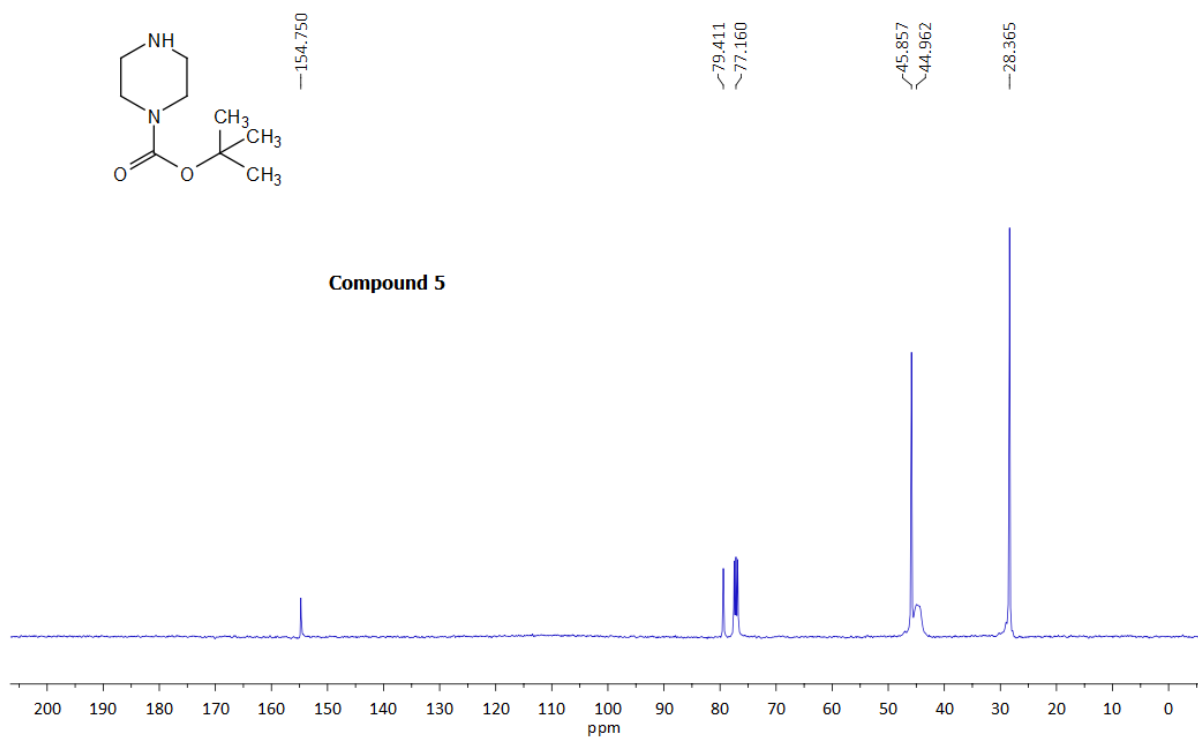
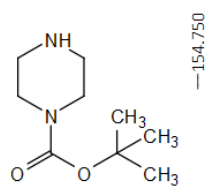
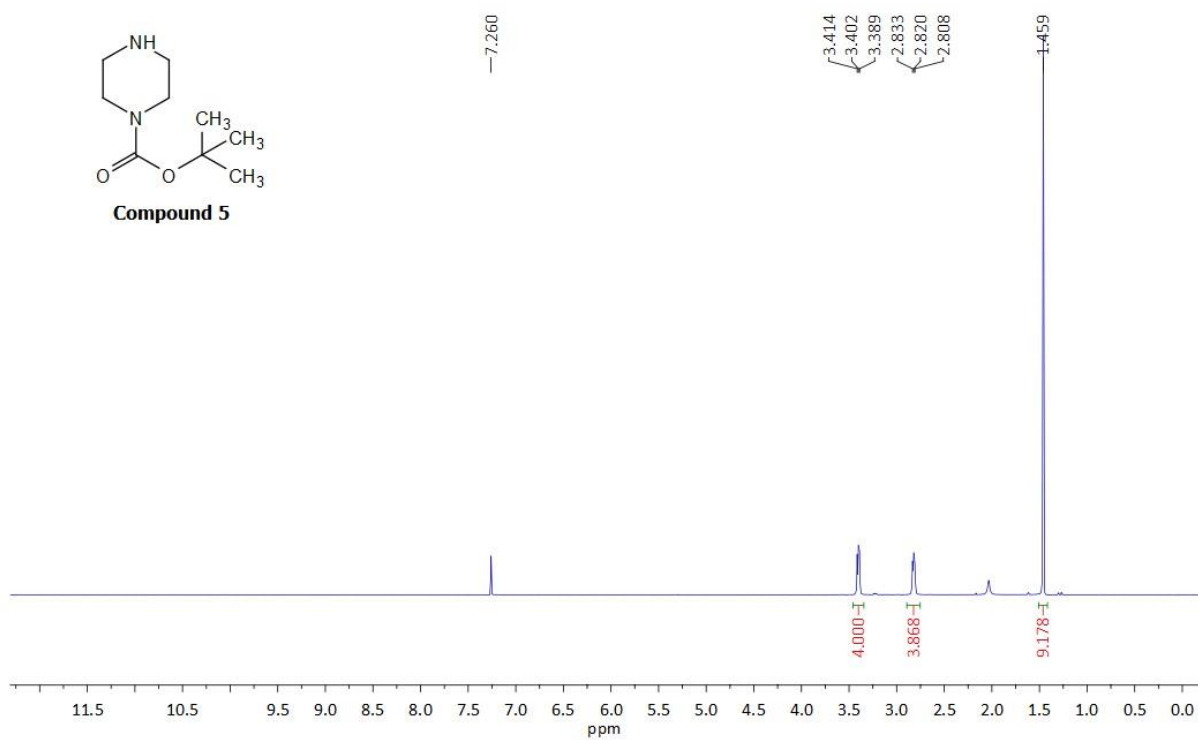
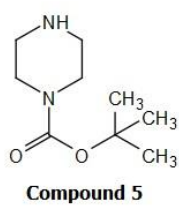
**Compound 3:  $^1\text{H}$  NMR (400 MHz) &  $^{13}\text{C}$  NMR (101 MHz)  $\text{CDCl}_3$**



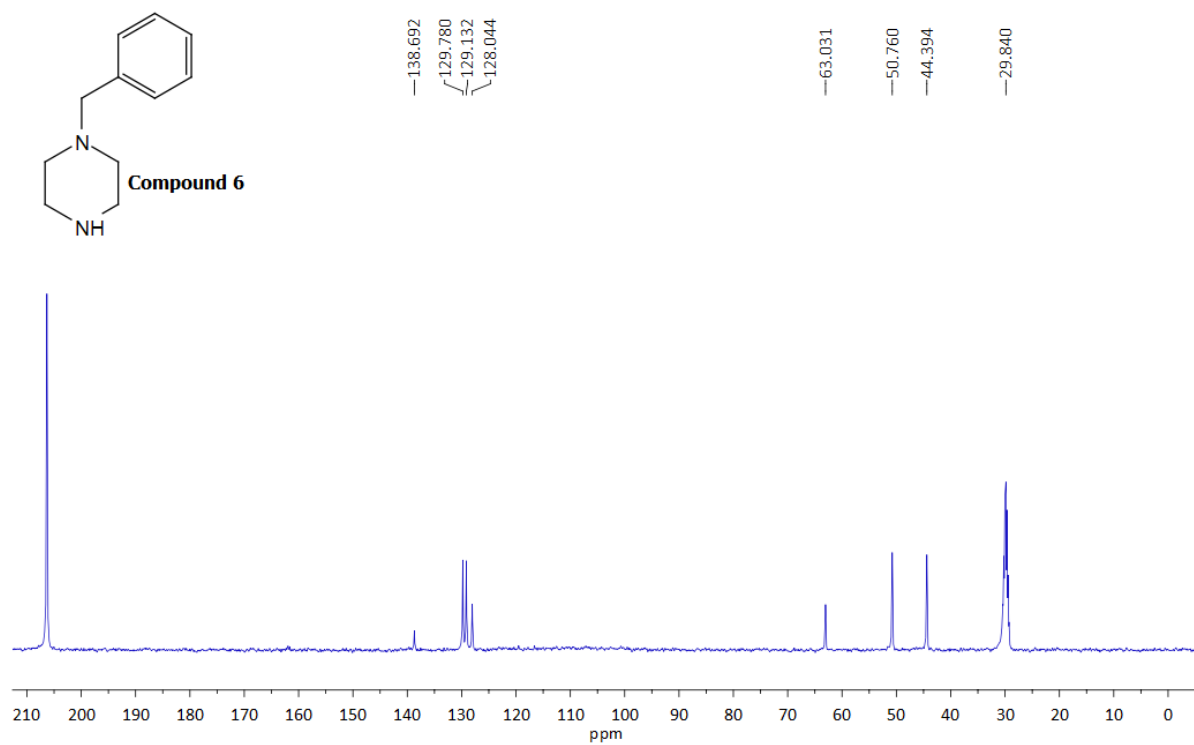
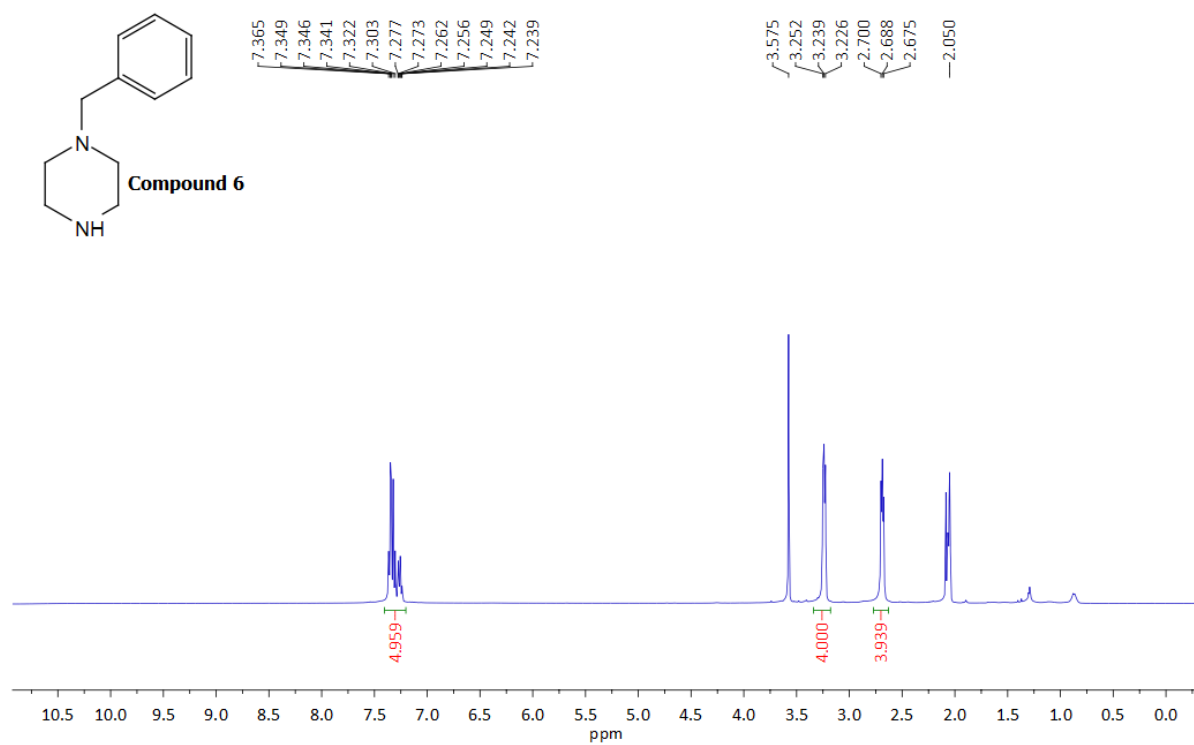
**Compound 4:  $^1\text{H}$  NMR (400 MHz) &  $^{13}\text{C}$  NMR (101 MHz)  $\text{CDCl}_3$**



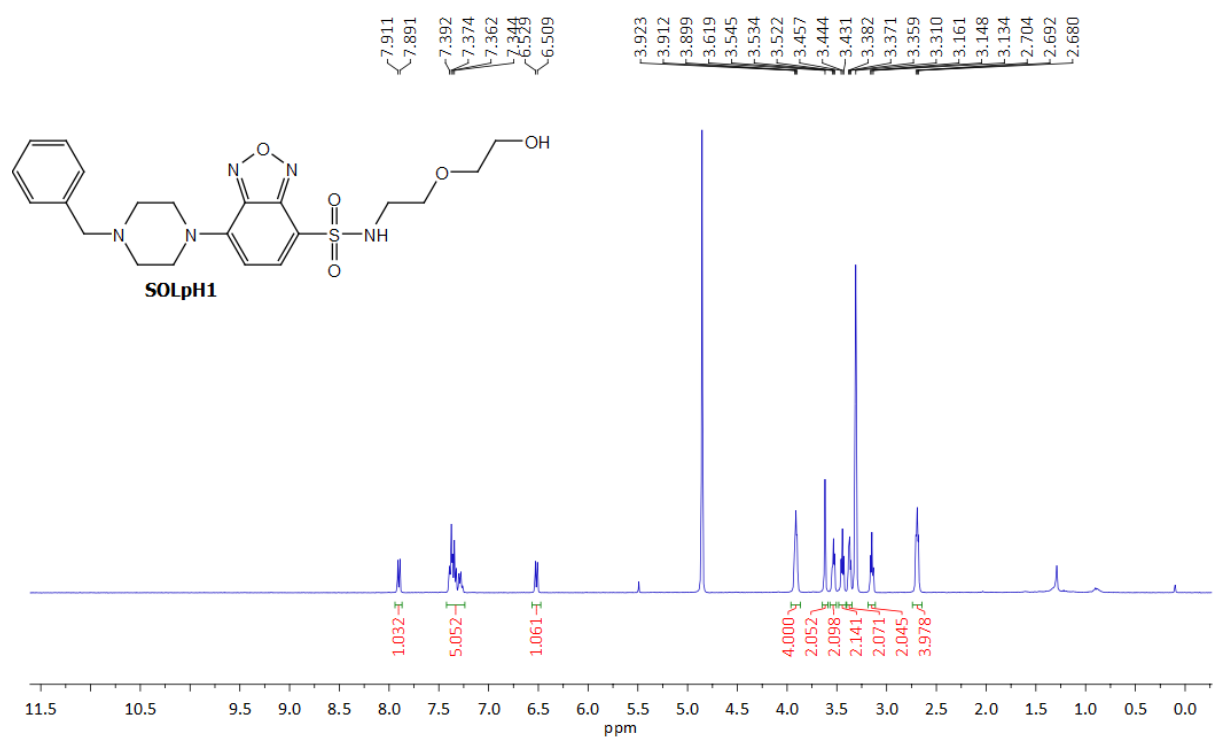
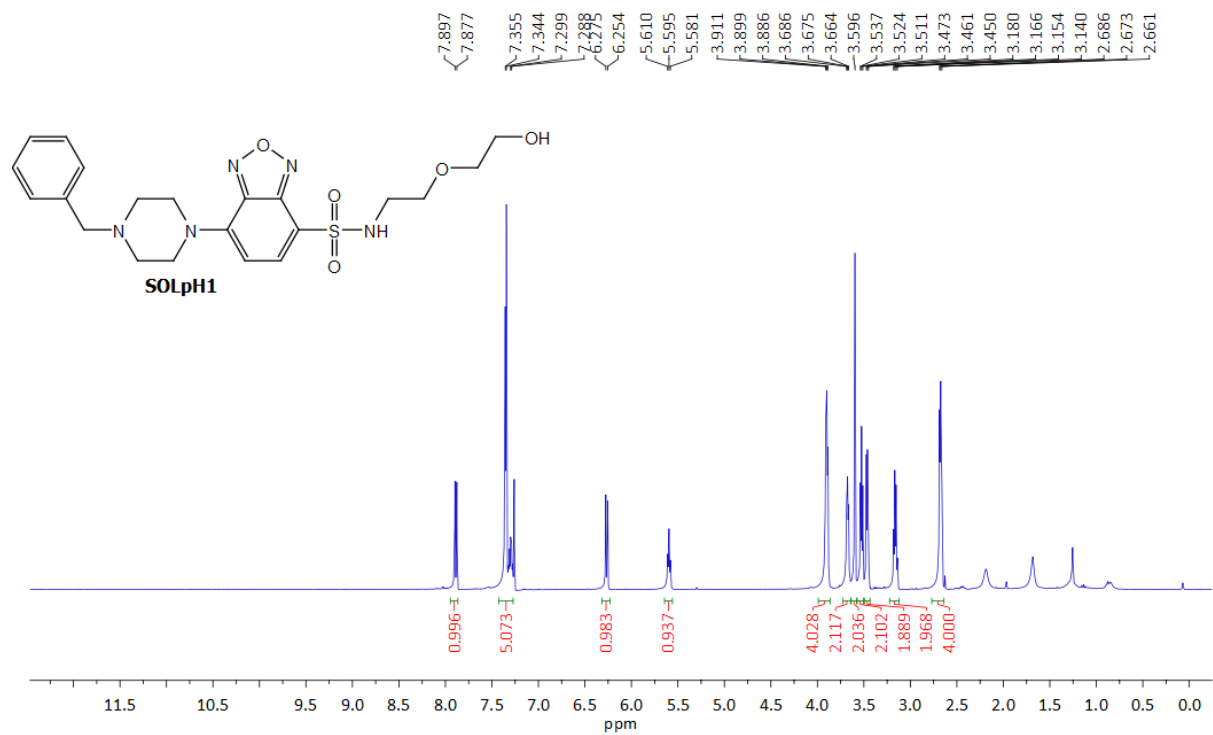
Compound 5:  $^1\text{H}$  NMR (400 MHz) &  $^{13}\text{C}$  NMR (101 MHz)  $\text{CDCl}_3$



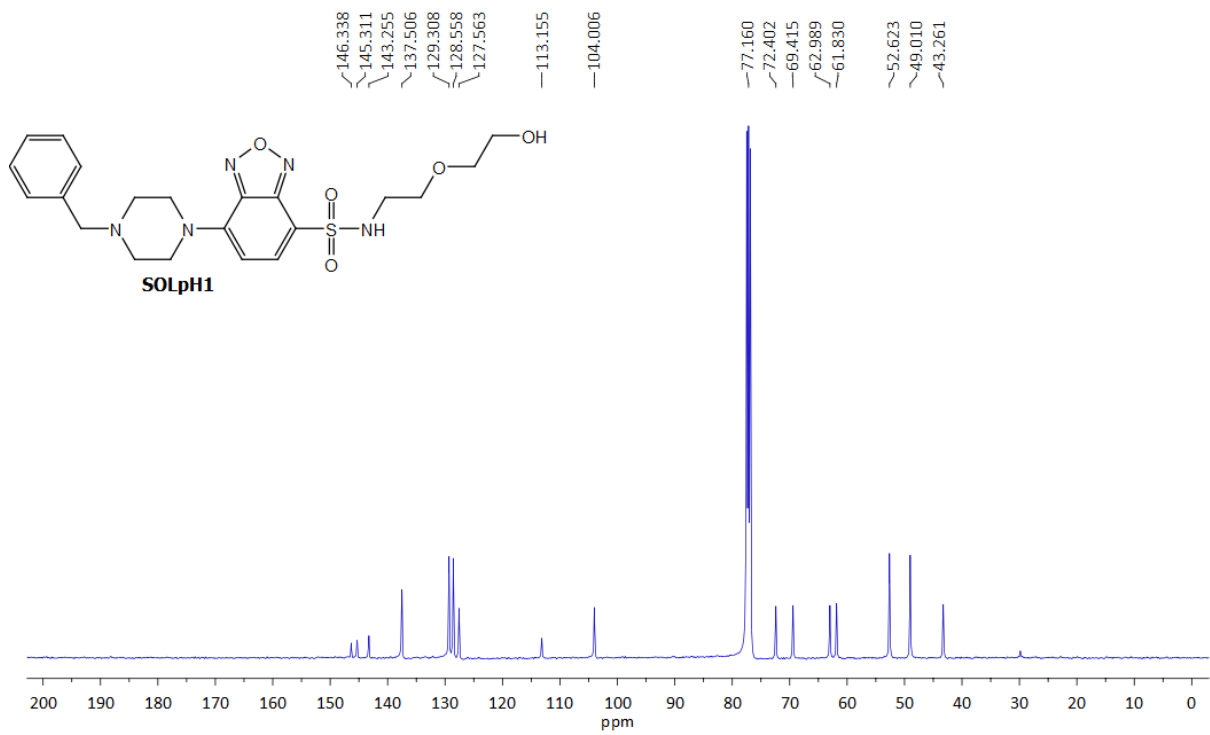
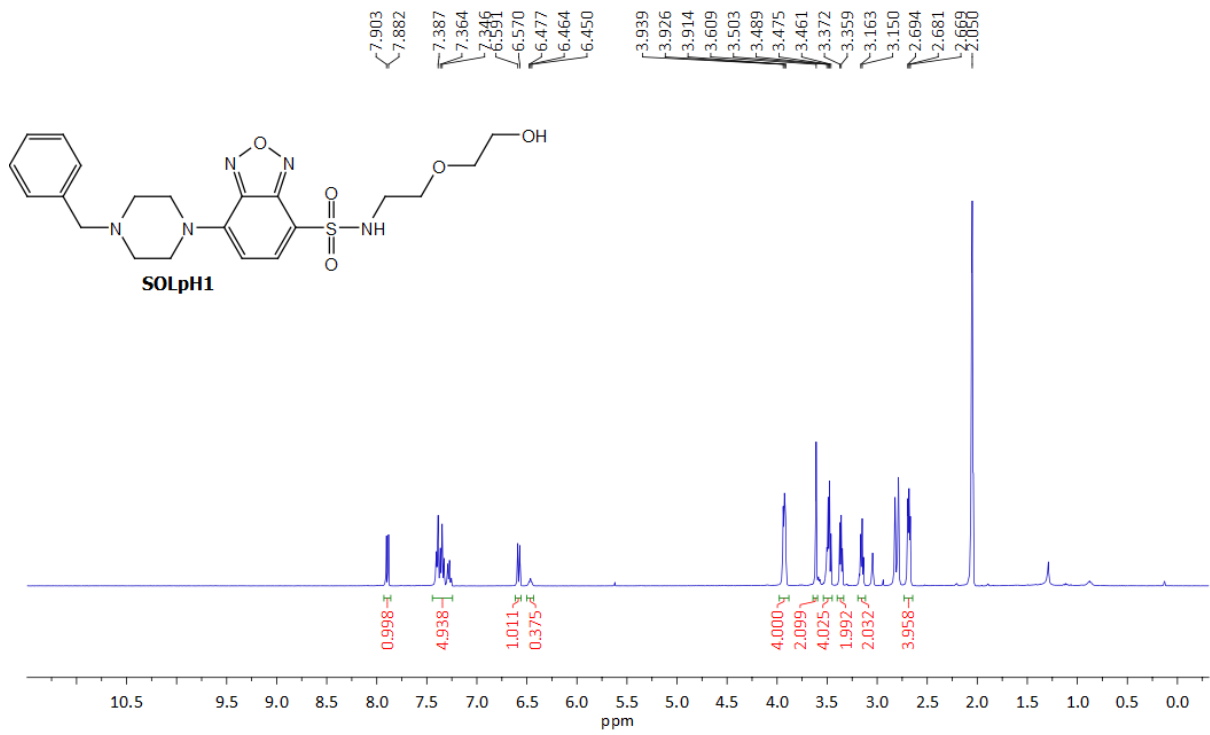
Compound 6:  $^1\text{H}$  NMR (400 MHz) &  $^{13}\text{C}$  NMR (101 MHz) Acetone- $\text{d}_6$



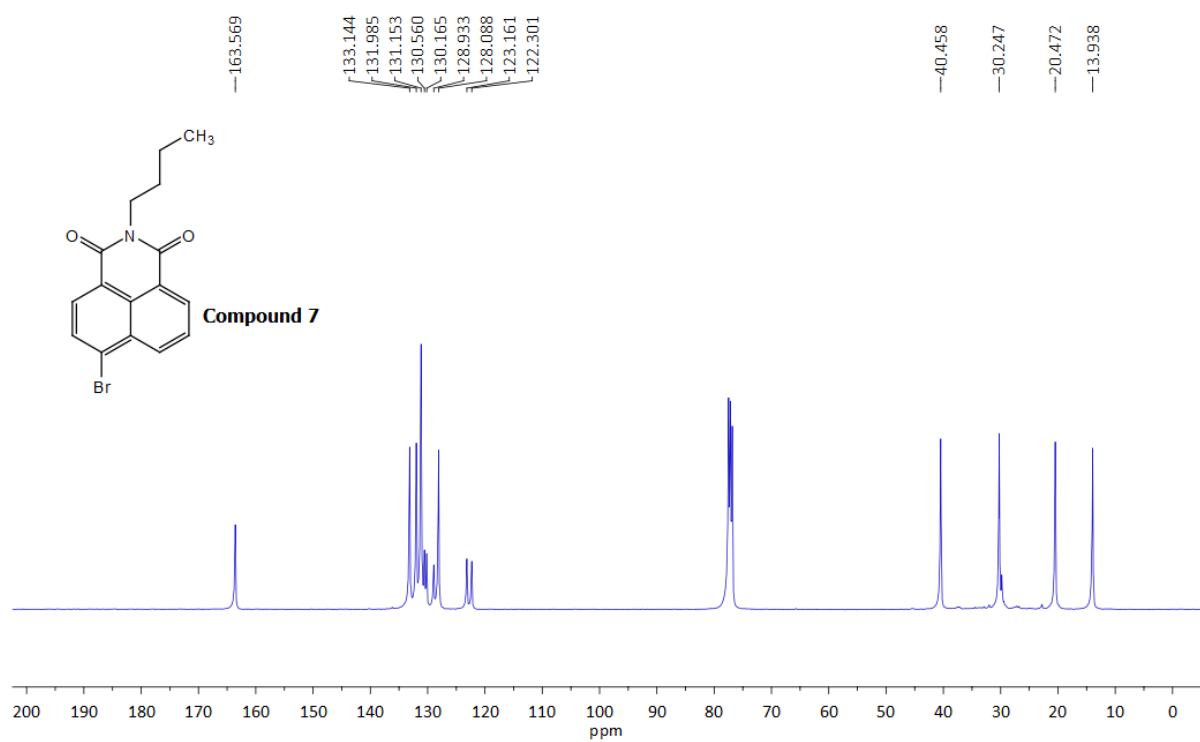
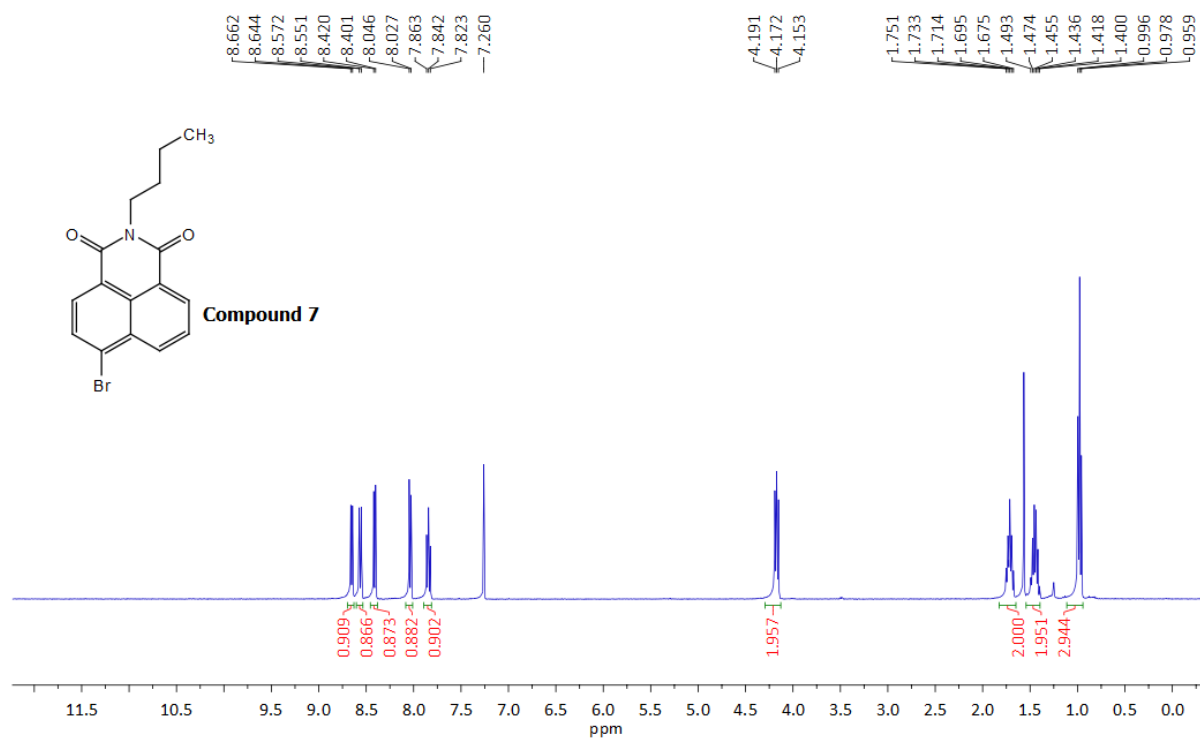
SOLpH1:  $^1\text{H}$  NMR (400 MHz)  $\text{CDCl}_3/\text{CD}_3\text{OD}/\text{Acetone-}d_6$  &  $^{13}\text{C}$  NMR (101 MHz)  $\text{CDCl}_3$



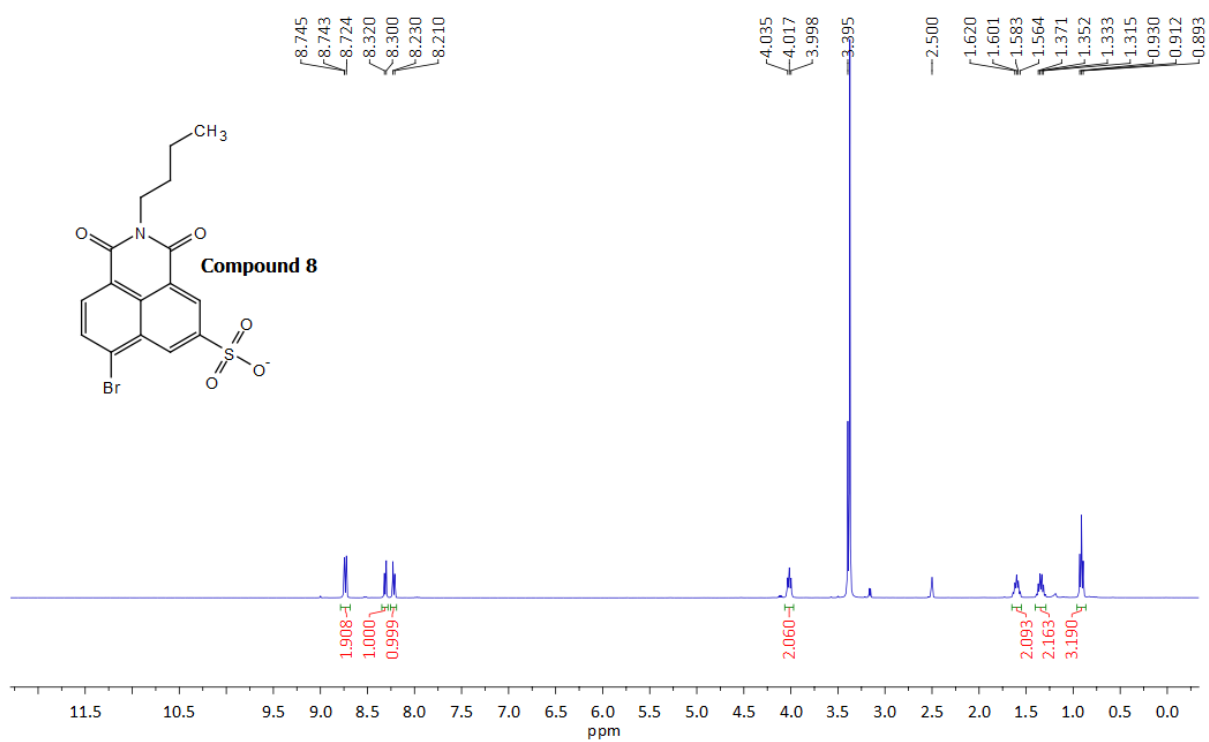




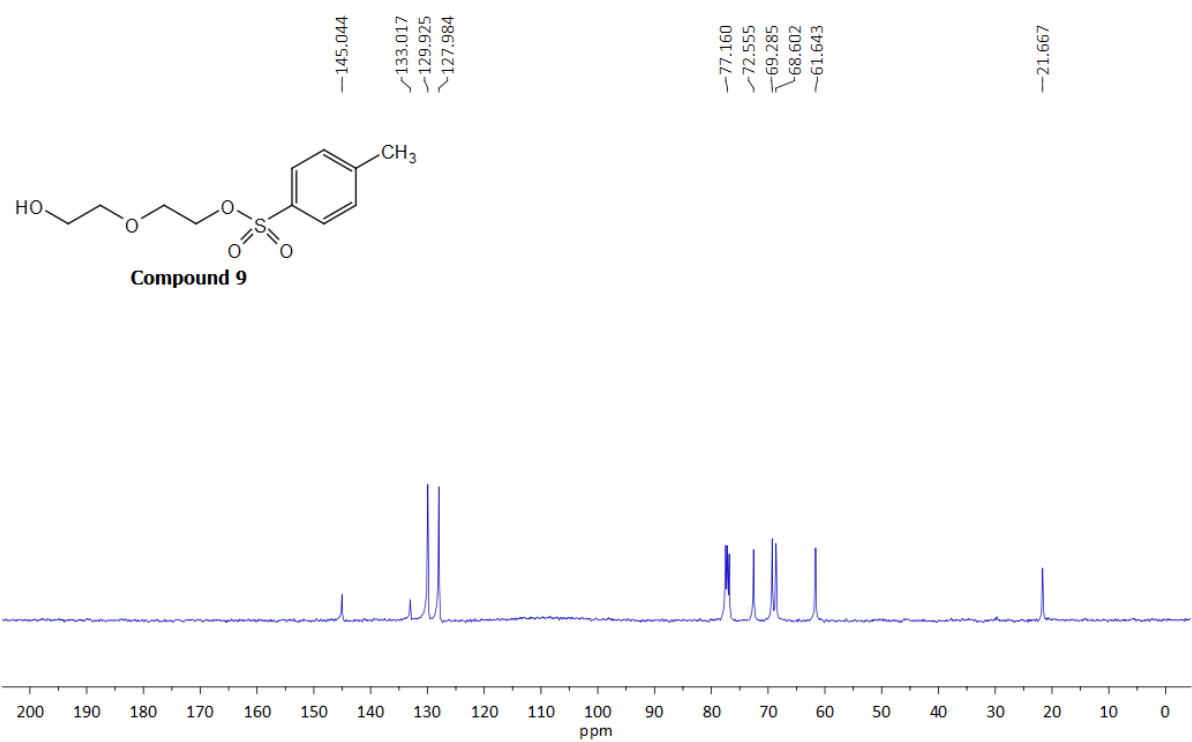
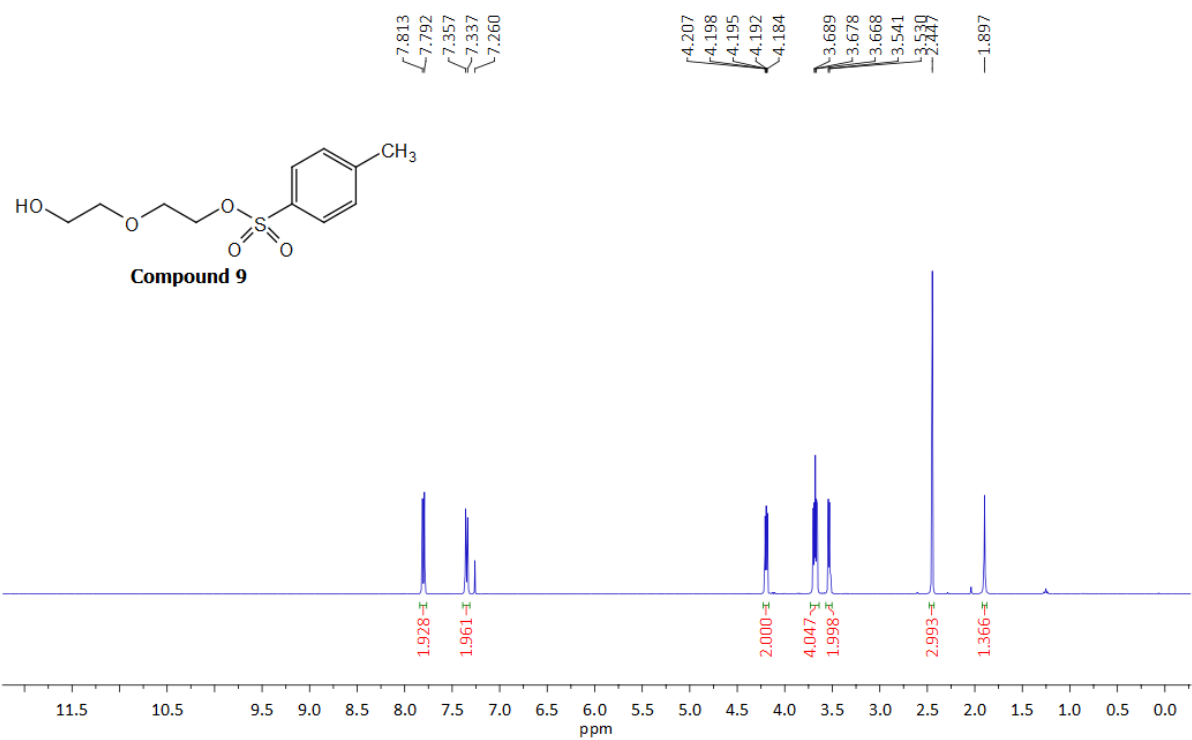
**Compound 7:  $^1\text{H}$  NMR (400 MHz) &  $^{13}\text{C}$  NMR (101 MHz)  $\text{CDCl}_3$**



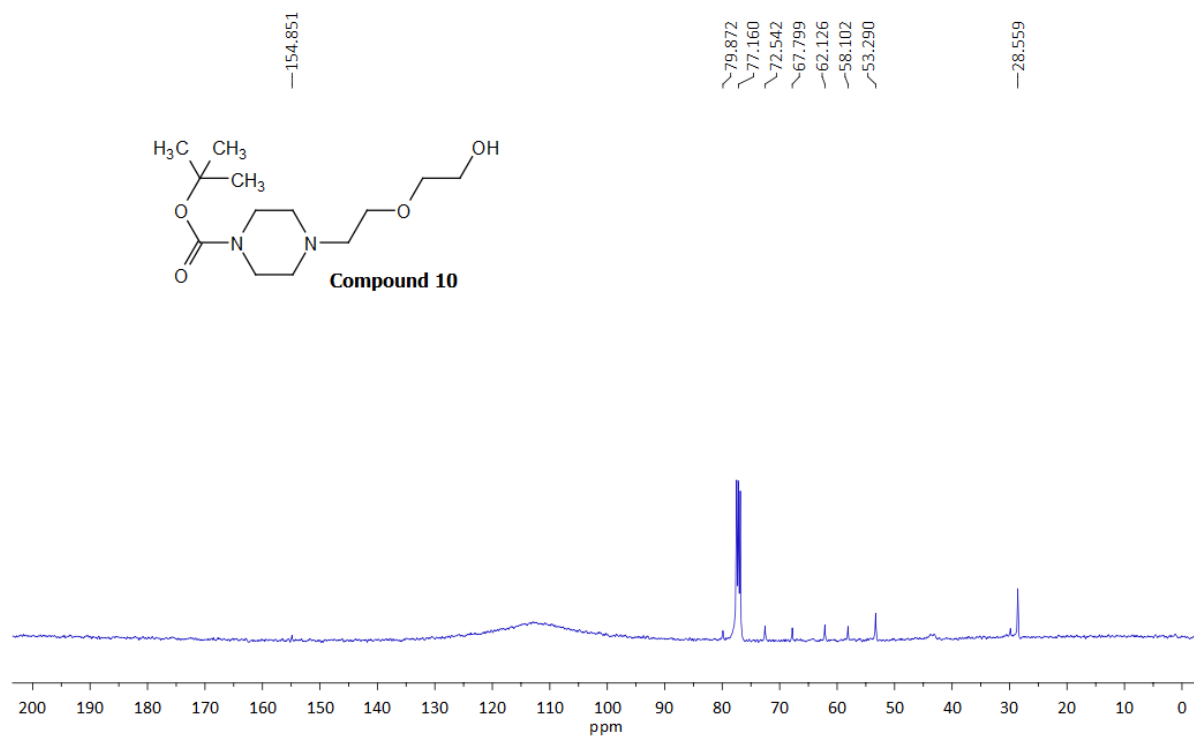
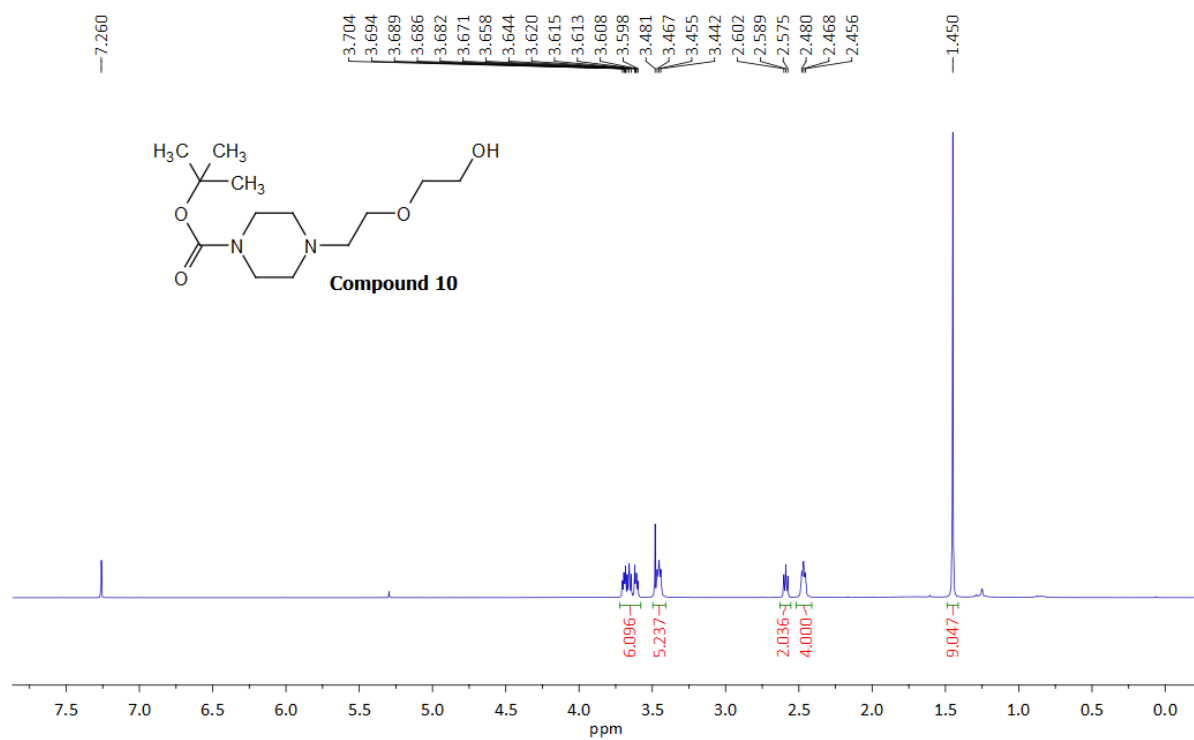
Compound 8:  $^1\text{H}$  NMR (400 MHz)  $\text{DMSO-d}_6$



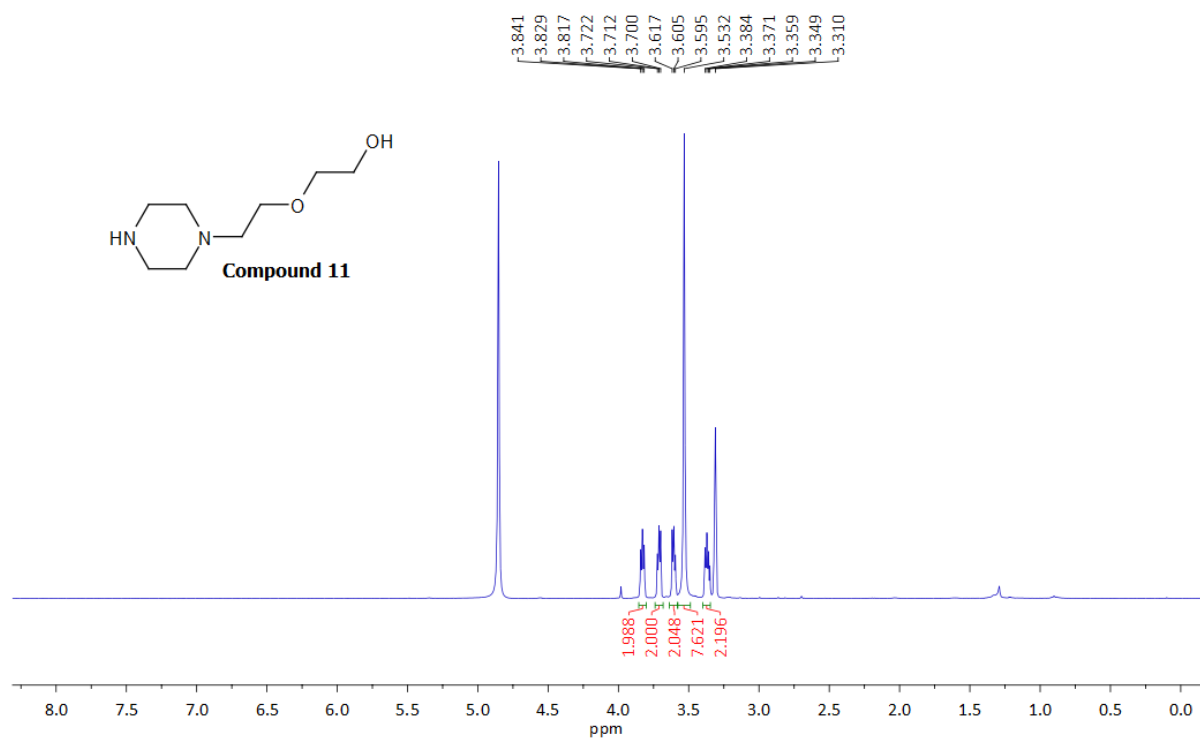
Compound 9:  $^1\text{H}$  NMR (400 MHz) &  $^{13}\text{C}$  NMR (101 MHz)  $\text{CDCl}_3$



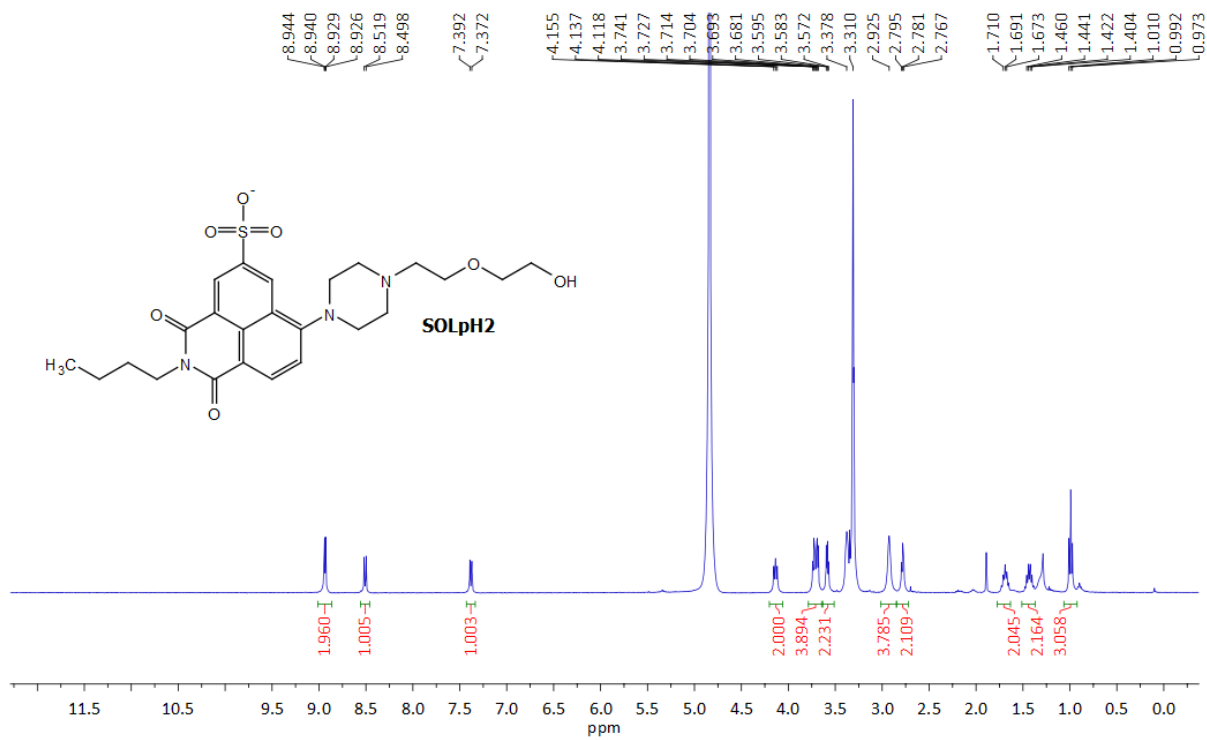
**Compound 10:  $^1\text{H}$  NMR (400 MHz) &  $^{13}\text{C}$  NMR (101 MHz)  $\text{CDCl}_3$**

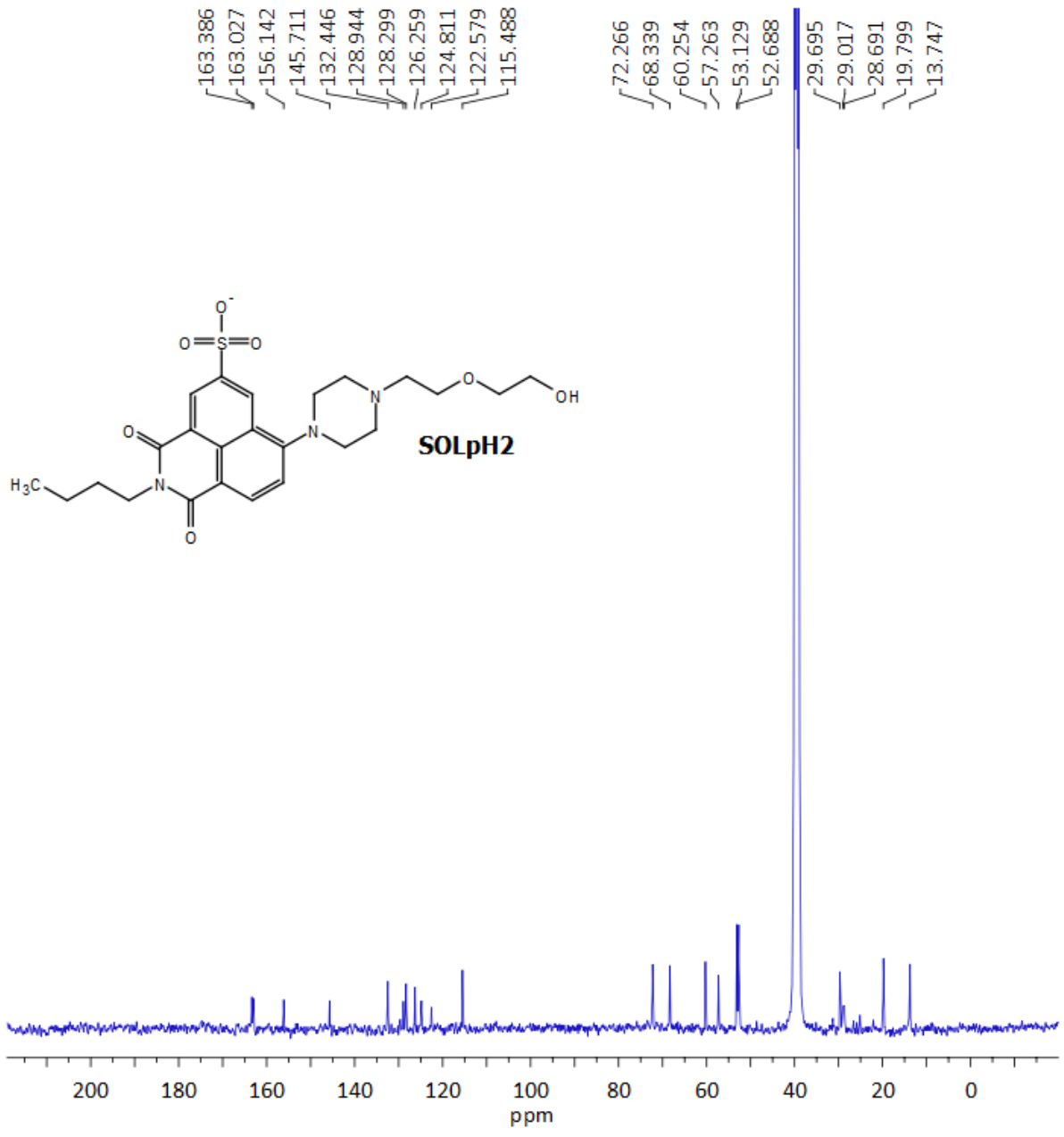


Compound 11:  $^1\text{H}$  NMR (400 MHz)  $\text{CD}_3\text{OD}$



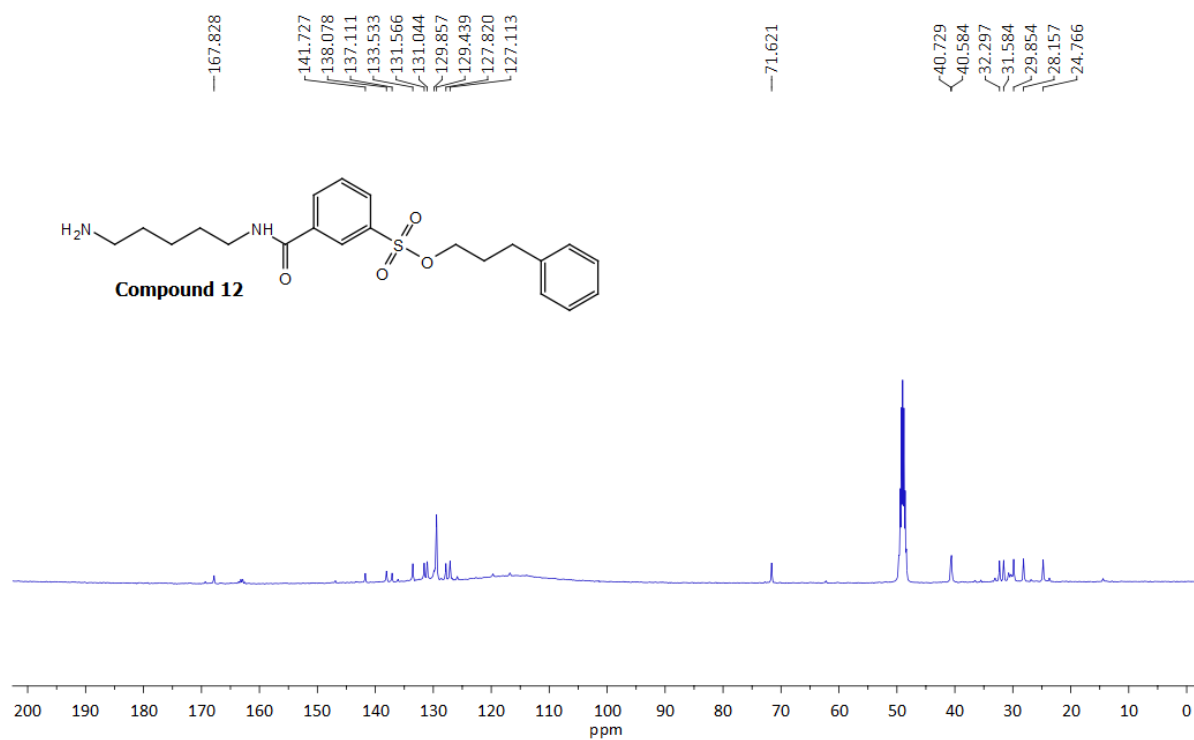
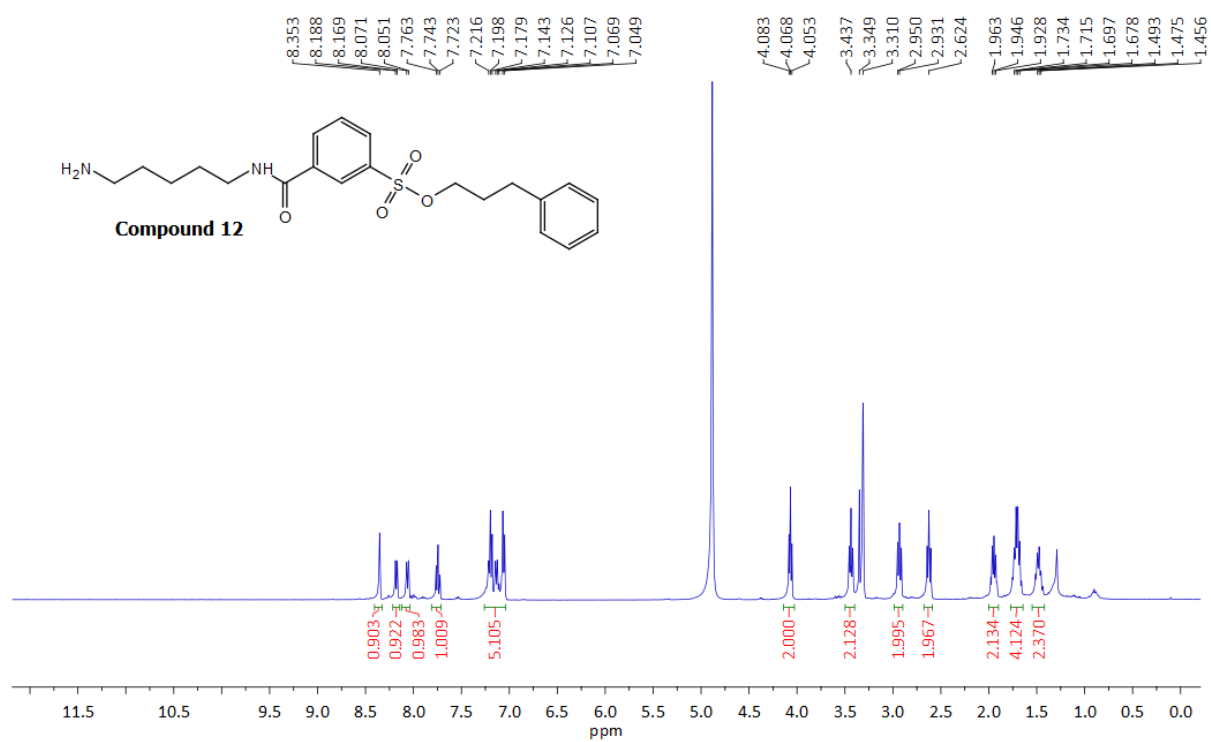
SOLpH2:  $^1\text{H}$  NMR (400 MHz)  $\text{CD}_3\text{OD}$  &  $^{13}\text{C}$  NMR (101 MHz)  $\text{DMSO-d}_6$



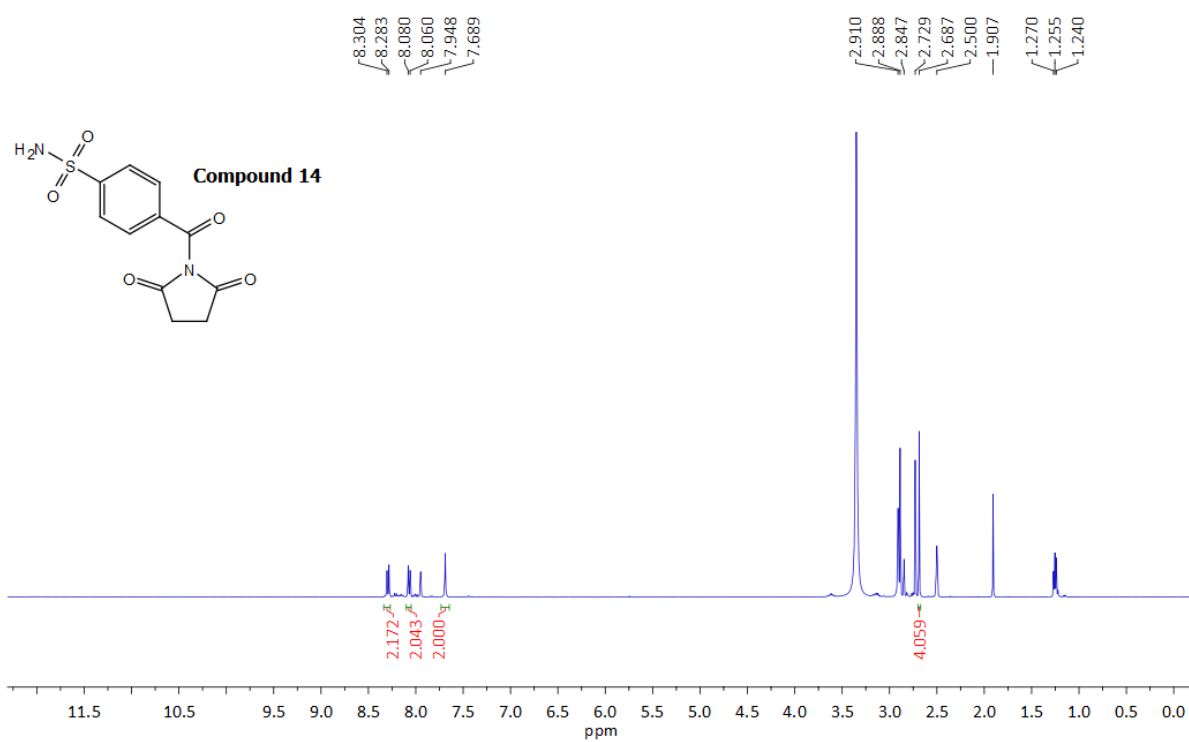




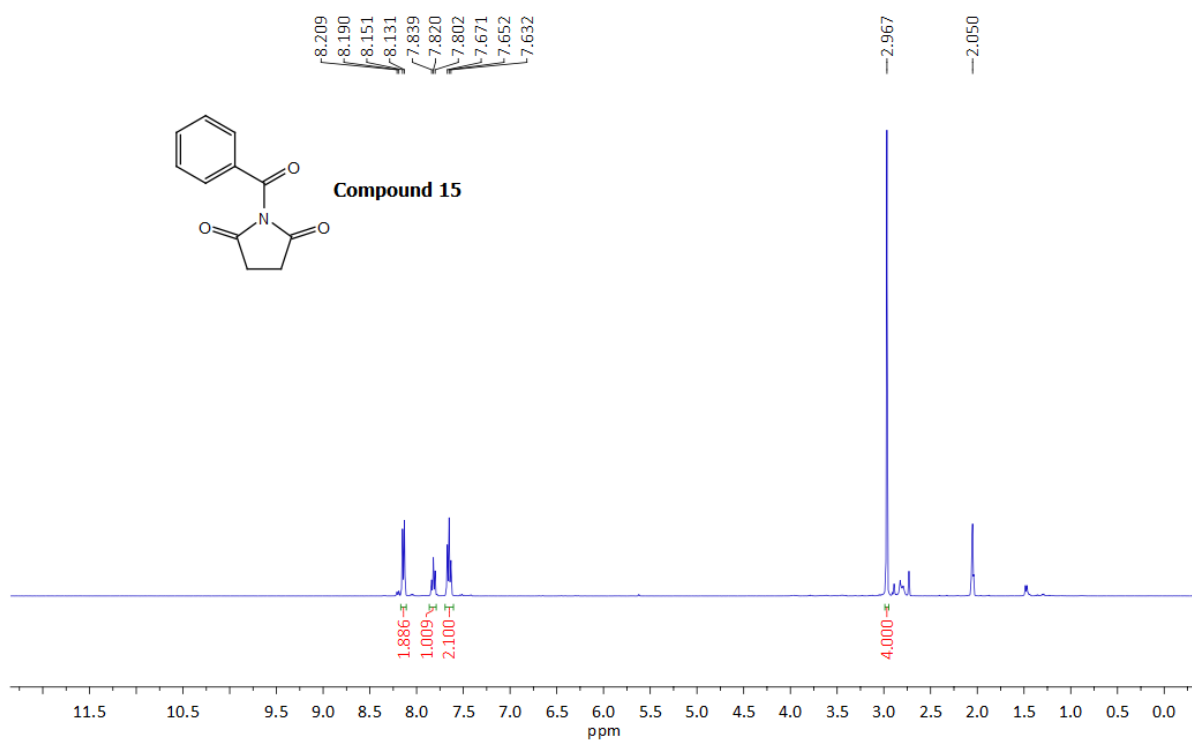
**Compound 12:  $^1\text{H}$  NMR (400 MHz) &  $^{13}\text{C}$  NMR (101 MHz)  $\text{CD}_3\text{OD}$**



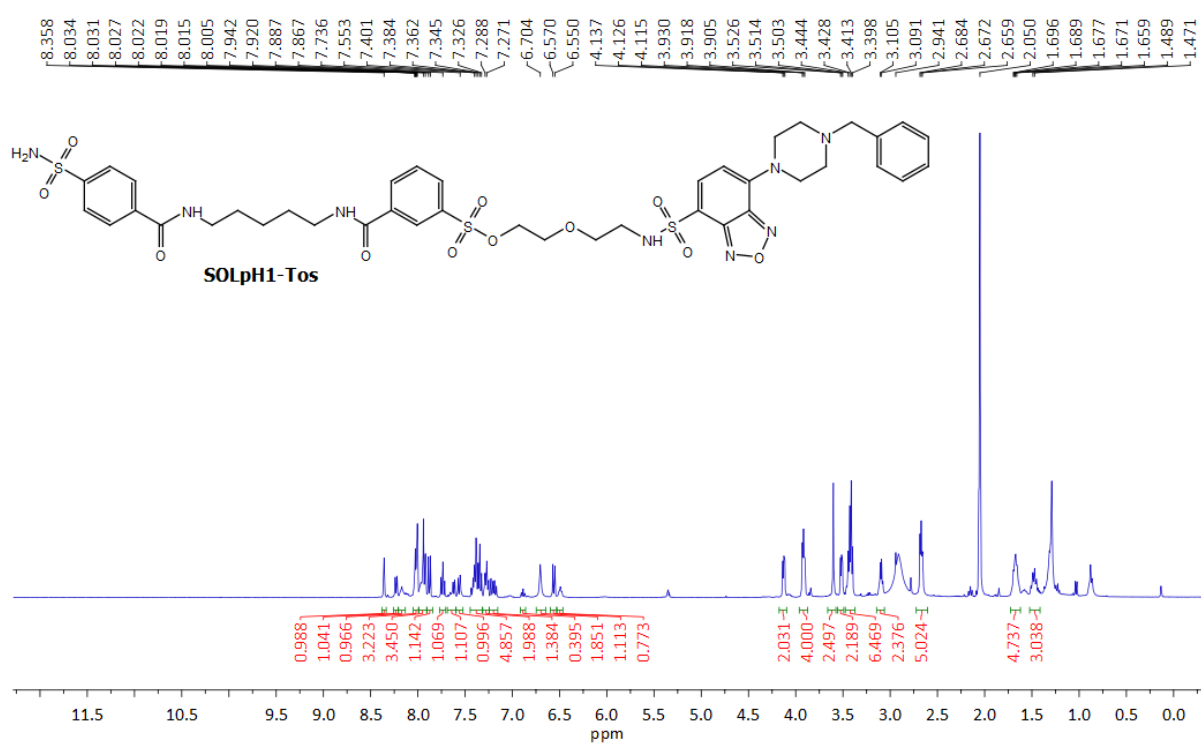
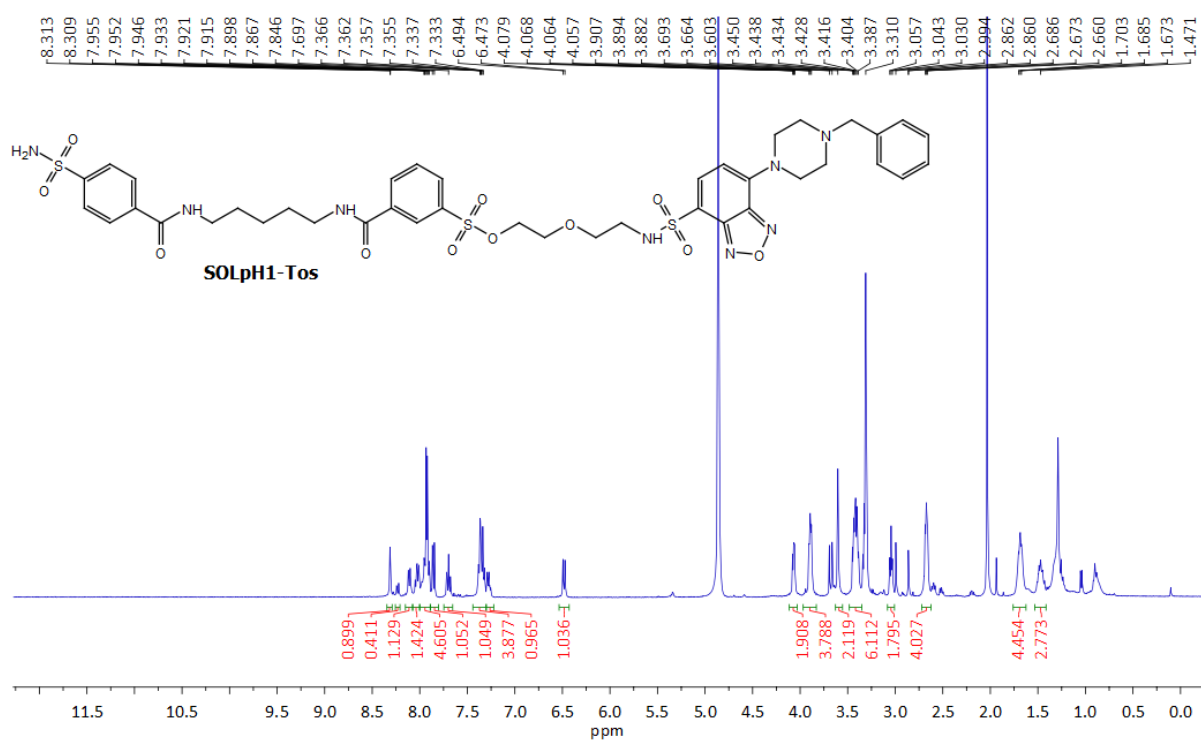
**Compound 14:  $^1\text{H}$  NMR (400 MHz)  $\text{DMSO-d}_6$**



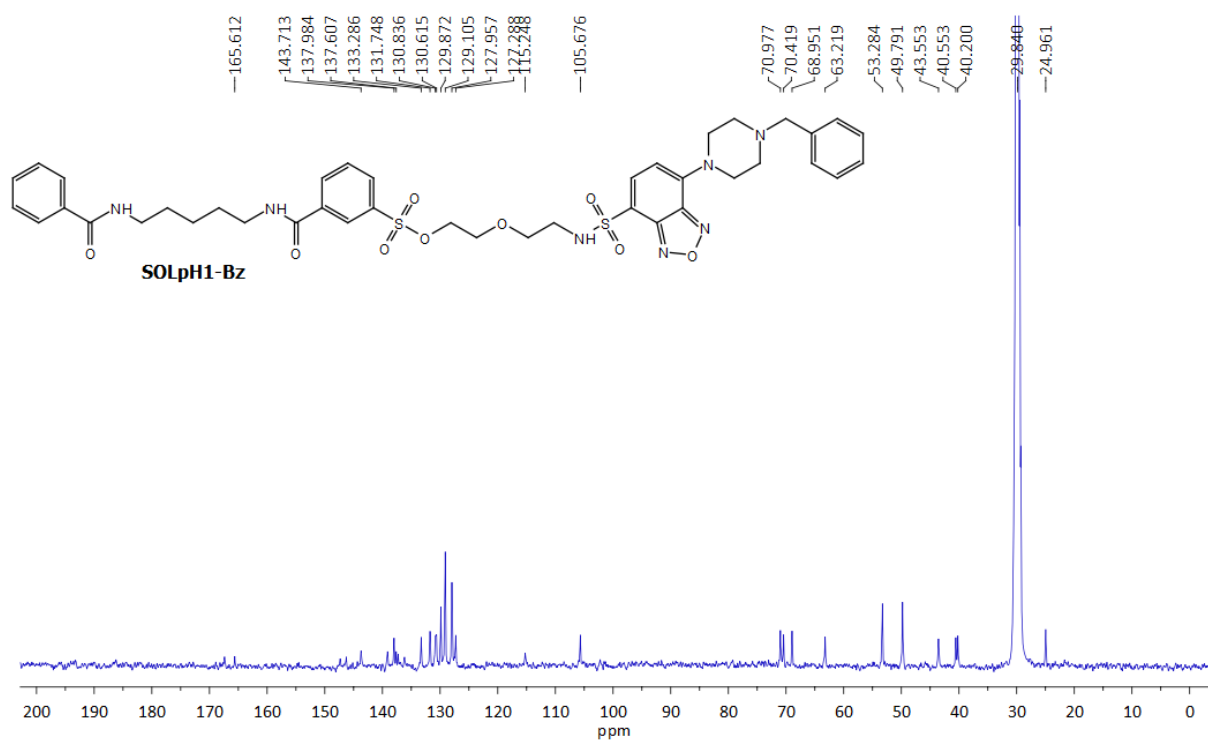
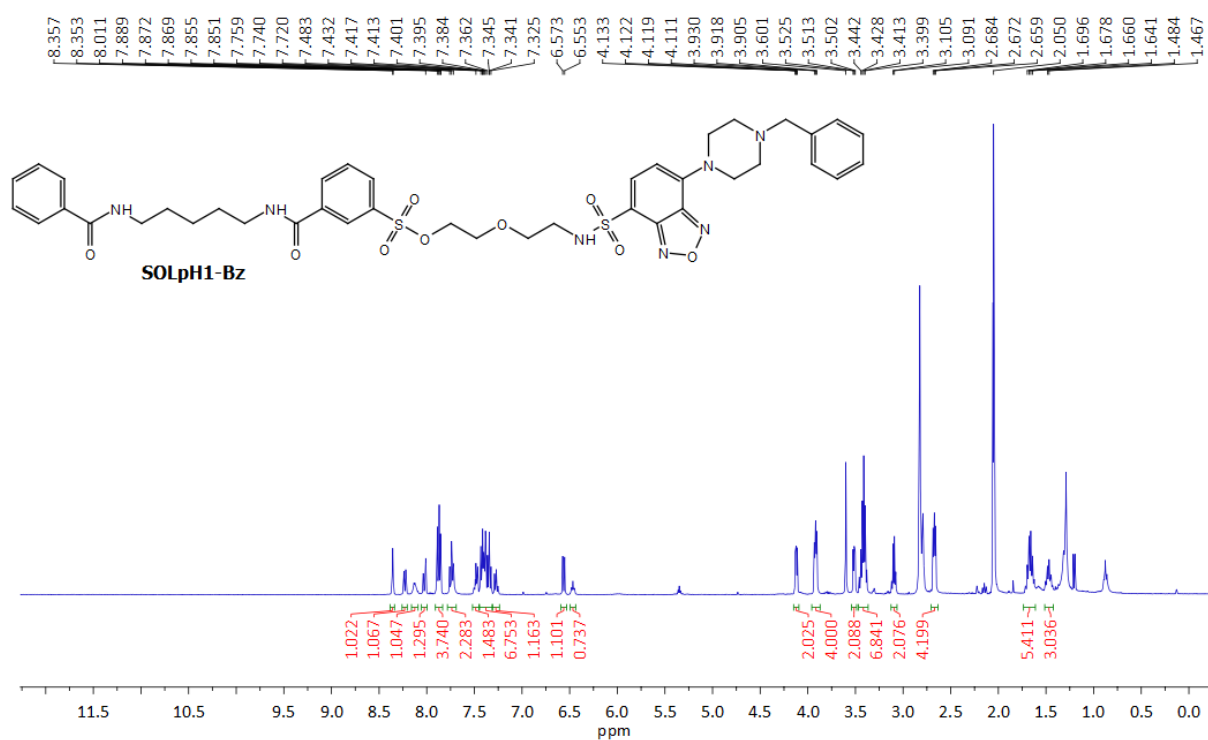
**Compound 15:  $^1\text{H}$  NMR (400 MHz)  $\text{Acetone-d}_6$**



**SOLpH1-Tos:  $^1\text{H}$  NMR (400 MHz)  $\text{CD}_3\text{OD}/\text{Acetone-}d_6$**



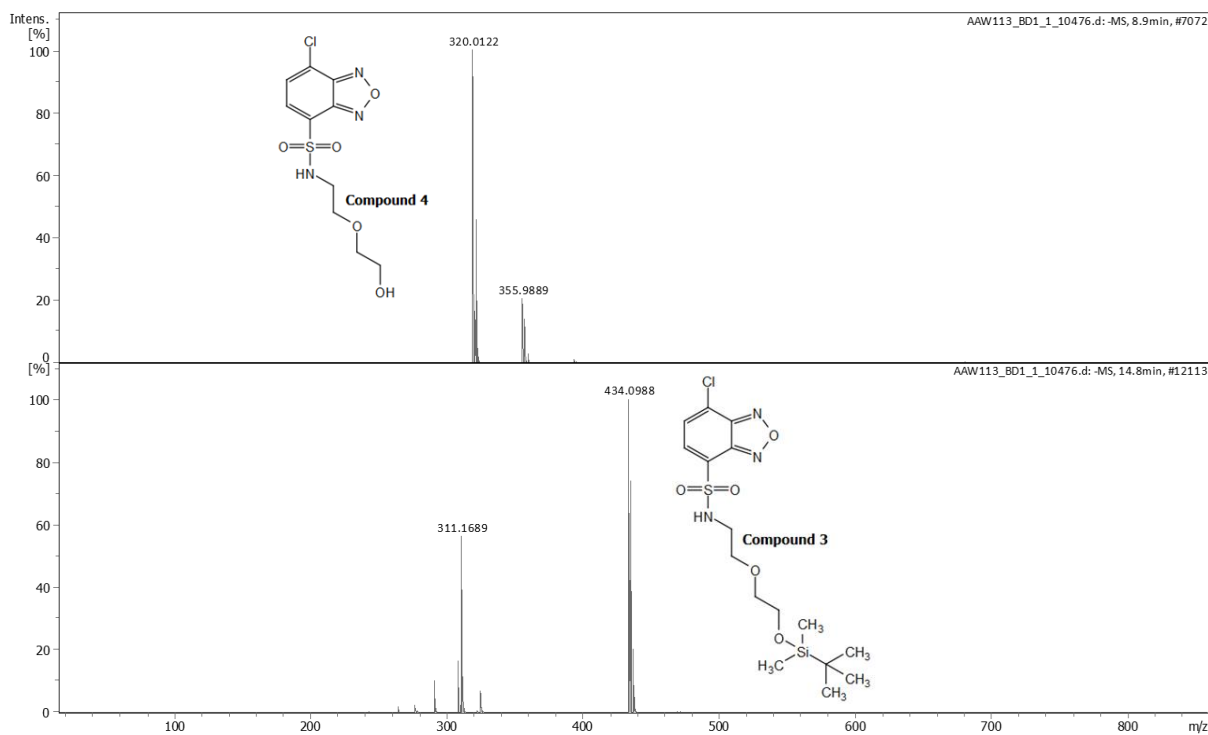
**SOLpH1-Bz:  $^1\text{H}$  NMR (400 MHz) &  $^{13}\text{C}$  NMR (101 MHz) Acetone- $d_6$**



## 7.2. HRMS-ESI spectra

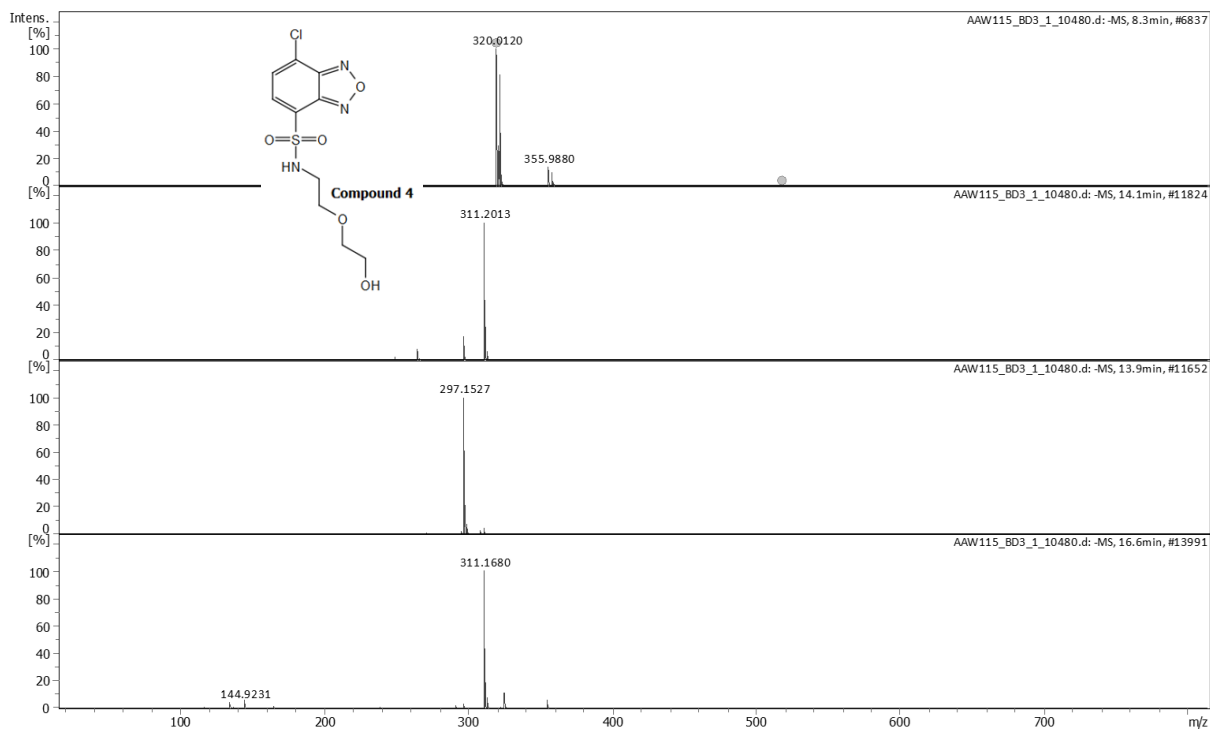
### Compound 3:

HRMS-ESI (m/z) Calcd for (C<sub>16</sub>H<sub>25</sub>ClN<sub>3</sub>O<sub>5</sub>SSi<sup>-</sup>) ([M-H]<sup>-</sup>): 434.0973, found: 434.0988



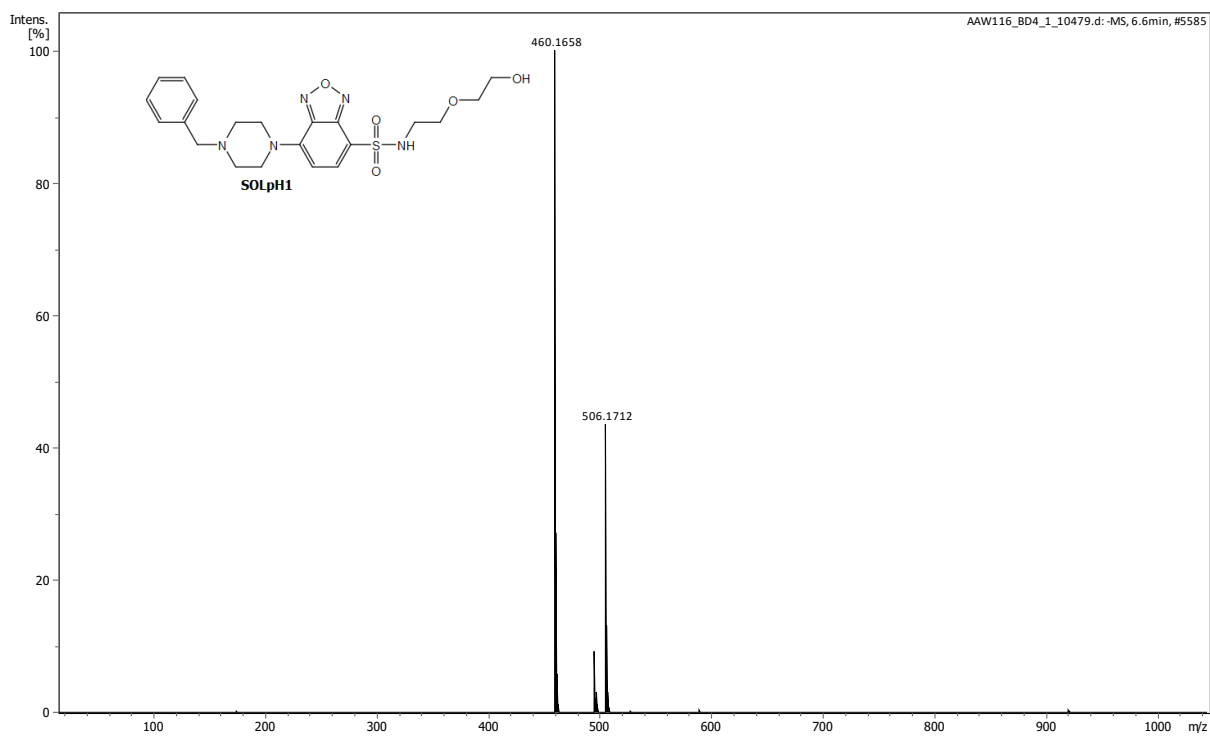
### Compound 4:

HRMS-ESI (m/z) Calcd for (C<sub>10</sub>H<sub>12</sub>ClN<sub>3</sub>O<sub>5</sub>S<sup>-</sup>) ([M-H]<sup>-</sup>): 320.0108, found: 320.0120



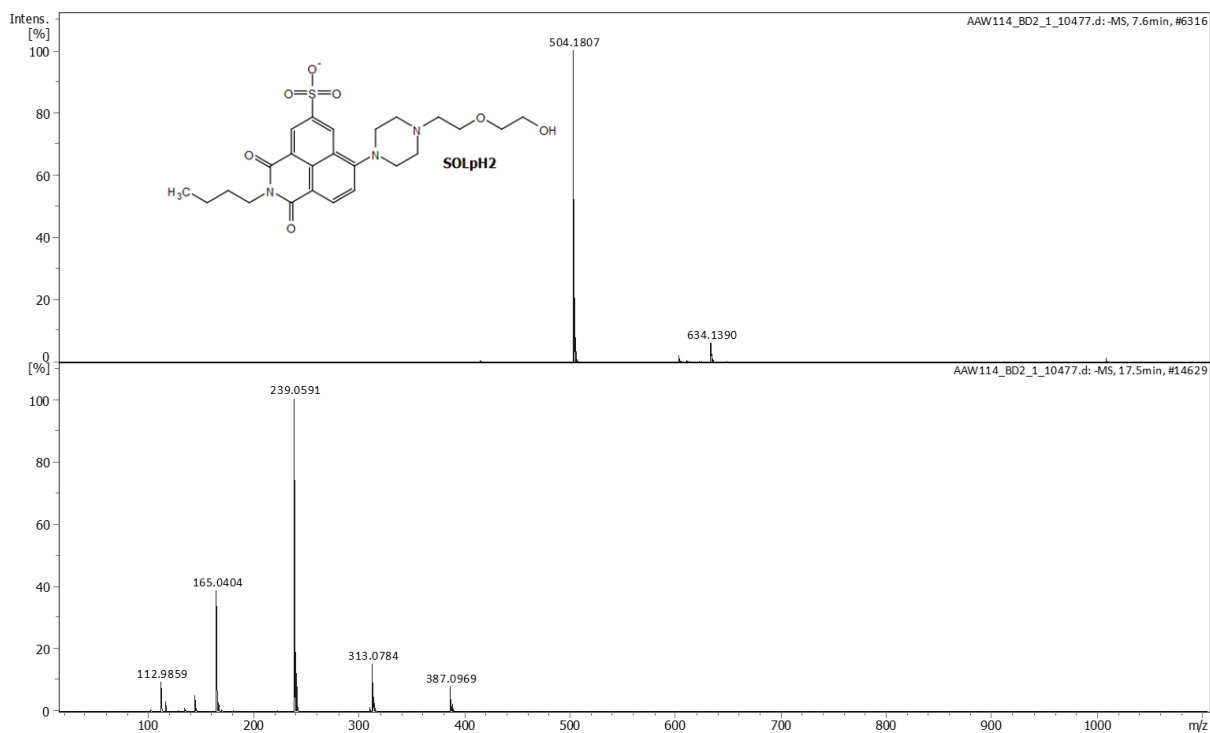
### SOLpH1:

HRMS-ESI (m/z) Calcd for (C<sub>21</sub>H<sub>26</sub>N<sub>5</sub>O<sub>5</sub>S<sup>-</sup>) ([M-H]<sup>-</sup>): 460.1655, found: 460.1658



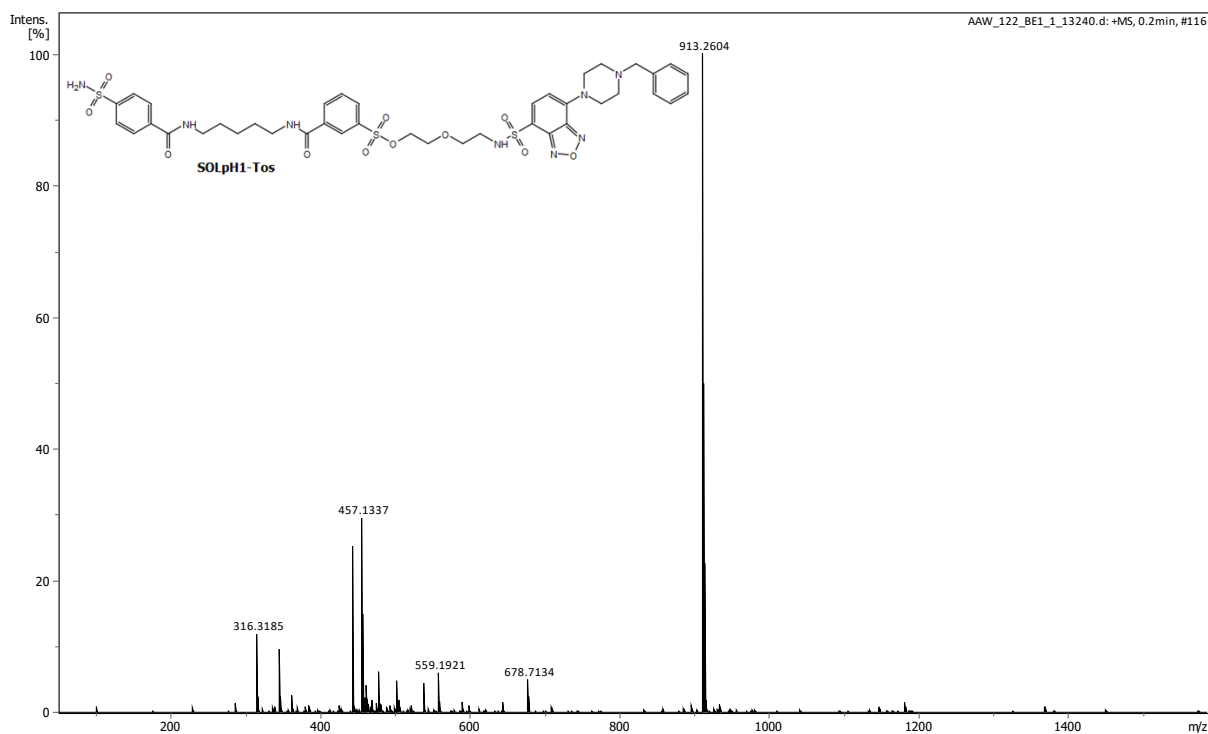
### SOLpH2:

HRMS-ESI (m/z) Calcd for (C<sub>24</sub>H<sub>30</sub>N<sub>3</sub>O<sub>7</sub>S<sup>-</sup>) ([M]<sup>-</sup>): 504.1810, found: 504.1807



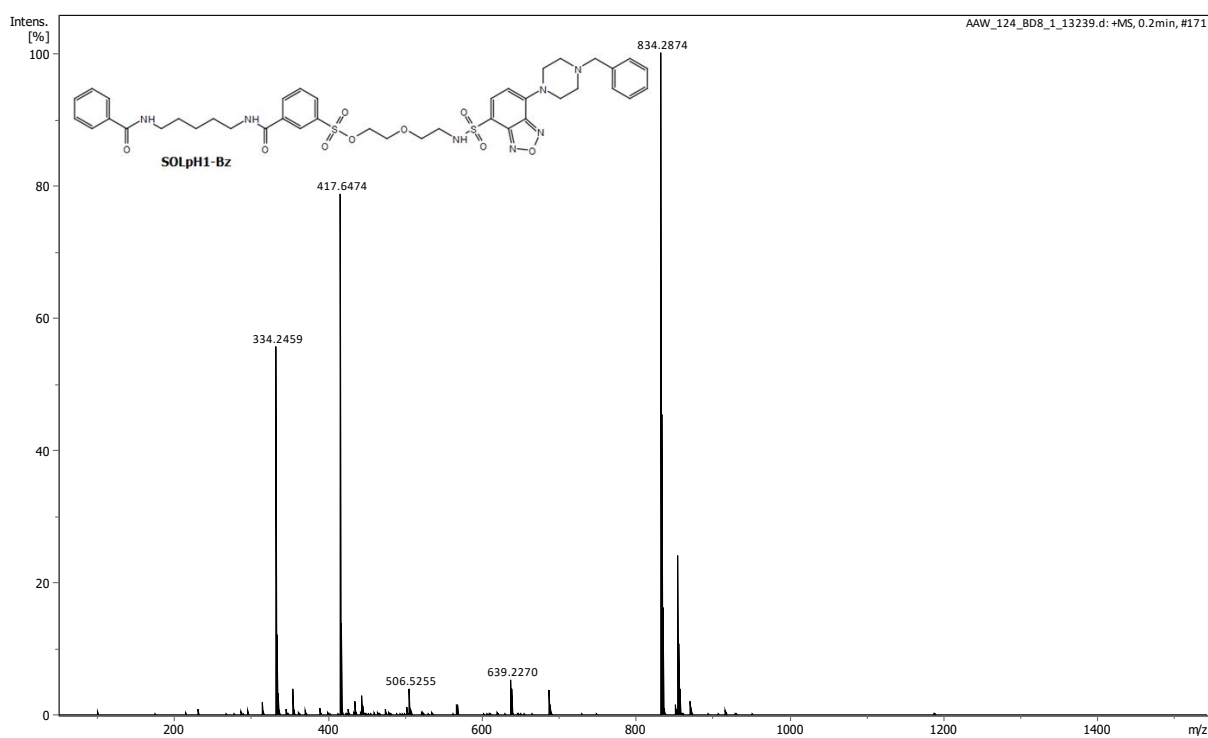
### SOLpH1-Tos:

HRMS-ESI (m/z) Calcd for (C<sub>40</sub>H<sub>49</sub>N<sub>8</sub>O<sub>11</sub>S<sub>3</sub><sup>+</sup>) ([M+H]<sup>+</sup>): 913.2682, found: 913.2604



### SOLpH1-Bz:

HRMS-ESI (m/z) Calcd for (C<sub>40</sub>H<sub>48</sub>N<sub>7</sub>O<sub>9</sub>S<sub>2</sub><sup>+</sup>) ([M+H]<sup>+</sup>): 834.2955, found: 834.2874



### 7.3. Spectroscopic studies

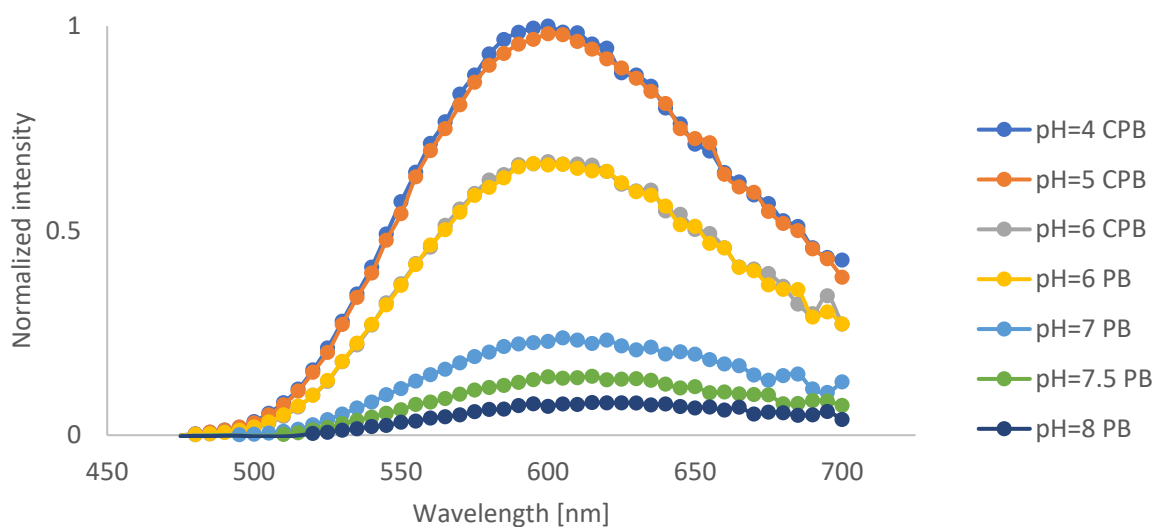


**Figure 105.** Fluorescence spectra of **SOLpH1** (20  $\mu\text{M}$ ) at changing pH 4.0-8.0,  $\lambda_{\text{exc}}=435$  nm. CPB – citrate phosphate buffer; PB – phosphate buffer. The values were normalized to the highest emission intensity. Experimental data points, averaged over 3 repeats ( $n = 3$ ) were connected with a line, which is there as a guideline for eyes to obtain a visual effect of the continuous line.

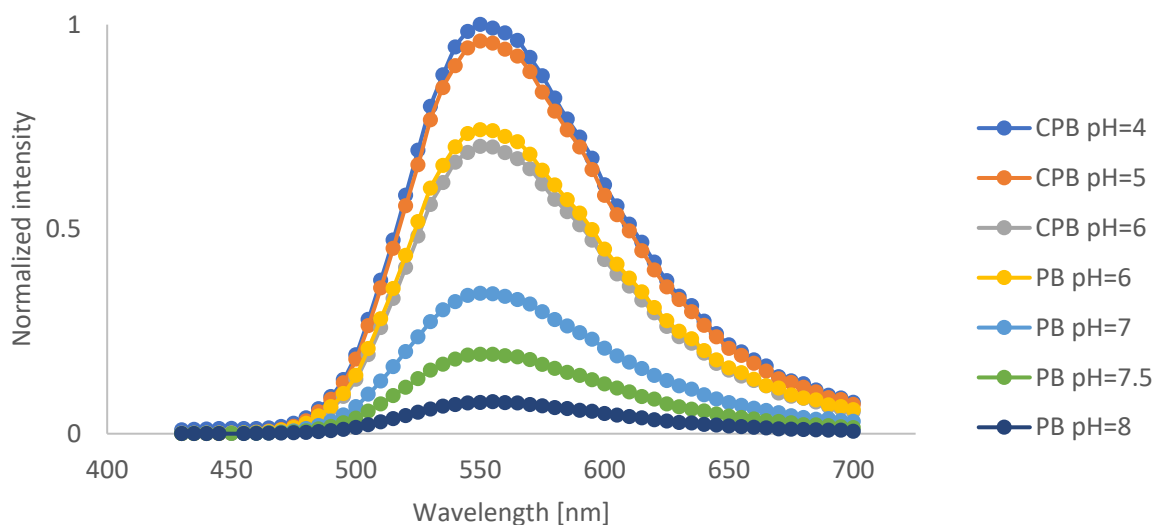


**Figure 106.** Fluorescence spectra of **SOLpH2** (15  $\mu\text{M}$ ) at changing pH 4.0-8.0,  $\lambda_{\text{exc}}=390$  nm. CPB – citrate phosphate buffer; PB – phosphate buffer. The values were normalized to the highest emission intensity. Experimental data points, averaged over 3 repeats ( $n = 3$ ) were connected with a line, which is there as a guideline for eyes to obtain a visual effect of the continuous line.



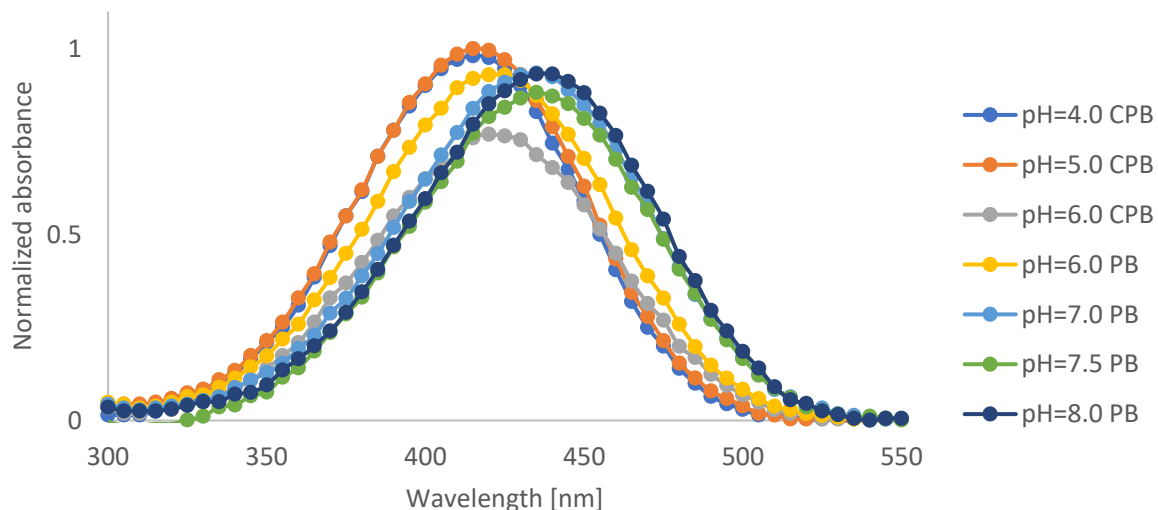


**Figure 107.** Absorbance spectra of **SOLpH1** (50  $\mu\text{M}$ ) at changing pH 4.0-8.0,  $\lambda_{\text{abs}}=300-700$  nm. CPB – citrate phosphate buffer; PB – phosphate buffer. The values were normalized to the highest absorption value. Experimental data points, averaged over 2 repeats ( $n = 2$ ) were connected with a line, which is there as a guideline for eyes to obtain a visual effect of the continuous line.

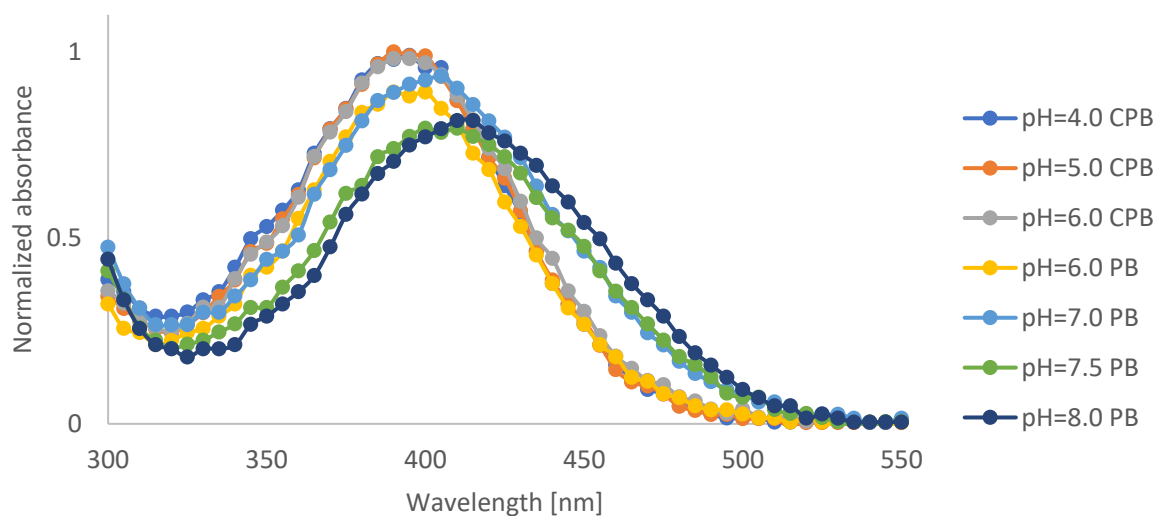


**Figure 108.** Absorbance spectra of **SOLpH2** (15  $\mu\text{M}$ ) at changing pH 4.0-8.0,  $\lambda_{\text{abs}}=300-700$  nm. CPB – citrate phosphate buffer; PB – phosphate buffer. The values were normalized to the highest absorption value. Experimental data points, averaged over 2 repeats ( $n = 2$ ) were connected with a line, which is there as a guideline for eyes to obtain a visual effect of the continuous line.

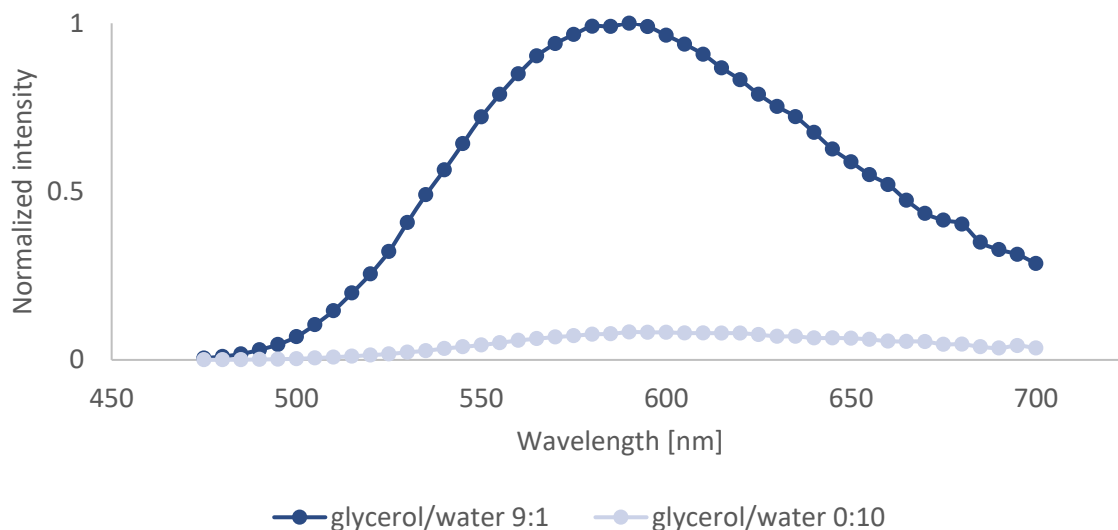


**Figure 109.** Fluorescence spectra of **SOLpH1** (20  $\mu\text{M}$ ) in glycerol:water mixtures with changing ratio (top) and direct comparison between the two most extreme conditions (bottom),  $\lambda_{\text{exc}}=435$  nm. g – glycerol; w – water. The values were normalized to the highest emission intensity. Experimental data points, averaged over 2 repeats ( $n = 2$ ) were connected with a line, which is there as a guideline for eyes to obtain a visual effect of the continuous line.

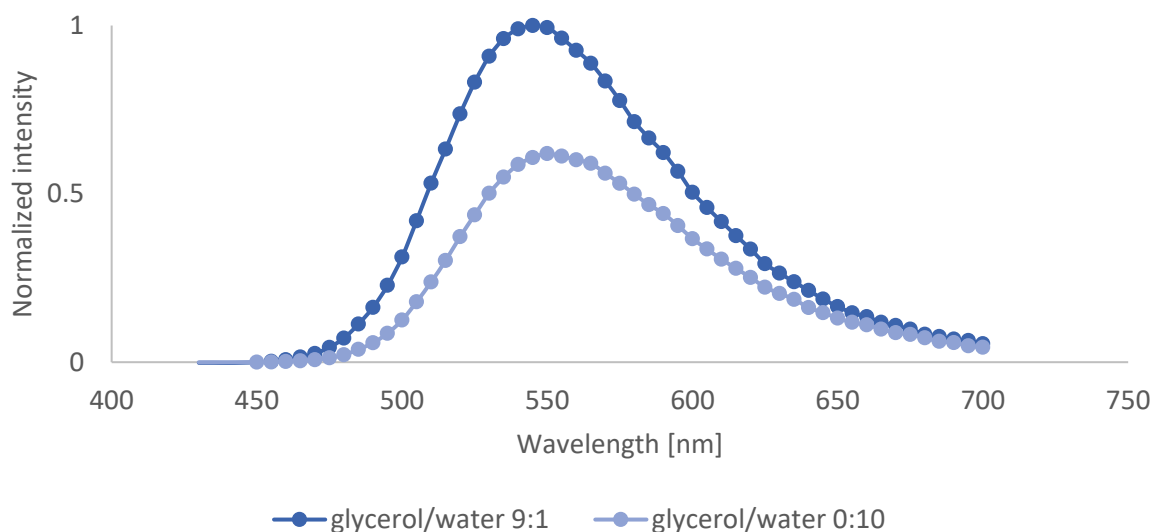


**Figure 110.** Fluorescence spectra of **SOLpH2** (15  $\mu\text{M}$ ) in glycerol:water mixtures with changing ratio (top) and direct comparison between the two most extreme conditions (bottom),  $\lambda_{\text{exc}}=390$  nm. g – glycerol; w – water. The values were normalized to the highest emission intensity. Experimental data points, averaged over 2 repeats ( $n = 2$ ) were connected with a line, which is there as a guideline for eyes to obtain a visual effect of the continuous line.

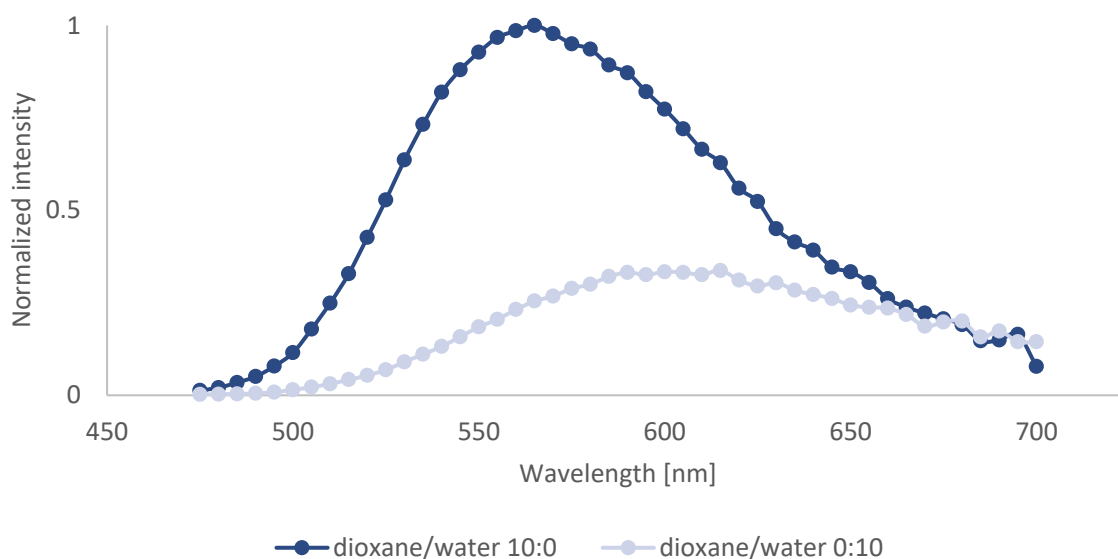


**Figure 111.** Fluorescence spectra of **SOLpH1** (20  $\mu\text{M}$ ) in dioxane:water mixtures with changing ratio (top) and direct comparison between the two most extreme conditions (bottom),  $\lambda_{\text{exc}}=435$  nm. d – dioxane; w – water. The values were normalized to the highest emission intensity. Experimental data points, averaged over 2 repeats ( $n = 2$ ) were connected with a line, which is there as a guideline for eyes to obtain a visual effect of the continuous line.

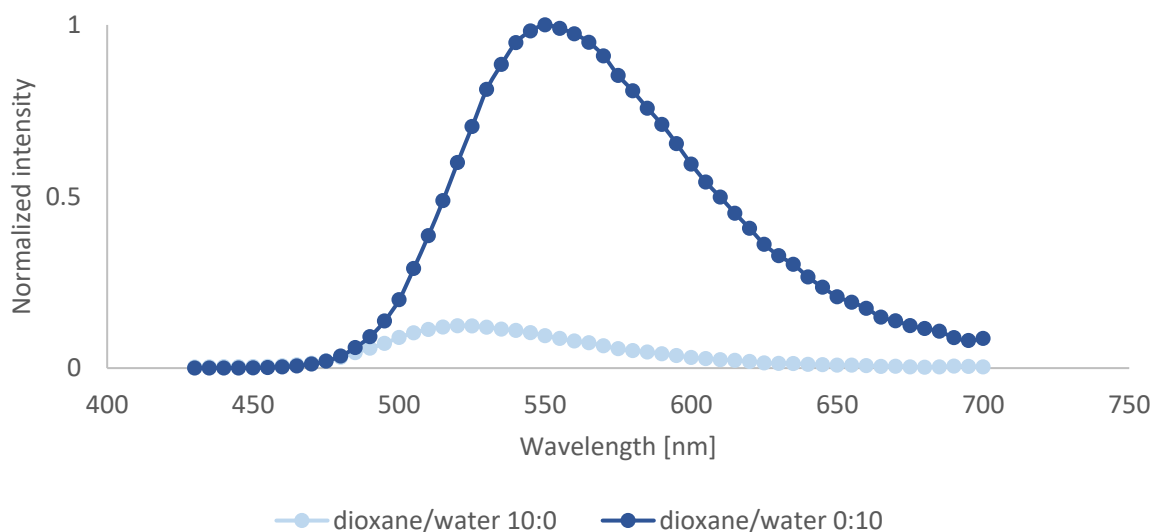


**Figure 112.** Fluorescence spectra of **SOLpH2** (15  $\mu\text{M}$ ) in dioxane:water mixtures with changing ratio (top) and direct comparison between the two most extreme conditions (bottom),  $\lambda_{\text{exc}}=390$  nm. d – dioxane; w – water. The values were normalized to the highest emission intensity. Experimental data points, averaged over 2 repeats ( $n = 2$ ) were connected with a line, which is there as a guideline for eyes to obtain a visual effect of the continuous line.

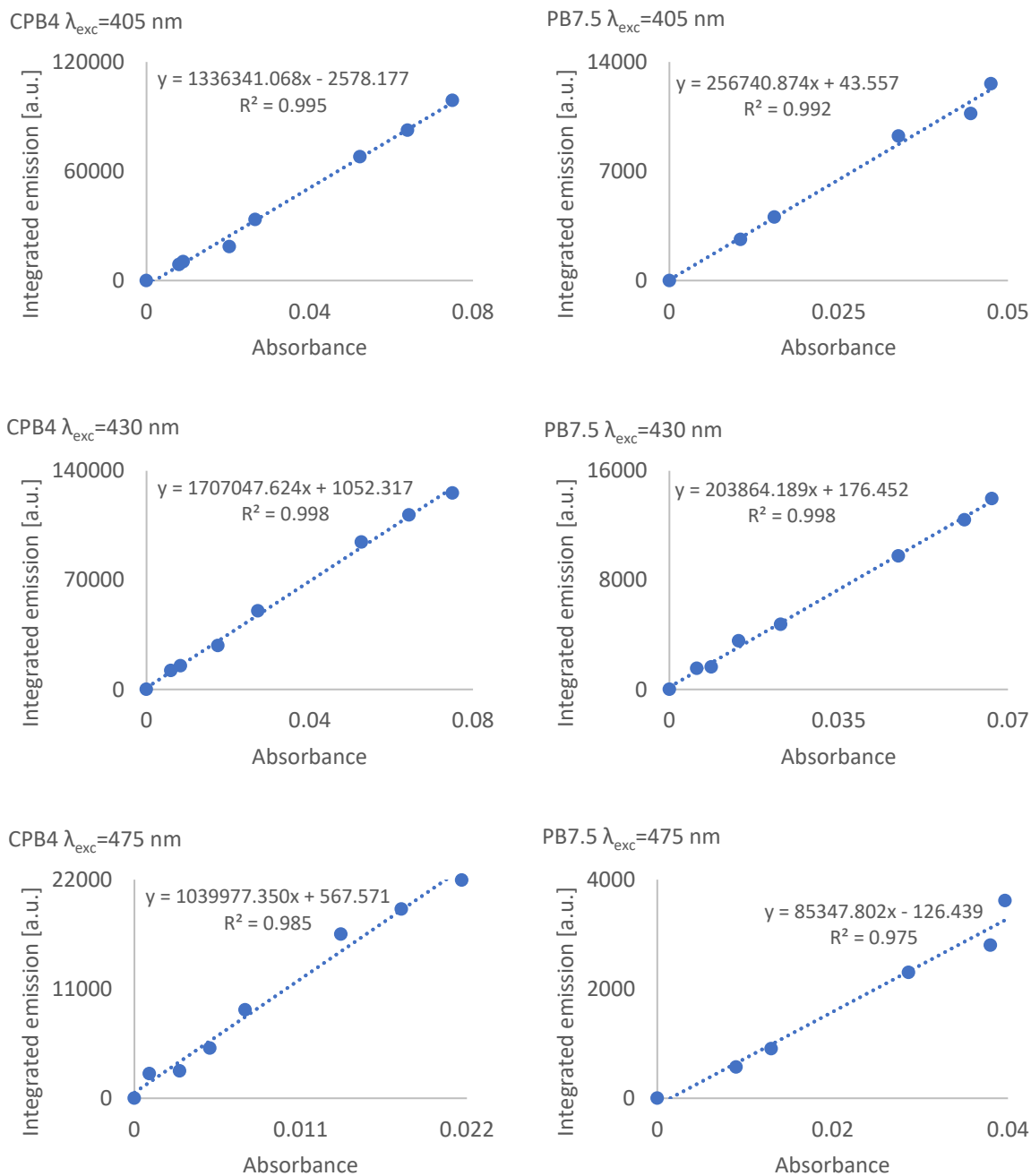


**Figure 113.** Linear plots for the **SOLpH1** (2-30  $\mu\text{M}$ ) for quantum yield calculation. The gradient for each sample is proportional to that sample's fluorescence quantum yield. CPB4 – citrate phosphate buffer pH=4; PB7.5 – phosphate buffer pH=7.5. Experimental data points were averaged over 3 repeats ( $n = 3$ ).

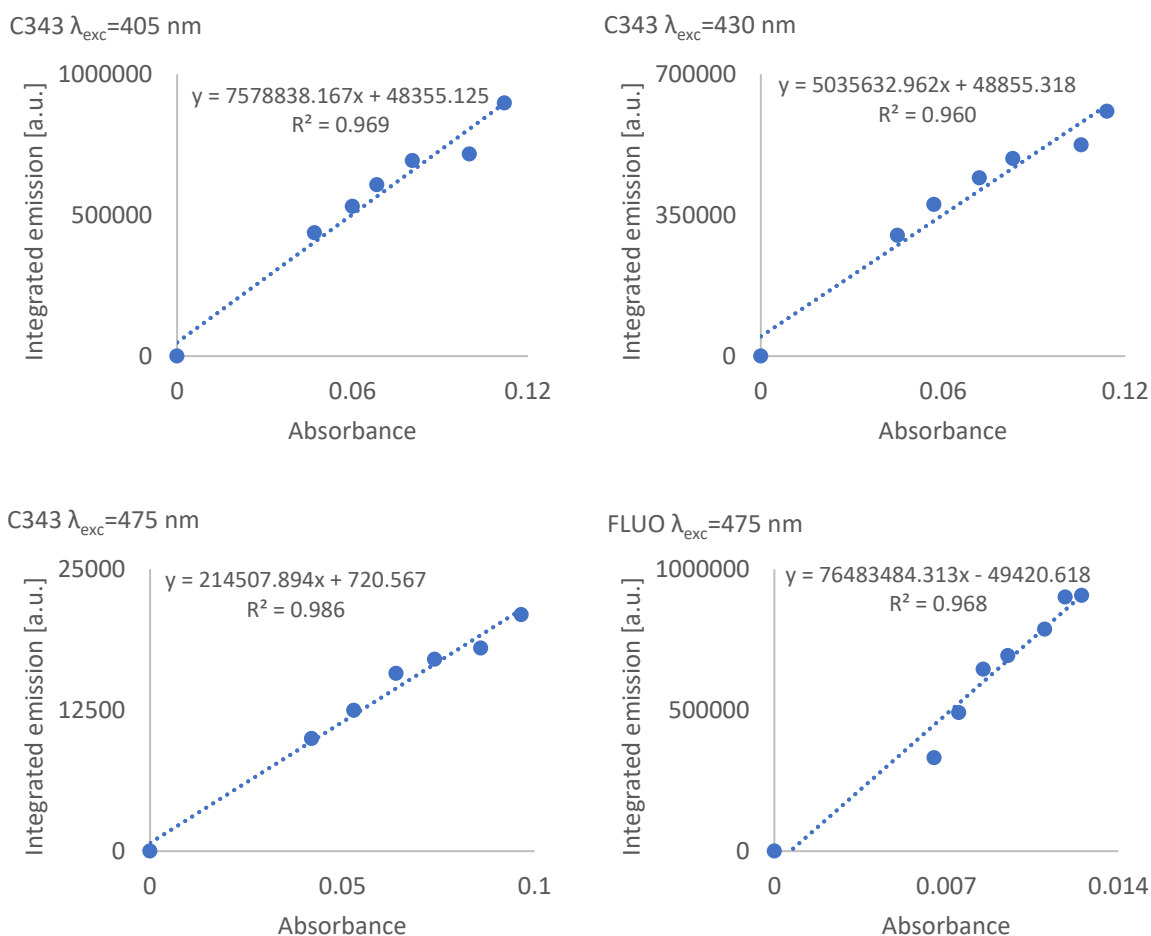


**Figure 114.** Linear plots for standards: coumarin 343 (C343; 1-2  $\mu$ M) and fluorescein (FLUO; 0.5-1.5  $\mu$ M) for quantum yield calculation. The gradient for each sample is proportional to that sample's fluorescence quantum yield. Coumarin 343 properties were measured in EtOH and fluorescein ones in 0.1M NaOH. Experimental data points were averaged over 3 repeats ( $n = 3$ ).

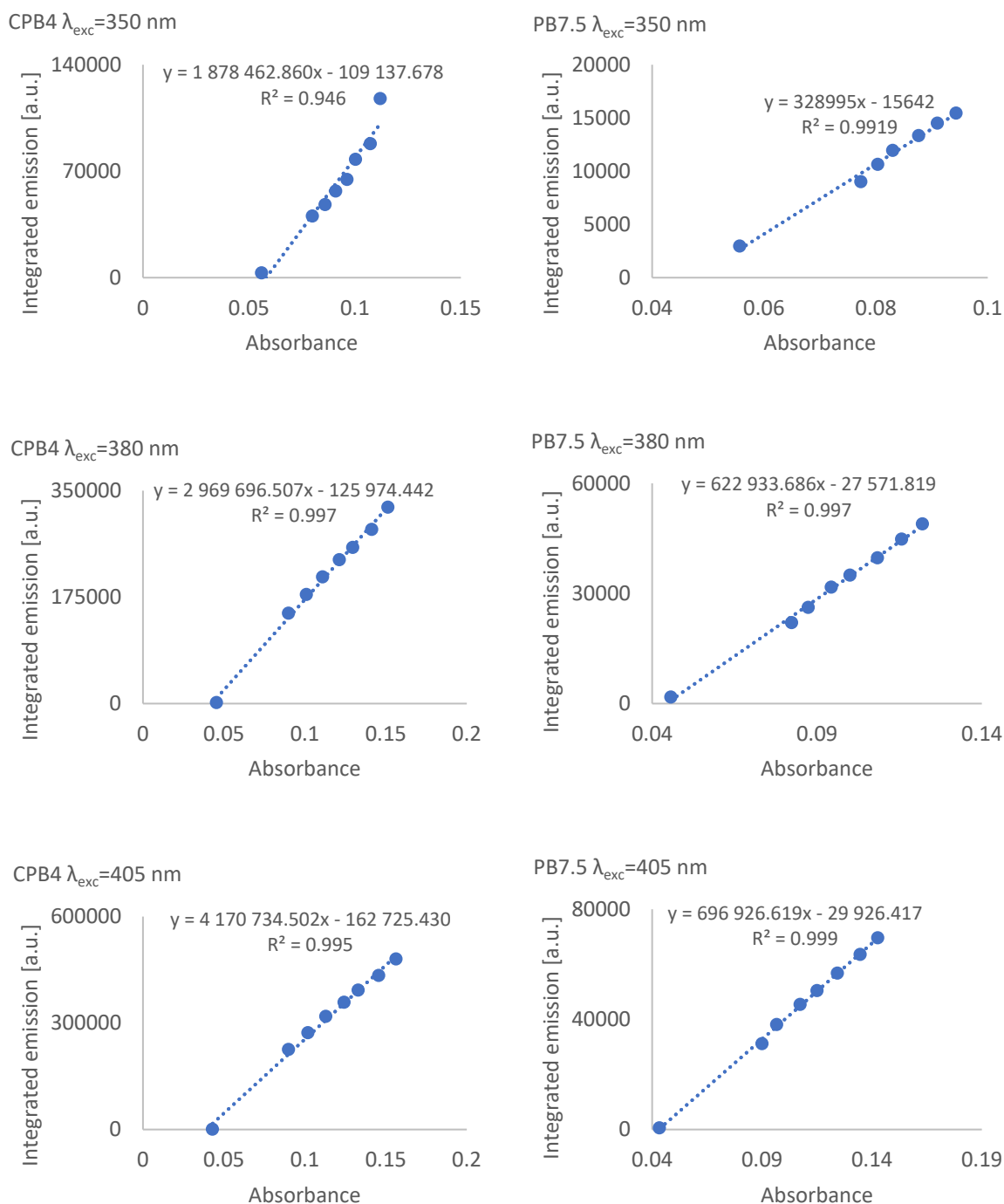


**Figure 115.** Linear plots for the **SOLpH2** (20-50  $\mu$ M) for quantum yield calculation. The gradient for each sample is proportional to that sample's fluorescence quantum yield. CPB4 – citrate phosphate buffer pH=4; PB7.5 – phosphate buffer pH=7.5. Experimental data points were averaged over 3 repeats ( $n = 3$ ). The intercept is not at 0,0 as the values of absorbance were not corrected by background absorbance values.

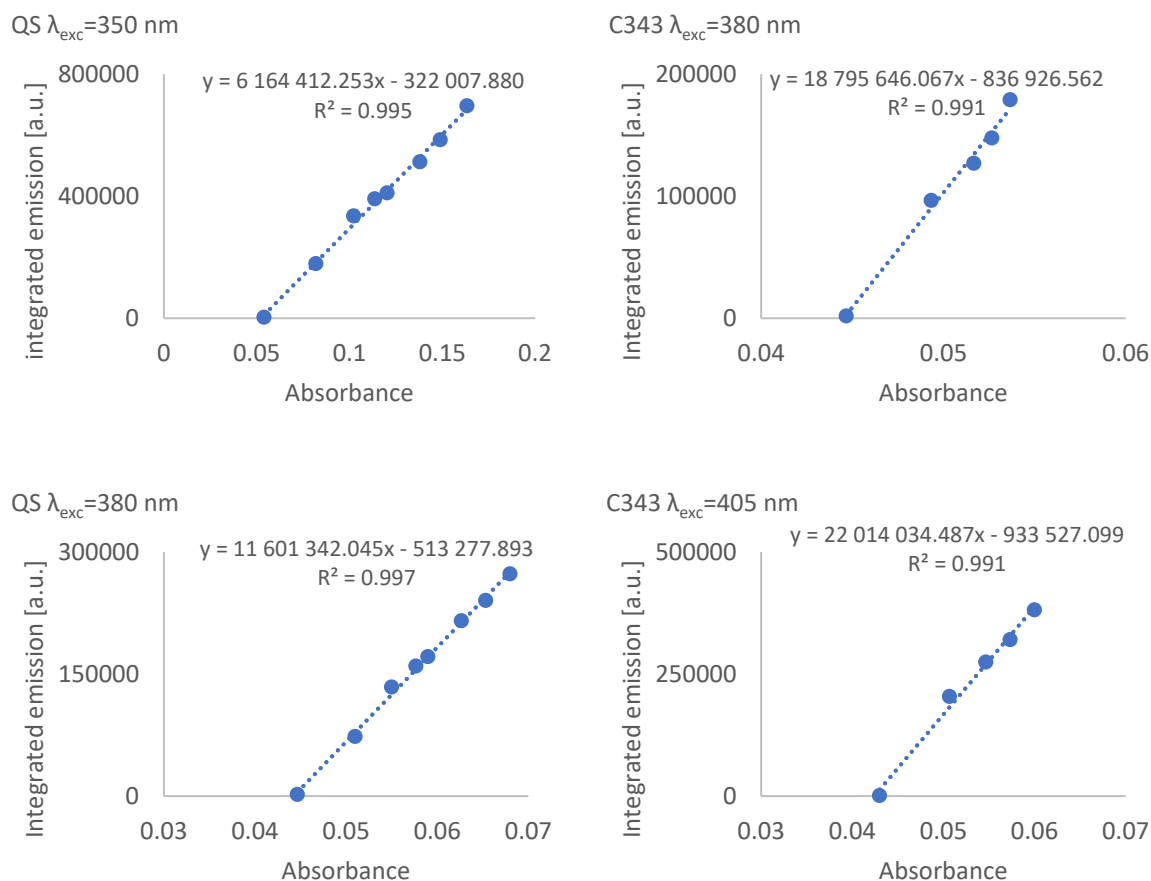


**Figure 116.** Linear plots for standards: coumarin 343 (C343; 2-3  $\mu$ M) and quinine sulphate (QS; 20-45  $\mu$ M) for quantum yield calculation. The gradient for each sample is proportional to that sample's fluorescence quantum yield. Coumarin 343 properties were measured in EtOH and quinine sulphate ones in 0.05M  $H_2SO_4$ . Experimental data points were averaged over 3 repeats ( $n = 3$ ). The intercept is not at 0,0 as the values of absorbance were not corrected by background absorbance values.

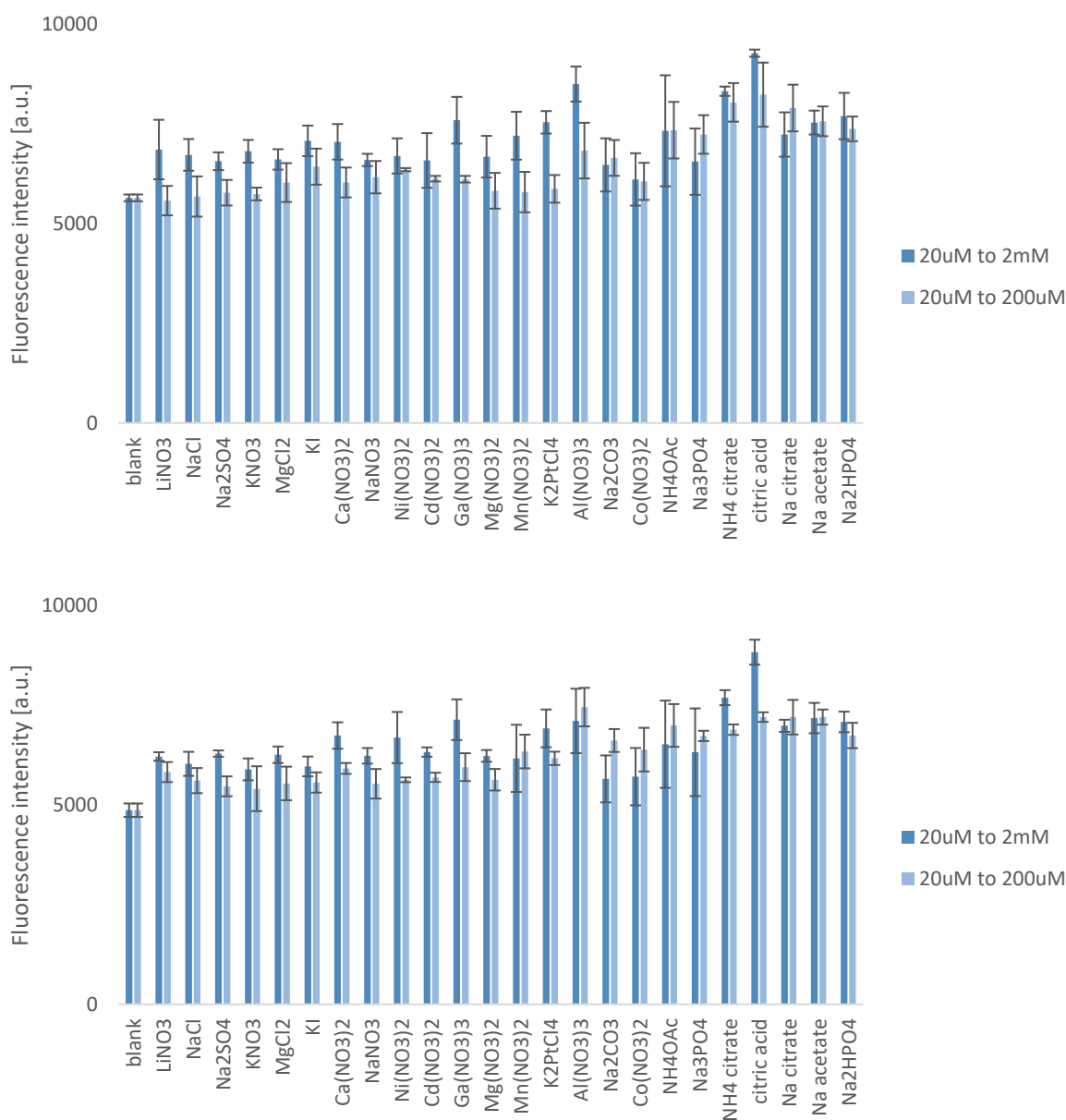


**Figure 117.** Interference tests of fluorescence intensity signal of the **SOLpH1** (20  $\mu$ M) at 605 nm with presence of different salts (ratio 1:100 and 1:10) at 0 min (top) and 60 min (bottom) in 100mM HEPES pH=7.5.  $\lambda_{exc}$ =430 nm,  $\lambda_{em}$ =605 nm. Experimental data points, averaged over 3 repeats ( $n = 3$ ) were connected with a line, which is there as a guideline for eyes to obtain a visual effect of the continuous line.



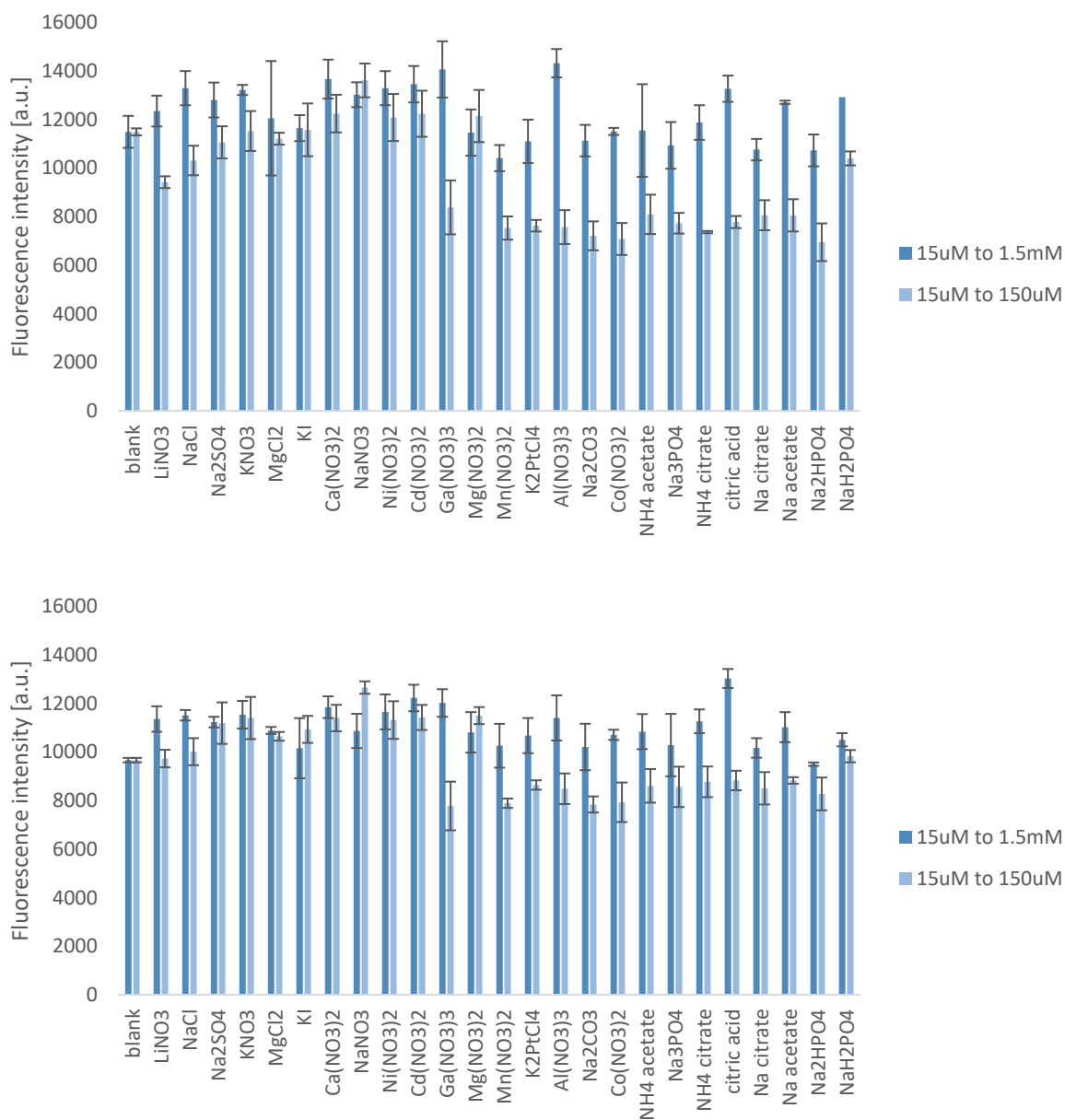


**Figure 118.** Interference tests of fluorescence intensity signal of the **SOLpH2** (15 μM) with presence of different salts (ratio 1:100 and 1:10) at 0 min (top) and 60 min (bottom) in 100mM HEPES pH=7.5.  $\lambda_{exc}=405$  nm,  $\lambda_{em}=550$  nm. Experimental data points, averaged over 3 repeats (n = 3) were connected with a line, which is there as a guideline for eyes to obtain a visual effect of the continuous line.

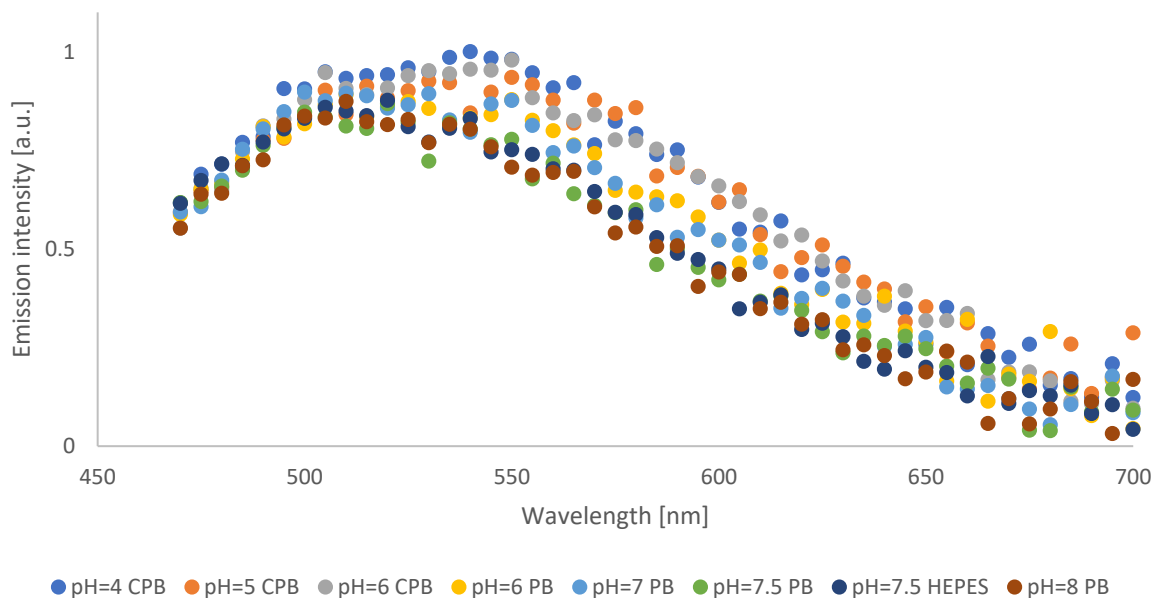


**Figure 119.** The emission spectra of **SOLpH1**-labeled human carbonic anhydrase II at 0 min. The values were normalized to the highest value of emission in CPB pH=4.0. The emission was measured at 5 nm steps. The final concentration of DMSO was kept at 0.5%. Experimental data points, averaged over 3 repeats ( $n = 3$ ) were connected with a line, which is there as a guideline for eyes to obtain a visual effect of the continuous line. The spectra were normalized to the highest value (pH=4.0 CPB).  $\lambda_{exc}=430$  nm,  $\lambda_{em}=470-700$  nm.

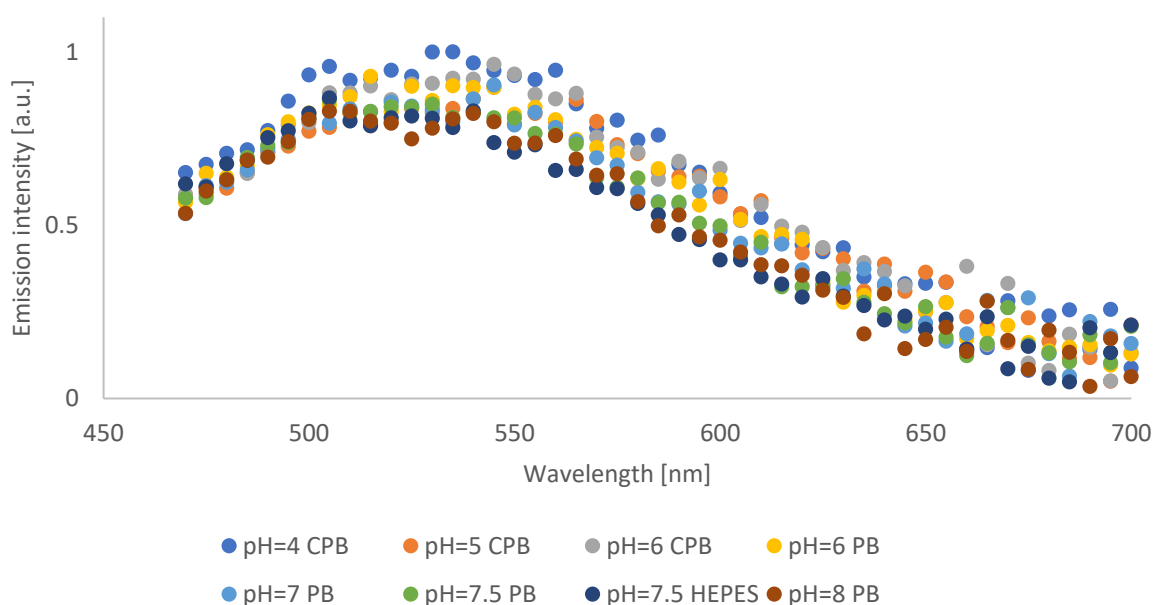


**Figure 120.** The emission spectra of **SOLpH1**-labeled human carbonic anhydrase II at 30 min. The values were normalized to the highest value of emission in CPB pH=4.0. The emission was measured at 5 nm steps. The final concentration of DMSO was kept at 0.5%. Experimental data points, averaged over 3 repeats ( $n = 3$ ) were connected with a line, which is there as a guideline for eyes to obtain a visual effect of the continuous line. The spectra were normalized to the highest value (pH=4.0 CPB).  $\lambda_{exc}=430$  nm,  $\lambda_{em}=470-700$  nm.

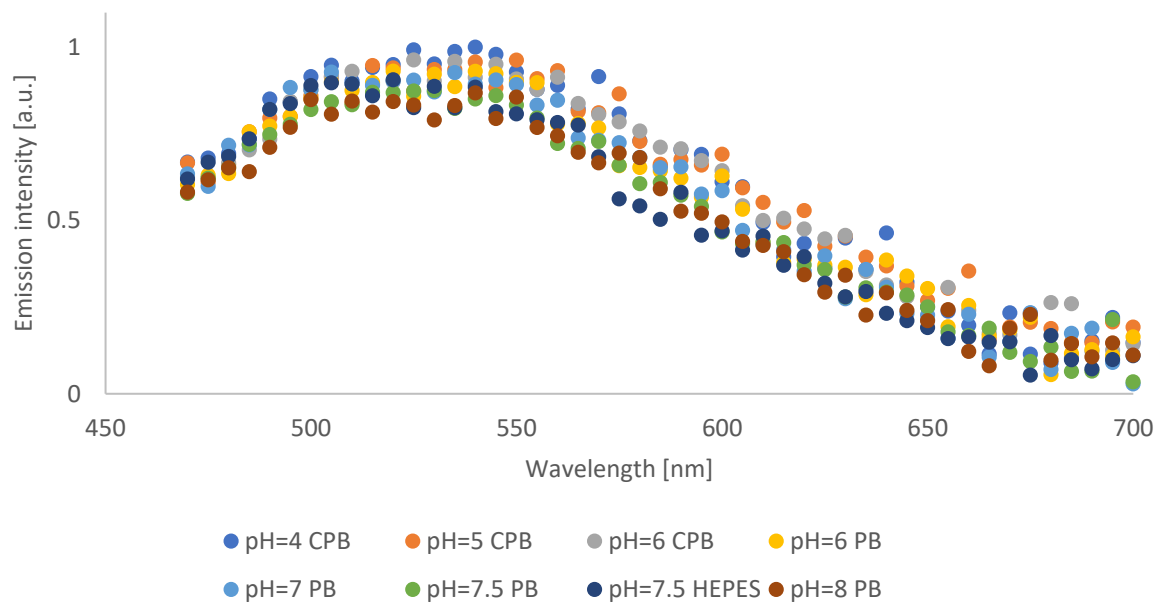


**Figure 121.** The emission spectra of **SOLpH1**-labeled human carbonic anhydrase II at 60 min. The values were normalized to the highest value of emission in CPB pH=4.0. The emission was measured at 5 nm steps. The final concentration of DMSO was kept at 0.5%. Experimental data points, averaged over 3 repeats ( $n = 3$ ) were connected with a line, which is there as a guideline for eyes to obtain a visual effect of the continuous line. The spectra were normalized to the highest value (pH=4.0 CPB).  $\lambda_{exc}=430$  nm,  $\lambda_{em}=470-700$  nm.